UNIVERSITY OF LIÈGE

FACULTY OF APPLIED SCIENCES

Characterization of multiple sclerosis lesioned brain tissues using quantitative MRI

Nora Vandeleene

Supervisor:
Christophe PHILLIPS

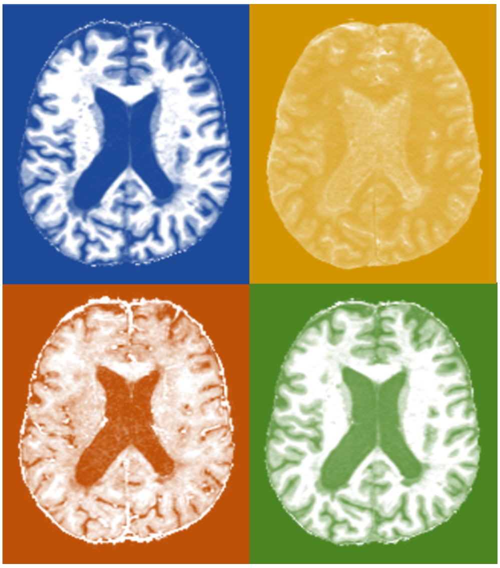

Thesis submitted in partial fulfillment of the requirements for the academic degree of **Doctor of Philosophy (PhD) in Engineering Science**, College of Electricity, Electronics and Informatics

- December 2022 -

Characterization of multiple sclerosis lesioned brain tissues using quantitative MRI

Nora Vandeleene
Master in Biomedical Engineering, University of Liège, Belgium, 2018

Thesis submitted in partial fulfillment of the requirements for the academic degree of Doctor of Philosophy (PhD) in Engineering Science

In the Faculty of Applied Sciences (University of Liège), College of Electricity, Electronics and Informatics

Supervisor

Christophe Phillips, *PhD, GIGA CRC In Vivo Imaging, ULiège, Belgium*

Examining board

Emilie Lommers, *PhD, Clinical Neuroimmunology Unit, Neurology Department, CHU Liège, Belgium*

Laurent Lamalle, *PhD, GIGA CRC In Vivo Imaging, ULiège, Belgium*

Pierre Geurts, *PhD, Department of Electrical Engineering and Computer Science, ULiège, Belgium*

Pierre Sacré, *PhD, Department of Electrical Engineering and Computer Science, ULiège, Belgium*

External examiners

Jeroen Van Schependom, *PhD, Department of Electronics and Informatics (ETRO), Vrije Universiteit Brussel, Belgium*

Muhamed Barakovic, *Department of Biomedical Engineering, University Hospital Basel and University of Basel, & Roche Innovation Center, Basel, Switzerland*

UNIVERSITY OF LIÈGE
- December 2022 -

LIÈGE université
Sciences Appliquées

LIÈGE université
GIGA CRC In vivo Imaging

Acknowledgments

Abstract

Multiple sclerosis (MS) is a chronic, autoimmune, inflammatory, neurological disease of the central nervous system, which affects more than 2 million people worldwide and up to now remains incurable. Nowadays, conventional Magnetic Resonance Imaging (cMRI) is vastly adopted to support the diagnosis and monitoring of MS. In this thesis, we describe a specific protocol of the quantitative MRI (qMRI) family, named multi-parameter mapping (MPM), which improves the characterization of MS-related cerebral processes, compared to cMRI techniques. Those enable the quantification of microstructural properties of tissues in standardized units. With this protocol, 4 parametric maps reflecting MR physical parameters are estimated: magnetization transfer saturation (MTsat), proton density (PD), transverse relaxation rate (R1) and effective longitudinal relaxation rate (R2*). These parameters were shown to be linked to different microstructural aspects, such as the myelin, water and iron content. With their specific ranges of intensities arising from physical measurements, the processing of MPM maps require particular adjustments of the existing tools. The traditional "Unified Segmentation" (US) algorithm, and its derivative "US-with-Lesion", must be adapted to function with these maps, preferably in a multi-channel approach to take advantage of all MPM parameters. A further analysis is conducted to investigate the advantages of MPM-based lesion segmentation over common techniques based on FLAIR and T1 images. Also, the MPM protocol has already proven its efficiency in cross-sectional studies comparing MS patients to healthy controls; here the analysis is extended to a longitudinal setting, with at least two scanning sessions, assessing the evolution of the parameters within normal appearing and lesion tissues. Ultimately, MPM is contrasted to another parametric protocol, from the diffusion MRI family, named "neurite orientation dispersion and density imaging" (NODDI), to determine whether or not NODDI attributes could improve MS-related tissue characterization. The present thesis enters in the list of a variety of qMRI investigations on MS and other conditions working in collaboration to bring closer the implementation of this sequence in clinical settings.

Résumé

La sclérose en plaques (SeP) est une maladie neurologique chronique, autoimmune et inflammatoire du système nerveux central, qui affecte plus de 2 millions de personnes dans le monde, et qui reste jusqu'ici incurable. Actuellement, l'Imagerie par Résonance Magnétique conventionelle (IRMc) est largement adoptée pour le diagnostique et le monitoring de la SeP. Dans cette thèse, nous décrivons un protocole spécifique de la famille de l'IRM quantitative (IRMq), nommé “modélisation multi-paramétrique” (MPM), qui permet d'améliorer la caractérisation des processus cérébraux liés à la SeP, comparé aux techniques d'IRMc, en quantifiant les propriétés micro-structurelles des tissues avec des unités standardisées. Avec l'aide de ce protocole, 4 cartes paramétriques reflétant des paramètres physiques de l'IRM sont estimées : la saturation en transfert de magnétisation (MTsat), la densité de protons (PD), le taux de relaxation transverse (R1) et le taux effectif de relaxation longitudinale (R2*). Il a été montré que ces paramètres sont liés à différents aspects micro-structurels, tels que le contenu en myéline, en eau ou en fer. Avec leurs gammes d'intensités spécifiques dûes aux mesures physiques, le traitement des cartes MPM requiert des ajustement particuliers dans les outils existants. L'algorithme traditionnel Segmentation Unifiée (US), et son dérivé “US-avec-Lésion”, doivent être adaptés pour fonctionner avec ces cartes, de préférence avec une approche multi-canaux pour profiter de tous les paramètres MPM. Une analyse approfondie est réalisée pour investiguer l'avantage de segmenter les lésions avec les cartes MPM plutôt que les techniques traditionnelles basées sur les images FLAIR ou T1. Aussi, le protocole MPM a déjà démontré son efficacité dans des études transversales comparant des patients SeP et des sujets sains; ici l'analyse est étendue vers une configuration longitudinale, avec au moins 2 sessions de scan, évaluant l'évolution des paramètres dans les tissus d'apparence normale et les lésions. Finalement, MPM est contrasté à un autre protocole paramétrique, de la famille de l'IRM de diffusion, appelé “imagerie de la densité et dispersion de l'orientation des neurites” (NODDI), pour déterminer si oui ou non les attributs NODDI permettent d'améliorer la caractérisation des tissus atteints de SeP. Cette thèse entre dans la liste d'un nombre d'investigations de la SeP ou autres conditions utilisant l'IRM quantitative, qui travaillent en collaboration pour rapprocher l'implémentation de cette séquence dans des routines cliniques.

Contents

List of Figures

List of Tables

List of Abbreviations

ARoC	Annual Rate of Change
BG	Basal Ganglia
BIDS	Brain Imaging Data Structure
BOLD	Blood Oxygenation Level Dependent
BPF	Brain Parenchymal Fraction
CDP	Confirmed Disability Progression
CG	Camille Guillemin
CGM	Cortical Gray Matter
CIS	Clinically Isolated Syndrome
cMRI	Conventional Magnetic Resonance Imaging
CNS	Central Nervous System
CRC	Cyclotron Research Centre
CSF	Cerebrospinal Fluid
DGM	Deep Gray Matter
dMRI	Diffusion Magnetic Resonance Imaging
DMT	Disease-Modifying Treatment
DTI	Diffusion Tensor Imaging
DWI	Diffusion-Weighted Imaging
EC	Eddy Current
EDSS	Expanded Disability Status Scale
EL	Emilie Lommers
FA	Fractional Anisotropy

FDR	False Discovery Rate
F_{icvf}	Intra-cellular Volume Fraction
F_{iso}	Isotropic Volume Fraction
FLAIR	Fluid Attenuated Inversion Recovery
fMRI	Functional Magnetic Resonance Imaging
FWHM	Full Width at Half Maximum
Gd	Gadolinium
GM	Gray Matter
GMF	Gray Matter Fraction
GLMM	General Linear Mixed Model
HC	Healthy Control
hMRI	*In-vivo* Histology using Magnetic Resonance Imaging
LF	Lesion Fraction
LGA	Lesion Growth Algorithm
LST	Lesion Segmentation Tool
MCC	Matthew Correlation Coefficient
MD	Mean Diffusivity
MoG	Mixture of Gaussians
MPM	Multi-parametric Mapping
MRI	Magnetic Resonance Imaging
MS	Multiple Sclerosis
MT	Magnetization Transfer
MTR	Magnetization Transfer Ratio
MTsat	Magnetization Transfer Saturation
M_{xy}	Transverse Magnetization
M_z	Longitudinal Magnetization
NABT	Normal Appearing Brain Tissue
NACGM	Normal Appearing Cortical Gray Matter
NADGM	Normal Appearing Deep Gray Matter

NAWM	Normal Appearing White Matter
NEDA-3	No Evidence of Disease Activity
NMR	Nuclear Magnetic Resonance
NODDI	Neurite Orientation Dispersion and Density Imaging
ODI	Orientation Dispersion Index
RRMS	Relapsing-Remitting Multiple Sclerosis
PD	Proton Density
PMS	Progressive Multiple Sclerosis
PPMS	Primary Progressive Multiple Sclerosis
PRMS	Progressive-Relapsing Multiple Sclerosis
qMRI	Quantitative Magnetic Resonance Imaging
R1	Longitudinal Relaxation Rate = 1/T1 (Hz)
R2*	Effective Transverse Relaxation Rate = 1/T2* (Hz)
RF	Radio-frequency
SE	Spin-echo
SNR	Signal-to-Noise Ratio
SPM	Statistical Parametric Mapping
SPMS	Secondary Progressive Multiple Sclerosis
STAPLE	Simultaneous Truth and Performance Level Estimation
TE	Echo Time
TI	Inversion Time
TIV	Total Intracranial Volume
TPM	Tissue Probability Map
TR	Repetition Time
US	Unified Segmentation
USwL	Unified Segmentation with Lesion
VBM	Voxel-based Morphometry
VBQ	Voxel-based Quantification
WM	White Matter

Chapter 1

Introduction

Multiple sclerosis (MS) is a chronic, autoimmune, inflammatory, neurological disease of the central nervous system (CNS), affecting more than 2 million people worldwide. The causes of this pathology have not been established yet; and up to now it remains incurable. Nowadays, conventional Magnetic Resonance Imaging (cMRI) is vastly adopted to support the diagnosis and monitoring of MS. The characterization of pathological substrates related to MS is crucial to identify processes which can be further targeted with therapeutic intervention. One major obstacle is the poor specificity of current cMRI techniques towards the high complexity of the pathology, related to various lesional and tissue repair mechanisms, which can be assessed with histology but not *in vivo* in clinical settings. In addition, histological studies are most of the time performed either on late stages of the disease through autopsies, or in selected and partly atypical early cases, through biopsies [Filippi et al., 2012]. With such techniques the longitudinal assessment of the pathological modifications cannot be conducted. There exists a crucial need for advanced techniques focused on the *in vivo* characterization of tissues deterioration related to MS.

In clinical practice, specific cMRI sequences are of great interest in MS assessment, where both T2-weighted and Gadolinium(Gd)-enhanced T1-weighted MR images are useful. Indeed, T2w images provide measurements of the number and volume of lesions, quantifying the disease burden [Markovic-Plese and McFarland, 2001], while T1w+Gd images help to assess the current disease activity [Price, 2009]. Despite their high sensitivity in depicting white matter (WM) focal inflammatory activity, cMRI sequences are not able to efficiently assess gray matter (GM) lesions or detect diffuse changes in normal appearing brain tissues (NABT). This shortcoming is particularly apparent in the poor correlation of imaging results with short- and long-term clinical outcomes, at least at the individual level [Barkhof, 1999], termed “clinico-radiological paradox".

Quantitative MRI (qMRI) potentially overcomes these limitations by quantifying physical microstructural properties of NABT in standardized units, based on actual physical parameters estimated during acquisition; which modifications may provide information about MS-related microstructural alterations [Tabelow et al., 2019, Callaghan et al., 2014].

Theoretically, qMRI is independent of the scanner used for acquisition, as the parametric images rely on physical measurements of brain tissues. In the real world, the reproducibility is lower than expected, especially for semi-quantitative Magnetization Transfer (MT) maps [Gracien et al., 2020], but still allows quantitative longitudinal studies when identical sequences are used across scanning time points. In addition, qMRI is more sensitive but also more specific to microstructural properties of CNS tissues. Therefore, qMRI represents a good candidate for the analysis and longitudinal *in vivo* monitoring of MS lesions and NABT at the tissue microstructural level.

Thesis content

This thesis project was dedicated to the analysis of different quantitative parameters to study normal appearing and lesion tissues in MS patients brains, in a cross-sectional then longitudinal analysis. Methods and results are divided into five chapters.

The following chapter offers a theoretical introduction to quantitative MRI (qMRI) and to multiple sclerosis (MS) pathology. The two qMRI protocols used in this thesis are "multi-parameter mapping" (MPM) and "neurite orientation and dispersion and density imaging" (NODDI). The MPM protocol arose from an international collaborative effort and enables the characterization of different microstructural properties such as axonal, myelin, iron and water content within cerebral tissues [Weiskopf et al., 2013, Weiskopf et al., 2015], with the simultaneous construction of 4 parametric maps: Magnetization Transfer saturation (MTsat), proton density (PD), transverse relaxation (R1) and effective longitudinal relaxation (R2*) rates. It has already been used to study brain microstructure in various conditions including normal aging [Draganski et al., 2011, Callaghan et al., 2014, Thompson et al., 2018, Carey et al., 2018], brain tumor [Reuter et al., 2020], Parkinson's disease [Depierreux et al., 2021] as well as multiple sclerosis [Lommers et al., 2019, Lommers et al., 2020]. The majority of the results presented in this thesis are derived from this approach. Next to MPM, the NODDI protocol, from the family of diffusion imaging techniques, ex-tracts neurite morphology characteristics through a three-compartment model of cerebral tissues [Zhang et al., 2012], and estimates three parametric maps (among others): orientation dispersion index (ODI), intra-cellular volume franction (F_{icvf}) and isotropic volume fraction (F_{iso}). NODDI measurements have proven their efficiency in characterizing the microstructural complexity of dendrites and axons *in vivo*, both in the case of healthy aging populations [Merluzzi et al., 2016], or neurological disorders such as Alzheimer's disease [Slattery et al., 2017, Parker et al., 2018], Parkinson's disease [Kamagata et al., 2016, Mitchell et al., 2019] and multiple sclerosis [Hagiwara et al., 2019, Schneider et al., 2017, Granberg et al., 2017, Preziosa et al., 2021, De Santis et al., 2019].

The third chapter proposes a description of the MRI data collected for the project, some of it acquired before its beginning. In total, three types of MR images were available for analyses. Beyond MPM and NODDI data, "Fluid Attenuated Inversion Recovery" (FLAIR) images were also acquired, all of them at 3T mostly on site at the CRC (except for a limited number of FLAIR acquisitions). Details about the acquisition parameters, preprocessing procedures, and the various steps for data preparation preceding analysis will be described in the corresponding chapters.

Chapter 4 introduces the segmentation tool employed here: the "Unified Segmentation" (US) algorithm, available in the SPM toolbox[1], then its extension to handle images of lesion brains, i.e. "US-with-Lesion" (USwL). The diverse experiments conducted regarding the method and its parameters were presented as well. First, applying US to healthy brains images allowed to tune specific parameters, i.e. the number of Gaussians used to model the data and the combination of MPM maps, leading to the most accurate tissues segmentation. From there on, the resulting parameters were replicated in the application of USwL on MS patients brains, creating an *a priori* individual lesion mask, which was further compared to the one created from FLAIR images using a more common approach, called "Lesion Segmentation Tool" (LST).

Chapter 5 describes the longitudinal analysis investigating the MPM-measured cerebral microstructural alterations affecting MS patients over time. Seventeen patients were scanned twice, with at least one year separation between sessions, and the evolution of their parameters was evaluated within several tissue classes: normal appearing white matter (NAWM), normal appearing cortical and deep gray matter (NACGM and NADGM) as well as focal white matter lesions. We primarily examined the qMRI parameters annual rate of change between both scanning sessions and found a positive regression to the individual patient dis-

---

[1] `https://www.fil.ion.ucl.ac.uk/spm/`

ease status, suggesting repairs mechanisms in terms of increased myelin content and/or axonal density. As for white matter plaques, MPM parameters within surrounding NAWM showed modifications in term of reduction in MTsat, R1 and R2* combined with increased PD, even before any focal lesion is visible on conventional FLAIR MRI, opening the way for MS lesions growing/apparition prediction tools based on qMRI.

Finally, the last methodological chapter introduces an analysis comparing MPM and NODDI parameters within different tissues, both in global and voxel-based approaches. Median parametric voxels values were extracted in (NA)WM, (NA)GM and WM lesions (in the case of patients) after co-registration of all MPM, NODDI, and tissue *a posteriori* maps. In addition, two multi-modal voxel-based quantification (VBQ) procedures were conducted, evaluating the loco-regional significant differences between MS patients and controls. One included only MPM parameters, the second one gathered all MPM and NODDI maps, in the idea of assessing whether or not NODDI measurements help detect additional cerebral areas with MS-related changes. As the conclusions that could be drawn from our dataset are restricted due to the limited sample size and intra-individual variability, we briefly explored how the three NODDI parameters (ODI, F_{icvf} and F_{iso}) behaved in MS, but mainly by assessing their relationship with MPM indices.

The thesis eventually closes with some general discussion, including limitations and future perspectives of the approaches presented.

Personal contributions

Throughout this project, the main original contributions comprised different aspects, from the development of processing tools targeting specific tasks to the exploration of particular microstructural aspects related to MS. The majority of the data presented in this thesis was acquired several years before its beginning, and a cross-sectional analysis was already conducted and published [Lommers et al., 2019, Lommers et al., 2020].

Raw MPM and NODDI MRI data, as will be described in Chapter 3, are complex with lots of files (per subject) with crucial meta-data. These need to be properly organized but the proposed standard organization for qMRI data was “work in progress” until very recently and no software solution to handle such data was available at that time. Therefore the whole data preparation was developed from “scratch” with in-house scripts, which are now available for other users (Chapter 3). Data and results are also clearly organized, in specific folders for the distinct analyses, allowing potential future researchers to retrieve specific information.

A collection of computationally intensive preprocessing steps was completed for each study, for both types of parametric maps (MPM and NODDI). These comprise maps creation, inhomogeneities corrections, co-registration, segmentation and normalization, embedded within processing pipelines created for specific purposes (Chapter 3). The ultimate goal is to create reproducible and replicable methods. Indeed, these processed data, or the methodology which generated them, may benefit further and possibly inexperienced users for following analysis and save them valuable time.

For example, potential users of an SPM-based tissue segmentation with MPM data might get inspired by the results of Chapter 4, where the traditional US algorithm was tested with MPM maps and the best parameters were investigated. Besides US on healthy subjects, the examinations conducted with USwL could be extended to other patients, with MS or other types of lesions. Although these algorithms were implemented several years before the present project, the multi-channel segmentation using several MPM maps is state-of-the-art.

In addition, in the longitudinal study presented in Chapter 5, although our results should be interpreted with caution due to a number of limitations, our preliminary findings are promising and the study design and considerations may be helpful for the design of further studies with larger, more uniform study cohorts and standardized measurement intervals. Once again, all code is available for following studies, with very few changes required.

Finally, the comparison between MPM and NODDI parameters was a concern for a number of people manipulating these two acquisition types as well. Although the analysis did not highlight unexpected interpretations, these can prevent people from loosing time redoing the same experiments (Chapter 6).

These contributions have lead to the following journal articles:

1. **Vandeleene N.**, Guillemin C., Dauby S., Requier F., Charonitis M., Chylinski D., Balteau E., Maquet P., Lommers E., Phillips C., "Using quantitative magnetic resonance imaging to track cerebral damage in multiple sclerosis: a longitudinal study", currently in revision in *Brain and Behavior*, and available on MedRXiv [Vandeleene et al., 2022].

2. **Vandeleene N.**, Lommers E., Maquet P., Phillips C., "Exploring the relationship between MPM and NODDI measurements in healthy and

multiple sclerosis brain tissues”, in preparation.

Part of this work has also been presented in the following conferences:

1. Vandeleene N., Lommers E., Maquet P., Phillips C., “Comparison of multiple sclerosis lesions segmentation using quantitative or FLAIR MR images”. Poster session presented at OHBM 2020 [Vandeleene et al., 2020]
2. Vandeleene N., Lommers E., Maquet P., Phillips C., “Using qMRI to characterize lesioned tissues in MS patients: a longitudinal study”. Poster session presented at OHBM 2021 [Vandeleene et al., 2021]

Methodological developments were applied to other recent and on-going research projects, also about MS. Some explanations about these are provided in Appendix B.

Chapter 2

Technical and medical background

Contents

2.1 Magnetic Resonance Imaging (MRI)

Magnetic resonance imaging (MRI) is considered one of the most important technical advances of the century, in the medical field, bringing new insights of the human body. It reveals, in a non-invasive way, detailed structures and functions with acceptable resolution and contrast. It does not involve ionizing radiation like other imaging techniques such as radiography and Positron Emission Topography (PET). MRI covers several areas of science and technology, such as quantum physics, biophysics, image reconstruction, and hardware design. All those concepts work together to generate images of the body and brain, through a "pulse sequence". Several types of data can be acquired, the design and parameters of the pulse sequence are designed to fulfill specific imaging needs. The combination of high image quality and risk-free imaging has made MRI one of the most attractive medical imaging modalities.

2.1.1 Physics of magnetic resonance

The MRI signal arises from a physical phenomenon called "nuclear magnetic resonance" (NMR) in some nuclei of the body tissues. A number of atomic and subatomic particles possess a spin angular momentum, characterized by a precession with a specific frequency depending on the particle nature. The NMR phenomenon emerges when the particle is stimulated with an electromagnetic wave at the same frequency of its spin precession. Typically, in MRI, the targeted particles are the protons present in biological systems. Hence, the acquired signal mostly arise from water (composed of hydrogen) and fat (full of protons), which are largely present in body tissues [Prince and Links, 2015].

The MRI signal emerges when the protons with spin angular momentum, or simply referred as "spins", are placed within a large external fixed magnetic field (called B_0), then stimulated with a smaller variable radio-frequency (RF) magnetic field (called B_1). The wave frequency of the varying field B_1 is the same as the protons frequency, for the purpose of specifically exciting those particles. B_0 value lies in the order of the Tesla, while B_1 value is at the nanoTesla scale. In an MRI machine the spins align to the fixed magnetic field B_0. Protons are characterized by a spin quantum number of $\frac{1}{2}$, leading to two distinct levels of energy when they are at equilibrium. They correspond to two possible spin projection quantum number: $+\frac{1}{2}$ and $-\frac{1}{2}$. Thus, the spins align in a "spin up" ($+\frac{1}{2}$) or "spin down" ($-\frac{1}{2}$) configuration, with a respective energy level E_1 or E_2 (with $E_1 < E_2$). Since the number of spins "up" (with lower energy level) is larger than "down", a positive longitudinal magnetization arises along the B_0 axis, noted M_z [Bernstein et al., 2004]. A representation of the spins distribution of populations among possible energy levels in a static magnetic field is shown in Figure 2.1.

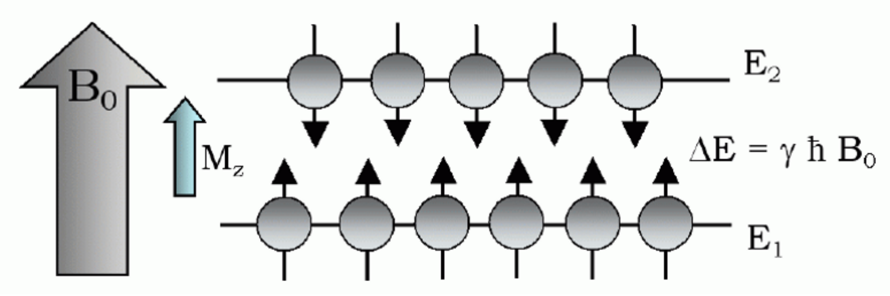

Figure 2.1: Representation of the spins distribution of populations among possible energy levels when a static magnetic field B_0 is applied, resulting in a longitudinal magnetization in the B_0 axis, M_z. This representation is for spin $\frac{1}{2}$ nuclei [Balteau, 2016].

The NMR phenomenon actually emanates as a consequence of the application of the external disturbance to the spins, with the B_1 RF excitation. After this excitation, the spins enter in phase and a transverse magnetization, noted M_{xy} appears in the plane perpendicular to the longitudinal one. In addition, due to the gain of energy, there is a re-distribution of the populations of possible energy levels. Consequently, the number of spins in the "spin down" configuration increases, which reduces the longitudinal magnetization M_z in the B_0 axis. The RF excitation induces a transverse magnetization M_{xy}, then the spins enter in relaxation and return to their equilibrium state. This relaxation phenomenon constitutes a measurable signal for the MRI machine, picked up by a coil of wire located close to the sample.

Tissue contrast originates from different parameters related to NMR, intrinsic of the tissue type. For instance, after the application of the RF pulse, the longitudinal and transverse magnetizations return to their initial condition as the spins move back to equilibrium, i.e. to the lower state of energy E_1 (in the spin "up" configuration) for the longitudinal magnetization M_z, and with a progressive spins dephasing for the transverse magnetization M_{xy}. The increasing M_z back to its equilibrium is termed "longitudinal relaxation", and is characterized by a time-constant T1, the "longitudinal relaxation time". Similarly, decreasing M_{xy} is called "transverse relaxation" and is associated with a "transverse relaxation time" T2, different from T1 (Figure 2.2). Tissues are described by different time-constants T1 and T2 (usually measured in milliseconds), creating contrast between them in the resulting image [Prince and Links, 2015]. T1 and T2 values for the most prominent brain tissues appear in Table 2.1. In Figure 2.2, blue and red lines would correspond to two different tissues.

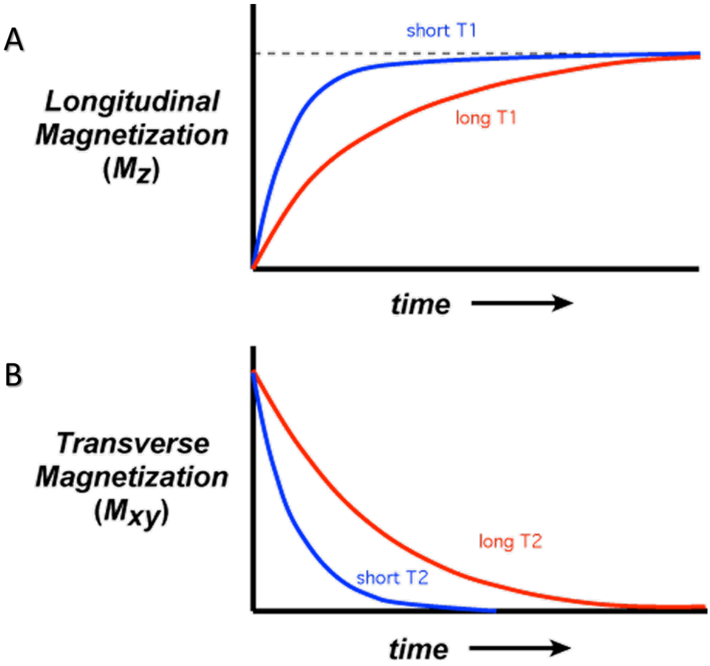

Figure 2.2: Outline of the longitudinal (A) and transverse (B) relaxations after the RF excitation, creating the NMR signal. Time-constants T1 (or longitudinal relaxation time) and T2 (transverse relaxation time) characterize the path back to equilibrium, and are different for each tissue type. Here two tissues are represented in blue and red, each time with short and long T1/T2 [1].

Actually, the T2 constant is only theoretical, the physical decay is more rapid in practice, affected by local perturbations present in the static field B_0. The

	T1 (ms)	**T2 (ms)**
White matter (WM)	500	75
Gray matter (GM)	750	90
Cerebro-spinal fluid (CSF)	3000	200
Fat	200	90

Table 2.1: T1 and T2 values (in ms) for principal brain tissues at 1,5T.

actual transverse relaxation time is noted T_2^* and satisfies the condition $T_2^* < T_2$ (Figure 2.3) [Prince and Links, 2015]. The relationship between the three transverse relaxation rate constants is:

$$\frac{1}{T_2^*} = \frac{1}{T_2} + \frac{1}{T_2'} \tag{2.1}$$

where T_2' is the time constant modelling the transverse magnetization decay due to field inhomogeneities.

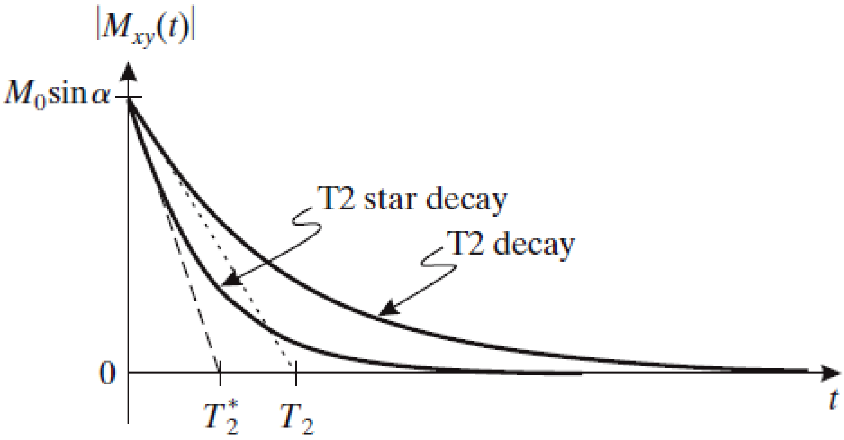

Figure 2.3: Outline of transverse magnetization decay with theoretical T2 and effective T2* time constants [Prince and Links, 2015].

2.1.2 MRI parameters

MRI acquisitions involve a variety of physical parameters, which can be adjusted by the operator or are tissue-dependent and potentially measurable. Therefore, we can divide them into two categories of user-dependent and independent parameters.

---

[1] `http://mriquestions.com/opposite-effects-uarrt1-uarrt2.html`

2.1.2.1 User-dependent parameters

Several parameters can be adjusted during an MRI acquisition, in order to generate different sequences and acquire distinct types of images [Bernstein et al., 2004]. For example, “spin-echo” (SE) sequences are characterized by the application of successive RF pulses, as shown in Figure 2.4 where RF pulses appear as green peaks, one at 90° followed by one at 180°. Such method allows a partial rephasing following the dephasing of spins to improve signal quality. The amplitude and succession of RF pulses is a parameter tuned by the operator.

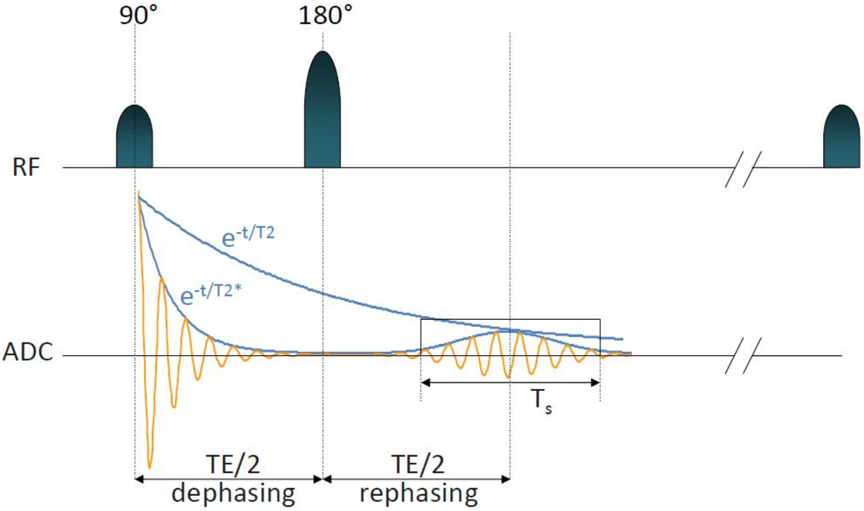

Figure 2.4: Example of a typical MRI sequence called “spin-echo” (SE) sequence, characterized by the application of a 90° RF pulse followed by a 180° one, allowing a spins partial rephasing after the dephasing and thus improving the signal.

Other timing parameters can be chosen by the operator to enhance tissue contrast:

- **The echo time (TE)** corresponds to the time between the first excitation RF pulse and the peak of the NMR signal,
- **The repetition time (TR)** corresponds to the time between successive RF excitations,
- **The inversion time (TI)** is the time between an initial 180° inversion pulse and the subsequent excitation pulse, in a specific sequence called “inversion recovery”.

Many other parameters can be adjusted by the operator for various purposes, such as the flip angle, receiver gain, image scaling etc. Those will not be addressed here as they were not investigated in the present study.

Adjusting user-dependent parameters allows to create different RF pulse sequences generating different contrasts, i.e. the signal highlights one property or another. For instance, combinations of specific sequences can be used to suppress precise tissues appearance, such as fat or water. Calibrating TR, i.e. choosing a small value around 500 ms, generates a T1 saturation effect due to the application of a new RF pulse before the signal reaches equilibrium. Such sequence creates what is called a “T1-weighted” (T1w) MR image. T2-weighted (T2w) images are constructed with another sequence combining a long TR ($\sim$2500ms) and a long TE ($\sim$120ms), while PD-weighted images (PDw) are characterized by a long TR ($\sim$2500ms) and a short TE ($\sim$10ms) [Bernstein et al., 2004]. Those are typical calibration values used in a 1.5T framework, as they depend on the tissue intrinsic parameters (e.g. T1 and T2), which vary with B_0. A visual example of those three types of images is shown in Figure 2.5.

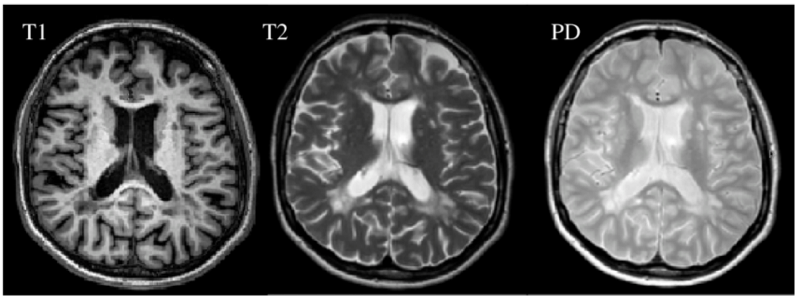

Figure 2.5: Example of three different types of contrasts T1-, T2- and PD-weighted MR images, in the transverse plane.

2.1.2.2 User-independent parameters

A number of other parameters cannot be chosen by the operator and are rather intrinsic of the tissues. Acquired images can be weighted towards one specific metric (such as T1- or T2-weighted MR imaging), but usually the signal measured during the MRI acquisition is a mixture of several of them.

Quantitative MRI, which will be discussed in following sections, aims at separating those parameters to study them individually, using specific sequences. Acquiring “pure” estimates of T1 and T2 can be relevant, and other MR features, such as Magnetization Transfer (MT) and Proton Density (PD), are also of interest. Separating individual measurements of these last four parameters is the basis of the multi-parameter mapping (MPM) protocol applied in this project (see Section 2.2.3 for a finer description).

2.1.3 Hardware

Regarding the MRI hardware, the system is composed of a large gantry with a tunnel through which the subject under study is inserted, lying on the back. Figure 2.6 displays the different components of the MRI machine: one can see the patient position and table, as well as the different devices necessary to acquire the data. The largest component constituting the MRI is the supra-conductive electromagnet generating the static B_0 field, with a typical intensity of 1.5, 3 or 7 Tesla for clinical applications. Signal-to-noise ratio (SNR) is dependent on B_0, in a more than linear relationship. This in turn affects the potential image spatial resolution: higher B_0 means higher SNR and better resolution. The magnetic field arises from a large coil of supra-conductive wire conducting electrical current. The coil produces a magnetic field inside the tunnel it forms. The wire must be cooled down with liquid Helium (around -270°C). Indeed, maintaining a large magnetic field requires a considerable amount of energy, and this is possible using superconductivity, which involves trying to reduce the resistance in the wires to almost zero. The resulting magnetic field is highly stable and uniform thanks to the geometry of the device.

The magnetic field B_1 generating the RF perturbations arises from the radio-frequency transmitter (with a voltage of around 240 Volts) showed in Figure 2.6, and the resulting signal is collected by the receiver (with a voltage of around 1 Volt). In this schematic overview, the transmitter and receiver devices are associated, but usually in practice it is too complicated as they must be protected from each other (due to their different voltage ranges of operation). Most of the time, they are well separated so that the signal can be acquired right after the RF excitation.

Finally, the gradient coils in the three spatial directions x, y and z shown in Figure 2.6 (right) crossed by an electric current induce secondary small fixed magnetic fields. The resulting gradient field distorts the main magnetic field in a slight but predictable pattern, causing the resonance frequency of protons to vary in a function of position. They are needed for the spatial encoding of the constructed image.

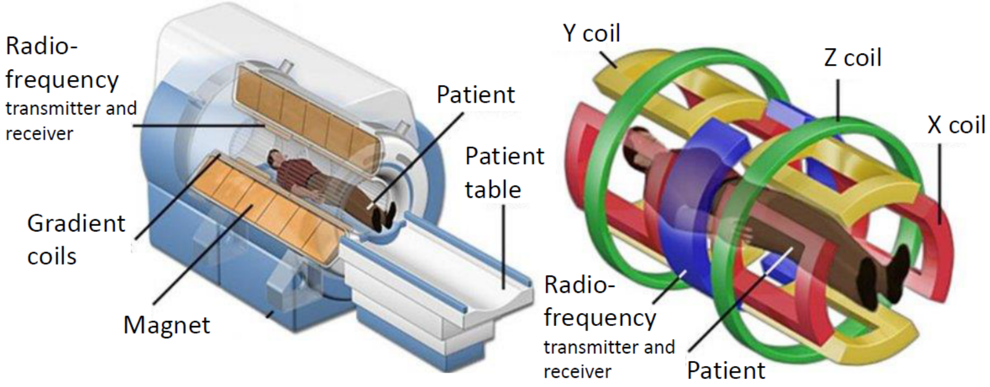

Figure 2.6: MRI hardware design.[2]

2.1.4 MRI main applications

MR imaging has the potential to depict normal anatomy and to detect abnormal conditions in several body organs and anatomical regions [Cammoun et al., 1985]. Here we focus on central nervous system (CNS) applications, comprising the encephalon but also the brainstem and the spinal cord. In clinical practice, structural MRI is mostly used to study body and brain anatomy rather than function. It produces high-contrast cross-sectional images throughout the body, and provides ways to construct images with different tissue contrast by adjusting the pulse sequence parameters in specific configurations. With such techniques different pathologies can be better revealed, such as tumors, strokes or brain lesions.

In neuroimaging, another important MRI application is "functional MRI", or fMRI. In MRI in general, a compromise must be made between spatial and temporal resolution. Structural MRI aims at constructing images with an optimized spatial resolution, and it is primarily used to study brain anatomy. However, in fMRI the focus is put on time resolution in order to study brain function and activity, and in consequence the spatial resolution is rather low. The acquired signal in fMRI is weighted in T2*, and modulated by an effect called "Blood Oxygenation Level Dependent", or BOLD [Logothetis, 2003]. In brief, BOLD reflects neuronal activity through changes in regional cerebral blood flow, volume and oxygenation, following a certain modification in neuronal activity induced, for example, by a stimulus or a task [Glover, 2011]. fMRI has

---

[2] `https://nationalmaglab.org/education/magnet-academy/learn-the-basics/stories/mri-a-guided-tour`

become a powerful research tool which complements anatomical imaging. In other special MRI sequences, the injection of paramagnetic contrast agents and tracers such as Gadolinium can improve the image contrast and help measuring additional functions.

Other widely used MRI advanced techniques comprise angiography, where a contrast agent is administered in order to visualize blood vessels and possibly detect vascular malformations or intracranial aneurysms [Edelman, 1993]; MR spectroscopy, providing metabolite/biochemical information about living tissues [Soares and Law, 2009]; diffusion MRI (dMRI) analyzing the water molecules thermal motion; and quantitative MRI (qMRI) assessing actual MR physical parameters associated to different biological features.

This list is certainly non-exhaustive. The present work is based uniquely on qMRI (actually comprising dMRI), which will be more thoroughly described in sections 2.2.3 and 2.2.4. A visual example for each of these MRI advanced techniques appears in Figure 2.7.

2.2 Quantitative MRI

Quantitative MRI encompasses various specific MRI sequences adjusted to generate precise quantitative maps, typically isolating measurable parameters which can be expressed in physical units. Such applications include magnetization transfer techniques, absolute T1 and T2 measurements (relaxometry) and diffusion imaging.

2.2.1 Principles

Conventional MRI (cMRI) is vastly used in the medical field, providing *in vivo* measurements of brain (and body) tissues and allowing to study many aspects of healthy and diseased inner workings. However, cMRI affords only a qualitative representation of the brain tissues, i.e. simply contrasting different tissue types. For example, in T1w structural MRI, grey matter appears darker than white matter but the numerical values of signal intensities within each tissue are arbitrary, depending on the sequence type and parameters, as well as the hardware and various physical tissue properties [Helms and Hagberg, 2009, Helms et al., 2009]. In addition, cMRI lacks histological specificity of biological characteristics of body tissues. Thus, these cMR images are rather used for visual inspection, or for morphometric studies through contrast-based tissue segmentation, but actual voxels measures usually cannot evaluate tissue biophysical properties. Quantitative MRI (qMRI) provides a solution to this

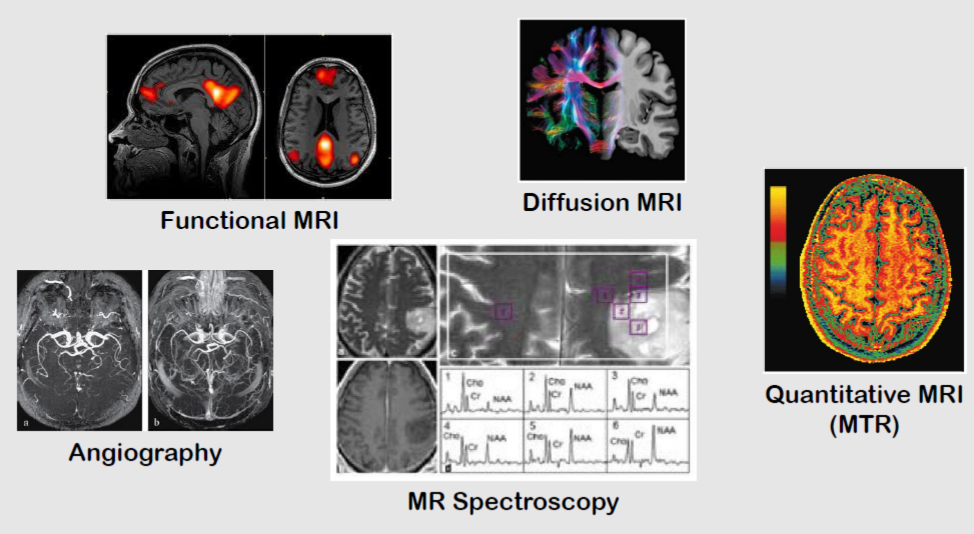

Figure 2.7: Example of some MRI advanced techniques. Functional MRI (top left) aims to highlight specific brain regions reacting to a task or stimulus. Diffusion MRI (top right) allows to display the trajectory of neuronal fibers present in certain brain regions. Here, quantitative MRI (bottom right) is represented by an MTR image, creating special contrast related to tissue microstructure. Angiography (bottom left) is mainly used to highlight blood vessels, and MR spectroscopy (middle left) yields the measurement of specific brain metabolites. See text for extended description.

challenge, by affording quantitative estimates of tissue characteristics, instead of qualitative ones. In this way, voxels designate a numerical value reflecting the physical properties of the tissue types belonging to that particular voxel, quantified in standardized units (e.g. in seconds) [Koenig et al., 1993]. Moreover, several qMRI parameters have been described as correlated to biological contents, such as myelin, water or iron [Cercignani et al., 2018].

2.2.2 Clinical challenge

The term "quantitative" characterizes an MRI approach where maps of meaningful physical or chemical variables are obtained, which can be expressed in physical units and compared between tissue regions and among subjects [Pierpaoli, 2010]. Most imaging studies are not considered quantitative as conventional clinical images rely on a combination of several factors, either specific to the tissue or to the experiment type. cMRI is undeniably beneficial for the diagnosis and prognostic of many clinical conditions, e.g. by detecting focal brain abnormalities revealed by contrast changes, but it lacks of sensitivity regarding global cerebral tissues microstructural alterations. In addition, it is poorly sensitive to the biological substrates inducing image contrast, different biological and/or pathological features might produce similar visual effect on cMR images.

Quantitative MRI aims at separating those factors into individual analyses, thus producing more communal measurements independent of the scanner or the type of experiment [Weiskopf et al., 2013, Tabelow et al., 2019]. Quantitative values in qMRI are not actually directly measured: they are estimated from several MR measurements, within a model of signal behavior. Their standardized nature increases the comparability across sites and time points [Deoni et al., 2008, Weiskopf et al., 2014], and improves the sensitivity of multi-site and longitudinal studies of development, plasticity and disease progression [Tabelow et al., 2019]. Individual factors can be associated to one or several biological features, supporting the characterization of tissue(s) microstructure and thus proposing new and more specific biomarker candidates for various neurological conditions. Quantitative MRI has become increasingly attractive in the field of computational neuroanatomy, for all of these reasons. Differences can be observed between groups of individuals or over time, in term of volumetric changes (e.g. regional atrophy due to aging or some neurological disorder) but also in term of tissue properties in a way similar to PET. One can therefore expect that it will lead to a better definition of the relationship between brain microstructure, function and behavior [Weiskopf et al., 2015].

Although its reliability at diagnostic might not outperform cMRI techniques, at least at the visual level, qMRI provides complementary information about a number of conditions; including it in conventional imaging routines should improve patient clinical description, treatment programming and prognosis.

2.2.3 Multi-parametric mapping (MPM)

One such qMRI acquisition protocol is called “multi-parametric mapping” (MPM). In this sequence, three series of multi-echo images, weighted towards MT, T1 and PD, are collected. From the original multi-echo raw data, four (semi-)quantitative maps can be estimated: magnetic transfer saturation (MTsat), proton density (PD), longitudinal relaxation rate (R1) and effective transverse relaxation rate (R2*), the latter two corresponding to the inverse of relaxation times (1/T1 and 1/T2* respectively) [Weiskopf et al., 2013, Weiskopf et al., 2015]. Those are typically MR parameters intrinsically combined in cMRI sequences, but their individual part yields a finer description of the tissue physical and biological properties. Interpreting the influence of each parameter [Callaghan et al., 2015, Stikov et al., 2015], individually or combined with biophysical modelling (e.g. [Henkelman et al., 2001, Assaf and Basser, 2005]), enables the *in vivo* characterization of important brain tissues features in terms of axonal, myelin, iron and water contents, which is not possible with *ex vivo* histology. For this reason, the term "*in vivo* histology using MRI" (hMRI) was chosen to describe the whole concept [Weiskopf et al., 2015]. In addition of delivering numerical information on the tissue physical and chemical attributes, MPM imaging promotes a more accurate delineation of cortical and subcortical structures in the brain.

2.2.3.1 MPM physical model

The MPM protocol typically involves acquiring six to eight images at different echo times (TE) for each of the PD-, T1-and MT-weighted acquisitions in an RF and gradient spoiled gradient echo sequence, in approximately 20 minutes at 3T for an isotropic voxel size of $1.0mm$. T1w, PDw and MTw images are extrapolated to TE=0 to increase signal-to-noise ratio and remove the otherwise remaining R2* bias. The PDw, T1w and MTw multi-echo signals are modelled with the Ernst equation with an exponential decay based on TE [Ernst and Anderson, 1966, Helms et al., 2008b, Helms et al., 2008a], as shown in Figure 2.8, and allow to calculate quantitative MT saturation, R1 and apparent signal amplitude A* maps. PD maps can further be derived from A* maps, which are proportional to proton density. These quantitative maps are estimated using approximations for small repetition time and flip angles, and then corrected for inhomogeneities from local RF transmit field (f_T). R1 quantitative maps must also be corrected for imperfect RF spoiling using the strategy of [Preibisch and Deichmann, 2009]. The receive bias field map (f_R) is used to correct PD maps for instrumental biases. On the other hand, R2* maps are derived from the ESTATICS model [Weiskopf et al., 2014], gathering the multi-echo data from all three contrasts into a single model, which provides a robust estimation of R2* with a high signal-to-noise ratio. Figure 2.8 displays a schematic overview of these processes for MPM maps creation. On a 3T MRI machine, the spatial resolution reaches $1mm^3$.

Here, we used the hMRI-toolbox [Tabelow et al., 2019], which is a comprehensive open-source toolbox standardizing all the processing steps necessary to generate MTsat, PD, R1 and R2* maps, and providing appropriate spatial processing for groups analysis[3].

---

[3] `http://hmri.info`

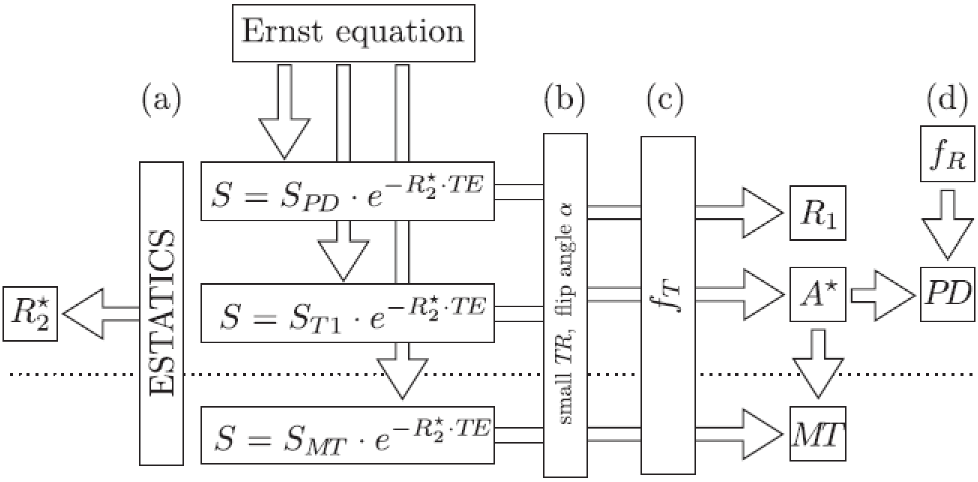

Figure 2.8: Overview of the MPM maps generation based on Ernst equations, as implemented in the hMRI-toolbox [Tabelow et al., 2019].

2.2.3.2 Parameteric maps

The MPM multi-echo protocol was introduced in [Weiskopf and Helms, 2008] and [Weiskopf et al., 2013] for estimating MTsat, PD, R1 and R2*, assembling a number of previous protocols individually creating such maps. Indeed, for a long time, there was a lack of standardized qMRI implementation in the neuroscience and clinical research community to estimate these parameters, despite their great utility. One great advantage of MPM is its ability to construct a 4-dimensional representation of the same brain, partitioning the MR physical parameters.

Magnetization transfer (MT) MT is the physical process by which protons in water molecules "bound" to macromolecules (referred to as "bound water") cross-relax with protons in "free" water molecules (referred to as "free water"). Free water molecules rotate very rapidly, and only a very narrow range of frequencies can be used to observe their transverse magnetization. In bound water, molecules have highly restricted motion. Their transverse relaxation is much more rapid than free water molecules, and the associated T2 value is so short that the direct signal from the decay usually cannot be directly recorded in routine MRI targeting free water protons. To observe MT, one must proceed in the opposite direction by applying an off-resonance (i.e. at a different frequency from the Larmor frequency of free water protons) RF pulse, which primarily targets the pool of bound protons. The bound water spins transverse magnetization becomes saturated, and exchanges of protons between both pools (free water vs. bound water) appear. A portion of the bound water saturated protons are transferred to the free water (and vice versa). In turn, free water protons become partially saturated, and consequently their observable signal, usually largely exceeding the bound protons one, decreases, which creates the MT contrast [Cercignani et al., 2018]. MT is an indicator of myelin and axonal contents within brain tissues, because together they encompass the majority of macromolecular cerebral load [Stanisz et al., 1999, Schmierer et al., 2004, Bjarnason et al., 2005].

MT is typically used to increase the contrast between tissues with different macromolecular contents, and thus, attempts for a quantification of this property have been developed. First, the **"Magnetization Transfer Ratio (MTR)"** was computed as the percentage difference of pixel intensities between two images, one acquired with off-resonance saturation and one without [Dousset et al., 1992]. MTR is characterized as "quantitative" due to its better reproducibility across time-points and subjects, but it does not have a direct biological or physical interpretation. Indeed, MTR is typically under the influence of various acquisition parameters, as well of T1 relaxation, which is particularly important to consider in case of demyelinating lesions in multiple sclerosis where the decrease of myelin can be partially hidden by a T1 increase [Henkelman et al., 2001].

The MPM protocol generates an alternative approach related to magnetization transfer, called **"Magnetization Transfer Saturation" (MTsat)**, which is minimally affected by T1 relaxation and less sensitive to B1 inhomogeneities [Lema et al., 2017]. It is obtained with a linear transformation of the inverse MT FLASH signal, combining PDw and T1w acquisitions, and represents the percentage saturation ensued from one off-resonance pulse during the repetition time. An example of an MTsat image is shown in Figure 2.9(A).

Proton Density (PD) PD relates to the number of MR-visible protons present in the tissues which contribute to the MRI signal [Cercignani et al., 2018]. PD is usually linked to water content, more specifically to free water molecules. Indeed, protons present in lipid membranes or tightly bound to macromolecules are characterized with a very rapid loss of signal, making them invisible in regular MR scans [Fischer et al., 1990, Horch et al., 2011]. In addition, protons present in mobile lipids (i.e. in fat) are MR-visible, but their contribution to PD signal is negligible due to the low presence of such tissues within the brain compared to water [Delikatny et al., 2011]. Therefore, it is commonly accepted to hold PD measurements in terms of water content. Unlike the rest of MR parameters estimated with MPM, PD is not influenced by the strength of the static magnetic field B_0. Analyzing water content signal during development, aging [Holland et al., 1986, Neeb et al., 2006a, Neeb et al., 2006b] or as part of different neurological diseases such as multiple sclerosis [Laule et al., 2004, Mezer et al., 2013], hepatic encephalopathy [Shah et al., 2008], stroke and tumors [Volz et al., 2012] offers an interesting insight of microstructural features regarding tissue water. An example of a PD image is displayed in Figure 2.9(B).

Longitudinal relaxation rate (R1) R1 corresponds to the inverse of the longitudinal relaxation time ($\frac{1}{T1}$). As stated earlier, T1 stands for a time constant, intrinsic to the tissue, characterizing the recovery of the longitudinal magnetization M_z back to equilibrium after the application of an RF pulse. T1 is measured in seconds (usually in the ms range), and thus R1 is measured in Hertz. T1 -and thus R1- measurements are particularly impacted by 1) the free water content [Fatouros et al., 1991, Gelman et al., 2001], 2) the concentration and type of macromolecular content [Rooney et al., 2007] such as myelin [Lutti et al., 2014] and 3) the iron content [Gelman et al., 2001]. These features have different influences on R1: increased water content reduces R1, while increased iron and myelin contents prolong it. A visual example of an R1 map is shown in Figure 2.9(C).

Effective transverse relaxation rate (R2*) R2* is the inverse of the effective transverse relaxation time, $\frac{1}{T2^*}$, which characterizes the transverse magnetization M_{xy} decay back to equilibrium. Actually, T2 is the relaxation rate constant describing the transverse magnetization decay following the application of an RF pulse, and T2* is the actually observed time constant considering the influence of field inhomogeneities [Prince and Links, 2015]. As for T1, T2 (and T2*) are time constants, measured in seconds, and R2* is measured in Hertz. In brain tissues, T2 values are longer in compartments where water moves freely (e.g. in the CSF) and shorter in restricted motion areas, such as in solid or semi-solid components like bone, cartilage, lipids and proteins [Cercignani et al., 2018]. Therefore R2, thus R2*, is an indicator of the presence of myelin and fiber orientation in living tissues [Carey et al., 2018]. But the R2* parameter is mainly influenced by local sources of field inhomogeneities, such as the presence of iron within the tissues [Gelman et al., 1999, Langkammer et al., 2010, Callaghan et al., 2015, Draganski et al., 2011]. R2* is consequently used to estimate iron content in the brain [Haacke et al., 2010, Ghadery et al., 2015], and monitor its load evolution occurring during aging [Cherubini et al., 2009, Péran et al., 2009] or different neurological diseases [Lehéricy et al., 2012, Popescu et al., 2017, Hametner et al., 2013]. An example of an R2* map appears in

Figure 2.9(D).

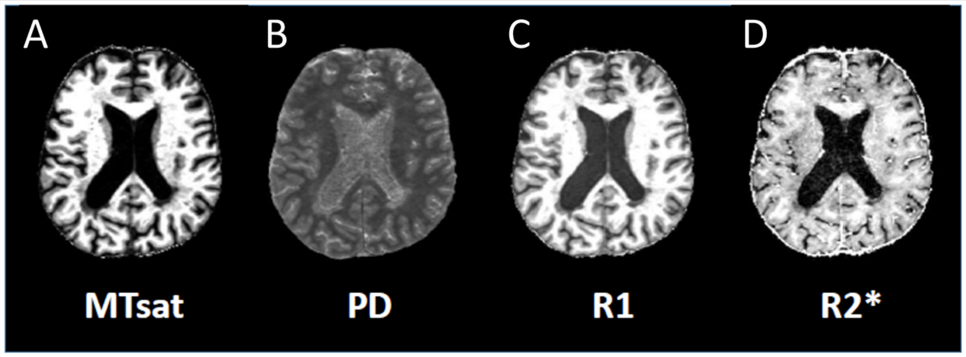

Figure 2.9: Example of quantitative MPM images, showing the 4 parametric maps MTsat, PD, R1 and R2*, in the transverse plane.

2.2.3.3 Biophysical modelling

Quantitative MRI has also brought improvements in the field of computational neuroanatomy, until now primarily based on morphometry measures from conventional MRI. This field of research typically combines brain imaging modalities and computational models to quantify the spatio-temporal dynamics of human brain structures in various conditions such as ageing [Callaghan et al., 2014, Good et al., 2001], Alzheimer's disease [Frisoni et al., 2010] or multiple sclerosis [Ceccarelli et al., 2008]. Habitually, morphometry measures rely on the evaluation of cortical and sub-cortical GM volume and thickness, compared between groups of subjects or followed in a longitudinal setting [Ashburner et al., 2003, Hutton et al., 2009].

However, the changes identified in such way lack of specificity as they might arise from a variation in shape or in image contrast (sometimes due to instrumental artefacts). With its voxel-wise quantitative measures of specific MR parameters combined with an appropriate biophysical modelling of the MR signal, qMRI provides new tools for the *in vivo* characterization of key microscopic brain tissue parameters. For example, with such advanced biophysical modelling, the axonal diameter can be estimated, which could previously only be obtained with *ex vivo* histology. This has opened the new field of *in vivo* histology using MRI, or "hMRI" [Weiskopf et al., 2015].

With this qMRI-based computational neuroanatomy technique, new information about brain microstructure, such as cortical myelo-architecture or axonal properties in WM, can be derived. Using appropriate biophysical models, hMRI offers a multitude of ways to convert MRI and qMRI data into specific biological measures such as myelin density, iron density, fiber orientation or g-ratio (i.e. the ratio between the inner axon radius and the outer, myelinated, axon radius) of myelinated fibers, as shown in Figure 2.10(c) [Stüber et al., 2014]. Going further, hMRI might provide detailed microstructural description of the brain, such as the myeloarchitectonic description of the cortical sheet (Figure 2.10(d)) [Judaš and Cepanec, 2010, Weiskopf et al., 2015].

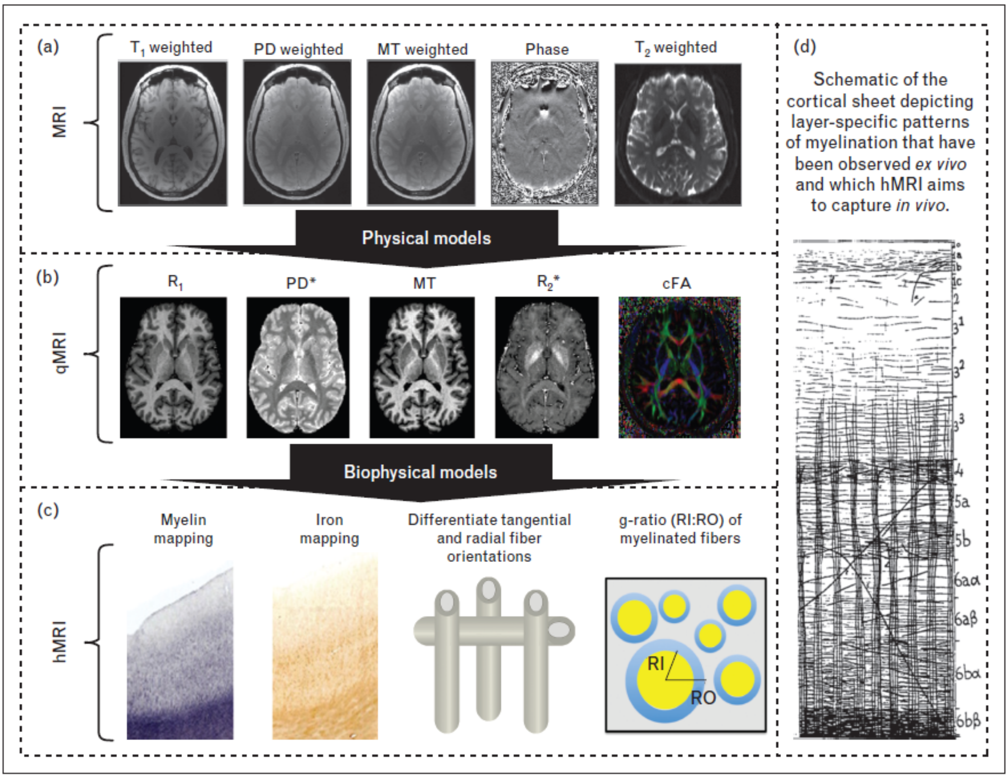

Figure 2.10: From standard MRI to *in vivo* histology using MRI (hMRI). (a) Several types of MRI contrasts weighted towards specific MR parameters (MT, PD, T1, T2, and susceptibility effects as visible in the phase of the MR signal). (b) Quantitative parameteric maps computed from physical models of the MR signal, such as MPM or DWI. (c) Specific biological metrics obtained by converting MRI/qMRI data through biophysical models, here myelin density, iron density, fibre orientation or g-ratio. (d) Myeloarchitectonic description of the cortical sheet [Stüber et al., 2014, Judaš and Cepanec, 2010, Weiskopf et al., 2015].

2.2.4 Diffusion-weighted imaging (DWI)

Beyond the quantification of MR physical parameters, qMRI offers alternative types of metrics, for instance the displacement of water molecules. Diffusion-weighted imaging (DWI) is sensitive to the molecular translational motion of tissue water. In biological tissues, water diffusion encounters different obstacles such as cell membranes and other intracellular and extracellular structures [von Meerwall and Ferguson, 1981]. Therefore, water molecules do not spread out with a Gaussian distribution, but instead their displacement is enclosed by these barriers. The measured signal is established from the volume-averaged propagation of diffusing molecules as they interact with cellular obstacles found in each voxel [Horsfield and Jones, 2002]. With such signal, DWI can provide insights into tissue microstructure by differentiating intracellular and extracellular water molecules displacement (represented respectively by a hindered diffusion with a Gaussian displacement pattern and a restricted diffusion with a non-Gaussian pattern) [Assaf and Cohen, 2000]. The differentiation of intra- and extra-cellular water helps at describing the neurite morphology [Zhang et al., 2012].

For a long time, the most widespread diffusion MRI model was the “diffusion tensor imaging” (DTI), which operates based on a diffusion tensor on each voxel describing their anisotropic diffusion behavior [Basser et al., 1994]. DTI is characterized by a good sensitivity to whole tissue microstructure but a rather poor specificity for individual tissue features [Pierpaoli and Basser, 1996]. Indeed, from the DTI model, simple indices are derived: fractional anisotropy (FA) and mean diffusivity (MD). They constitute two important biomarkers in the study of microscopic changes during normal brain development and aging, as well as neurological disorders, but changes in these parameters cannot always be attributed to specific variation in tissue properties [Zhang et al., 2012].

To overcome such issues, new models have arose, where the signal in a voxel is considered as the sum of contributions from several compartments. For instance, the “composite hindered and restricted model of diffusion” (CHARMED) approach provides a more complete physical description of the diffusion within white matter, where the signal decay observed in white matter is expressed in terms of Gaussian (hindered) and non-Gaussian (restricted) contributions. The hindered diffusion corresponds to the water molecules displacement in the extra-axonal volume (including extra- and intra-cellular spaces), while the restricted diffusion models the displacement in the intra-axonal volume, with a set of cylinders [Assaf et al., 2004, Assaf and Basser, 2005]. In this model, the cylinders are assumed with radii following a gamma distribution and to come together to one or more (crossing) bundles with different orientations. In the "minimal model of white matter diffusion" (MMWMD), the CHARMED model is simplified with a single cylindrical axon radius and a single fixed intrinsic diffusivity for both compartments [Dyrby et al., 2013]. In these two models, parallel cylinders for the intra-cellular diffusion cannot account for complex axonal configurations widespread in the white matter, such as the fanning and bending of fibers [Alexander et al., 2019].

Alongside those techniques, Zhang et al. have developed a technique for *in vivo* "neurite orientation dispersion and density imaging", named NODDI. The three-compartment tissue (intra-cellular, extra-cellular and CSF) model [Zhang et al., 2011] used is sufficiently simple yet complex enough to catch the important features of neurite morphology, such as neurite density and orientation dispersion. NODDI enables the simplification of the orientation-dispersed MMWMD model by designing neurites as a set of sticks rather than cylinders. The algorithm is embedded in an optimal acquisition protocol for clinical settings, with respect to time and scanner hardware constraints [Alexander, 2008].

Here we only present the methodology of the NODDI approach, because it was the only diffusion MRI protocol concerned in the present thesis, although there exist a large number of diffusion-based MRI sequences.

2.2.4.1 NODDI basis

NODDI uses an orientation-dispersed cylinder model associated with a two-shell "high-angular-resolution diffusion imaging" (HARDI) protocol, for which b-values were chosen to be easily achieved on clinical systems. The machine acquires 3-dimensional whole-brain scans with $2mm$ isotropic resolution in approximately 25 minutes [Zhang et al., 2012].

Diffusion imaging is typically performed using diffusion-weighted spin-echo echo-planar (EPI) images. EPI images are particularly sensitive to non-zero off-resonance fields. These fields emerge from 1) the susceptibility distribution of the subjects' head (known as a "susceptibility-induced off-resonance field") and 2) by eddy currents (EC) from the rapid switching of the diffusion weighting gradients (known as an "eddy current-induced off-resonance field"). Moreover, diffusion protocols can be quite long, making it almost inevitable for the subject to move, and result in largely noisy signals. Therefore, raw DWIs must be corrected in two ways: first with a correction of the susceptibility induced distortions, through a "Top Up" approach [Andersson et al., 2003], and then a correction for EC-induced bias and subject movement [Andersson and Sotiropoulos, 2016]. Those two steps help determining the field and any movement which may have occurred between two acquisitions, and correct for it.

2.2.4.2 The three compartment model

Following the bias correction steps applied to raw data, the actual NODDI maps are created using a specific model called "three compartment tissue model", considering individual compartments for 1) free water, 2) intra- and 3) extra-neurite spaces (Figure 2.11). Each compartment affects water diffusion within the environment in a specific way, which produces separate normalized MR signals [Zhang et al., 2012]. The full normalized signal A is as follows:

$$A = (1 - \upsilon_{iso})(\upsilon_{ic} A_{ic} + (1 - \upsilon_{ic}) A_{ec}) + \upsilon_{iso} A_{iso} \tag{2.2}$$

where A_{ic} and υ_{ic} are the normalized signal and volume fraction of the intra-cellular compartment; A_{ec} is the normalized signal of the extra-cellular compartment; and A_{iso} and υ_{iso} are the normalized signal and volume fraction of the free water compartment.

Each compartment is modeled with a certain configuration. The intra-cellular compartment, referring to the space bounded by neurites membranes, is modeled as a collection of sticks (i.e. cylinders of zero radius) to catch the highly bounded nature of diffusion perpendicular to neurites, while unhindered along them [Behrens et al., 2003, Panagiotaki et al., 2012, Sotiropoulos et al., 2012]. The normalized signal A_{ic} can be written as:

$$A_{ic} = \int f(\boldsymbol{n}) e^{-b d_{\parallel} (\boldsymbol{q}.\boldsymbol{n})^2} d\boldsymbol{n} \tag{2.3}$$

where $\boldsymbol{q}$ and b are the gradient direction and b-value of diffusion weighting; $f(\boldsymbol{n}) d\boldsymbol{n}$ gives the probability of finding sticks along orientation $\boldsymbol{n}$; $e^{-b d_{\parallel} (\boldsymbol{q}.\boldsymbol{n})^2}$ gives the signal attenuation due to unhindered diffusion along a stick with intrinsic diffusivity $d_{\parallel}$ and orientation $\boldsymbol{n}$. The orientation distribution function can be modelled with a Watson distribution:

$$f(\boldsymbol{n}) = M\left(\frac{1}{2}, \frac{3}{2}, \kappa\right)^{-1} e^{\kappa (\boldsymbol{\mu}.\boldsymbol{n})^2} \tag{2.4}$$

where M is a confluent hypergeometric function, $\boldsymbol{\mu}$ is the mean orientation and κ is the concentration parameter measuring the extent of orientation dispersion about $\boldsymbol{\mu}$.

Next, the extra-cellular compartment describes the space around neurites and axons, mainly occupied by various glial cells types and cell bodies in the case of

GM. In this compartment, the diffusion of water molecules can interfere with cellular obstacles but is not restricted to them, so its diffusion is modeled with a Gaussian anisotropic displacement. The normalized signal A_{ec} is written as follows:

$$\log A_{ec} = -b\boldsymbol{q}^T \left(\int f(\boldsymbol{n}) D(\boldsymbol{n}) d\boldsymbol{n} \right) \boldsymbol{q} \tag{2.5}$$

where $D(\boldsymbol{n})$ is a cylindrically symmetric tensor with the principal direction of diffusion $\boldsymbol{n}$, based on the diffusion coefficients $d_{\|}$ parallel to $\boldsymbol{n}$ and $d_{\perp}$ perpendicular to $\boldsymbol{n}$. The parallel diffusivity corresponds to the intrinsic free diffusivity used in the intra-cellular compartment, and the perpendicular diffusivity is set with a simple tortuosity model [Szafer et al., 1995] as:

$$d_{\perp} = d_{\|}(1 - v_{ic}) \tag{2.6}$$

Finally, the last compartment referring to the free water fraction, also called the CSF compartment, reflects the space occupied by CSF, which is modeled as isotropic Gaussian diffusion with diffusivity d_{iso} [Zhang et al., 2012].

This model enables the interpretation of the MRI signal in each voxel as the sum of the contributions from the individual compartments composing it. NODDI aims to disentangle the contribution from each compartment, thereby allowing their individualized characterization and isolating various quantitative parameters, described in the following section.

2.2.4.3 Parameters and interpretation

The NODDI sequence generates several quantitative parameters reflecting tissue microstructure and integration:

- The **intra-cellular volume fraction** (referred to as F_{icvf}) describes the density of axons and dendrites, computed based on the intra-cellular compartment described in the previous section.

- The **isotropic volume fraction** (referred to as F_{iso}) describes the free water diffusion, and thus constitutes an indirect measure of CSF [Zhang et al., 2012].

- The **orientation dispersion index** (ODI) describes the degree of the bending and fanning of axons and dendrites widespread throughout the white and gray matter [Zhang et al., 2011]. It is equal to 0 for perfectly aligned straight fibers and to 1 for completely isotropic fibers [Kamiya et al., 2020].

An example of these 3 main NODDI maps appears in Figure 2.11.

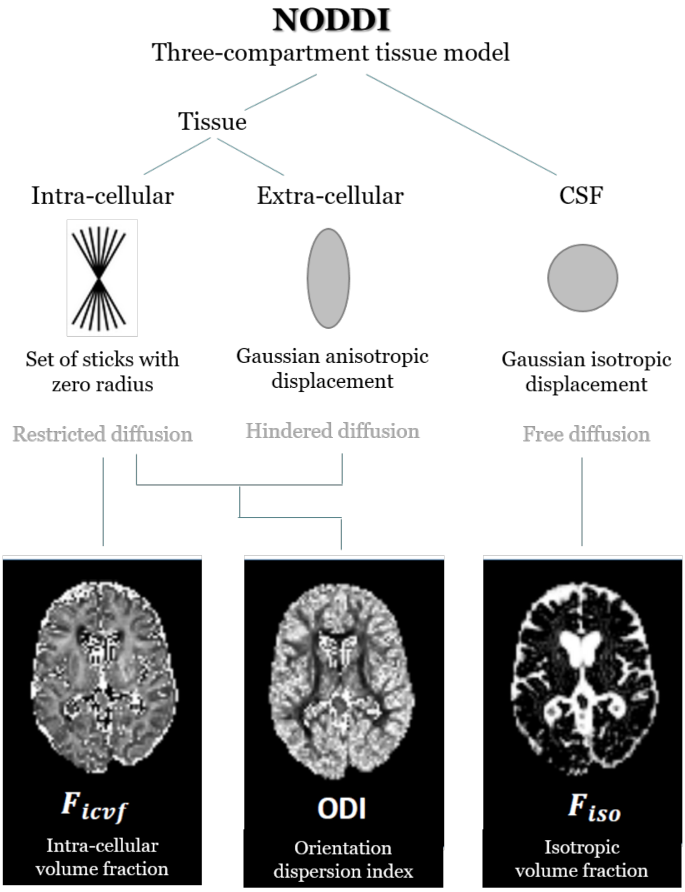

Figure 2.11: Top: Illustration of the three compartment tissue model used to create NODDI maps, showing the three types of compartments and their associated modelling configurations (Figure inspired from [Barritt et al., 2018]). Bottom: Examples of the three principle NODDI maps: F_{icvf}, ODI and F_{iso}, displayed in the transverse plane.

2.3 Multiple Sclerosis

Multiple sclerosis (MS) is a chronic, autoimmune, inflammatory, neurological disease of the central nervous system (CNS), which affects more than 2 million people worldwide[4] and up to now remains incurable. The causes of the disease have not been precisely established yet, it seems to come from a complex interplay between genetic and environmental factors. The pathogenesis of multiple

---

[4] `https://www.nationalmssociety.org/`

sclerosis remains largely unknown [Weinshenker, 1996]. The most frequently reported symptoms include, but are not limited to, sensory and visual perturbations, motor impairments, ataxia, fatigue, pain and cognitive deficits [Compston and Coles, 2008, Reich et al., 2018]. Clinical manifestations are correlated to lesional apparitions within the CNS [Kearney et al., 2015].

The course of MS may reflect the expression of two clinical phenomena: relapses of acute neurological symptoms followed by partial or complete recovery (remission), and progression, which refers to the steady and irreversible worsening of the clinical status. Relapses are mainly the expression of acute, focal, disseminated and recurrent inflammation occurring within the white matter (WM) (i.e. plaques). Tissue deterioration emerges from the interaction between the immune system, glia and neurons [Reich et al., 2018]. Four major categories of patients, based on their disease course, were defined [Hauser and Goodin, 2017, Goldenberg, 2012, Confavreux and Vukusic, 2014] (Figure 2.12):

1. Relapsing-remitting MS patients (RRMS) reflecting the first clinical phenomenon mentioned here above, and affecting about 85% of MS patients,

   Clinical progression can be further categorized into:

2. Secondary progressive MS patients (SPMS) where the disease course continues to worsen with or without periods of remission, developing after an initial period of RRMS form,

3. Primary progressive MS patients (PPMS) affecting about 10% of MS patients, for which the worsening of symptoms occurs gradually from the beginning,

4. Progressive-relapsing MS patients (PRMS), a rare form affecting only 5% of patients, with progressive phenotype from the start, with intermittent flare-ups of worsening symptoms along the way, and no periods of remission.

Most of the time, a progressive clinical course develops in patients from the first category, after typically 10 to 20 years [Reich et al., 2018]. A number of disease-modifying treatments is available to reduce the frequency of episodes of neurological disability as well as the accumulation of focal WM lesions, but nowadays no medication is able to completely prevent (or reverse) the progressive neurological deterioration [Reich et al., 2018, Goldenberg, 2012].

An additional MS disease course can be considered: the “Clinically Isolated

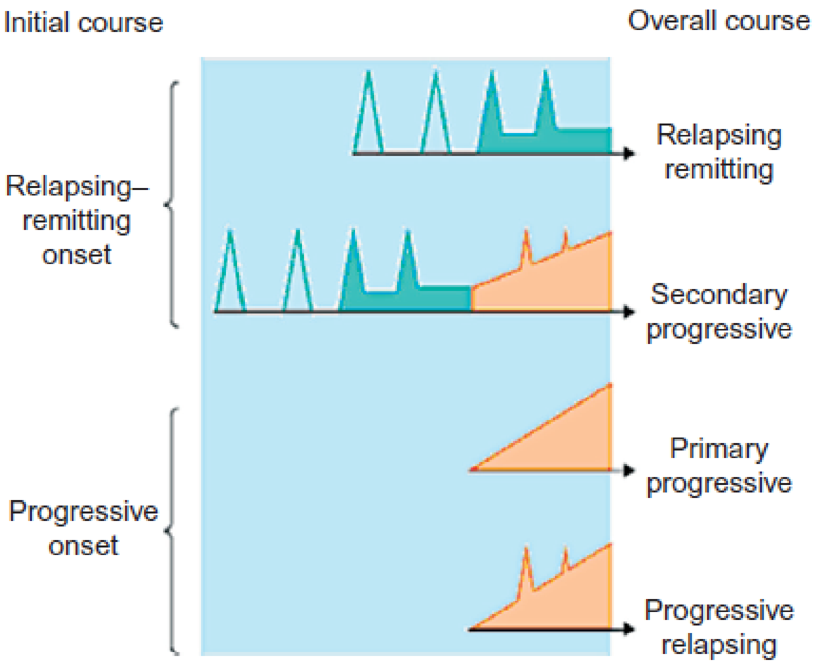

Figure 2.12: Representation of the four phenotypes of MS disease [Confavreux and Vukusic, 2014], sketching the evolution of the clinical state of each type of patients. Peaks symbolize relapses [Confavreux and Vukusic, 2014].

Syndrome" (CIS). It refers to a first episode of neurological symptoms, accompanied with confirmed CNS inflammation or demyelination, which is followed by a complete or partial recovery. Individuals experiencing CIS may or may not go on to develop MS[5].

MS diagnosis and follow-up principally depend on MRI assessments, efficiently depicting focal WM damage and gross brain atrophy. However, despite its great abilities at MS characteristics evaluation, MR imaging only exhibits the tip of the iceberg of the underlying pathogenesis of MS. Anatomopathology analyses remain the leading way for an accurate (yet incomplete) understanding of MS initiation and development.

---

[5] `https://www.nationalmssociety.org/What-is-MS/Types-of-MS/Clinically-Isolated-Syndrome-(CIS)`

2.3.1 Plaques evolution

WM plaques are the pathological hallmark of MS, clearly noticeable in conventional scans, typically composed of areas of myelin and oligodendrocyte loss, as well as inflammatory cells such as lymphocytes and macrophages [Goldenberg, 2012]. Similarly, focal demyelinating damage emerges in GM, but its visual detection is generally more laborious, usually involving advanced sequences and MRI machinery (e.g. at higher magnetic field) [Calabrese et al., 2015]. Lesion emergence involves several levels and can be classified into successive stages based on the presence or absence of inflammatory activity and/or demyelination [Kuhlmann et al., 2017].

Lesions onset New lesions appear with a perivenular cuffing of inflammatory cells (T cells and macrophages), infiltrating across the blood-brain barrier (BBB), which promotes an inflammatory cascade creating injuries such as demyelination, gliosis and neuroaxonal degeneration in previously normal brain tissues [Hauser and Goodin, 2017, Compston and Coles, 2008, Frischer et al., 2009]. Plaques are not restricted to white matter, but are also present in the cortex and deep grey matter, as well as in the spinal cord, the brainstem and the optic nerve [Confavreux et al., 2000, Zivadinov et al., 2016, Filippi et al., 2012, Reich et al., 2018].

Several lesion stages (Figure 2.13) can be recognized based on 1) the composition of myelin breakdown products released by the macrophages on-site, indicating the level of demyelination, and 2) the numerical density of macrophages and microglia, as they slowly exit the lesional area, giving an idea on the age of a given lesion [Kuhlmann et al., 2017].

Active lesions Active lesions are most frequently found in patients with a young disease, sometimes in progressive forms, and their number decreases in frequency with disease duration [Frischer et al., 2015, Kutzelnigg et al., 2005]. They are characterized by a hypercellularity caused by a dense infiltration of microglial macrophages, and an active destruction of myelin sheaths. Such lesions can be further subcategorized into “active and demyelinating” (Figure 2.13.A) and “active and post-demyelinating” (Figure 2.13.B), which refers to the presence (in the first case) or absence (in the second case) of degradation products of myelin components generated by macrophages and microglia in their cytoplasm [Kuhlmann et al., 2017].

Mixed active/inactive lesions In mixed active/inactive lesions, one observes a demyelination accompanied with a hypocellular center and a rim of activated iron-laden microglia/macrophages at the lesion margin [Elliott et al., 2019]. Such lesions are rather rare in patients with early MS, they are usually detected in patients with disease duration of more than 10 years and/or in progressive phenotypes [Frischer et al., 2015].

As for active lesions, a subdivision can be made into "demyelinating" (Figure 2.13.C) and "post-demyelinating" (Figure 2.13.D) with the same characteristics. Mixed active/inactive demyelinating lesions are also termed "**smoldering lesions**", or "**slowly expanding lesions**", in which a chronic tissue loss is observed without other histological signs of acute inflammation [Prineas et al., 2001, Elliott et al., 2019].

Inactive lesions Finally, inactive lesions are identified by a sharp demarcation, a hypocellularity and a quasi-complete depletion of oligodendrocytes, with a marked decreased density of microglia compared to other lesion types and white matter [Hametner et al., 2013]. Macrophages/microglia are not found at the lesion borders, but they form a gliotic scar instead (Figure 2.13.E) [Kuhlmann et al., 2017]. Inactive lesions are most frequently found in patients with a disease duration of more than 15 years and/or in secondary progressive disease course [Frischer et al., 2015].

Diffuse neurodegeneration Besides focal WM and GM lesions, diffuse axonal injury and demyelination with profound microglia activation occurs within normal appearing tissues (NAWM and NAGM), indicating an accumulation of global brain inflammation triggering slowly progressive neural loss with chronicity [Kutzelnigg et al., 2005]. This effect is more pronounced in progressive MS phenotypes but actually present in all forms [Filippi and Rocca, 2007, Enzinger et al., 2015]. Several studies support the concept that structural damage in focal lesions further induces degradation or dysfunction of connected areas in NAWM [Werring, 2000], as well as NAGM atrophy [Sepulcre et al., 2009]. Actually, the progressive accumulation of patient disability and cognitive impairments principally correlates with this early, diffuse and chronic inflammation [Hayton et al., 2009, Rovaris et al., 2008, Ranjeva et al., 2005, Amato et al., 2008].

2.3.2 Biological mechanisms underlying multiple sclerosis

MS is considered autoimmune as its initiation arises from an autoreactive lymphocytes response against CNS autoantigens, but it remains unknown whether the initial inflammatory reaction emerges by itself or in response to primary events impacting the brain cells [Prat and Antel, 2005, Dendrou et al., 2015].

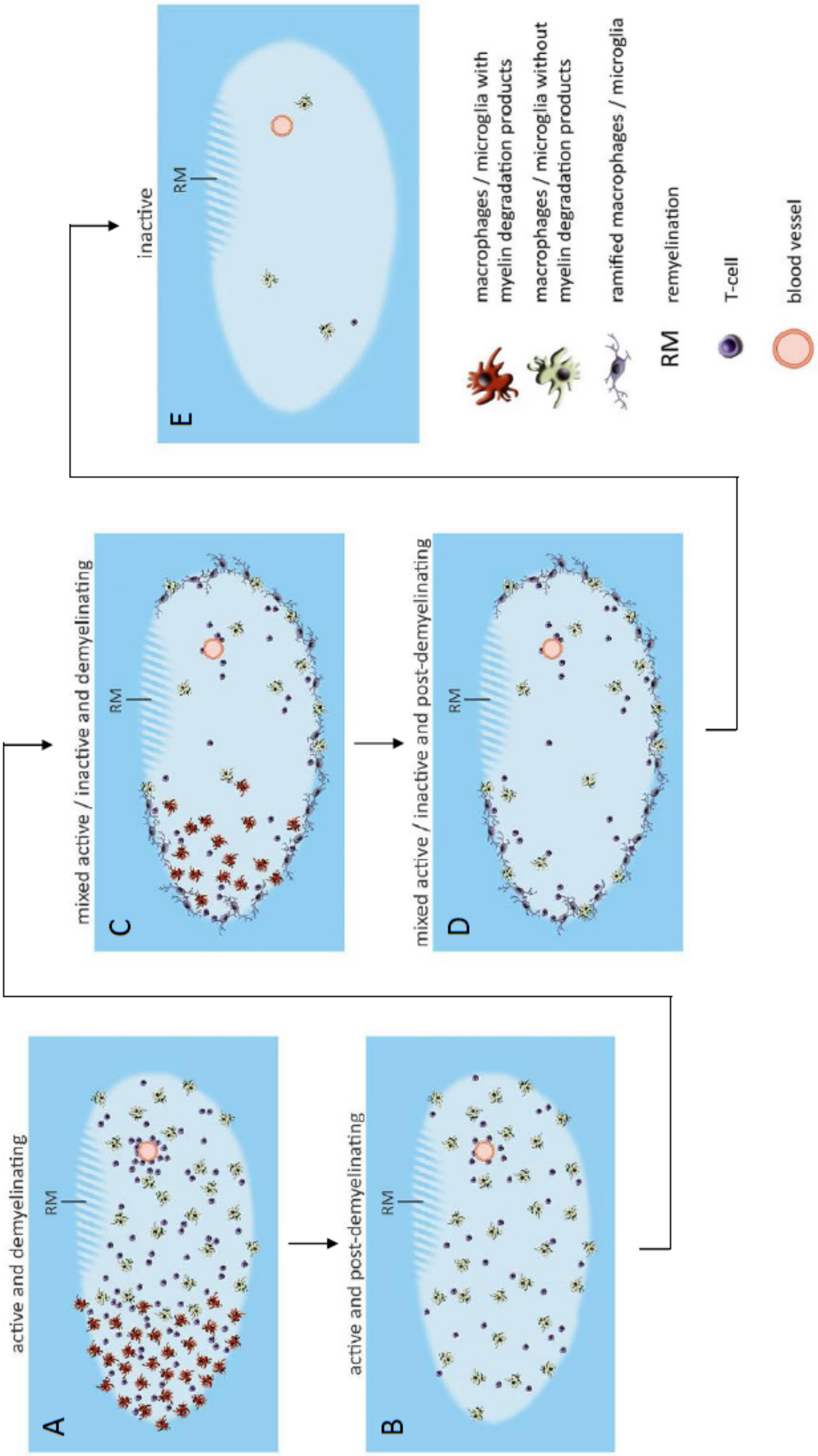

Figure 2.13: Stages of MS lesions [Kuhlmann et al., 2017]

MS-related neuronal damage arises from a cascade of biological mechanisms which were unraveled on the grounds of many previous histological studies. The major phases implicate inflammation, microglial activation, oxidative injury and mitochondrial damage, which are thought to constitute triggers of demyelination and neurodegneration.

Inflammation Initially, inflammation was thought to be the cause of axonal and neuronal degeneration in multiple sclerosis, but this theory was increasingly challenged in the past decades [Frischer et al., 2009]. Studies of MRI combined with spectroscopy reported a very weak correlation between inflammation (picked up by Gd-enhancement) and markers of neurodegeneration such as brain and spinal cord atrophy [Bielekova et al., 2005, Filippi and Rocca, 2005, Anderson et al., 2006]. Instead, neuronal damage and inflammation seem to depict two associated but independent mechanisms related to MS [Trapp and Nave, 2008].

Inflammation is observed at all stages of MS [Frischer et al., 2009]. In the earliest stages of lesion initiation, it starts around small veins and venules in the CNS tissue, and it increases with lesion activity. Inflammation arises from the infiltration of T lymphocytes and macrophages across the blood-brain barrier (BBB), which ultimately closes and, as a consequence, the inflammatory cells remain trapped in the CNS [Hochmeister et al., 2006].

The chronic inflammatory reaction induced by the immune system ultimately triggers a microglia activation, which creates oxidative bursts responsible for a supplementary neurodegeneration [Correale, 2014]. Oxidative bursts have an additional impact on mitochondrias, which start to dysfunction and provoke the destruction of oligodendrocytes by the release of apoptotic-inducing factors (AIF) translocating into the nuclei and inducing irreversible damage into their DNA [Lassmann et al., 2012]. All these events contribute to the development of MS in the CNS.

Iron deposition Iron accumulation is another sub-product of the inflammatory process in the brain. In healthy aging, iron deposition increases over time, and is most prominent after the age of 40-50 [Hallgren and Sourander, 1958, Confavreux et al., 2000]. This age range is considered a milestone for the beginning of MS progressive forms [Tutuncu et al., 2013, Confavreux and Vukusic, 2006]. The maintenance of appropriate iron concentration in the CNS is crucial for the functioning of several biological processes such as oxygen transport, myelination, DNA replication, glucose metabolism and synthesis of neurotransmitters. The majority of stainable iron is contained within oligodendrocytes and myelin [Connor and Menzies, 1995, Todorich et al., 2009].

In mutliple sclerosis, histopathological studies focusing on individual lesions showed that in active lesions, dying oligodendrocytes discharge iron ions which are in turn taken up by microglia and macrophages at the lesion borders [Hametner et al., 2013]. In normal appearing brain tissues, iron accumulation depends on the disease phenotype: patients with a short disease duration (usually relapsing-remitting MS patients) display an age-related increase of iron in NAWM; while progressive MS patients present a significant decrease of iron in NAWM, corresponding with disease duration, and a significant higher iron accumulation in NADGM than NACGM [Haider et al., 2014]. The decrease in NAWM originates from a destruction of oligodendrocytes and myelin, accompanied with an upregulation of iron-exporting ferroxidases associated with chronic inflammation [Hametner et al., 2013]. The *in vivo* monitoring of iron deposition is of great interest for the understanding of pathological mechanisms related to MS.

Remyelination Opposite to the diffuse and focal inflammations in WM and GM, an effective remyelination process arises in some plaques, following demyelination [Brown et al., 2014], but the whole process is not yet well understood. The difficulty of acquiring histopathological data on patients at various disease stages makes it challenging to describe the time course of the evolution of healthy white matter into fully demyelinated lesions [Patrikios et al., 2006]. One longstanding hypothesis proposes that MS lesions routinely remyelinate, although not completely, and the fully demyelinated chronic lesions seen at autopsy are the result of repeated episodes of demyelination in the same tissue [Ludwin, 1980]. Plaques are highly complex and heterogeneous, some of them are subject to remyelination, for others the inflammation resolves by itself [Reich et al., 2018, Frischer et al., 2015]. Treatments promoting neuroprotection by enhancing myelin regeneration would constitute a potential solution to counteract neurodegeneration [Lubetzki et al., 2020]. Recent longitudinal studies suggest that lesions developing in younger patients might repair more effectively [Absinta et al., 2016], but some questions remain unanswered, such as whether remyelination can still occur once a smoldering lesion is established, and whether remyelinated lesions have increased susceptibility to recurrent demyelination [Reich et al., 2018]. There is an important need of new imaging techniques for the *in vivo* monitoring of lesion formation, progression and repair in MS [Wang et al., 2019].

2.3.2.1 Brain atrophy

As a consequence of the irreversible neuronal tissue destruction, an undeniable atrophy of the brain appears in MS patients (Figure 2.18), although it is not pathologically specific to multiple sclerosis [Brück et al., 1997]. It appears from the early stages and progresses throughout the disease course, at a much higher rate than healthy aging cortical atrophy [De Stefano et al., 2010, Eshaghi et al., 2018]. The cutoff between physiological and pathological atrophy was suggested to around -0.4% of annualized percentage brain volume change [De Stefano et al., 2015]. Interestingly, GM atrophy is significantly more important in advanced disease stages, while WM atrophy rates hang in a rather constant way over time [Fisher et al., 2008, Shiee et al., 2012].

Several studies linking brain atrophy to clinical impairments exposed that, as opposed to lesion-load measurements which only partially correlate to physical disability in cross-sectional studies, atrophy measures constitute a stronger (yet moderate) predictor of future disability [Zivadinov and Bakshi, 2004, Dastidar et al., 1999, De Stefano et al., 2007, Fisher et al., 2002, Losseff et al., 1996, Lukas et al., 2010, Miller, 2002, Cagol et al., 2022].

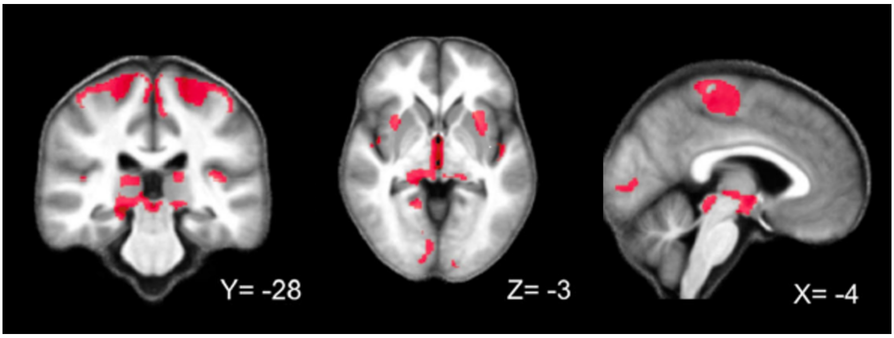

Figure 2.14: Example of a typical cortical atrophy observed in MS patients compared to controls, obtained with a VBM analysis, displaying decreased gray matter (GM) volume in red. [Lommers et al., 2020]

2.3.3 Diagnosis

An early and accurate diagnosis is of great importance in MS as the majority of disease-modifying treatments are accessible for relapsing-remitting phenotypes [Reich et al., 2018]. Historically, diagnosis of MS included both clinical and paraclinical laboratory assessments [Schumacher et al., 1965, Poser et al., 1983], and relied on three different criteria: 1) the space dissemination criterion, met when at least two different lesions (plaques or scars) in the CNS are detected, 2) the time dissemination criterion, implying that at least two episodes in the disease course have occurred, and 3) the inflammation criterion, when a chronic inflammation of the CNS is discovered in cerebrospinal fluid (CSF) analysis [Goldenberg, 2012]. In addition, alternative diagnosis must be excluded.

Nowadays, general guidelines for MS diagnostic are constantly evolving. Those are provided by the International Panel on the Diagnosis of Multiple Sclerosis in the form of a list of criteria called "McDonald criteria" [McDonald et al., 2001], which are now widely used in research and clinical practice. There have been successive versions of the criteria in 2001, 2005, 2010 and 2017 [McDonald et al., 2001, Polman et al., 2005, Polman et al., 2011, Thompson et al., 2018] with different requirements for lesions spatio-temporal dissemination, as current guidance for clinicians and researchers evolves over the years. Presently, MRI enables the detection of both dissemination types with a single acquisition, even in patients who have experienced only one attack of MS-like symptoms. On the MRI scan, one can find evidence of damage in at least two separate areas of the CNS, as well as in two different time points, based on their activity. In some circumstances, the presence of oligoclonal bands in the CSF analysis is sufficient to replace the detection of dissemination in time to confirm the MS diagnosis.

2.3.4 Clinical measures

A large number of clinical measurements exist for the quantification of disability in MS patients and the monitoring of changes in the level of disability over time. The "Expanded Disability Status Scale" (EDSS) is widely used both in clinics and in research. It helps for the assessment of MS patients status, and can be correlated to other manifestations of the disease. The scale was developed by a neurologist called John Kurtzke in 1983 [Kurtzke, 1983] and ranges from 0 to 10 in 0.5 unit increments with increasing disability levels. Scoring is based on an examination by a neurologist.

Another score of disease activity is NEDA-3 (No Evidence of Disease Activity [Pandit, 2019]), a composite of three related measures of disease activity. A score of 0 is assigned in the presence of new clinical relapses and/or MRI activity (new or enlarged lesions visible on FLAIR T2 or Gd-enhanced images) and/or sustained disability progression over six months based on EDSS.

2.3.5 Conventional MRI in multiple sclerosis

Conventional MRI (cMRI) is currently vastly adopted to support the diagnosis and monitoring of multiple sclerosis, considering its sensitivity to the disease, as well as its non-invasiveness, reproducibility and repeatability. cMRI techniques readily depict focal lesions on T2-sequences, such as the "fluid-attenuated inversion recovery" (FLAIR) sequence. This sequence is characterized by a suppression of the CSF signal (in a way that periventricular abnormalities stand out against the hyperintense CSF signal in ventricles) by combining a long inversion recovery sequence with long echo-time [Filippi et al., 1996]. The heterogeneous pathological features of MS, comprising an increased water content accompanied with a decrease in myelin, typically result in increased T2 intensities [McDonald et al., 1992], making T2 sequences the reference for WM plaques examination. With suppression of CSF signal, lesions appear hyperintense in FLAIR images, as shown in Figure 2.15, and their detection is eased with high intensity thresholds. Generally, T2-detected MS plaques aggregate in periventricular, posterior fossa and deep subcortical and juxtacortical white matter, but also in optic nerve and spinal cord [Price, 2009].

Although the FLAIR sequence remains the most suitable technique for the clinical diagnosis, monitoring and prognosis of MS, some T1-sequences have also shown their applicability in those fields, especially standard T1w+Gd MRI. Indeed, a number of factors may create hyperintense abnormalities within the brain, and T2-detected lesions are highly sensitive to MS, but nonspecific. Variations in T2 signal might emerge from various factors, such as edema, demyelination, gliosis and axonal loss [Grossman et al., 1986, Simon et al., 2006, Filippi et al., 1996]. Such poor specificity of T2 lesions partly justifies the weak correlation between brain lesion volume and patient disability [Filippi et al., 1995]. Gd-enhanced MR imaging, however, facilitates the detection of underlying blood-brain barrier (BBB) disruption from active perivascular inflammation [Kermode et al., 1990], and thus the distinction between active and inactive lesions [Lee et al., 1999, Grossman et al., 1986]. As areas of enhancement are transient, T1w+Gd imaging is basically a monitor of disease activity [Miller et al., 1993]. Such T1w+Gd MR technique is compared to a typical T2-weighted image, both illustrating plaques of inflammation/demyelination, in Figure 2.16.

cMRI may display areas of abnormalities suggesting MS, but itself is not sufficient for an accurate diagnosis. Together with the clinical status assessed by the neurologist, spinal fluid testing to estimate the immune system activity, MRI findings constitute a valuable tool for the diagnosis, monitoring, prognosis and

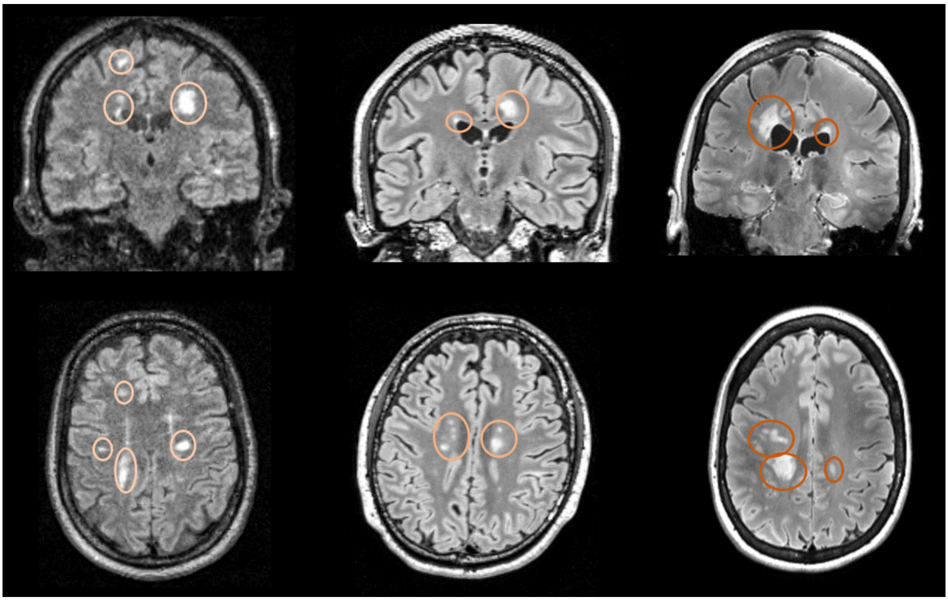

Figure 2.15: Example of three typical FLAIR images (up: coronal plane and down: axial plane), either acquired in clinics at 1.5T (left), or for research at 3T (middle) and 7T (right) for the assessment of MS disease. It can be seen that CSF signal is nulled (ventricles appear darker than the other tissues) while periventricular lesions look hyperintense. Images were acquired either in the CHU of Liège or in the Cyclotron Research Centre, Liège, Belgium. Circles highlight (major) lesions.

treatment planning of MS patients, based on the McDonald criteria [Gracien et al., 2017b]. However, their lack of histopathological specificity to MS substrates points at the necessity of new *in vivo* biomarkers of disease progression and/or response to treatment. Quantitative MRI provides new insights of the cerebral microstructure and could fill the gap between clinical parameters and imaging features.

2.3.5.1 Atrophy-based measures

In addition to focal lesions inspection, cMRI is used to *in vivo* assess cortical and deep gray matter atrophy [Bermel and Bakshi, 2006]. It can either be visually estimated in routine clinical practice, or more precisely evaluated through quantitative three-dimensional measures, typically based on segmented T1w images [De Stefano et al., 2014, Amiri et al., 2018]. Several studies linking brain atrophy to clinical impairment measurements exposed that tissue destruction is an important biomarker of disease progression, bringing additional informa-

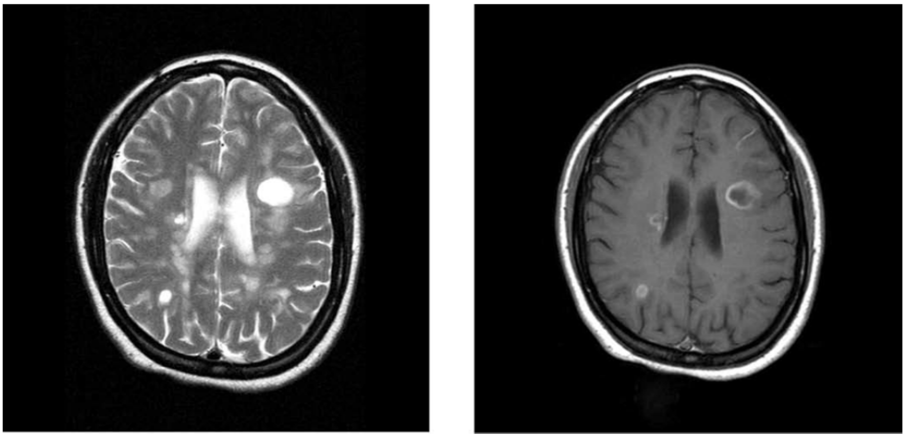

Figure 2.16: Comparison of a typical T2w (left) with a T1w+Gd (right) MR images showing MS lesions in periventricular areas of white matter. In the T1w+Gd image, the juxtacortical location and enhancement are suggestive of active lesions [Price, 2009]. Both images display only the transverse plane.

tion than what can be explained by conventional lesion analysis [Bermel et al., 2005, Dalton, 2004, Ge et al., 2001, Rudick and Fisher, 1999].

2.3.6 Quantitative MRI in multiple sclerosis

In clinical field, conventional MRI remains an important tool for the diagnosis and monitoring of multiple sclerosis. However, its lack of histopathological specificity hinders it at assessing tissue microstructure. Quantitative MRI (qMRI), however, quantifies properties of normal appearing tissues in standardized units, based on actual physical parameters, which are in turn correlated to biological contents [Tabelow et al., 2019]. Modifications in qMRI metrics may provide information about MS-related microstructural alterations.

2.3.6.1 General qMRI parameters

In MS, many cross-sectional studies have probed the cerebral changes occurring in patients compared to healthy controls, considering several MR parameters and patients characteristics (regarding age, disease duration, MS phenotypes, etc.). In addition to better characterizing MS-related microstructural alterations, MR parameters substantially improve the clinical-radiological correlation as compared to cMRI measures of disease [Lommers et al., 2019, Bonnier et al., 2014].

Magnetization transfer imaging MT imaging has been largely employed to quantify the extent of damage in focal WM lesions as well as in normal appearing brain tissues, especially regarding myelin destruction, with MTR measures (see reviews: [Filippi and Rocca, 2007, Ropele and Fazekas, 2009, Enzinger et al., 2015]). In agreement with a large number of studies, MTR is reported to decrease to variable degrees in acute and chronic MS lesions [Bonnier et al., 2014], predominantly in chronic lesions appearing hypointense in T1w+Gd images [Ropele and Fazekas, 2009]. As MTR is known to be correlated to myelin and/or axonal content [Schmierer et al., 2004], such results are consistent with histopathological studies performed on MS brains [Geurts et al., 2005, Seewann et al., 2012], and suggest diverse levels of tissue destruction within different lesion types. Signs of future lesions can be detected in NAWM, as the reduction of MTR is observed days to weeks before the formation of a new lesion [Filippi et al., 1998b].

Beyond and opposite to this MTR reduction, researchers have discovered a percentage of lesions subject to an increase in MTR, during the subsequent 6 months after its enhancement in conventional scans [Dousset et al., 1998]. MTR increase is concomitant with a remyelination mechanism, and is highly dependent on the disease phenotype [Chen et al., 2008, Fazekas et al., 2002].

Within normal appearing tissues, MTR imaging appears to more effectively capture subtle MS-related microstructural changes in NAWM and NAGM [Gracien et al., 2016a, Gracien et al., 2016b, Laule et al., 2003], in which MTR reduction indicates a slow and diffuse demyelination in brain regions which go visually undetected in conventional clinical scans. Such reduction appears in the earliest stages of the disease (e.g. in clinically isolated syndromes) [Fernando et al., 2005, Traboulsee et al., 2002], but is substantially more pronounced in progressive forms.

Contrary to cMRI-derived factors, MTR measurements constitute an indicator of the accumulation of disability in patients and could predict clinical disease evolution, especially in NAGM [Rocca et al., 1999, Agosta, 2006, Ramio-Torrenta, 2006, Traboulsee et al., 2003]. Besides MTR, MTsat was significantly correlated to EDSS and T25FW scores in median whole-brain and NAWM values [Lema et al., 2017]. An appropriate comparison between the sensitivity of MTsat and MTR to MS clinical scores has still to be conducted, but there is preliminary evidence that MTsat in the cervical spinal cord better correlates with disability than MTR [Lema et al., 2017, Bischof et al., 2021]. MTsat preliminary results as part of the MPM protocol are presented in section 2.3.6.2.

Longitudinal and transverse magnetization imaging The longitudinal relaxation time T1 and its rate R1 ($=\frac{1}{T1}$) within the CNS are highly indicative of myelin and water presence, as well as iron but in a smaller degree than T2* (or R2*) [Stüber et al., 2014]. In multiple sclerosis, most of the time, R1 measurements show a similar behavior as MTR (and thus opposite in case of T1), decreasing in normal appearing white and gray matter which indicates a progressive loss of myelin outside of lesions [Neema et al., 2007, Bonnier et al., 2014, Engström et al., 2014, Gracien et al., 2016a], again more pronounced in progressive MS patients; as well as globally decreasing inside lesions [Reitz et al., 2017].

Regarding the effective transverse relaxation time T2* and its corresponding rate R2* ($=\frac{1}{T2*}$), they are mostly correlated to myelin and iron contents (mostly ferritin and hemosiderin), as well as to water content to a lesser extent [Bagnato et al., 2018, Hametner et al., 2018, Langkammer et al., 2010, Stüber et al., 2014]. In MS, T2* (R2*) values were observed to be increasing (respectively decreasing) in NAWM [Bonnier et al., 2014] and NACGM [Gracien et al., 2016b] in patients compared to controls, which could indicate the presence of subtle microedema. An opposite course was observed in NADGM, for which R2* significantly increases [Elkady et al., 2017, Khalil et al., 2009, Khalil et al., 2011, Paling et al., 2012], in a more pronounced way in PMS patients, and with a positive correlation with brain atrophy and disability [Khalil et al., 2011, Ropele et al., 2014]. In agreement with histopathological studies, increased R2* in deep gray matter (less myelinated structures) adheres to an increase in iron concentration. Although, the interpretation of increased R2* values within deep gray matter structures in terms of iron accumulation must be taken with caution [Hernández-Torres et al., 2019, Pontillo et al., 2021]. Indeed, increased iron concentration do not necessarily translate into increased total iron content, i.e. accumulation. With a constant iron content, a diminution of the structure volume (as it is the case with MS-related NADGM atrophy) induces an increased concentration, even without iron accumulation. Thus, it is important to measure both the iron content and concentration to accurately consider accumulation. T2* measures were also shown to decrease in MS lesions [Reitz et al., 2017].

Proton density imaging PD imaging studies alone are rather scarce in quantitative MR studies of multiple sclerosis, and act as complementary material with other investigations instead. PD is predominantly influenced by water content; it was reported to increase in NABT [Gracien et al., 2016a, Reitz et al., 2017] and in lesions [Reitz et al., 2017] in patients compared to healthy controls.

2.3.6.2 Multi-parameter mapping

The MPM protocol as presented in a previous section basically gathers these parameters (MTsat, PD, R1 and R2*) into one session with three consecutive acquisitions, in a relatively short scanning time (around 20min at 3T for $1.0mm^3$ resolution) with whole-brain coverage. This results in four-dimensional data where each voxel is characterized by 4 MR metrics, in the same idea as an RGB pixel in a colored image.

MPM was previously employed to inspect MS-related pathological substrates at the Cyclotron Research Centre, as reported in Dr. Lommers' thesis report [Lommers, 2020] and papers [Lommers et al., 2019, Lommers et al., 2020]. At that point, the focus was put on a cross-sectional analysis comparing MS patients (both RRMS and PMS phenotypes) and healthy controls, which was extended in a longitudinal research for the present work, as described in Chapter 3.

[Lommers et al., 2019] and [Lommers et al., 2020] (Figure 2.17) found a decrease in MTsat, R2* and R1 within NAWM and NACGM; while in NADGM, they observed a decrease in MTsat, but R2* and R1 remained normal. All comparisons were more pronounced in progressive patients. The correlation with clinical parameters was also examined, such as the clinical score EDSS, which was significantly related to R1 in NACGM and R2* in NADGM. Cognitive score was best related to MTsat within lesions [Lommers et al., 2019].

The second study was dedicated to a voxel-based analysis characterizing the topography of GM microstructural and volumetric alterations in MS patients compared to healthy controls (HC), using brain atrophy measures combined with MTsat, R1 and R2*. Three configurations of GM volumetric/microstructural deterioration were identified [Lommers et al., 2020], as displayed in Figure 2.18:

1. Co-localization of GM atrophy with significant reduction of MTsat, R1 and/or R2*, observed in primary cortices,
2. Microstructural changes in hippocampus and paralimbi cortices (reduced MTsat and/or R1 values) without significant GM atrophy,
3. GM atrophy without significant microstructural alterations in deep GM nuclei.

Such results position qMRI as a valuable tool to study multiple sclerosis, investigating the microstructural changes invisible in cMRI scans, and providing insights in the biological and pathological evolution of cerebral tissues. In addition, qMRI metrics correlate to clinical performance, and suggest a diffuse

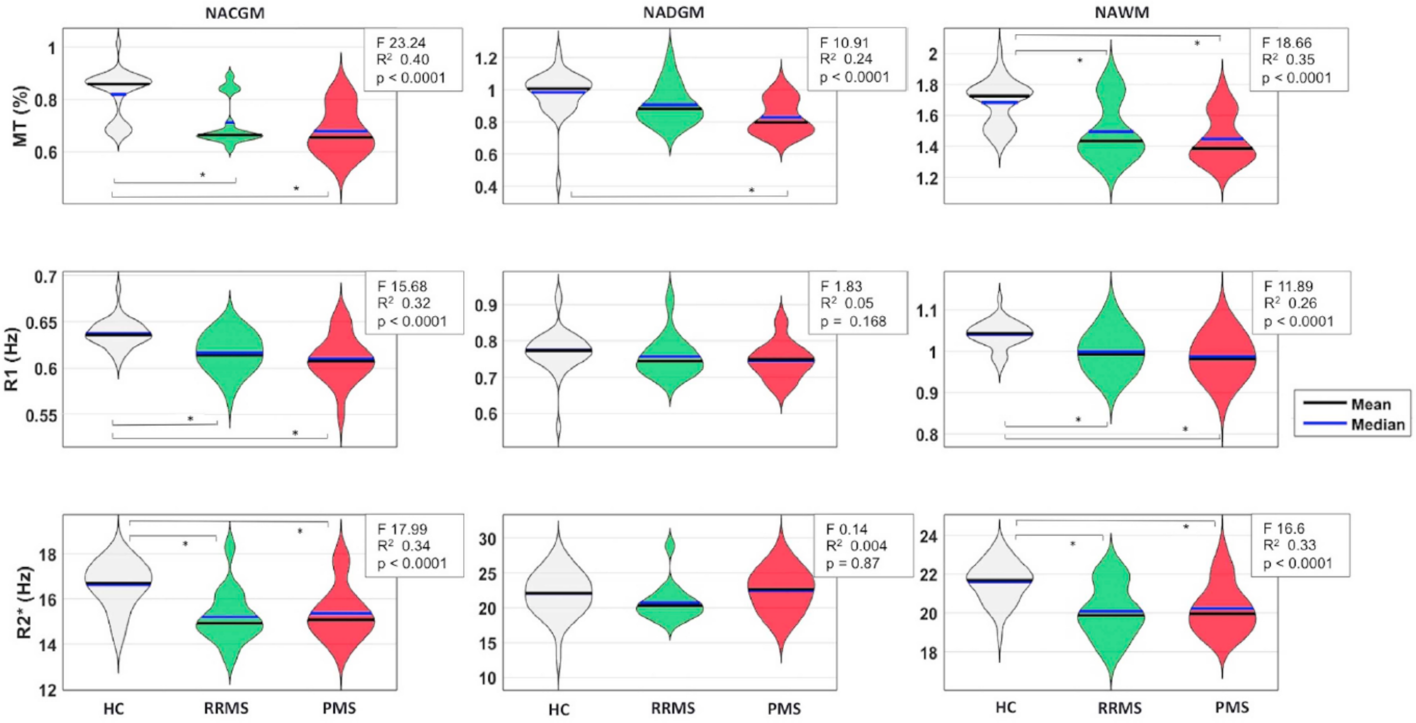

Figure 2.17: Plots and post-hoc results for each MPM parameter (MTsat, R1, R2*) in each tissue class (NACGM, NADGM, NAWM), across the 3 groups of subjects (HC, RRMS, PMS) [Lommers et al., 2019]

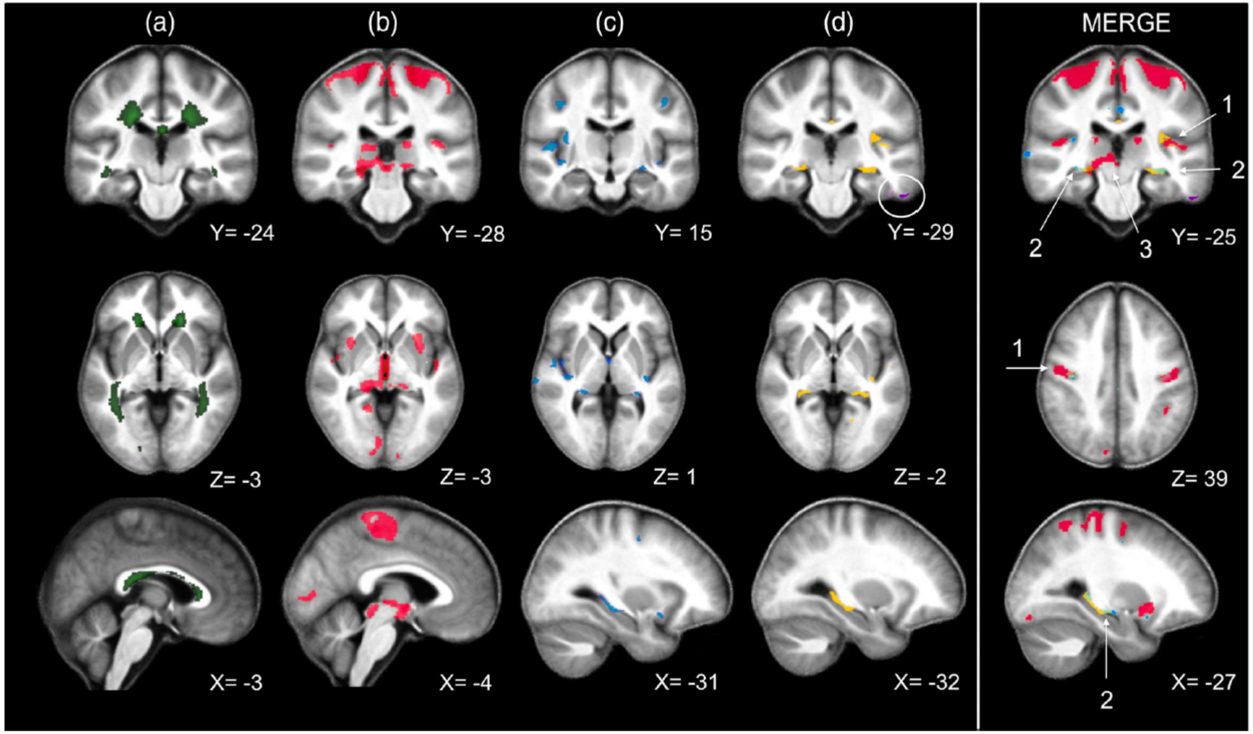

Figure 2.18: VBM and VBQ results from [Lommers et al., 2020] superimposed on the group mean MTsat map. Green: Average WM lesion probability map of MS patients, thresholded at 90% (a); Voxels showing a significant difference between MS and HC: decreased gray matter (GM) volume in red (b), MTsat reduction in blue (c), R1 reduction in yellow and R2* reduction (circled) in violet (d)

reduction in myelin and/or iron content within NABT of patients compared to healthy controls.

In this thesis, the analysis of MS-related pathological substrates was pursued a bit further in a following study assessing MR parameter evolution over time. Indeed, longitudinal quantitative studies about MS are very scarce. A progressive shortening of T2/T2* [Bonnier et al., 2017] or increase in R2* [Elkady et al., 2018, Elkady et al., 2019, Khalil et al., 2015], or a PD and T1 increase within a year [Gracien et al., 2017a] were reported within the basal ganglia, and MTR was reported to progressively decrease in NAWM of MS patients over one [Laule et al., 2003] or two years [Hayton et al., 2012], but longitudinal studies based on the MPM acquisition protocol have not been driven yet.

2.3.6.3 Diffusion MRI

Literature combining multiple sclerosis and diffusion imaging is quite extensive; here the focus will be put on NODDI only, as it was the only diffusion technique investigated in this project.

NODDI NODDI allowed to assess neurite morphology alterations in the CNS [Hagiwara et al., 2019, Schneider et al., 2017, Granberg et al., 2017, Preziosa et al., 2021, De Santis et al., 2019] or the spinal cord [Collorone et al., 2020, By et al., 2017, Grussu et al., 2017]. Yet, regarding the three main parameters under study here, no consensus seems to have been found, as studies report highly dissimilar results comparing MS patients and healthy subjects [Alotaibi et al., 2021].

The **orientation dispersion index** (ODI) refers to the degree of bending and fanning of neurites, and constitutes a relevant component describing the loss of fibers coherence in MS-lesioned tissues. [Hagiwara et al., 2019] and [Schneider et al., 2017] measured an increase in ODI in NAWM of MS patients compared to controls, and a decrease in WM lesions. In opposition, another larger study (in [Schneider et al., 2017] the dataset comprised only 5 patients) showed an increased ODI in lesions and no significant difference in normal appearing tissues comparing patients to controls [Granberg et al., 2017]. Such dissimilarities could be partially explained by the inclusion criteria regarding disease duration, as Granberg et al. 2017 selected only patients with early diagnosis (i.e. $<$ 5 years). This suggests a loss of fiber coherence in early plaques, with relatively preserved axonal density, which leads to an increase in ODI, whereas complete loss of neuronal fibers may cause a decrease in ODI in chronic lesions, due to fewer fibers signals [Hagiwara et al., 2019]. Additionally, [Sacco et al., 2020] estimated ODI in two different types of lesions: Gd-enhancing and non-Gd-enhancing lesions, depicting two levels of activity. They found an increased ODI in Gd-enhancing lesions compared to non-Gd-enhancing, proposing this index as an promising tool for the detection of acute MS inflammation and partially explaining the inconsistency among ODI results. [De Santis et al., 2019] found a trend, however not significant, of reduced ODI in both NAWM and NAGM in patients compared to controls. Therefore, further investigations considering larger and more heterogeneous populations are required to characterize ODI as an accurate biomarker of MS.

The other two parameters correspond to the theoretical compartments designed as part of the NODDI diffusion model: the **intra-cellular volume fraction** (F_{icvf}) with restricted diffusion, related to the density of neurites, and the **isotropic volume fraction** (F_{iso}) describing the free water diffusion [Zhang et al., 2012]. F_{iso} was observed to be higher in NAWM, while F_{icvf} showed the opposite in MS patients compared to matched HC [De Santis et al., 2019, Granberg et al., 2017, Schneider et al., 2017, Collorone et al., 2020, Preziosa et al., 2021], suggesting a destruction of axons accompanied with an edema apparition within normal appearing tissues. [Margoni et al., 2022] reported increasing F_{icvf} in the main white matter bundles in patients compared to healthy subjects, and no significant correlation to the disability measured with EDSS.

F_{icvf} was also reported as decreasing in normal appearing gray matter in patients compared to HC [Rahmanzadeh et al., 2021]. In lesioned tissues, results showed a decrease of F_{icvf} and an increase of F_{iso} in WM lesions compared to the NAWM of the same subjects or from a healthy controls population [De Santis et al., 2019, Schneider et al., 2017]. In addition, [Rahmanzadeh et al., 2021] reported varying F_{icvf} values in different lesions locations: periventricular lesions exhibited lower F_{icvf} values compared to juxtacortical lesions. In white matter lesions, no correlation was found between F_{icvf} measures and EDSS, at least when the entire cohort of patients was considered. However, in patients with clinical deficits (i.e. with an EDSS below 1), the F_{icvf} value was associated to EDSS [Rahmanzadeh et al., 2021].

A decreased F_{icvf} was reported in cortical lesions compared to the NAGM of the same patients or from a healthy population [Preziosa et al., 2021] [Rahmanzadeh et al., 2021].

Longitudinal studies assessing cerebral microstructural changes in patients with multiple sclerosis reported an unexpected increase of F_{icvf} in NAWM and WM lesions over one year, compared to matched controls [York et al., 2022]. F_{iso} showed no significant changes in NAWM, but a significant raise in lesions. A biological interpretation of this observed increase in F_{icvf}, while no change in F_{iso} could partly arise from axonal swelling [Moll et al., 2011], axonal bundling or changes in cytoskeleton composition after demyelination [Brady et al., 1999], or axonal repair [York et al., 2022]. In [Sacco et al., 2020], at follow-up after one year, previously Gd-enhanced lesions showed two different kinds of behavior regarding F_{icvf}: some were increasing, and the others were decreasing. This observed heterogeneity might correspond to different levels of severity and clinical recovery following an acute phase. In the same study, they reported a significant increase of F_{icvf} in NAWM of MS patients compared to healthy subjects [Sacco et al., 2020].

2.3.6.4 Limitations

The major limitation associated with quantitative MRI analysis is the lack of histological validation that voxels classified as lesions, based on qMRI measurements, actually correspond to lesioned tissues. Histopathological studies on cadavers of patients with multiple sclerosis are required for that, as it was performed to assess the pathological sensitivity of FLAIR imaging [Geurts et al., 2005,Seewann et al., 2012]. One validation procedure for the qMRI-based lesion detection would be to conduct a similar study, by comparing qMRI-detected lesions to the true lesion histopathological segmentation, and confirm/infirm whether qMRI is more accurate at detecting lesions. Also, correlations between histological findings regarding tissue microstructure and the MPM protocol have not been investigated yet. Although such studies were performed with similar individual estimates of MR parameters (i.e. other sequences than MPM), a histological validation of the MPM measures is missing. However, such analyses are limited to the fact that quantitative parameters considerably vary before and after fixation of the cadaver brain with formalin [Schmierer et al., 2008, Jonkman et al., 2015].

Other limitations include, but are not restricted to, the lack of fully automatized tools and standardization of MRI acquisition parameters across centers, the absence of large longitudinal studies to define normative value and pathological cut-offs, the difficulty of integrating the method in clinical protocols, and the risk for errors from the user. Indeed, the MPM sequence is not (yet) broadly available on clinical machines, and it requires several steps for the construction and processing of quantitative maps, increasing the risk of miscalculation for inexperienced users. Moreover, clinical settings introduce additional complications, such as the difficulty of organizing several scanning sessions separated in relatively short time periods for longitudinal analyses, considering that some patients might die before the end.

This thesis is part of a collection of qMRI investigations on multiple sclerosis and other conditions which aim at brining the multi-parameter mapping protocol within clinical frameworks, despite the current limitations.

Chapter 3

Data description

Contents

Analyses performed in this thesis relied on data from two datasets, acquired by Dr. E. Lommers (EL), as part of a clinical study relying on multimodal and quantitative assessment of progressive forms of multiple sclerosis [Lommers et al., 2019, Lommers et al., 2020], and Dr. C. Guillemin (CG), conducting a study evaluating the cognitive load on cognitive fatigue in early MS [Guillemin et al., 2022]. Therefore the number of MS patients and healthy controls, their demographic and clinical profile, as well as the type of images differ in each line of research.

One intrinsic limitation of the current dataset (regarding only EL data) is that the acquisitions were conducted on two different MRI scanners: either on a 3T head-only MRI-scanner (Magnetom Allegra, Siemens Medical Solutions, Erlangen, Germany), which later was replaced by a 3T whole-body MRI-scanner (Magnetom Prisma, Siemens Medical Solutions, Erlangen, Germany). In certain analyses, e.g. for the longitudinal study, only subjects scanned on the

Prisma MRI were included. Theoretically, MPM data are independent of the scanner used for acquisition, as the parametric images rely on physical measurements of brain tissues, but in the real world the reproducibility is lower than expected. Consequently, in some sections where very precise qMRI measures comparisons were desired, we decided to investigate MPM-based processes when identical protocols are used across subjects and scanning time points (i.e. with the MRI Prisma).

3.1 Population

For the three studies (Chapters 4, 5 and 6), patients and healthy controls were selected from E. Lommers' study, which included in total thirty-six patients, recruited at the specialized MS outpatient clinic of the CHU Liège, Belgium, with a diagnosis of MS according to McDonald criteria 2010 [Polman et al., 2011]. The inclusion criteria were (1) age between 18 and 65 years ; (2) EDSS inferior or equal to 6.5 ; (3) absence of relapse within the previous four weeks ; (4) compatibility with MRI. The whole study was approved by the local ethic committee (approval number B707201213806). Patients were divided into relapsing-remitting MS (15 RRMS) or progressive MS (primary and secondary progressive 21 PMS) subsets. Twenty-one patients were receiving disease-modifying treatments (DMT; 11 first lines, 8 second lines, 2 non-validated therapies). Thirty-six healthy control (HC) participants, matched for age and gender, free from neurological or psychiatric disorder, followed the exact same experimental protocol. Written informed consent was obtained from all participants [Lommers et al., 2019].

For the longitudinal analysis (Chapter 5), in addition to EL dataset, 8 supplementary MS patients were recruited from a different study taking place at the CRC, in order to increase the small available sample size. Those participants came from C. Guillemin project, comprising in total nineteen MS patients. Every participant presented either a RRMS or a Clinically Isolated Syndrome (CIS) course of the disease, according to the 2017 McDonald criteria [Thompson et al., 2018]. Inclusion criteria comprised (1) age between 18 and 45 years ; (2) disease duration below or equal to 5 years ; (3) absence of relapse for at least 6 months prior to the study ; (4) EDSS score between 0 and 4 ; (5) compatibility with MRI. The exclusion criteria included the existence of other neurological or psychiatric diseases, a history of mild or severe traumatic brain injury, the use of medication impacting fatigue state and/or alertness, substance abuse, colorblindness and native language other than French. The whole study was approved by the local ethics committee (approval number B707201835630). As these patients were scanned only once during CG study, follow-up scanning sessions were scheduled. One subject, out of the 8 additional ones, had to be rejected due to poor image quality.

First study (Chapter 4) In summary, the first analysis assessing the advanced segmentation method, called "US-with-Lesion" (USwL), involved on one side 25 healthy controls, and on the other side 36 patients with multiple sclerosis from E. Lommers' dataset. For optimal conditions, the images acquired with the Prisma MRI only were selected (hence the 25 and not 36 controls). For USwL, unlike the first US parameters estimation study, we decided to keep all the subjects (i.e. from both Allegra and Prisma MRI scanners).

Second study (Chapter 5) For the second study investigating the longitudinal evolution of qMRI parameters, the entire dataset contained 10 patients from E. Lommers' study, from which we adjoined 7 additional patients from C. Guillemin's research. All patients were followed up and scanned twice on the same 3T MRI scanner (i.e. Prisma), every 1 to 3 years. A restricted number of patients (3 in total) were scanned three times. For each of the 17 patients with multiple sclerosis, data from two or three MRI sessions were available, at T0 and T1, separated by a median time interval of 30 months (range: 14-61).

Third study (Chapter 6) The final study comparing MPM and NODDI parameters included 17 MS patients and 15 healthy controls from EL study. The number of participants was limited by the NODDI protocol and MRI machine, which were not identical among all participants (initially 36). In addition, a few subjects did not undergo all acquisitions and MPM or NODDI data were sometimes missing.

A visualization of the data retained for each study appears in Figure 3.1. Demographic data for each individual study appear in Table 3.1.

3.2 BIDS formatting

The first step prior to any processing was to convert acquisitions filenames and metadata from their raw MRI outputs into a structured arrangement called "Brain Imaging Data Structure", or BIDS[1]. This configuration was proposed due to the lack of organization in neuroimaging experiments naming, resulting in complicated datasets which can be arranged in many different patterns. Moreover, associated DICOM headers come with major drawbacks too: 1) they are very long with much acquisition details not useful for processing, and 2)

	Brain tissues segmentation		**MS longitudinal study**	**MPM and NODDI**	
	MSHS N = 25	MSPA N = 36	MSPA N = 17	MSHS N = 15	MSPA N = 17
Age, y, median (range)	50.46 (33 - 63)	45,69 (22 - 65)	36 (25 - 65)	49.93 (40 - 63)	48.29 (28 - 65)
Sex F/M	16/9	21/15	7/10	9/6	9/8
MS phenotype (RRMS/PMS)	N/A	15/21	11/6	N/A	7/10
Disease duration, y, median (range)	N/A	13 (0.5 - 35)	3.4 (0.3 - 28)	N/A	14.5 (0.5 - 28)
EDSS, median (range)	N/A	4.0 (1.0 - 6.5)	2.5 (1.0 - 6.5)	N/A	3.5 (1.0 - 6.0)

Table 3.1: Demographic data for the three main studies

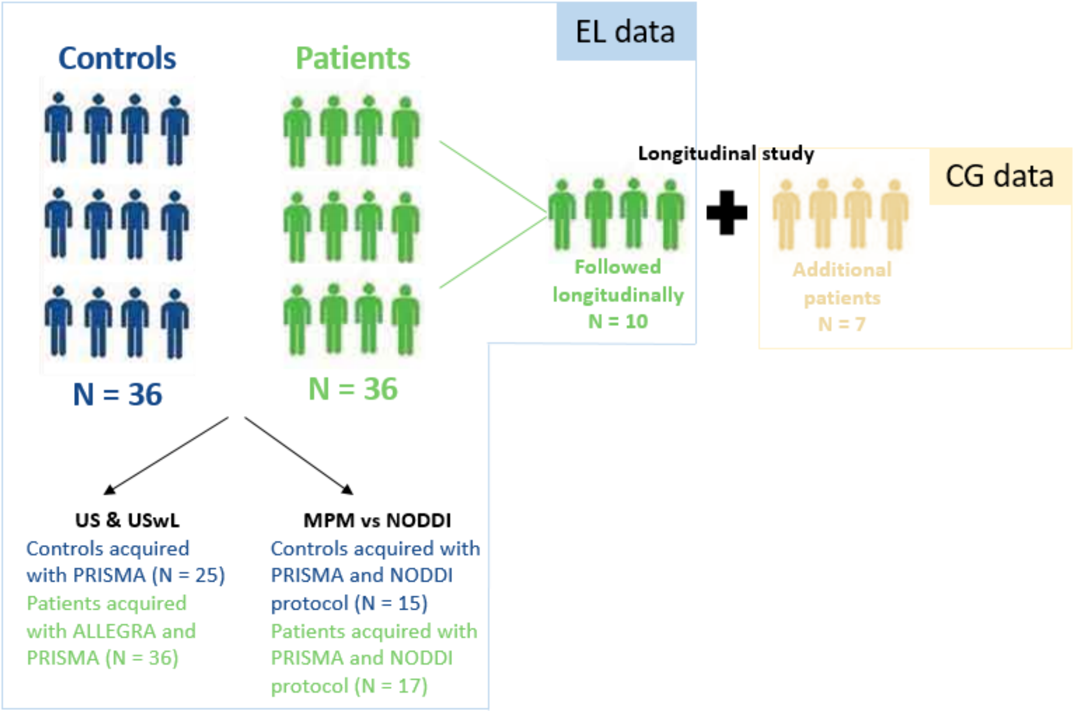

Figure 3.1: Visualization of the data retained for each of the three studies. The larger portion came from E. Lommers' dataset (EL data). In this sample, 10 patients were followed longitudinally. The acquisitions parameters were not stable, patients and controls were acquired either on the ALLEGRA or PRISMA MRI, and the same NODDI protocol was not always used. For the longitudinal study only, additional patients were recruited from G. Guillemin dataset (CG data).

their format is system and sequence specific. A standardized metadata structure with clear and fixed ontology is of great interest, as proposed in BIDS. In addition of improving data structuring, BIDS format enables data sharing in a simple, easy to adopt and organized way. Behavioral data and various other modalities can also be included in this standard. In some circumstances, BIDS-arranged data can be published in an anonymized way, but it requires a "scramble face" procedure beforehand to prevent face reconstruction. However, for patients with distinctive lesion pattern, such as in our situation, a complete anonymization is unachievable.

The principle of BIDS format is to rearrange data into hierarchical folders, each of them providing information about the type of images stored inside. Basically, data are categorized into studies, then into subjects individual folders (each subject is associated with a new and unique ID). Subdivisions are also made at the session level (indicating the session number) where necessary, and at the modality level, when acquisitions encompass more than one modality. Files and metadata are stored in the final branch. In addition of being classified into specific folders, data filenames are modified in order to contain information about the acquisition type. A complementary metadata file is constructed describing the bare minimum of parameters useful for a proper description of the type of data and for further processing.

For example, in our MS dataset including two sets of subjects, several sessions, and different types of acquisition, it typically consists of a tree structure (Figure 3.2) where the first level describes the type of subject (MS patients and HC), each containing individual subjects folder named after their unique ID. It should be noted that this level of separation between patients and controls was added specifically in our study to ease the (re)use of both groups of subjects across various analyses (e.g. in the longitudinal study we used only MS patients data), but does not actually belong to the BIDS official directives. In individual subject folders, a division is made for the acquisition sessions (session 1, session 2, etc.). The following level consists of a separation into acquisition types (for instance, anatomical or diffusion images). Inside those last folders, data is organized with the rest of the important information included in their filenames (e.g. in the MPM protocol the echo time is specified). An example of our data arrangement appears in Figure 3.2, demonstrating the ultimate filenames of the MPM maps. Prior to any further processing, data gathered from the different studies was converted to BIDS format.

It should be noted that BIDS specifications for MPM data were still under con-

---

[1] `https://bids.neuroimaging.io/`

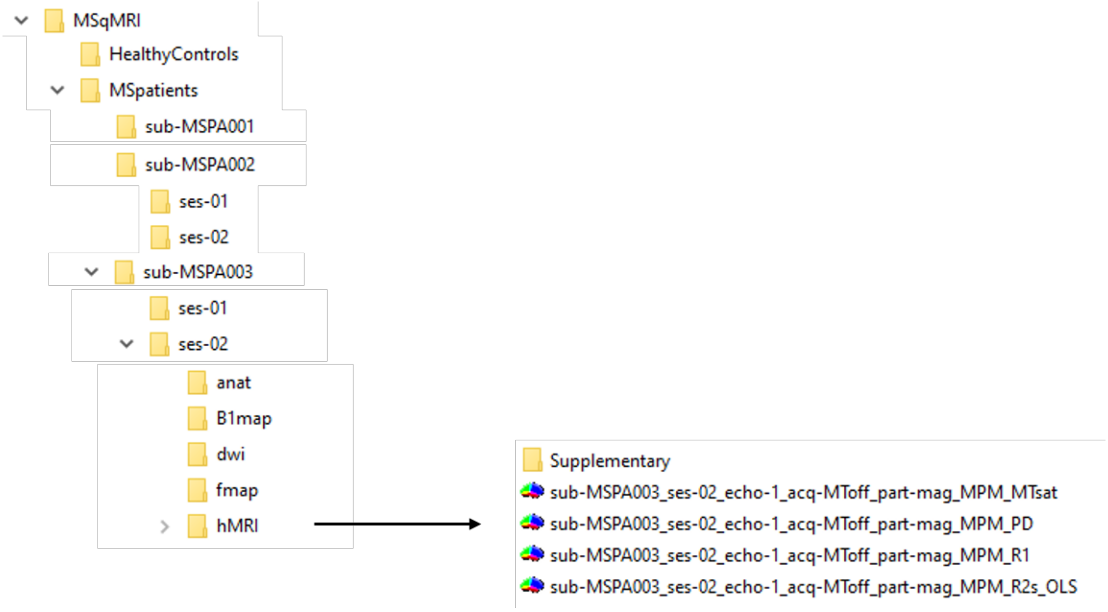

Figure 3.2: Example of our data rearrangement based on the BIDS format.

sideration at that time, and the format chosen here consisted of a first version of the final specifications. See [Karakuzu et al., 2022] for a description of the final version.

3.3 MRI data available

In addition to quantitative maps (MPM and NODDI), a conventional MR image, i.e. FLAIR, or “Fluid Attenuated Inversion Recovery” sequence, was acquired.

The acquisitions were conducted either with a 32- or 64-channels antenna, in the case of EL or CG dataset, respectively.

3.3.1 FLAIR

Nowadays FLAIR remains the most commonly used imaging technique for the diagnosis and follow-up of MS disease. Indeed, it is particularly useful for the visualization of the scope of MS lesions in the central nervous system, and a large number of automatic lesions segmentation tools rely upon this type of acquisition, such as the LPA algorithm described in Section 3.3.2.2.

Here, we acquired a FLAIR image for the detection of hyperintense lesions. It was recorded with spatial resolution of $1mm^3$ and TR/TE/TI = 5000 ms/516 ms/1800 ms, either on the 3T Prisma or Allegra MRI scanner, or in a restricted number of cases on a clinical 1,5T MRI at the hospital (for those acquisition parameters are unknown). An example of a FLAIR image acquired as part of EL study appears in Figure 3.4.

3.3.2 Multi-parametric maps

The largest portion of data included parametric maps acquired with the MPM protocol, constructing 4 maps MTsat, PD, R1 and R2*, reflecting different physical and biological tissue features.

3.3.2.1 MR acquisition

The MPM protocol consists of three co-localized 3D multi-echo fast low angle shot (FLASH) acquisitions at $1 \times 1 \times 1mm^3$ resolution and two additional calibration sequences to correct for inhomogeneities in the RF transmit field [Lutti et al., 2010, Lutti et al., 2012]. The FLASH datasets were acquired with predominantly PD, T1 and MT weighting, referred to in the following as PDw, T1w and MTw echoes. All three had high bandwidth (Prisma: 465 Hz/Px, Allegra: 425 Hz/Px) to minimize off-resonance and chemical shift artifacts. Sagittal 3D volumes were encoded in 176 sagittal slices using a 256×224 voxel matrix (FH × AP). GRAPPA parallel imaging (with an acceleration factor of 2) was combined with partial Fourier acquisition (with phase partial 6/8) to speed up acquisition time to approximately 20 min. Extra B1 field mapping images (transmit B+ and receive B- fields) were also acquired to reduce spatial heterogeneities related to B1 effects. This was essential for proper quantification of T1 (or R1=1/T1) in particular. Finally, B0 field mapping images, corresponding to both magnitude images and pre-subtracted phase image, were acquired for image distortions corrections. A summary of the acquisition parameters at 3T appears in Table 3.2.

3.3.2.2 Preprocessing

All data processing was performed in Matlab R2015b (The MathWorks Inc., Natick, MA, USA) using SPM12[2] (v12.0) and three additional dedicated SPM extensions:

- the "quantitative MRI and *in vivo* histology using MRI" (hMRI) toolbox, version 0.2.4[3] for the estimation of MPM maps [Tabelow et al., 2019],

---

[2] `www.fil.ion.ucl.ac.uk/spm`

[3] `http://hmri.info`

	PDw		**T1w**		**MTw**	
	Allegra	*Prisma*	*Allegra*	*Prisma*	*Allegra*	*Prisma*
TR [ms]	23.7	24.5	18.7	24.5	23.7	24.5
Flip angle [°]	6	6	20	21	6	6
Bipolar gradient echoes/TE [ms]	8/TE 2.2 - 19.7	8/TE 2.34 - 18.72	6/TE 2.2 - 14.7	8/TE 2.34 - 18.72	6/TE 2.2 - 14.7	6/TE 2.34 - 14.04
Off-resonance Gaussian MT pulse	N/A	N/A	N/A	N/A	FA: 200° Frequency offset: 2000 [Hz]	FA: 220° Frequency offset: 2 [kHz]
Bandwidth [Hz/Px]	425	465	425	465	425	465

Table 3.2: Multi-echo 3D FLASH acquisition parameters for Siemens ALLEGRA and PRISMA MRI.

- the “Lesion Segmentation Tool” (LST), version 1.2.3[4] for the creation of an *a priori* FLAIR-derived lesion mask [Schmidt et al., 2012],
- the “US-with-Lesion” (USwL) tool[5] for the segmentation of lesions and normal-appearing tissues, downloaded on 06/11/2018.

Maps creation Quantitative maps - MTsat, PD, R1 and R2*- were estimated using the hMRI toolbox, as described in section 2.2.3.1. The whole process yielded to the construction of the parametric maps, as well as contrast-weighted images (MTw, PDw and T1w) extrapolated to TE=0 as Supplementary material. A visual example of the four MPM maps, as well as the three TE=0 images appears in Figure 3.3. As reported in Chapter 2, histological studies demonstrated that MTsat is usually associated to myelin and axonal content; R2* is mostly an indicator of myelin and iron, and PD of water content. R1 interpretation is a bit more complex and represents myelin and water content, as well as gliosis and axonal dysfunction. The contrast-weighted images extrapolated at TE=0 are also of interest in following analyses, as their signal-to-noise ratio is greater than that of the raw MTw, PDw and T1w images.

Bias-field inhomogeneity correction Prior to any computations, the TE=0 and FLAIR images were corrected for inhomogeneity bias with a 30 mm FWHM Gaussian smoothness implemented in SPM12. Figure 3.3 presents an example

---

[4] `www.statisticalmodelling.de/lst.html`

[5] `https://github.com/CyclotronResearchCentre/USwLesion`

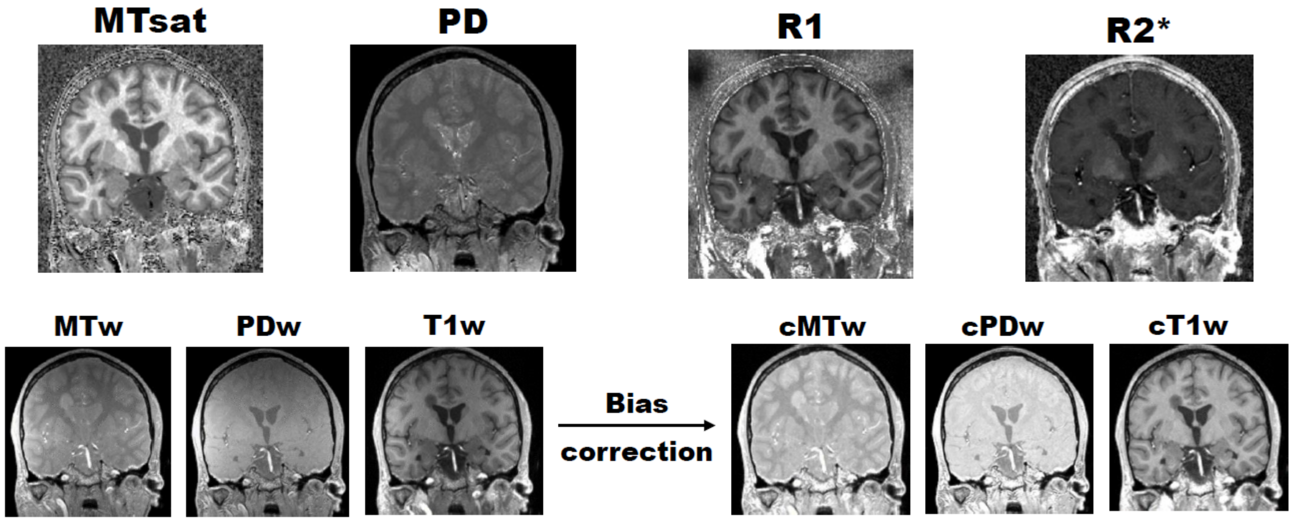

Figure 3.3: Example of MPM maps (above) and raw contrast-weighted images extrapolated at TE=0 (bottom left) and after bias correction (bottom right) acquired on an MS patient and generated with the hMRI-toolbox.

of such bias field and its correction for the three TE=0 images.

***A priori* mask creation** Before USwL segmentation, a preliminary lesion mask was generated from FLAIR and T1w images extrapolated at TE=0 (as computed during the hMRI process) by the lesion growth algorithm (LGA) [Schmidt et al., 2012] as implemented in the LST toolbox. This automatic tool is an iterative process based on T2-hyperintense white matter detection.

First, the FLAIR image was co-registered to T1w native space, and both images were segmented into basic tissue classes. Then, the lesion growth model was initiated. First, three lesion belief maps were created based on the detection of FLAIR hyperintense outliers within each of the three main tissues (B_{WM}, B_{GM} and B_{CSF}), and then summed up (B). At initialization, seed regions were constructed for the expansion of lesions, coming from a binary version of B_{GM} after the application of an arbitrary threshold κ. An initial binary lesion map, called L_{init}, was created, where voxels were assigned to 1 if their value was above κ in B_{GM}, 0 otherwise.

After that, the lesion growth model expanded L_{init}, a conservative assumption for lesions, towards the lesion belief map (B), a liberal assumption for lesions. The process is iterative, lesions beliefs neighboring voxels were analyzed and assigned to lesions under certain conditions, until no further voxel was added [Schmidt et al., 2012]. The cutoff value κ was decided after visual inspection; in our analysis it was set to 0.3. Manual corrections by an MS expert (EL) were performed to remove aberrant/artefactual lesion detections. An example of a mask generated based on FLAIR and T1w images appears in Figure 3.4.

Longitudinal registration When two or three acquisition sessions were available (i.e. for the longitudinal analysis presented in Chapter 5), an additional spatial processing procedure was included: within-patient registration brought the serial MR datasets into the individual T0 space, corresponding to the space of the first MPM image of the longitudinal follow-up. For that, we used the longitudinal registration tool from SPM [Ashburner, 2013].

Tissues segmentation Ultimately, images were segmented into cerebral tissues of interest: (NA)WM, (NA)CGM, (NA)DGM and WM lesions in the case of MS patients. Healthy subjects brains were segmented with the traditional US algorithm, as implemented in SPM. However, in the case of MS lesioned brains, we used the US-with-Lesion toolbox, which consists of an extended version of

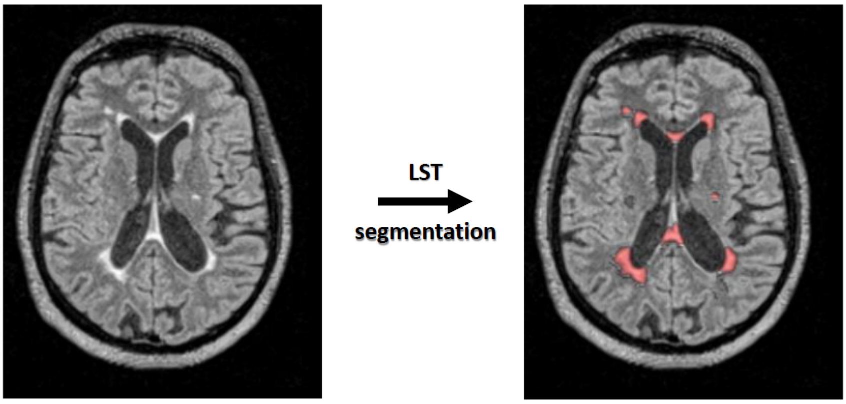

Figure 3.4: Example of a FLAIR image and the *a priori* lesion mask generated with the LGA algorithm, both in the transverse plane.

US [Ashburner and Friston, 2005] and includes an additional tissue class representing the WM lesion(s). This approach requires an *a priori* map of lesions locations, hence the previous LGA mask creation. See Chapter 4 for a precise description of the method.

3.3.3 Diffusion images

The second type of parametric maps were acquired with a NODDI protocol, generating images related to different water molecules displacements and characterizing specific tissue properties.

3.3.3.1 MR acquisition

NODDI data were acquired using a spin-echo echo-planar imaging sequence with 2.3 mm isotropic spatial resolution. Acquisition parameters included: TR = 9600 ms, TE = 78 ms, 58 transverse slices, slice thickness = $2.3mm$, in-plane resolution $2.3 \times 2.3mm^2$ (field of view = $220 \times 220mm^2$, matrix = 96×96) and acceleration factor 2, bandwidth per pixel = 2604 Hz/Px. The multi-shell DWI scheme included 193 volumes in an A»P phase encoding direction. The first volume was discarded to avoid T1 saturation effect. The remaining 192 volumes correspond to a total of 172 DW images interleaved with 20 $b = 0$ images. The set of diffusion directions was created using electrostatic repulsion and is defined over three shells ($b = 0$, 1000 and $2500s/mm^2$). One additional $b = 0$ volume with identical acquisition parameters but inverted phase encoding direction was acquired for the estimation of susceptibility-induced distortions.

In addition to diffusion-weighted images, a bvals file (i.e. a text file with b-values describing the "strength" of diffusion weighting) and a bvecs file (i.e. a text file with normalized vectors describing the direction of the diffusion weighting) are provided along with the raw images.

3.3.3.2 Processing

Before all else, the raw DWIs were corrected in two ways: first with a *Top Up* correction for the estimation and correction of the susceptibility induced distortions, and then with an *Eddy* correction, correcting eddy currents-induced bias and subject movements. Since those processes are computationally intensive, the corrections were performed on the cluster from the CECI[6] at ULiège, using pre-defined functions from the FSL toolbox, version 6.0[7]. *Top Up* uses two opposite phase encoding directions, in such a way that the deformation occurs in one direction or the opposite one, allowing the estimation of the deformation field. The first regular and inverted phase encoding direction $b = 0$ images were selected for that purpose. An example of the two $b = 0$ images and the generated distortion *Top Up* field appear in Figure 3.5.

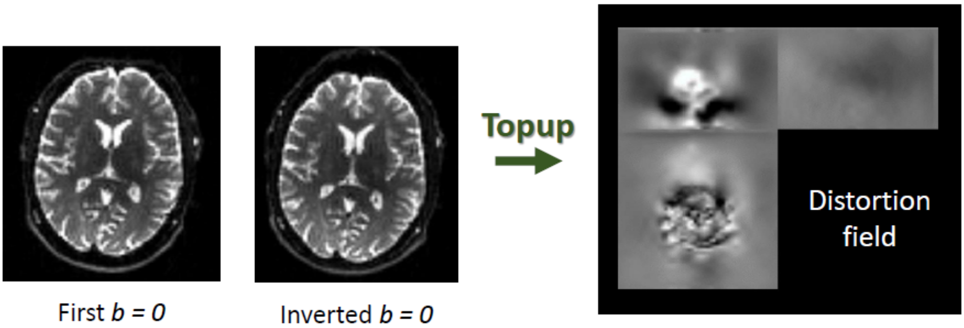

Figure 3.5: Example of the two $b = 0$ DWI images (left) used to construct the distortion field (right) during *Top Up* correction.

The resulting *Top Up* deformation field was applied to all DWIs prior to following corrections and processing. For *Eddy* correction, the diffusion signal was modelled based on the diffusion direction/weighting used for each DWI volume (contained in the *bvals* and and *bvecs* files), as well as other global acquisition parameters noted in a separate file. In addition, unnecessary out-brain signal

---

[6] `https://www.ceci-hpc.be/`

[7] `https://fsl.fmrib.ox.ac.uk/fsl/fslwiki`

was removed during computation, using an intra-cranial volume (ICV) binary mask. With all that, *Eddy* correction provided processed DWIs with significantly reduced susceptibility, eddy currents and movement induced distortions, as displayed in Figure 3.6.

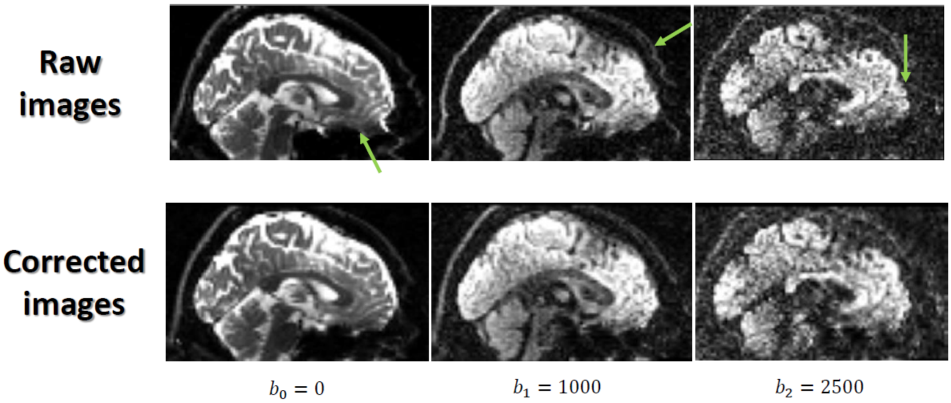

Figure 3.6: Example of raw and *Eddy* corrected DWI images, taken in the saggital plane for the three b-values (0, 1000 and 2500 s/mm^2). Arrows point at three particularly noticeable corrected/smoothed areas.

Finally, several NODDI maps were estimated with the NODDI toolbox, version 1.01, from Matlab[8], implemented as the three compartment tissue model presented in section 2.2.4.2. The compartments represent intra-neurite material, extra-neurite material and surrounding water, and are modeled respectively as a set of sticks with 0 radius, a set of water molecules with normal anisotropic diffusion, and a set of water molecules with isotropic Gaussian diffusion [Zhang et al., 2012]. Seven parameters were retrieved: the intra-cellular volume fraction (F_{icvf}), the isotropic volume fraction (F_{iso}), the orientation dispersion index (ODI), as well as three direction parameters, and the concentration parameter of Watson distribution. Due to their better interpretability and presence in literature combining NODDI and MS, we used only the first three parameters for the analysis (Chapter 6).

---

[8] `http://mig.cs.ucl.ac.uk/index.php?n=Tutorial.NODDImatlab`

Chapter 4

Brain tissues segmentation

Contents

In this chapter, the two segmentation tools used in the following chapters of this thesis are presented. First the parameter space of the “Unified Segmentation” algorithm is explored to accommodate MPM data from healthy subjects. Then the segmentation of normal appearing and abnormal (i.e. lesioned) tissues in MS patients, with the extended US-with-lesion tool, is studied, based on the parameters setting found in the first setup.

4.1 Introduction

Nowadays “Unified Segmentation” (US), as available in SPM, is one usual approach to warp brain images into a standard reference space, i.e. perform spatial normalization, and derive posterior probability maps of the brain tissues, typically gray matter (GM), white matter (WM), and cerebrospinal fluid (CSF). Other head tissues, i.e. skull, “soft tissues” and “air”, are also extracted but are of little interest here [Ashburner and Friston, 2005]. The US algorithm combines a voxel classification procedure based on a “mixture of Gaussians” (MoG) model of the intensity distribution, with a registration, where a template is warped to match the brain volume to be segmented. The template space is defined by “tissue probability maps” (TPMs) of the head tissues spatial distribution, which act as priors on the spatial distribution of the different tissue classes. These priors are used in US Bayesian framework, to estimate posteriors of warping and MoG parameters. Additionally, a model for the correction of the potential (smooth) intensity bias across the image is included in the algorithm. The bias correction parameters are iteratively updated by optimizing the objective function, thus integrating at the same time a registration of the image, a segmentation, and a bias correction. Intensity distributions can be uni- or multi-variate depending on the number of modalities considered as inputs, aka. channels.

Initially, the TPMs related to US were developed for and from conventional T1/T2-weighted MR images, in which signal intensities are arbitrarily scaled and only provide a qualitative representation of the tissues, i.e. contrasting different tissue types. The TPMs were modified from one version of SPM to the next: in the previous version SPM8, only three tissue classes were considered (WM, GM and CSF), the rest of them being implicitly defined as “other”. In the latest version SPM12, the other tissues are further divided into skull, “soft tissue” and “air”. Furthermore, to avoid miscalculation from zero values within the TPMs, the minimal value is 10^{-6} for all tissue classes, except for WM, GM and CSF in the intracranial volume, for which the minimal value is 10^{-3}. Indeed, the log of these values is computed in the US process, and since $\log 0 = -\infty$, it would break the calculation. However, despite those improvements, those T1/T2w TPMs come with major drawbacks. They are typically missing regions, for instance some GM inclusion in the sub-cortical area. The delineation of this specific region remains challenging with T1/T2w images. This is mainly due to the high concentration of iron, which provokes limited gray/white matter contrast [Haacke et al., 2005, Lorio et al., 2014].

Contrary to typical T1/T2w MRI, qMRI covers a broad range of intensities with physical information specific of the brain region. Therefore, improved TPMs were introduced for the usage of US in single-channel MPM-based segmentation, named “eTPMs”, derived from MTsat and R2* data [Lorio et al., 2016]. Due to their high sensitivity to iron content within living tissues, MPM maps display optimally contrasted gray/white matter structures in these subcortical areas, and better delineate the deep GM in the corresponding TPM.

For segmentation, the focus was put on the three main tissue classes: GM, WM and CSF. However, it has been noticed that the basal ganglia (BG) in some cases depicts very different ranges of intensities than the rest of GM in MPM maps. This is especially the case in PD, where they appear much darker, and R2*, much brighter. One can particularly catch this effect in older populations, in which the iron deposition within the BG is increased, and caught up by PD and R2*. Therefore, when we investigate multi-channel segmentation based on one or several MPM maps, it seems important to take this issue into account.

One solution is to include a specific TPM of the BG area into the initial US model, in order to catch this specific range of voxel values. At the same time, the initial TPM representing GM tissue must be updated by keeping only cortical areas (and remove the BG regions). Basically, the original TPM of GM is split into two independent maps, based on BG structures templates: cortical gray matter (CGM) and deep gray matter (DGM). This new set of TPMs is named "eTPM_wBG" and was applied to all segmentation procedures (with US or USwL).

Up to now, the US algorithm has not been validated for multi-channel segmentation based on MPM data, taking advantage of the multi-dimensional aspect of the MPM protocol. Several parameters must be adjusted to account for the changes in intensity distributions (e.g. the number of Gaussians in the MoG model, or the best maps combination). This is the first purpose of the present chapter. A succession of US parameters settings were tried out in order to determine the one leading to the best segmentation.

The second part focuses on the adaptation of US to lesioned brains. When dealing with data from patients with focal brain lesions, e.g. tumors or multiple sclerosis lesions, a direct application of the US approach is inadequate because it cannot account for the abnormal tissue distribution. Image distortions and overall tissue mis-classification can appear because of the mismatch between the signal in the lesion area and the *a priori* TPMs. A common work around is the "cost function masking" (CFM) approach [Brett et al., 2001, Crinion et al., 2007] where the region of abnormal tissues is masked out from the processing using a (manually) pre-defined binary mask of the lesion [Seghier et al., 2008, Schmidt et al., 2012]. The model optimization can thus be performed on the rest of the healthy looking brain tissues, excluding the lesion area. While this is sensible for small focal lesions, in case of extended or multiple lesions, a large part of the brain could end up masked out, which could affect the estimated segmentation and deformation.

To account for lesioned tissues, the US approach was extended to provide a more principled solution for brain images with focal lesions, with a twofold aim: 1) generate a more accurate warping into the reference space of the healthy tissues allowing further inter-subject comparisons, and 2) produce an updated (more precise) delineation of the lesion(s) through *posteriori* probability map of lesion tissues. This US extension is named "Unified Segmentation with lesion" (USwL) and it relies on a prior approximate mask of the lesion area. This approximate mask is first used to extend the standard eTPMs_wBG mentioned here above, with an extra lesion tissue class, then US is applied with this extended model. USwL is a semi-automatic method, as it requires an *a priori* mask, but it does not involve a training phase based on a reference segmentation.

In this study, the *a priori* mask was previously derived from the FLAIR and T1 images by the lesion growth algorithm (LGA), as implemented in the LST toolbox [Schmidt et al., 2012]. More details appear in section 3.3.2.2, in Chapter 3.

Here, we considered MPM parametric maps MTsat, PD, R1 and R2* to investigate USwL, using the setting determined for US. It was employed to construct lesion masks based on MPM data from MS patients. The MPM-derived mask was compared in several ways to the *a priori* FLAIR-derived mask, in order to investigate whether the MPM-based mask is more accurate at detecting lesion voxels. We benefit from the quantitative nature of MPM maps to inspect the distribution of voxel values within each brain region, including the lesion volume.

4.2 Unified segmentation

As mentioned, the US algorithm has not been calibrated for qMRI maps. Thus, here it was applied on the MPM maps from healthy subjects.

4.2.1 Algorithm of US

The Unified Segmentation model is based on a mixture of Gaussians (MoG) of the intensities distribution, and is extended to incorporate a smooth intensity variation and nonlinear registration with tissues probability maps (TPMs) [Ashburner and Friston, 2005].

If we consider the distribution modelled with a mixture of K Gaussians (clusters), the kth Gaussian is modelled by its mean (μ_k), variance (σ_k^2) and mixing proportion (γ_k, where $\sum_{k=1}^{K} \gamma_k = 1$ and $\gamma_k \geq 0$). The MoG model is fitted by maximizing the probability of observing the I elements of data $\boldsymbol{y}$ (set of intensities), given the parametrization of the Gaussians. The probability of obtaining an intensity y_i given that is belongs to the kth Gaussian ($c_i = k$) and that the kth Gaussian is parametrized by μ_k and σ_k^2 is:

$$P(y_i|c_i = k, \mu_k, \sigma_k) = \frac{1}{(2\pi\sigma_k^2)^{\frac{1}{2}}} \exp\left(-\frac{(y_i - \mu_k)^2}{2\sigma_k^2}\right) \tag{4.1}$$

The prior probability of any voxel, irrespective of its intensity, belonging to the kth Gaussian, given the proportion of voxels that belong to that Gaussian is:

$$P(c_i = k|\gamma_k) = \gamma_k \tag{4.2}$$

The joint probability of cluster k and intensity y_i, with the Bayes rule, is:

$$P(y_i, c_i = k|\mu_k, \sigma_k, \gamma_k) = P(y_i|c_i = k, \mu_k,_k)P(c_i = k|\gamma_k) \tag{4.3}$$

We obtain the probability of y_i given the set of parameters, by integrating over K clusters:

$$P(y_i|\boldsymbol{\mu}, \boldsymbol{\sigma}, \boldsymbol{\gamma}) = \sum_{k=1}^{K} P(y_i, c_i = k|\mu_k, \sigma_k, \gamma_k) \tag{4.4}$$

Then, on the entire dataset $\boldsymbol{y}$, the probability is derived by assuming that all elements are independent:

$$\begin{aligned} P(\boldsymbol{y}|\boldsymbol{\mu}, \boldsymbol{\sigma}, \boldsymbol{\gamma}) &= \prod_{i=1}^{I} P(y_i|\boldsymbol{\mu}, \boldsymbol{\sigma}, \boldsymbol{\gamma}) \\ &= \prod_{i=1}^{I} \left(\sum_{k=1}^{K} \frac{\gamma_k}{(2\pi\sigma_k^2)^{\frac{1}{2}}} \exp\left(-\frac{(y_i - \mu_k)^2}{2\sigma_k^2}\right)\right) \end{aligned} \tag{4.5}$$

Since the parameters $\boldsymbol{\mu}$, $\boldsymbol{\sigma}$ and $\boldsymbol{\gamma}$ are unknown, the previous probability is maximised with respect to those parameters when the following cost function (ε) is minimised:

$$\begin{aligned} \varepsilon &= -\log P(\boldsymbol{y}|\boldsymbol{\mu}, \boldsymbol{\sigma}, \boldsymbol{\gamma}) \\ &= -\sum_{i=1}^{I} \log \left(\sum_{k=1}^{K} \frac{\gamma_k}{(2\pi\sigma_k^2)^{\frac{1}{2}}} \exp\left(-\frac{(y_i - \mu_k)^2}{2\sigma_k^2}\right)\right) \end{aligned} \tag{4.6}$$

However, the assumption that voxels are independent is implausible, actually the conditional probability that a voxel belongs to a tissue class contains spatial dependencies.

To account for that, priors were generated by registering a large number of subjects together, assigning voxels to different tissues classes and averaging tissues types over subjects. They consist of the tissue probability maps (TPMs) as presented in the previous Introduction section, and displayed in Figure 4.4(B). These maps provide the prior probability of any voxel in a registered image being of any of the tissue classes, irrespective of its intensity.

The model is modified to account for these spatial priors. The previous stationary mixing proportions ($P(c_i = k|\gamma) = \gamma_k$) are updated so that prior probabilities can vary over voxels, and the prior probability of voxel i being drawn from the kth Gaussian becomes:

$$P(c_i = k|\gamma) = \frac{\gamma_k b_{ik}}{\sum_{j=1}^{K} \gamma_j b_{ij}} \tag{4.7}$$

where b_{ik} is the tissue probability for class k at voxel i. This formulation can be refined further by allowing the TPMs to be deformed according to parameters $\boldsymbol{\alpha}$. Doing that, the inclusion of the registration to a standard space within the same generative model is possible. The objective function becomes:

$$\begin{aligned}\varepsilon = -\sum_{i=1}^{I} \log \left(\frac{\rho_i(\beta)}{\sum_{k=1}^{K} \gamma_k b_{ik}(\boldsymbol{\alpha})} \sum_{k=1}^{K} \gamma_k b_{ik}(\boldsymbol{\alpha}) (2\pi\sigma_k^2)^{-\frac{1}{2}} \right. \\ \left. \times \exp\left(-\frac{(\rho_i(\beta) y_i - \mu_k)^2}{2\sigma_k^2} \right) \right)\end{aligned} \tag{4.8}$$

The model is fitted by minimizing this objective function. This is performed with an “Iterated Conditional Modes” (ICM) approach. It starts by assigning starting estimates for the different parameters and then iterating until a locally optimal solution is found. Iterations are characterized by an alternation between the estimation of different group parameters, while holding the other fixed at their current best solution (i.e. the conditional mode). The MoG parameters are updated using an Expectation Maximization (EM) algorithm, while holding the bias and deformations fixed at their conditional modes. The bias is estimated while holding the MoG parameters and deformation constant. Finally, the deformations of the TPMs are re-estimated while fixing te MoG parameters and bias field [Ashburner and Friston, 2005].

4.2.2 Methods

In the current analysis, two kinds of US settings were investigated: the number of Gaussians in the MoG model of the four main tissue classes (CGM, DGM, WM and CSF) intensity distributions, and the combination of the four quantitative maps (MTsat, PD, R1 and R2*) used for multi-channel segmentation.

In total, all combinations of MPM maps were tested, and the number of Gaussians in the MoG models varied between 1 and 8 for the four main tissues. The rest of the tissues were arbitrarily modelled with 2 Gaussians. The process involved two steps in an iterative procedure (Figure 4.1, light gray). We started by determining the optimal numbers of Gaussians with a fixed combination of maps (initially with MTsat), then tested the maps combinations with a fixed MoG setting (established in the previous step). At each step, all possibilities were ranked based on several criteria as described here under. The one reaching first position was considered the best one. The optimal set of parameters was retrieved when the obtained results were stable in both steps (i.e. the optimal MoG setting lead to the optimal maps combination and vice versa).

Due to limited computational resources, we could not test all the combinations of number of Gaussians, otherwise we would have to generate 25 (subjects) × 8 ˆ 4 (number of Gaussians) ˆ (tissue classes) = 102 400 segmentations. Each segmentation procedure takes approximately 3 minutes, resulting in a time period of around 213 days, and this only for the first step. Thus, we divided the search for optimal MoG setting into two procedures (Figure 4.1, dark gray). We started by investigating the best number of Gaussians identical in the 4 tissues classes and ranging from 1 to 8 (8*25 tests in total). Then, we tested the range $[G-1; G; G+1]$, G being the optimal number of Gaussians determined in the previous step. This time the range was applied to each class individually (except for CSF to reduce once again the number of tests, we fixed it at G Gaussians). In total, the number of experiments reached 8*25 + 27*25 = 875 instead of 102 400 for the optimal MoG setting search. After those two procedures, the best combination of maps was estimated.

Due to the lack of ground truth for MPM segmented data, a method called “Simultaneous Truth and Performance Level Estimation” (STAPLE) was employed to assess segmentation results [Bouix et al., 2007, Warfield et al., 2004]. This expectation-maximization algorithm creates a probabilistic estimate of the true segmentation based on a number of segmentation outputs generated from different methods and/or set of parameters. The STAPLE algorithm works as following: supposing that we have a set of 3 distinct segmentation outputs, those three segmentations are combined into a test segmentation, by simple majority voting on each voxel. Then, the accuracy of each of the three outputs is rated compared to this initial test segmentation. From there on, a second test segmentation is constructed by weighting the votes of the three outputs according to their accuracy.

The process is iterative, i.e. the estimation of the accuracy of each output followed by the construction of a new test segmentation with decisive weights continues until convergence (i.e. when the test segmentation stops changing). The final test segmentation constitutes the probabilistic estimate of STAPLE. Individual performance metrics (sensitivity and specificity scores) are computed for each output based on this probabilistic estimate.

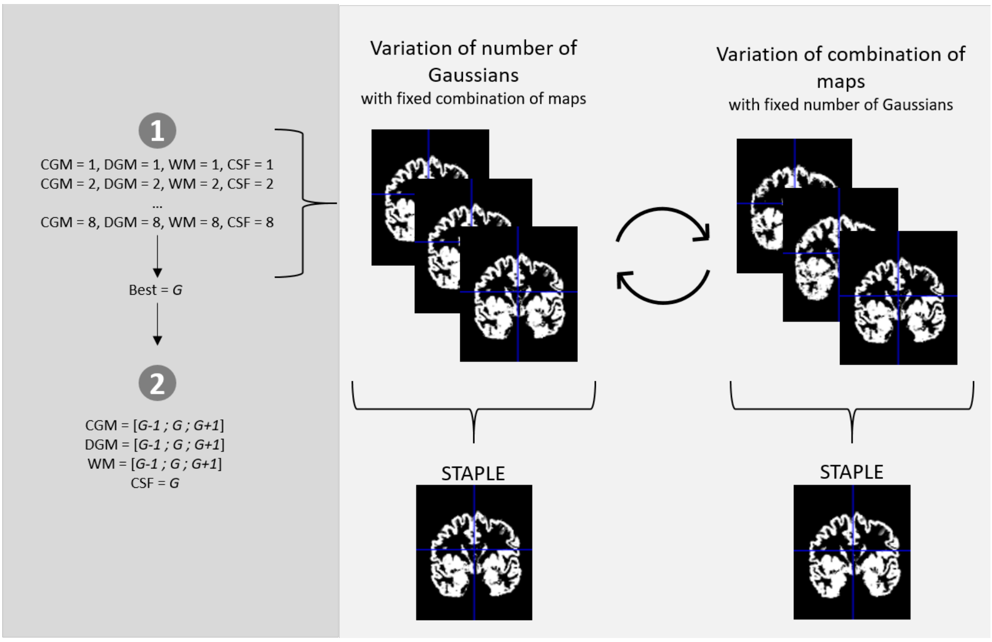

Figure 4.1: Representation of the iterative process using STAPLE to derive the best set of parameters for US multi-channel segmentation based on MPM maps.

Here, we used STAPLE to determine the optimal segmentation at each step of the process shown in Figure 4.1. We computed sensitivity and specificity scores for each output. Besides these STAPLE performance metrics, three other criteria were included: Dice, Jaccard and Matthew correlation (MCC) coefficients computed between each segmentation result and the probabilistic estimate. Those are statistics of similarity between two samples, widely accepted for binary classification tasks and often used to assess resemblance between segmentation outputs. The Jaccard index is the volume of overlap between the segmentation candidate and the STAPLE estimate divided by the volume of union between them. The Dice score is 2 * the volume of this overlap divided by the total number of voxels in both images. Those two scores range between 0 and 1, 1 signifying the greatest similarity between predicted and truth. MCC summarizes the classical confusion matrix and its four entities - true positives (TP), true negatives (TN), false positives (FP), false negatives (FN) - with the following formula:

$$MCC = \frac{TN \times TP - FN \times FP}{\sqrt{(TP + FP)(TP + FN)(TN + FP)(TN + FN)}} \tag{4.9}$$

This time, MCC ranges from -1 to 1, indicating perfect correlation, respectively negative and positive. Positive correlation is when the classifier is perfect, negative correlation is when it always misclassifies. When MCC = 0, it means that there is no agreement, the prediction is random.

Those five scores were computed for each segmentation output, testing different parameters (MoG setting or maps combination). Results were averaged among the four main tissues, i.e. WM, CGM, DGM and CSF. At each step, segmentations were ranked based on the mean value of these criteria.

4.2.3 Results

In the first step with an MTsat segmentation, we found an optimal value of 5 Gaussians for all tissues. Thus we tested the range 4-5-6, this time ranging in each tissue class separately (except for CSF fixed at 5 Gaussians). The combination CGM = 5, DGM = 4, WM = 5 lead to the best results.

With this fixed MoG setting, we tested the best combination of maps among MTsat, PD, R1 and R2*, and found MTsat + PD + R1. The iterative process continued until convergence. Mean comparison scores at each step are placed in the Appendix.

In the end, the following setting was derived: the number of Gaussians in the MoG model should be 5 for CGM, 5 for DGM, 6 for WM and 5 for CSF, and the optimal combination of maps is MTsat, PD and R1. A visual example of one STAPLE estimate constructed from a set of segmentation outcomes appears in Figure 4.2 (right), next to three examples of maps combinations used in the multi-channel segmentation (left). One can observe small differences in the segmented CGM, where the combination MTsat + PD + R1 seems the closest to STAPLE.

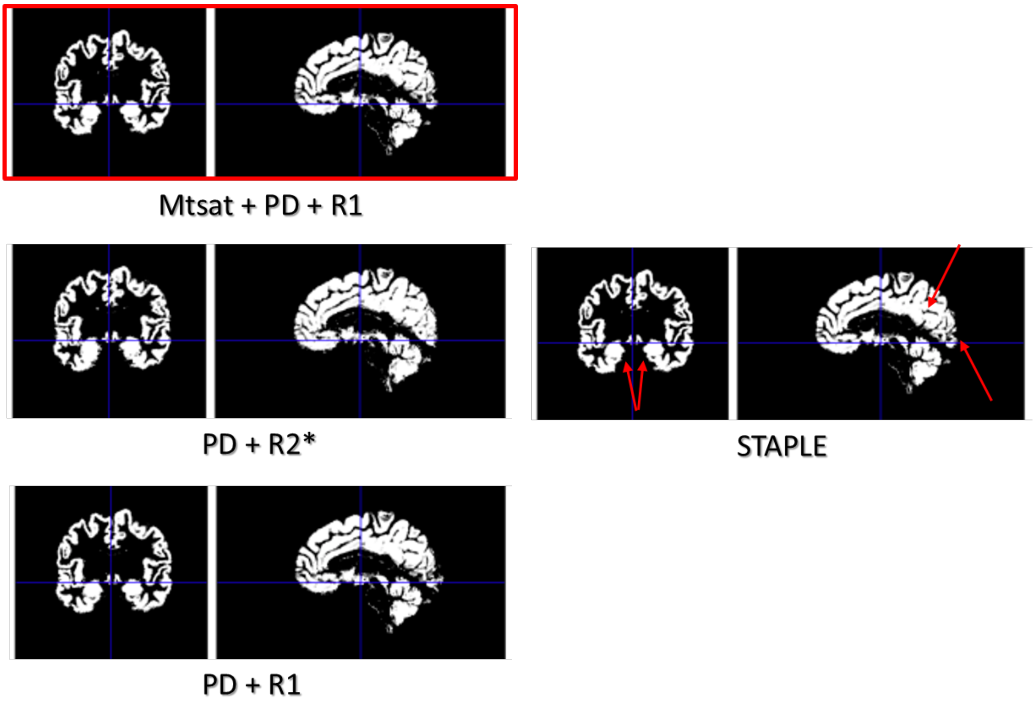

Figure 4.2: Example of one STAPLE image (right) generated with a set of segmentation outcomes, three of them depicted for visual comparison (left). Arrows point at specific locations where differences are specifically noticeable. The best outcome is framed in red.

That setting could then be applied to MS data, leaving place to the analysis of normal appearing tissues and lesions.

4.3 Unified segmentation with lesion

The “unified segmentation with lesion” (USwL) method is an extension of the US approach, relying on a prior approximate mask of the lesion area. This approximate mask is first used to extend the standard TPMs (as shown in Figure 4.4(B)) with an extra lesion tissue class, then US is applied with this extended model. The key ideas of this “US-with-Lesion” approach are:

- The prior binary lesion mask is combined with the healthy TPMs to become an additional subject-specific smooth *a priori* tissue probability map;

- The posterior probability lesion map obtained will combine prior information of all tissue classes and image intensities, providing a possibly updated lesion map;

- The spatial deformation will also account for the full set of healthy and lesion tissues in the brain.

This first lesion mask can be manually delineated by an expert or algorithmically generated, e.g with the Lesion Segmentation Toolbox [Schmidt et al., 2012] as in the present study.

The whole process is illustrated in Figure 4.3 and detailed in the next 2 subsections.

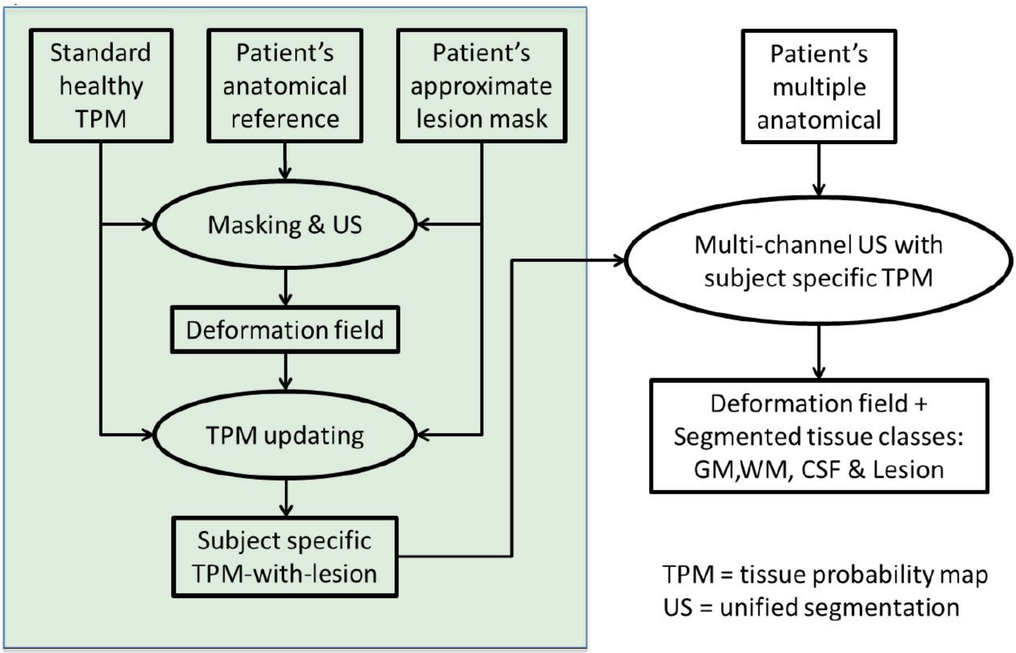

Figure 4.3: Workflow of the "Unified Segmentation with Lesion" (USwL) approach. The green box summarizes the creation of the subject-specific TPM-with-lesion.

4.3.1 Extending TPMs

Beyond the (approximate) lesion mask, one should also decide *a priori* which tissue class(es) is/are affected by the lesion: GM or WM only, or both considered together, or the whole brain volume, i.e. GM, WM and CSF together. Then this extension of the TPMs proceeds in two successive steps, see left part of Fig. 4.3.

First the original lesion mask is naturally provided in the so-called “subject space” and needs to be normalized in order to integrate it with the TPMs. This can be achieved with a “cost function masking” (CFM) approach applied on one anatomical image of the subject [Brett et al., 2001]. This then provides a first warping, possibly slightly biased due to the extent of the lesion area, from subject to template space. To ensure the complete delimitation of lesion tissue, one could also grow the original mask by 1 or 2 voxels to get a larger cover of the lesion and its surrounding. The resulting warp can then be applied on the binary lesion mask itself. The point is to (approximately) align the lesion mask in the same space as the TPMs, not necessarily to get an accurate whole-brain normalization.

Second the now normalized (binary) lesion mask is smoothed with a full width at half maximum (FWHM) Gaussian kernel matching the smoothness of the TPM maps, by default this is set to $4mm$. This smooth warped lesion mask is then integrated in the TPMs, according to the chosen affected tissue class prior map and a predefined “load ratio”, by default set to 80%. This way, the “lesion probability map”, to be added to the healthy tissue TPM, is simply proportional to 1) the *a priori* chance of being a lesion, 2) the chance of being part of the target tissue class, 3) an arbitrary ratio to down weight it a bit (the load ratio at 80%). For example, in the case of a lesion limited to WM, a voxel with 95% chance of being part of the lesion and 99% chance of being WM itself ends up having a $.95 * .99 * .8 = .7524$ and $.99 - .7524 = .2376$ *a priori* probability of being lesion and WM respectively. Moreover, to match the requirements of the US algorithm that no prior should be exactly zero (because it works with the log of these values), voxels of this lesion probability map with a very small or zero value are set to a minimal value of 10^{-6}, like in the TPMs provided with SPM. Additionally, within the intra-cranial volume, the minimal lesion probability map is set to 10^{-3}, again as in SPM TPMs for GM, WM and CSF. This last value ensures that a lesion can be detected *a priori* anywhere in the brain volume provided that the likelihood strongly points in that sense. Finally other untouched tissue probability maps are updated such that the probabilities of being any of the 7 tissue classes (5 healthy tissues, lesion, and air) sums up to 1.

4.3.2 US with extended TPMs

Once the the subject-specific extended TPMs are constructed, one can simply apply the standard US approach with this extra tissue class on the subject image(s) for a single- or multi-channel segmentation. Consequently a lesion-informed deformation field from subject to template space is estimated, allowing further inter-subject comparison. Figure 4.4 shows an example of the whole process, and the obtained results, with one MS patient.

Preliminary results for the validation of USwL on conventional MRI data were presented, as part of an international conference, using two publicly available datasets for brain tumors and MS lesions [Phillips et al., 2017].

4.3.3 Application to multi-parametric maps

The USwL approach was tested on MPM maps using data from 36 patients with multiple sclerosis. Acquisitions, which took place either on the Allegra or Prisma MRI scanner, consisted in multi-parametric maps MTsat, PD, R1 and R2* generated from the MPM protocol (Section 2.2.3), and a FLAIR image. See Chapter 3 for more details about the population and available data considered for this study.

4.3.3.1 Methods

With USwL, several cerebral tissue classes were isolated: NACGM, NADGM, NAWM and focal WM lesions. On the one hand, for each patient individually, a preliminary lesion mask was generated based on FLAIR and T1w images, as exposed in section 3.3.2.2, referred as FLAIR-based mask, or mask A, in the following. On the other hand, the MPM-based mask, or mask B, corresponds to the one constructed using MPM maps and USwL. Mask A was included as prior into the USwL method to generate the subject-specific lesion TPM, and the white matter prior map was updated accordingly [Moon et al., 2002]. The gray matter TPM was not updated due to a very low number of lesions present in the cortical ribbon. Mask B was derived from a multi-channel approach using the parameters settings as found with US applied MPM images (Section 4.2), with these updated patient-specific TPMs.

Here, the purpose was to compare the two masks (FLAIR-based with MPM-based). To begin with, both were “cleaned” by removing lesions smaller than $10mm^3$, the clinical size threshold to be considered as actual lesion. Lesions from both masks were matched, under the condition of sharing a minimum of three voxels to avoid errors from adjacent lesions. Multiple matches for one le-

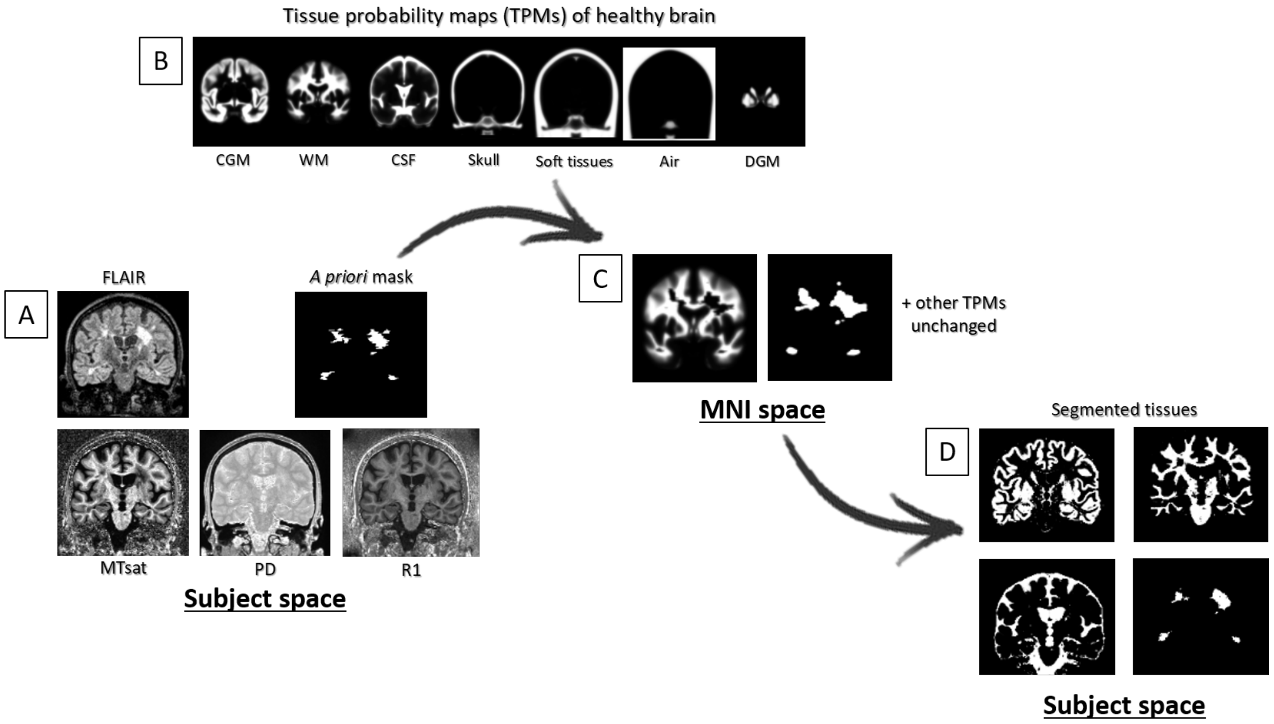

Figure 4.4: Example of USwL application on an MS patient (data from the GIGA-CRC). (A) FLAIR and *a priori* lesion mask constructed with LST, as well as MPM maps (MTsat, PD, R1); (B) TPMs of a healthy brain in MNI space, used as is in US; (C) updated WM and lesion prior probability maps; (D) *a posteriori* probability maps for GM, WM, CSF and lesion classes.

sion were possible. Different regions were delimited in each couple of matching lesions, inside which the parameters values were extracted:

- The intersection between both masks ($A \cap B$),
- The region in FLAIR-derived mask not comprised in MPM-derived mask ($A \backslash B$),
- The region in MPM-derived mask not comprised in FLAIR-derived mask ($B \backslash A$),
- The normal appearing white matter (NAWM).

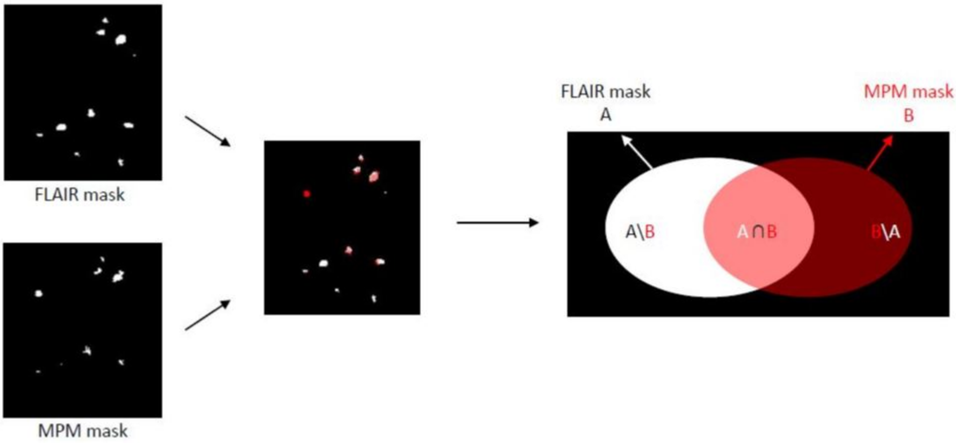

Figure 4.5: Schematic representation of a couple of matching lesions, showing sub-regions.

All sub-regions (excluding NAWM) are represented in Figure 4.5, corresponding to a schematic representation of a couple of matching lesions. The intersection region, where both masks are in agreement, is most likely covering lesion tissue, because it contains both FLAIR hyperintensities and MPM alterations. Thus, this region constituted a reference for “lesion specific” area for the rest of the analyses. On the other hand, NAWM established a reference for the surrounding healthy tissue as opposition to lesions. Parameters values (MTsat, PD, R1 and R2*) as well as FLAIR intensities were extracted in each region from each couple of matching lesions, then summarized to a median value.

First, a morphological characterization of both masks was performed by assessing 1) the mean Dice score between both masks, and 2) the thickness of regions $A \backslash B$ and $B \backslash A$ around region $A \cap B$. To do so, we computed for each region subtracted from the entire mask the number of erosion steps with a one-voxel-kernel needed before it is no longer seen on the binary mask. The final number of erosion step indicates the thickness in voxel, or in mm in our case.

Then, we compared the voxels distributions of each region, individually for each of the five images (4 MPM and FLAIR). One-way ANOVAs tested the hypothesis of all distributions drawn from populations with the same mean, against the alternative hypothesis that population means are not all similar, with a corresponding p-value. Statistical significance was considered when $p < .05$, after correction for multiple comparisons (using Tukey's procedure).

In order to detect potentially misclassified voxels (i.e. voxels classified as lesion instead of normal appearing tissue), we used three approaches:

1. The Chi-squared distance between histograms of data distributions, to assess whether $A\backslash B$ region is actually more comparable to NAWM than $B\backslash A$, and the opposite compared to $A \cap B$.
2. The means and mixing proportions of the two components of a bimodal Gaussians mixture model fitted to the voxels distribution in regions $A\backslash B$ and $B\backslash A$. This approach should illustrate the repartition of voxels correctly vs. erroneously classified as lesions within each region.
3. The k-means algorithm, to search natural clusters in the voxels values from both regions individually. An optimal number of one cluster would correspond to a majority of correctly classified voxels, while two clusters would suggest a portion of voxels probably indicating another tissue. The optimal number of clusters is derived from the gap criterion [Tibshirani et al., 2001] investigating the presence of one and two clusters.

4.3.3.2 Results

The two masks (FLAIR-based and MPM-based) obtained were overall quite similar, with a mean Dice score of 0.6246 ± 0.12 across subjects. On average over all lesions and subjects, regions $A\backslash B$ and $B\backslash A$ constitute a two$-mm-$thick layer around the intersection region, independently of the lesion size.

Distributions of all regions, i.e. $A \cap B$, $A\backslash B$, $B\backslash A$ and $NAWM$, for each parameter separately appear in Figure 4.6. Visually, one can observe that the four MPM parameters are characterized with a $B\backslash A$ region closer to $A \cap B$, and an $A\backslash B$ region closer to NAWM, which is not apparent in FLAIR distributions. One-way ANOVAs applied in each modality separately showed significantly different means among all distributions, corrected for multiple comparison (MTsat:

$F_{4106} = 97.65$, $p < .0001$; PD: $F_{4106} = 88.74$, $p < .0001$; R1: $F_{4106} = 79.77$, $p < .0001$; R2*: $F_{4106} = 73.34$, $p < .0001$, FLAIR: $F_{4106} = 72.64$, $p < .0001$).

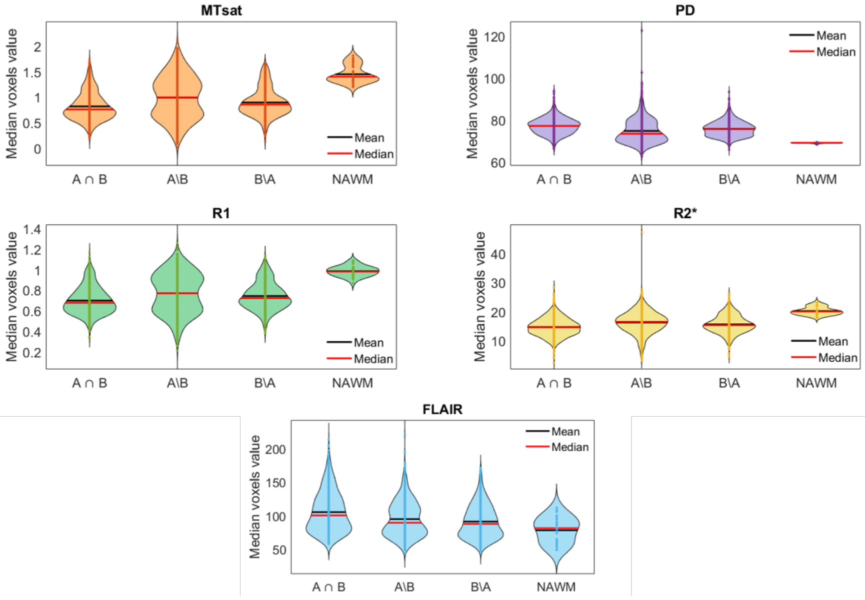

Figure 4.6: Violin plots of the median voxel values in all lesions, comparing sub-regions and parameters (MTsat, PD, R1, R2* and FLAIR)

Mean value differences were computed; their estimates measurements are gathered in Table 4.1. Two main observations can be highlighted:

- For the four MPM parameters, the difference between the intersection and the MPM-based mask only (third column) is always smaller than the difference between the intersection and the FLAIR-based mask only (first column).
- Similarly, the difference between the FLAIR-based mask only and NAWM (fourth column) is always smaller than the difference between the MPM-based mask only and NAWM (fifth column).

Such results suggest that extra lesion voxels picked up by the MPM-based segmentation are more comparable to (what is considered) "lesion specific" region than the FLAIR-based one, and the opposite compared to surrounding NAWM. This is observable in MPM metrics, but not in FLAIR, indicating that FLAIR imaging alone is not able to capture all microstructural alterations in MS lesions, as picked up by MPM maps. Indeed, the WM alterations picked up by MPM maps are more likely to truthfully revealing MS lesions due to their histological correlations. However, FLAIR images alone might exhibit only the tip of the iceberg, or the captured hyperintensities may not be specific to MS lesions.

	Estimate of mean value differences					
	$A \cap B$ vs $A \backslash B$	**$A \backslash B$ vs $B \backslash A$**	**$A \cap B$ vs $B \backslash A$**	**$A \backslash B$ vs NAWM**	**$B \backslash A$ vs NAWM**	**$A \cap B$ vs NAWM**
MTsat	-0.1722	0.0952	-0.0769	-0.4571	-0.5524	-0.6293
PD	2.3640	-1.0193	1.3447	5.7389	6.7582	8.1028
R1	-0.0715	0.0271	-0.0444	-0.2150	-0.2421	-0.2865
R2*	-1.5629	0.6399	-0.9230	-3.9195	-4.5594	-5.4824
FLAIR	10.4467	3.6416	14.0884	16.7031	13.0615	27.1498

Table 4.1: Estimates of group mean value differences between each lesion region, for each modality.

The high variability of the $A \backslash B$ distribution, almost in the shape of a bimodal Gaussian distribution, suggests that a proportion of voxels correctly depict lesion, while another one is more likely to pertain to NAWM. Especially in the case of MTsat, PD and R1, it looks like one peak of the distribution is rather close to the distribution of the intersection region, while the other peak draws nearer to NAWM. The following analysis of the distributions histograms enables to go a bit further.

Indeed, the histograms of each region values (Figure 4.7) demonstrate an important overlap (especially in MTsat, PD and R1 distributions) between regions $A \backslash B$ and NAWM, which is less apparent for region $B \backslash A$, much closer to the intersection distribution. The Chi-squared distances between $A \cap B$ and $B \backslash A$, between $A \cap B$ and $A \backslash B$, between NAWM and $B \backslash A$, and between NAWM and $A \backslash B$, help to confirm these visual observations, as presented in Table 4.2. For all MPM parameters, the region of mask B only is closer to the intersection region (first column values are smaller than second column) than mask A, and the region of mask A only is closer to NAWM (fourth column values are smaller than third column) than mask B.

When fitting a bimodal Gaussians mixture model to voxels distributions in $A \backslash B$ and $B \backslash A$ and comparing the mixing proportions and means of both components, as gathered in Table 4.3, we observe that the repartition of data is

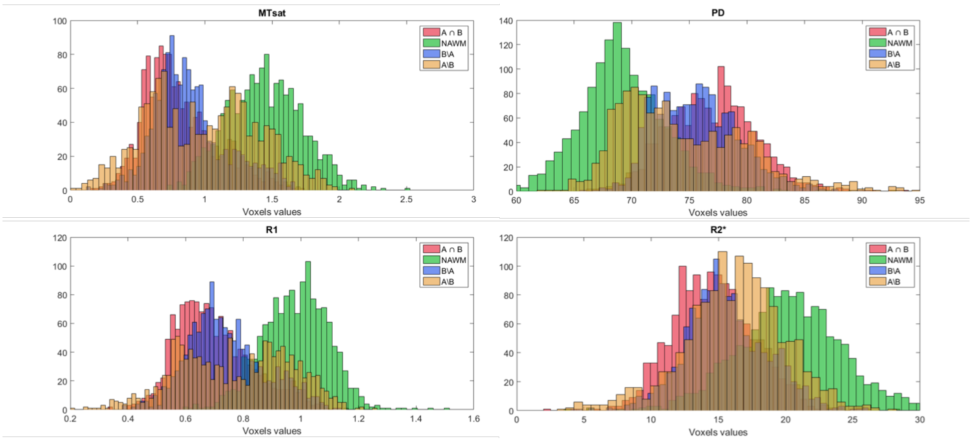

Figure 4.7: Histogram distributions of each region, for MTsat, PD, R1 and R2* independently.

	Chi-squared distance			
	A ∩ B vs B\A	**A ∩ B vs A\B**	**NAWM vs B\A**	**NAWM vs A\B**
MTsat	0.0106	0.0357	0.1002	0.1060
PD	0.0391	0.0972	0.2334	0.2645
R1	0.0034	0.0100	0.0260	0.0297
R2*	0.1091	0.2448	0.6565	0.6719

Table 4.2: Chi-squared distances of data distribution histograms.

approximately $50\% - 50\%$ in region $A \backslash B$ (except in the case of PD), while it lies around $80\% - 20\%$ for $B \backslash A$. This suggests that the latter one depicts a rather high proportion of voxels correctly classified as lesions (since the higher mixing proportion has a mean value close to the $A \cap B$ mean value), while region $A \backslash B$ comprises a higher proportion of potential erroneously classified voxels.

Ultimately, the search for natural clusters within regions $A \backslash B$ and $B \backslash A$ indicated that region $A \backslash B$, for MTsat and R1, comprises an optimal number of two clusters in the majority of subjects (83% for MTsat and 63% for R1 - centroids median values are 0.6981 and 1.0598 for MTsat, 0.6314 and 0.8569 for R1). However, region $B \backslash A$ is characterized by one cluster in the majority (94% of subjects for MTsat and 91% for R1). This implies the co-existence of two groups of voxels (in MTsat and R1 at least) in the FLAIR-based only region: one set of correctly annotated lesion voxels, and one set of possible segmentation errors.

	A\B				**B\A**			
	Component 1		*Component 2*		*Component 1*		*Component 2*	
	Mixing prop	**Mean**	**Mixing prop**	**Mean**	**Mixing prop**	**Mean**	**Mixing prop**	**Mean**
MTsat	0.4374	0.6175	0.5626	1.2751	0.8392	0.8023	0.1608	1.3619
PD	0.3779	70.3526	0.6221	77.2468	0.8435	76.3579	0.1565	71.9058
R1	0.4561	0.9395	0.5439	0.6249	0.8530	0.7035	0.1470	0.9602
R2*	0.5004	15.8557	0.4996	16.5371	0.7844	15.8558	0.2156	14.4666

Table 4.3: Mixing proportion and mean of the two components of the bimodal Gaussians mixture model fitting voxels distributions in regions $A\backslash B$ and $B\backslash A$

Such results do not appear in PD and R2*, where both regions comprise only one cluster in the majority of cases.

4.4 Discussion and conclusion

In this chapter, we presented an original segmentation technique developed at the GIGA-CRC, derived from the traditional US algorithm from SPM, but accounting for lesions as an additional tissue class. It was previously validated for MS lesions and tumors segmentation based on conventionnal MR images, here we investigated its application to parametric MPM maps.

We started by applying the US algorithm for a multi-channel segmentation of MPM maps of healthy controls. We determined the combination of MPM maps as well as the number of Gaussians to use to model the three main tissue classes leading to the best outcome. We found that modelling the intensities of CGM with 5 Gaussians, DGM with 5, WM with 6 and CSF with 5, and including the MTsat, PD and R1 maps in the multi-channel segmentation gave the most accurate segmentation. These parameters were then transferred to USwL, for which we segmented normal appearing tissues and MS lesions using MPM data from MS patients.

In the different analyses conducted in this study, we compared in several ways the generated MPM-based lesion mask from USwL to one based on FLAIR intensities only. Up to now, FLAIR imaging is the traditional MRI technique used in clinical routines to assess MS lesion load estimation. Our results suggest that MPM parameters bring more information regarding MS lesions than conventional FLAIR imaging. The extend of WM damage detected with MPM maps is characterized by actual physical and biological tissues modifications. Besides, those changes are in accordance with histological studies of MS brains. On the contrary, FLAIR hyperintensities cannot be attributed to such measurable properties, and thus bring less confidence about the underlying tissues alterations. In parametric maps, each tissue is characterized by a specific range of voxel values [Weiskopf et al., 2013], easing the detection of outliers, e.g. potential lesion voxels.

In the literature investigating multiple sclerosis with qMRI, lesions are most of the time delineated either manually by experienced users, or with some algorithms based on FLAIR, T1w or MPRAGE intensities [Filippi et al., 1998a, Alfano et al., 2000, Chen et al., 2008, Lema et al., 2017, Bonnier et al., 2014]. In only a restricted number of studies the segmentation of lesions was derived from the quantitative maps themselves. Brown et al. have compared a lesion segmentation automatic tool based on the identification of "significant" changes of MTR values at several time points to Gd-enhanced lesions detected with a Bayesian classifier with PDw, T1w and T2w images [Brown et al., 2013]. Engström et al. have constructed lesion probability maps based on PD, R1 and R2 estimates comparing a group of MS patients against healthy controls [Engström et al., 2014]. None of these techniques enables the creation of a patient-specific lesion mask for one scanning session derived from quantitative parameters. To the best of our knowledge, the direct use of MPM maps for MS lesion segmentation is state-of-the-art.

Here, we showed that "extra" lesion voxels detected by the MPM-based mask, not comprised in the FLAIR-based mask, are closer to the voxels distribution of the region certainly covering MS plaques (i.e. the intersection of both masks, containing both MPM-related tissue alterations and FLAIR hyperintensities). This is true for the four parameters (MTsat, PD, R1 and R2*) but not for FLAIR, suggesting that a certain combination of qMRI maps, with the appropriate algorithm, is able to better delineate lesions even when they are not visible on conventional scans. However, FLAIR images are still included in the MPM-based lesion mask construction, because of their high sensitivity to intensities outliers, probably revealing lesions (at least a portion of them). Therefore, qMRI maps act more as complementary tools for accurate plaques delineation, by improving and/or correcting FLAIR-based masks, but could probably not fully replace cMRI techniques. Combining USwL, MPM and FLAIR imaging leads to a finer delineation of lesions, as well as a better characterization of tissues for the understanding of the mechanisms underlying their emergence, while working *in vivo*.

Chapter 5

Multiple sclerosis longitudinal study

Contents

This section is based upon the following research article submitted for publication in *"Brain and Behavior"*, currently in revision (preprint available in MedRXiv [Vandeleene et al., 2022]):

Vandeleene N., Guillemin C., Dauby S., Requier F., Charonitis M., Chylinski D., Balteau E., Maquet M., Lommers E., Phillips C., "Using quantitative magnetic resonance imaging to track cerebral alterations in multiple sclerosis: a longitudinal study"

5.1 Introduction

In multiple sclerosis, it has been shown that the early, diffuse and chronic inflammation within NAWM and NAGM is ultimately responsible for diffuse neuro-axonal loss and neurodegeneration, which is deemed responsible for a progressive accumulation of disability [Kutzelnigg et al., 2005, Frischer et al., 2009, Haider et al., 2016].

By contrast, effective repair mechanisms can occur within focal lesions but probably also in normal appearing tissues [Brown et al., 2014]. However, our understanding of these complex processes is still fragmentary. The difficulty of acquiring histopathological data on MS patients at various stages of the disease makes it challenging to describe the time course of injury and potential repair mechanisms in multiple sclerosis. Consequently, there is a need for new imaging techniques to improve the *in vivo* monitoring of brain damages formation, progression and repair in MS [Wang et al., 2019].

Conventional MRI (cMRI) sequences do not sensitively detect cortical lesions and diffuse changes in NABT, due to a rather low sensitivity of conventional MR imaging for cortical lesions, mixed contrast weight, and an overall limited histopathological specificity within cerebral tissues. Quantitative MRI (qMRI), however, is more sensitive but also more specific to microstructural properties of CNS tissues.

Few studies addressed the longitudinal variations in qMRI. R2* [Elkady et al., 2018, Elkady et al., 2019, Khalil et al., 2015], PD and T1 were reported to increase in the basal ganglia over a period of a year [Gracien et al., 2017b], whereas a decrease in magnetization transfer ratio (MTR) in normal appearing white matter was reported over one [Laule et al., 2003] or two years [Hayton et al., 2012]. No significant correlations or regressions were demonstrated between those measurements and clinical measures [Elkady et al., 2019, Khalil et al., 2015, Laule et al., 2003, Gracien et al., 2017b]. However, [Hayton et al., 2012] reported an increase in mean WM lesion MTR over 24 months associated with a sustained increase in EDSS. Authors have proposed as a possible explanation that subjects experiencing a sustained increase in EDSS have higher levels of inflammation, axonal edema and dysfunction at baseline, and that the MTR increase corresponds to edema resolving and attrition of dysfunctional axons [Hayton et al., 2012].

Regarding focal white matter plaques, qMRI emerges as an appealing biomarker to describe the dynamic processes of demyelination and remyelination. For instance, MTR was shown to sharply decrease within gadolinium enhancing lesions before recovering during the subsequent months [Dousset et al., 1998, Levesque et al., 2010, van den Elskamp et al., 2010], and within NAWM days to weeks before the formation of a new active lesion [Filippi et al., 1998b, Fazekas et al., 2002].

Because each qMRI parameter is differently sensitive to histologically measured iron and myelin contents, this approach might become a fundamental tool for longitudinal *in vivo* monitoring of MS lesions and NABT evolution at the tissue microstructural level.

In this longitudinal study, we investigate the evolution of the four simultaneously acquired qMRI parameters (MTsat, PD, R1, R2*) within NABT and WM lesions of 17 MS patients - relapsing remitting (RRMS) and progressive MS (PMS) - who were scanned two times with at least a one-year interval, following the multi-parameter mapping (MPM) protocol at 3 Tesla [Weiskopf et al., 2013]. Segmentation of different cerebral tissue classes was computed using the segmentation technique presented in the previous chapter: Unified Segmentation with Lesion (USwL). We assessed the time course of parameter values in several tissue classes: NAWM, NACGM and NADGM as well as focal WM lesions. We related the changes in NABT to clinical course, and looked at the tissue directly surrounding WM lesions that changed status over time, i.e., switching from NAWM to lesion.

5.2 Methods

A description of the population, seventeen MS patients (RRMS and PMS) who underwent two 3T MRI acquisitions separated with a median time interval of 30 months (range: 14-61) appears in Chapter 3, along with a summary of the acquisition sequences comprising FLAIR and MPM protocols. Extended demographic data appears in Table 5.1.

5.2.1 Preprocessing

Based on the preliminary WM lesion mask constructed with LST, the images were segmented using the USwL method presented in Chapter 4. Multi-channel segmentation was conducted, using MTsat, PD, R1 and FLAIR images. A chartflow resuming the processing steps appears in Figure 5.1. The preliminary lesion mask was used as input for the first session data (at T0) then the *a posteriori* lesion map generated at this initial step served as prior to the subsequent session (at T1).

	Age range	**Sex**	**Disease duration (in years)**	**MS type**	**Disease Modifying treatment**	**Total number of relapses**
sub-001	36-40	F	0.8	RRMS	First line	1
sub-002	26-30	F	0.7	RRMS	Second line	2
sub-003	31-35	M	1.6	RRMS	First line	1
sub-004	26-30	M	1.8	RRMS	Second line	2
sub-005	36-40	F	3.4	RRMS	Second line	1
sub-006	21-25	M	0.3	RRMS	First line	1
sub-007	31-35	F	1.6	RRMS	Second line	2
sub-008	61-65	M	16	PMS	None	N/A
sub-009	31-35	M	11.4	RRMS	Second line	2
sub-010	31-35	M	10	PMS	None	N/A
sub-011	61-65	M	25	PMS	None	N/A
sub-012	26-30	F	4	RRMS	First line	1
sub-013	61-65	F	23.7	PMS	None	N/A
sub-014	51-55	F	28	RRMS	First line	4
sub-015	46-50	M	8.9	PMS	Ocrelizumab	N/A
sub-016	36-40	M	2	PMS	Ocrelizumab	N/A
sub-017	46-50	M	0.5	RRMS	Second line	2

Table 5.1: Demographic data for the longitudinal study. Age, disease duration and number of relapses values were taken at baseline.

Segmentation teased out the different tissue classes of interest: NAWM, NACGM and NADGM, as well as WM lesions. To analyze the microstructure within those tissue classes, *a posteriori* tissue maps were binarized and tissue-specific independent masks were constructed: each voxel was assigned to one single tissue class with the highest probability for that voxel (provided that this probability was above 0.2). The lesion binary mask was further cleaned for lesions with a volume less than $10mm^3$ which likely resulted from segmentation errors. Finally, binarized tissue class masks were in turn applied on the MPM maps to extract voxel values inside them.

5.2.2 Brain volume change

Volumetric changes were investigated using the USwL *a posteriori* tissue probability maps. The following measures of brain volume were computed for each session of each participant: (1) Total intra-cranial volume (TIV) = volume (NAWM + GM + CSF + lesions), (2) brain parenchymal fraction (BPF) = volume (NAWM + GM + lesions)/TIV, (3) GM fraction (GMF) = volume (GM)/TIV, and (4) lesion fraction (LF) = volume (lesion)/TIV. The percent-

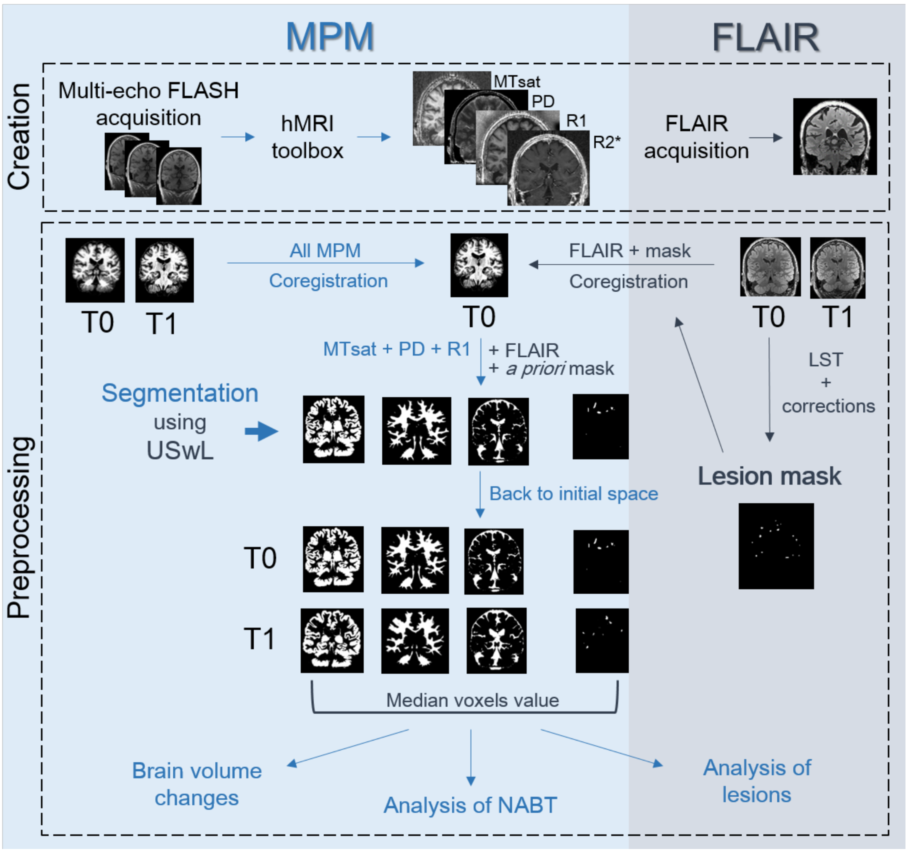

Figure 5.1: Chartflow of data creation and processing. MPM maps were created with the hMRI-toolbox, FLAIR images were directly acquired for both sessions (T0 and T1). A preliminary mask was constructed based on T0 FLAIR. All images (MPM and FLAIR, T0 and T1) were co-registered to the MPM T0 space. Segmentation using USwL allowed to isolate the different tissue classes.

age of change between both scanning sessions was evaluated for each volumetric measurement, then annualized changes were computed by dividing these measures by scan intervals (in years). Results were directly analysed with a t-test (testing if significantly different from 0 at $p < .05$), but also in the same way as the normal appearing tissues MR parameters in relation to the patients clinical status (see next section).

5.2.3 Analysis of normal appearing tissues

The median value of qMRI parameters was extracted from the three normal appearing tissues (NAWM, NACGM and NADGM), and an individual annual rate of change (ARoC) was computed for each parameter in each tissue class, based on the initial and final values and accounting for the time interval (in years) between scans. This rate of change in qMRI parameters served as dependent variable in a general linear model testing the effect of clinical status:

$$Y = \beta_0 + \beta_1 X_{status} + \varepsilon \tag{5.1}$$

Y is the ARoC for a qMRI parameter and tissue class, β's are the regression parameters corresponding to the associated regressor (with β_0 the intercept), and ε the residuals. X_{status} is a binary categorical variable representing the patient disease activity status: a status score of 1 was assigned to patients stable or improving from T0 to T1.

This patient status X_{status} was derived from one score of disease activity: NEDA-3 (No Evidence of Disease Activity [Pandit, 2019]), a composite of three related measures of disease activity. A score of 0 was assigned in the presence of new clinical relapses (only concerning relapsing remitting patients) and/or MRI activity (new or enlarged lesions visible on FLAIR T2 or Gadolinium-enhanced images) and/or sustained disability progression over six months based on EDSS. For both RRMS and PMS patients, disability progression was defined as a 1.0-point increase if the EDSS score was $\leq$ 4.0 at baseline and as a 0.5 point increased if the baseline EDSS score was $>$ 4.0. The threshold of 4.0 was proposed in this study because it is considered as a milestone regarding ambulatory performance.

NEDA-3 was evaluated at mid- and end-scanning interval, and a final status score of 0 was given only to patients for which disease activity or progression was noted in both cases, indicating a clear progression of the disease over the whole interscan interval.

Longitudinal clinical information allowing to derive the disease activity status for each subject appears in Table 5.2.

Permutation tests were employed for inferences [Anderson, 2001]. The R-squared value was tested against computed statistics after permutation of the data. For a number n of permutations, the X_{status} values were randomly shuffled (constructing a new regressor written X^{π}_{status}), tested against the unchanged response Y, and generating each time a permuted R-squared value (noted R_{π}, R_{obs} being the true R-squared value computed without permutation of the data). The condition $X_{status} \neq X^{\pi}_{status}$ is verified at each permutation. After n permutations (with $n = 5000$ here), a p-value was computed based on the

	EDSS T0	**EDSS T1/2**	**New lesion T1/2**	**Relaspe T1/2**	**NEDA T1/2**	**EDSS T1**	**New Lesion T1**	**Relapse T1**	**NEDA T1**	**Time period T0-T1**	**Score**
sub-001	2	2	None	None	YES	2	None	None	YES	30	1
sub-002	1.5	1.5	None	None	YES	1.5	None	None	YES	27	1
sub-003	2	2	None	None	YES	2	None	None	YES	27	1
sub-004	3	3	None	None	YES	3.5	None	None	YES	25	1
sub-005	1	1	None	None	YES	1	None	None	YES	24	1
sub-006	1.5	1.5	None	None	YES	1.5	None	None	YES	24	1
sub-007	2	2	None	None	YES	2	None	None	YES	22	1
sub-008	3.5	4.5	None	N/A	NO	5	None	N/A	NO	51	0
sub-009	2	2.5	None	None	YES	2.5	None	None	YES	57	1
sub-010	6	6	Yes	N/A	NO	6.5	None	N/A	NO	14	0
sub-011	6	6	None	N/A	YES	6.5	None	N/A	YES	14	1
sub-012	1	1.5	None	None	YES	1.5	None	None	YES	55	1
sub-013	5.5	6	None	N/A	NO	6.5	None	N/A	NO	60	0
sub-014	2.5	3.5	Yes	Yes	NO	3	None	None	YES	57	1
sub-015	4	4.5	None	N/A	NO	5	None	N/A	NO	51	0
sub-016	5	4.5	Yes	N/A	NO	4.5	None	N/A	YES	61	1
sub-017	2	3	Yes	Yes	NO	3	Yes	Yes	NO	56	0

Table 5.2: Longitudinal clinical information and derived disease status score. The time period between T0 and T1 is expressed in months.

following formula:

$$p = \frac{(\#(R_{\pi} > R_{obs})}{(n+1)} \tag{5.2}$$

which estimates the probability of obtaining R_{obs} under the null hypothesis that Y is not correlated to X_{status}. The null hypothesis is rejected if $p < .05$ FDR-corrected for multiple comparisons [Benjamini and Hochberg, 1995], for the 12 tests performed (3 tissue classes with 4 qMRI parameters).

Two-tailed t-tests were applied *post-hoc* on the significant results of permutation tests to compare the ARoC distribution between disease status, i.e., $X_{status} = 0$ against $X_{status} = 1$. Inferences were conducted at a significance level of .05.

The same pipeline was applied to the brain volumetric changes (BPF, GMF and LF) to test their correlation to the disease activity status.

5.2.4 Analysis of lesions and peripheral tissues

For white matter lesions analysis, we did not use the annual rates of change (ARoC) but exploited directly the qMRI parameters voxel values. Importantly, with USwL, the prior lesion mask is only used in a probabilistic way and the estimated posterior lesion map, obtained using MTsat, PD, R1 and FLAIR images, typically showed more extended lesion than clinically visible on the FLAIR image alone.

Therefore, we separated focal lesions detected on FLAIR images, with LST and visual inspection, from their peripheral regions detected on qMRI maps. Two different peripheral regions were considered: one for each time point (T0 and T1). Therefore, at T0, three distinct lesion-related regions were isolated:

- The lesions, as clinically defined, pertaining to hyperintensity on the conventional FLAIR MR image acquired at T0. These are referred to as “focal FLAIR lesion”.
- The peripheral region detected on qMRI maps at T0, at the borders of (but not including) the focal FLAIR lesion. Those are referred to as “initial peripheral lesion”.
- The peripheral region, detected on qMRI maps at follow up, bordering (but not including) the initial peripheral lesion, further referred to as “later peripheral lesion”. This was computed by masking out the T1 lesion mask with the T0 lesion mask. This region allows us to determine whether

its microstructure at T0 forebodes a full-blown plaque, detectable during follow up. Those sometimes appear hyperintense on FLAIR images.

The three areas were compared between each other and with NAWM, in order to characterize them on a microstructural basis (Figure 5.2). For an accurate lesion-by-lesion analysis, only enlarging lesions, i.e., present in the three masks, were considered for these comparisons. NAWM region consisted of all white matter voxels which did not belong to any of the three lesion-related regions. The four areas are not overlapping as no voxel could belong to more than one class at the same time.

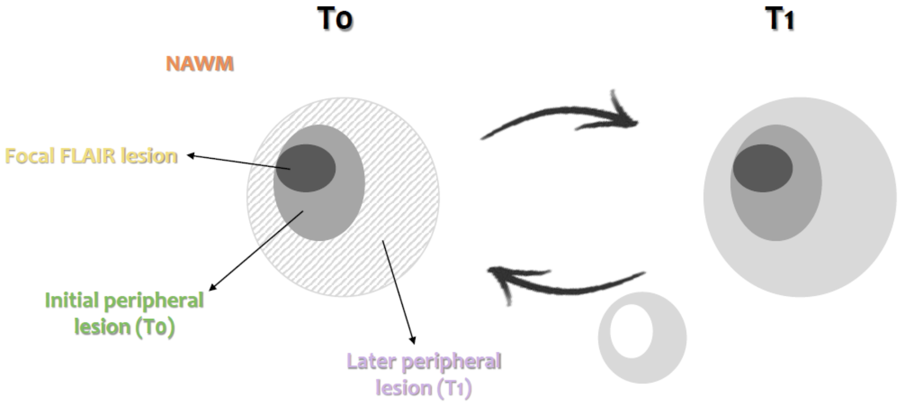

Figure 5.2: Schematic illustration of the NAWM and 3 lesions-related areas: focal FLAIR lesion (dark gray area), initial peripheral lesion detected at T0 (medium gray area), later peripheral lesion detected at T1 (dashed, left, and light gray, right, area)

For all participants, MTsat, PD, R1 and R2* median values were extracted from each lesion area, considering lesions individually (between 2 and 66 measurements per subject). Similarly, the median qMRI values within NAWM were also extracted (one measurement per subject). These values were extracted from T0 and T1 scans separately. Statistical analyses were performed in SAS 9.4 (SAS Institute, Cary, NC). None of the qMRI parameters was normally distributed, therefore we applied a log transformation on each of them prior to statistical analysis. For each qMRI parameter, a separate Generalized Linear Mixed Model (GLMM) tested the effect of areas (NAWM and the three lesion-related areas), and time points (T0 and T1), as well as their interaction (i.e., $area * time$), on the median qMRI parameter value, with a first-order autoregressive variance/covariance model and participants as a random factor (intercept). The degrees of freedom were estimated using Kenward-Roger's method. Statistical significance was estimated at $p < .05$ after adjustment for multiple comparison using Tukey's procedure.

5.3 Results

5.3.1 Volume changes

Brain parenchymal fraction (BPF) annually decreased between T0 and T1 by $-0.67 \pm 1.12\%$ (significantly different from zero; paired-sample t-tests; $t(16) = 2.57; p = .0204$) whereas lesion fraction (LF) significantly increased by $22.88 \pm 26.13\% (t(16) = -3.70; p = .0019)$. Gray matter fraction (GMF) non-significantly decreased by $-0.30 \pm 1.44\%$.

5.3.2 Analysis of normal appearing tissues

As expected, changes in MTsat and R2* within NABT between T0 and T1 varied across subjects (Figure 5.3). PD and R1 exhibited similar behaviors, see Figure 5.4.

At the group level, with the GLM analysis and permutation inference, we observed that the ARoC of MTsat and R2* positively regressed with disease status as follows (Table 5.3): MTsat in NAWM and NACGM and R2* in NAWM significantly increased in patients who fare well ($X_{status} = 1$).

	NAWM	**NACGM**	**NADGM**
MTsat	*0.039 (.011)**	*0.017 (.007)**	0.004 (.749)
PD	-0.018 (.670)	0.405 (.225)	0.250 (.552)
R1	0.009 (.139)	0.004 (.471)	0.010 (.111)
R2*	*0.295 (.002)**	0.121 (.092)	0.066 (.770)
BPF	- 0.884 (.156)		
LF	21.23 (.108)		

Table 5.3: Regression coefficients and their associated p-values (in parentheses) for the effects of X_{status} on the individual ARoC for each qMRI parameter (MTsat, PD, R1 and R2*) and for volumetric measurements (BPF and LF). * Results significant at $p < .05$, FDR corrected.

Post-hoc t-tests applied on these significant results for a clearer illustration of the difference in disease status (Figure 5.5) were all significant at a level of $p < .05$. Regarding BPF and LF, their correlation to the disease activity sta-

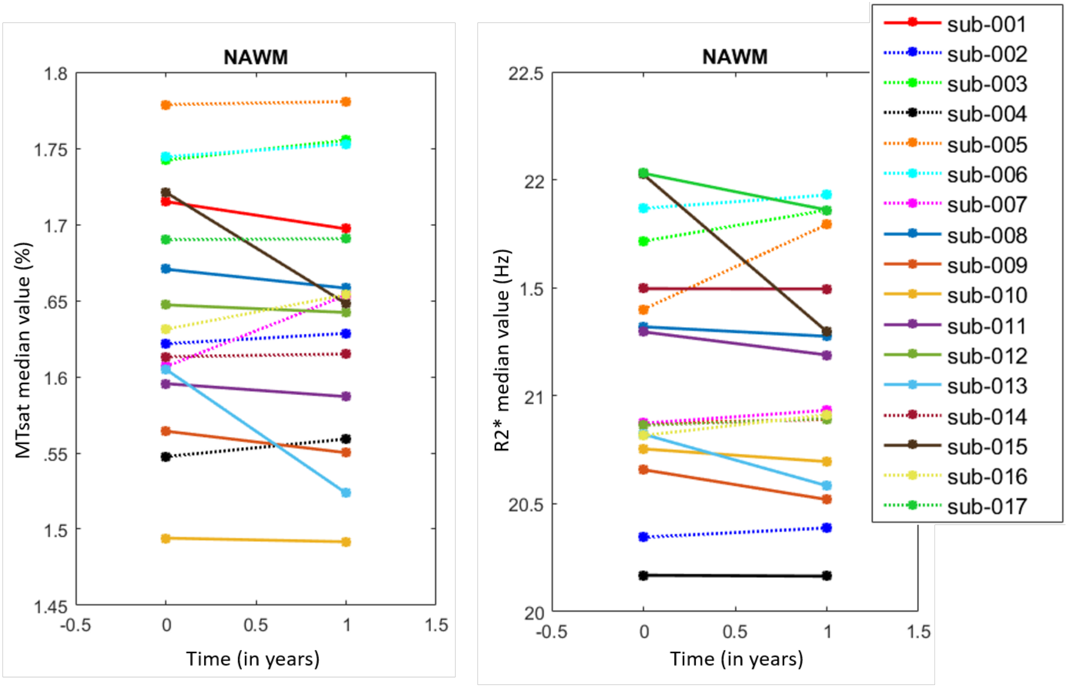

Figure 5.3: Line plots illustrating individual ARoC for MTsat (left) and R2* (right) in NAWM. Each line corresponds to one subject. Dotted lines represent increasing rates.

tus was not significant (Table 5.3), suggesting that qMRI parameters are more sensitive to subtle microstructural changes in NABT over time than global morphological measurements.

5.3.3 Analysis of lesion microstructure

The number of enlarging white matter lesions between T0 and T1 varied from 2 to 66 across patients, for a total of 741 identified enlarging lesions among all subject, corresponding on average among patients to 63% (±31%) of the amount of initial focal lesions. Lesions were considered “enlarging” when they appear in the two (or three) lesion masks, excluding new or “disappearing” plaques. The number of enlarging lesions did not significantly differ between patients’ disease status groups ($t(15) = .244, p = .811$).

GLMMs found a significant effect of areas (3 lesional regions and normal appearing white matter) for MTsat, R1, R2* and PD median (MTsat: $F_3 = 35.34, p < .0001$, PD: $F_3 = 68.03, p < .0001$, R1: $F_3 = 40.26, p < .0001$, R2*:

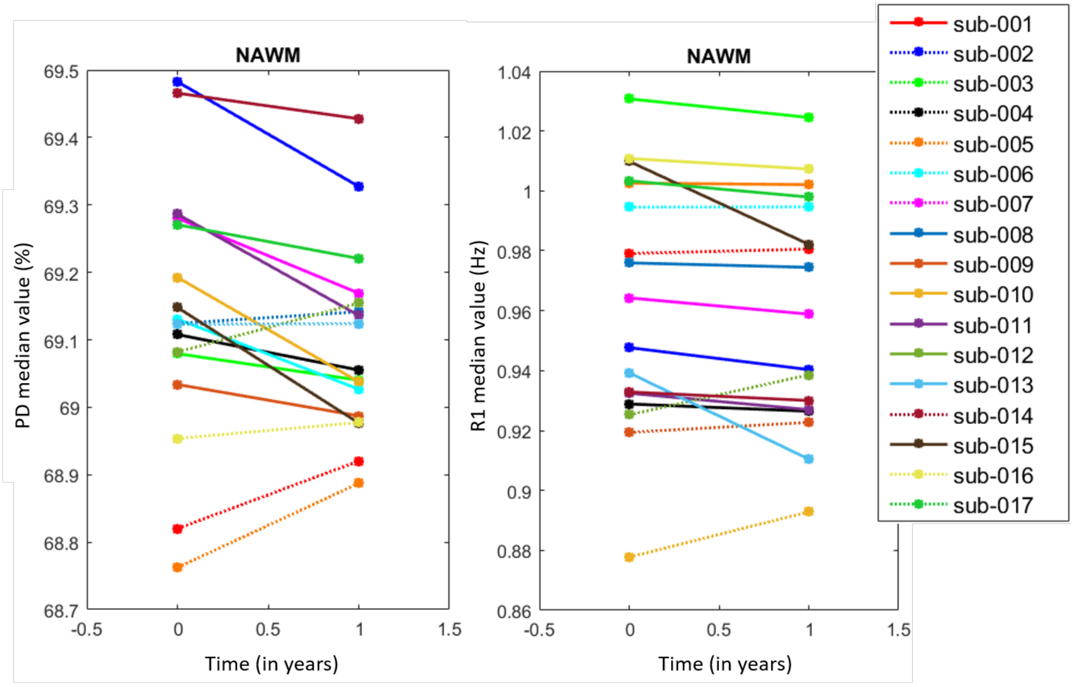

Figure 5.4: Line plots illustrating individual ARoC for PD (left) and R1 (right) in NAWM. Each line corresponds to one subject. Dotted lines represent increasing rates.

$F_3 = 32.32, p < .0001$). By contrast, neither time effect (T0 vs T1; MTsat: $F_3 = 0.36, p = .5481$, PD: $F_3 = 1.20, p = .2735$, R1: $F_3 = 2.05, p = .1520$, R2*: $F_3 = 2.86, p = .0911$), nor the $area * time$ interaction (MTsat: $F_3 = 0.09, p = .9671$, PD: $F_3 = 0.14, p = .9346$, R1: $F_3 = 0.14, p = .9331$, R2*: $F_3 = 0.40, p = .7565$) were significant, suggesting the microstructural stability of the initial lesion core. *Post-hoc* tests confirmed significant differences between the four tissue areas.

At T0 and T1, MTsat, R1 and R2* values were significantly larger in the initial peripheral lesion than FLAIR lesion, in the later peripheral lesion than the initial one, and in the NAWM than later peripheral lesion. The reverse was observed for PD. The significant difference in parameters between initial and later peripheral lesion at T0 suggests that subtle microstructural changes appear in the periphery of the initial lesion, months before their detection as focal FLAIR lesions at T1. Adjusted p-values appear in Figure 5.6.

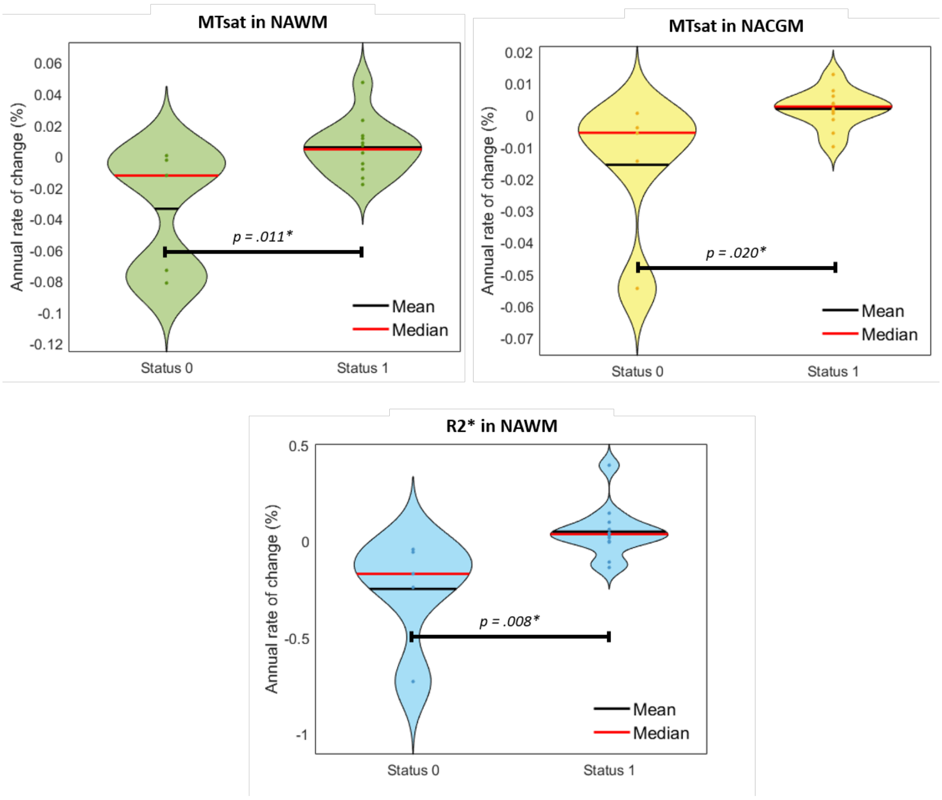

Figure 5.5: Violin plots of significant change rates in microstructure with respect to X_{status}. From left to right: MT in NAWM, MT in NACGM, R2* in NAWM. * $P < .05$.

5.4 Discussion

This longitudinal study followed up volumetric data and qMRI brain metrics (MTsat, PD, R1, R2*) in 17 MS patients for a median time interval of 30 months. The main results are threefold. First, the microstructure of normal appearing brain tissues changes over time and these modifications concur with, and potentially drive, clinical evolution. This critical finding suggests that repair mechanism and edema resorption can be monitored *in vivo*. Second, the microstructure within WM plaques is remarkably heterogeneous. Importantly, at their periphery, microstructural alterations foreshadow their expansion, as detected by conventional MRI. Third, as expected, we observed a small but significant brain atrophy and lesion load increase with time.

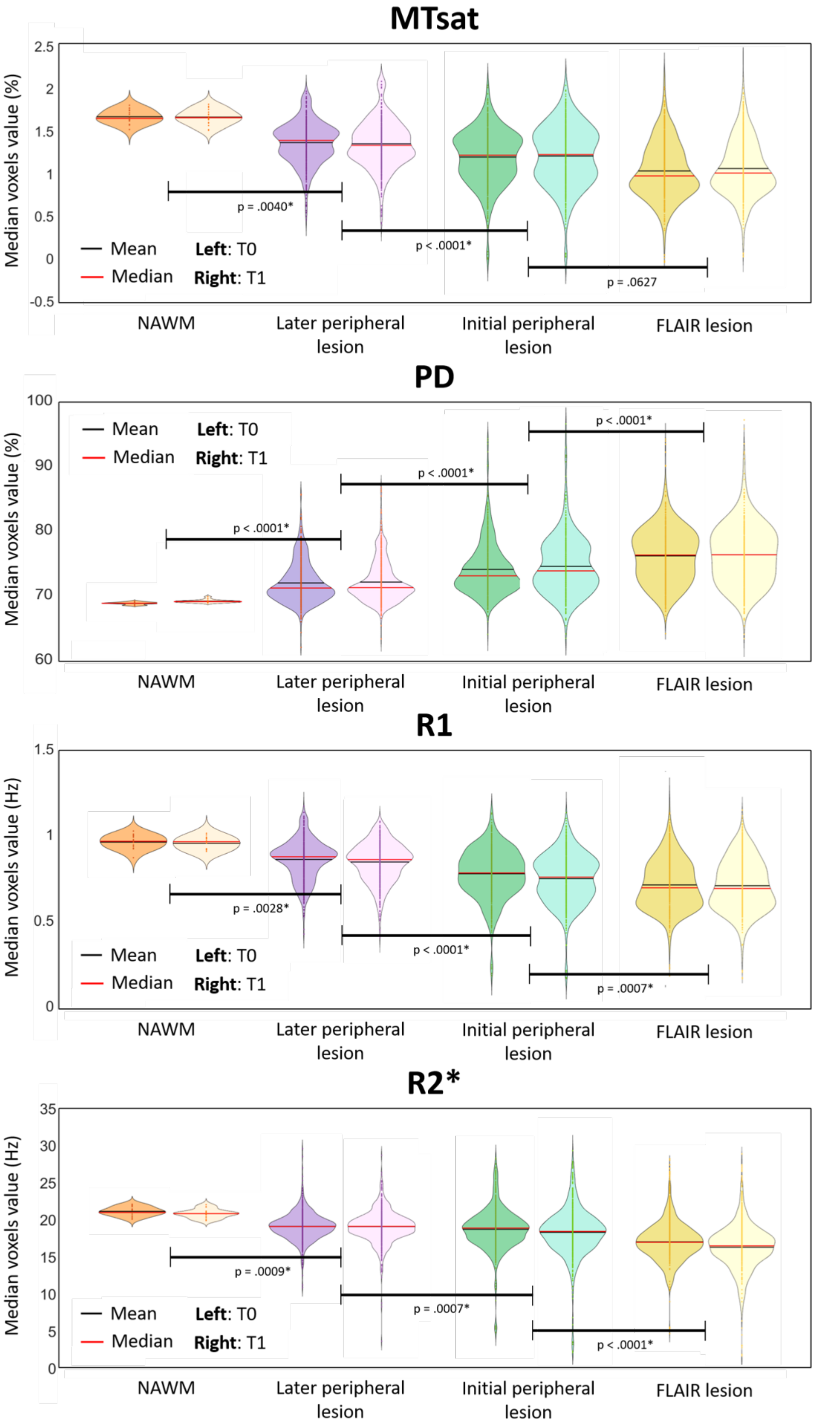

Figure 5.6: Microstructural parameters in NAWM and the 3 lesion-related areas, for each scanning time T0 and T1. P-values were obtained with *post-hoc* tests on the tissue area effect. * $P < .05$.

Quantitative MRI parameter time course within NABT Longitudinal analyses of multiparameter qMRI data are scarce. A progressive shortening of T2/T2* [Bonnier et al., 2017] or increase in R2* [Elkady et al., 2018, Elkady et al., 2019, Khalil et al., 2015] was reported within the basal ganglia, suggesting increased of myelin and/or iron contents as well as edema resorption. Likewise, PD and T1 increased within a year, suggesting a demyelination and/or axonal loss [Gracien et al., 2017a]. MTR progressively decreases in normal appearing white matter of patients with multiple sclerosis over one [Laule et al., 2003] or two years [Hayton et al., 2012]. These abnormalities tend to be more pronounced in progressive phenotypes [Rocca et al., 1999] and were associated to a slow, diffuse and global myelin pathology.

Here, we showed that MTsat within normal appearing white and cortical gray matter, and R2* values within normal appearing white matter increase in clinically stable or improving patients. Because MTsat and R2* both correlate with myelin content, our results suggest repair mechanisms within NABT of patients who are responding to disease modifying treatments, despite the initial myelin/axonal loss and independently from WM focal lesion evolution. Such increases could also be explained by an edema/inflammation resorption, but less likely than myelin/axonal density changes since MTsat is the least dependent to water content among the four qMRI parameters. These results echo cross-sectional analyses showing that healthy controls have higher MTsat and R2* values within the same tissue classes compared to MS patients [Lommers et al., 2019].

Lesion microstructure Focal inflammatory demyelinating lesions have been extensively characterized and are traditionally classified as active, chronic active (smoldering) or inactive plaques according to the presence and distribution of plaque-infiltrating macrophages/microglia [Frischer et al., 2015, Dutta and Trapp, 2007, Lassmann et al., 2001]. Focal WM pathology is a constantly evolving process including episodes of demyelination and remyelination but also accumulation of irreversible axonal damage. Age, disease duration, clinical phenotype as well as disease modifying treatment all contribute to the dynamic nature of focal white matter pathology [Frischer et al., 2015, Lucchinetti et al., 2000, Lassmann et al., 2001]. This accounts for the large inter- and intra-individual heterogeneity of multiple sclerosis, which conventional MRI is largely unable to capture.

By contrast, quantitative MRI parameters are sensitive to myelin, axonal as well as iron contents and appear as promising markers of plaque dynamics. For instance, Magnetization Transfer Ratio (MTR) was shown to sharply decrease within gadolinium enhancing lesions before recovering during the subsequent months [Dousset et al., 1998, Levesque et al., 2010, van den Elskamp et al., 2010]. Likewise, reduction of MTR within NAWM, days to weeks before the formation of a new active lesion was also demonstrated [Filippi et al., 1998b, Fazekas et al., 2002], and long-term MTR changes in white matter plaques were observed in relation with disease progression [Rocca et al., 1999, Zheng et al., 2018]. The present study broadens the quantitative characterization of plaque dynamics, in keeping with previous longitudinal studies [Bonnier et al., 2017, Chawla et al., 2018].

Two important findings emerge from the results. First, qMRI refines lesion segmentation, as compared to the processing based on the sole FLAIR image. In consequence, the initial lesion revealed by qMRI is typically wider that the plaque detected in FLAIR. Its periphery is characterized by a decrease in MTsat and R2* as compared to NAWM, suggesting an incipient demyelination, reminiscent of the so-called “periplaques” [Lieury et al., 2014]. Moreover, MTsat, R2* and R1 values progressively decrease from normal appearing white matter to plaque core, suggesting a centripetal loss of myelin content. Second, plaque microstructure is altered in plaque periphery before any observable change in conventional MRI signals. This finding suggests, in keeping with neuropathological observations [Frischer et al., 2015, Kuhlmann et al., 2017, Lucchinetti et al., 2000, Lassmann et al., 2007] that subclinical ongoing inflammation and/or demyelination takes place in the periphery of an active plaque, well before it is detectable on FLAIR or T1 post-gadolinium sequences. If confirmed on larger population samples, and with precise biophysical modelling, these observations could be taken a step further and derive a model of the lesion expansion over time. With such a tool, one would be able to predict how lesions are going to expand and/or even appear in normal appearing tissues. Taking advantage of the range of physical voxels values specific to each tissue class, advanced tool could automatically detect the future behavior of lesions. However, this type of analysis would probably require a substantial amount of data, not currently available. These findings might significantly modify treatment management in MS patients.

Another plausible hypothesis explaining the progressive decrease of R2* in initial and later peripheral regions is that iron-containing macrophages could be removing iron from the lesions through perivascular drainage into the extracellular compartment. Previous neuropathological studies have reported an iron loss at the edges of a subset of MS lesions, depending on their type (active, inactive, smoldering, etc.) as well as the patient age and disease duration [Hametner et al., 2013, Popescu et al., 2017]. Due to the limited sensitivity of R2* to local iron concentration as compared, for example, to the combined use of R2* and quantitative susceptibility mapping (QSM) [Hametner et al., 2018], validating this theory would require additional measures which can better describe iron dynamics in MS lesions and normal appearing white matter.

Volumetric Data In this study, the annual brain percentage volume loss at the group level was 0.67%, which is in line with previous publications [De Stefano et al., 2015]. We also showed a significant increase in lesion fraction. Volumetric data (ARoCs) were highly variable across subjects: changes in BPF range from -2.52 to 1.17% and LF from -0.78 to 103.06%. This variability arises from a large number of factors which do not necessarily relate to MS: age, disease duration, disease phenotype, disease modifying treatment, circadian rhythm, hydration, ... [Bermel and Bakshi, 2006, Zivadinov et al., 2008].

Moreover, annual changes in brain parenchymal fraction as well as lesion fraction only partially correlated to patients disease status, in accordance with a large number of publications [Enzinger et al., 2015, Gracien et al., 2017b]. This highlights the lack of specificity and sensitivity of volumetric measurements, at least at the individual level.

It can appear odd that brain atrophy progresses in parallel to repair mechanisms, as suggested by qMRI parameters. However, gray matter fraction reduction is minimal, and is not significant (see Table 5.3) between T0 and T1. One should keep in mind that cortical atrophy is an irreversible phenomenon. Given the inter- and intra-individual heterogeneity of multiple sclerosis progression, it is possible that patients who have undergone neuron-axonal loss at some point in the disease might be able to remyelinize their remaining axons, hopefully through therapeutic intervention or lifestyle changes. Besides, axonal remyelination is not always effective. Here we showed that variations in MTsat and R2* correlated to the disease activity status, but our clinical evaluation based on EDSS is undoubtedly imprecise. Once again, the size and heterogeneity of our cohort limits the interpretation of such results.

5.5 Limitations

As mentioned earlier, the small size and heterogeneous aspect of the present dataset constitute major limitations of this study. Indeed, it is composed of only 17 patients, with a rather broad range of characteristics such as age, disease duration, disease phenotype, disease modifying treatment, etc., which are known to influence the disability state of the patient and thus their ability to put together repair mechanisms within cerebral tissues [Lassmann et al., 2001, Lassmann, 2013, Frischer et al., 2015, Patrikios et al., 2006, Lucchinetti et al., 2000, Bodini et al., 2016]. In addition, the time interval between two scanning sessions varied rather widely across patients (between 14 and 61 months), although it was brought back to an annual rate where possible. All of these parameters were imposed by standard clinical follow up. Therefore, these results should not be over-interpreted but are nevertheless promising and call for a replication with a larger and more homogeneous or controlled set of MS patients. Larger longitudinal studies are currently being held and will probably confirm these preliminary results.

The second significant limitation is the absence of longitudinal MRI data acquired in a control group of healthy subjects. However, we considered that literature of longitudinal studies of healthy subjects that analysed tissue microstructure could constitute a solution for comparison with MS patients. For example, in [Bonnier et al., 2017], the control group did not show any significant differences regarding T1, T2* or MTR measurements over two years, and the median age of their group is quite similar to ours (34,3 vs 36 years). Also, in [Elkady et al., 2018], they found no longitudinal R2* effect in their control groups, even with an age range superior to ours. Moreover, the median age of our population (< 60 years), as well as the short period between two scanning sessions (median of 14 months), suggests that microstructural alterations would not be noticeable in a healthy participants group, as many quantitative ageing studies detected differences over much larger time periods [Gracien et al., 2017a, Draganski et al., 2011, Callaghan et al., 2014].

Chapter 6

MPM and NODDI parameters

Contents

This chapter is dedicated to the analysis of NODDI parameters (Orientation Dispersion Index (ODI), intra-cellular volume fraction (F_{icvf}), and isotropic volume fraction (F_{iso})) as additional quantitative features. These could help further characterize brain tissues microstructural modifications in relation to multiple sclerosis, as compared to MPM parameters presented in the previous chapters. Here, the ultimate goal would be to include such attributes to improve tissues characterization based on MPM only, but first the relationship between MPM and NODDI measurements was assessed.

6.1 Introduction

NODDI metrics have proven their efficiency in characterizing the microstructural complexity of dendrites and axons *in vivo* on clinical MRI images, both in the case of healthy aging [Merluzzi et al., 2016], or neurological disorders such as Alzheimer's disease [Parker et al., 2018, Slattery et al., 2017], Parkinson's disease [Kamagata et al., 2016, Mitchell et al., 2019] and multiple sclerosis [Hagiwara et al., 2019, Schneider et al., 2017, Granberg et al., 2017, Preziosa et al., 2021, De Santis et al., 2019]. NODDI provides a set of quantitative neurites indices that are more specific biomarkers of tissue microstructural properties than conventional diffusion imaging indices. Indeed classic estimates of fractional anisotropy (FA) and mean diffusivity (MD), from a diffusion tensor model, remain sparsely sensitive and specific to microscopic tissue structures [Pierpaoli and Basser, 1996]. Variations in these metrics may originate from different sources and cannot be specifically attributed to microstructural alterations (e.g. reduced neurite density and increased dispersion of neurite orientation distribution both lead to a reduction of FA) [Beaulieu, 2009].

NODDI and MPM (MTsat, PD, R1, R2*) parameters provide complementary information regarding tissue microstructural properties: F_{icvf} relates to the density of axons and dendrites, and ODI to the degree of the bending and fanning of axons and dendrites, two measurements describing axonal fibers. On the other hand, MPM measures such as R2* providing insights on the orientation and density of myelin fibers [Bagnato et al., 2018, Hametner et al., 2018, Stüber et al., 2014], MTsat detecting myelin content and axons density [Tabelow et al., 2019, Schmierer et al., 2004, Callaghan et al., 2015], and R1 reflecting tissue myelination and associated axons content [Stüber et al., 2014, Kolb et al., 2021], all contribute to a complementary representation of axons and dendrites microstructure when associated with F_{icvf} and ODI. Additionally, F_{iso} describes the free water diffusion, while PD mostly reflects the free water content of the brain [Edwards et al., 2018] and R1 is affected by extracellular water content among others [Granziera et al., 2021]. With such complementary information from both protocols regarding fibers function and water occupation, gathering information from several of these NODDI and MPM parameters should improve the characterization of brain tissue microstructure.

Although literature combining NODDI and MS disease is rather extensive, no consensus seems to have been found regarding the interpretation of the three main NODDI parameters (F_{icvf}, F_{iso} and ODI) in patients with multiple sclerosis over time or compared to healthy populations. Such dissimilarities possibly arise from the choice of inclusion criteria which vary a lot from one study to the other. Some studies showed increased ODI in normal appearing white matter, while decreased in lesions, comparing patients to healthy controls [Hagiwara et al., 2019, Schneider et al., 2017]. Another one showed a increased ODI in lesions and no significant differences in normal appearing tissues [Granberg et al., 2017].

The other two parameters, F_{icvf} and F_{iso}, lead to more stable observations across studies. In normal appearing white matter, F_{iso} tends to increase while F_{icvf} shows a reduction in cross-sectional studies analyzing the difference between MS patients and healthy controls [De Santis et al., 2019, Granberg et al., 2017, Schneider et al., 2017, Collorone et al., 2020, Preziosa et al., 2021]. In lesional tissues, results showed a decrease in F_{icvf} and an increase in F_{iso} in lesions comparing to the NAWM of the same subjects or from a healthy controls population [De Santis et al., 2019, Schneider et al., 2017].

An extended review of the literature findings when combining NODDI maps and multiple sclerosis appears in section 2.3.6.3.

In the present study, we started by assessing the difference in NODDI parameters between MS patients and controls, inside lesions and in normal appearing tissues, in order to try and replicate results from other studies. Our dataset is quite heterogeneous regarding age, disease duration and MS phenotype (see Table 3.1 in Chapter 3), but larger than certain studies.

In the second phase, we tested the correlation between NODDI and MPM parameters within specific brain tissues, i.e. WM, GM and lesions when available, in both MS patients and healthy controls.

Finally, we conducted a whole-brain exploratory voxel-based quantification (VBQ) analysis in order to detect possible local alterations in specific brain regions in patients with multiple sclerosis (compared to healthy subjects). A similar analysis has been published with the same dataset, using only MPM parameters [Lommers et al., 2020]. The idea here is to extend this cross-sectional analysis by including NODDI parameters in the search for local differences, with a multivariate VBQ analytical approach called "MSPM" [1] (v3.0), in the framework of SPM12. Contrary to previous multi-contrast MRI studies using simpler models fitting each contrast separately with GLMs [Gyger et al., 2021, Stefani et al., 2019], multivariate statistics offers to assess how a combination of dependent variables reflects an effect of interest, providing more information than individual univariate models [Stoyanov et al., 2019, McFarquhar et al., 2016].

6.2 Methods

All maps creation and preprocessing steps are described in Chapter 3, in section 3.3.2.2 for MPM and 3.3.3.2 for NODDI. In order to compare both maps in corresponding regions, all images were co-registered to the MPM space because of their better resolution. The registration was computed to match the first b0 image from the NODDI acquisition protocol to the MTsat map. Next, the transformation was applied to all NODDI maps. In previous processes the deformation field from MPM subject space to MNI space as well as *a poste-*

---

[1] `https://github.com/LREN-CHUV/MSPM`

riori tissue masks were already estimated, and could be directly applied to NODDI maps. Using the binary tissue masks lying in MPM space, both MPM and NODDI parameter values were extracted from each tissue class, then summarized by their median value. These measurements were then used for two different purposes: first to try and replicate results found in MS literature (although some studies found incompatible results) and then to illustrate (using scatter plots) and compute (using Pearson coefficients) the relation between pairs of parameters (linking NODDI and MPM parameters) within each tissue class.

Based on literature, we assessed the difference in distributions of median ODI and F_{icvf} values within NAWM and NAGM, comparing MS patients to HC, as well as their difference comparing NAWM and WM lesions (in patients only). In addition, for MS subjects wherever possible (i.e. in patients with asymetrical lesions, 4 subjects in total), we evaluated the difference in ODI between lesions and their contralateral NAWM area. Statistical significance was assessed using t-tests, with a $p < .05$ threshold. A graphical summary of the methodological pipeline of this section appears in Figure 6.1.

For the second (VBQ) analysis, the GM probability maps (including cortical and deep gray matter) as well as the parametric (four MPM and three NODDI) maps were spatially warped to standard MNI space, using the deformation field derived from the image registration step of the Unified Segmentation algorithm [Ashburner and Friston, 2005]. GM maps were modulated by the Jacobian determinants of the deformation, and the parametric maps were warped using the subject-specific deformation field but without modulation. The modulation with the inverse of the Jacobian determinant is applied in order to take the voxels volumetric changes into account; thus in a quantification analysis as VBQ, one wants to preserve the intensity values. Following that, all images and probability maps were smoothed with an isotropic Gaussian kernel of 6mm full width at half maximum (FWHM). Smoothed tissue-specific MPM and NODDI maps were created with a tissue weighted smoothing (6mm FWHM isotropic), which optimally preserved parameter values within each tissue class. Finally, the individual smoothed modulated warped GM probability maps were averaged across all subjects, and a gray matter mask was created by including voxels for which mean GM probability was larger than of WM and CSF, and above 0.2 [Callaghan et al., 2014]. The white matter was not considered here as it contained lesional tissue in subject-specific locations for MS patients. The resulting GM mask was further used as the explicit mask for the VBQ analysis.

Whole-GM voxel-wise VBQ analyses were carried out with SPM12, comple-

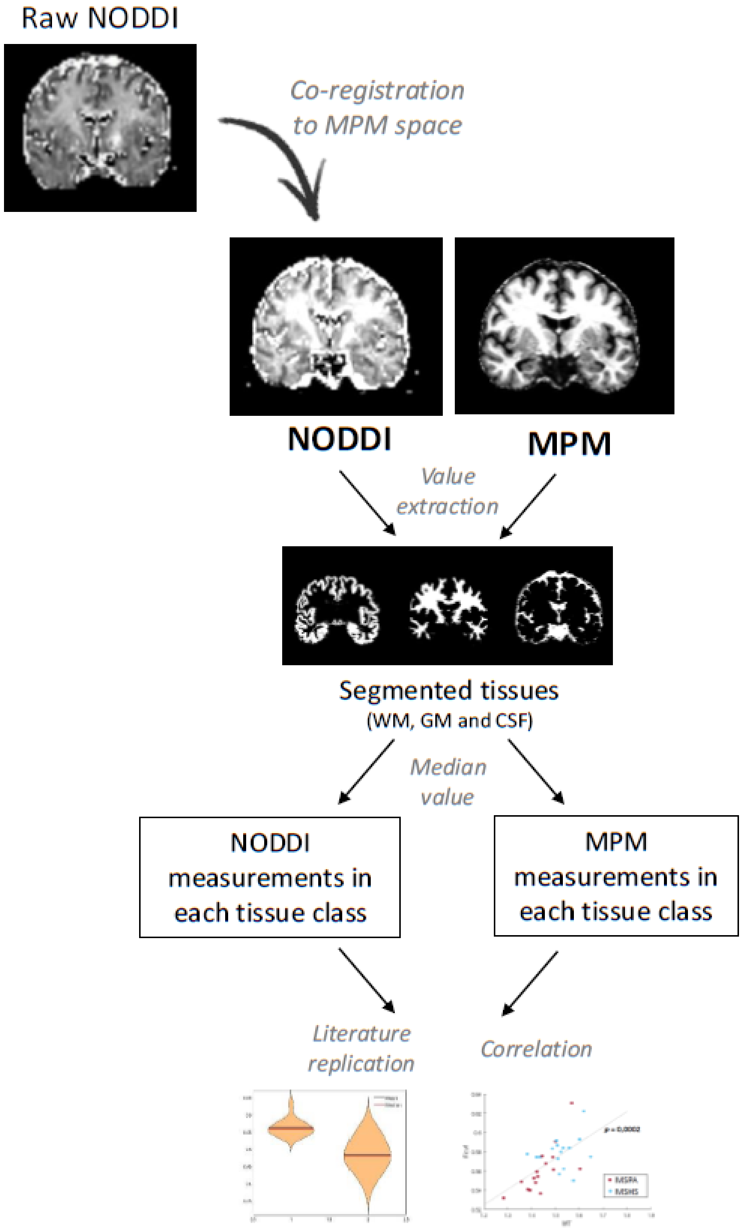

Figure 6.1: Chartflow of MPM and NODDI data processing for analysis (see text for details). NODDI maps were co-registered to MPM maps space, then median voxels values were extracted for each map and each tissue class in order to replicate literature results and assess correlations between pairs of parameters.

mented with MSPM in the case of multivariate statistics. First, we used a series of simple univariate models to test each NODDI modality with individual F-tests (the MPM parameters being already investigated in such way in [Lommers et al., 2020]).

Then, we tested the MSPM multivariate approach, on the four MPM parameters on one side, and on all MPM and NODDI (seven in total) parameters on the other side. The idea was to compare both multivariate analyses and determine whether or not the inclusion of NODDI criteria improved the detection of local differences between patients and controls. Prior to such analysis, data were scaled with a z-transform procedure to make them more comparable, as it is recommended in the MSPM manual. Indeed, as parametric maps reflect actual physical measurements, their range of values might differ a lot from one another. For all (uni- and multi-modal) tests, we used separate F-tests testing for the group (HC vs. patients) differences, with age, gender and total intracranial volume (TIV) entered as covariates of no interest. Post-hoc two-sample t-tests were used to explore significant effects. Cluster-level inferences were conducted at $p < .05$ after family-wise error rate (FWER) correction for multiple comparisons across the whole GM (p $<$ .0001 uncorrected cluster-defining threshold).

6.3 Results

For the replication of literature findings, the results obtained when testing the difference in ODI, F_{icvf} and F_{iso} measures, summarized by their median value in a tissue class, are presented in Figure 6.2. A supplementary test was conducted for ODI, comparing the median value within lesions to the contralateral NAWM area, illustrated in Figure 6.3. We found significant results for F_{icvf} measurements testing the difference between healthy subjects and MS patients in NAWM; and in F_{icvf} and F_{iso} testing the difference between NAWM and WM lesions in patients only. Such results agree with literature findings stating than F_{icvf} significantly decreases in NAWM compared to healthy subjects white matter, as well as in white matter lesions compared to the NAWM of the same subjects. Similarly, F_{iso} confirms previous observations [Schneider et al., 2017] when significantly increasing in WM lesions compared to NAWM, but with no significant differences in NAWM of patients compared to WM of healthy controls.

Regarding ODI, none of the analyses showed significant results, supporting the explanation that inconsistent results are obtained because of heterogeneous samples. It was proposed in previous studies that in early plaques, characterized with a relatively preserved axonal density, one would observe an increased

ODI due to the decline in fibers coherence, whereas in chronic lesions with complete loss of neuronal fibers, a decreased ODI could be found in consequence of fewer fibers signals [Hagiwara et al., 2019]. Considering the large differences of disease duration among the patients recruited for the study, it is highly likely that the lesion tissues among all subjects depict different levels of activity and thus, different ODI measures. Nonetheless, we showed increasing tendencies in NAWM compared either to white matter in controls, or white matter lesions in patients, in line with findings of [Hagiwara et al., 2019] and [Schneider et al., 2017] for which subjects samples were quite similar to ours. This tendency is however verified with a significant difference comparing ODI in white matter lesions and their NAWM contralateral region, but in a restricted sample.

One should note that a False Discovery Rate (FDR) correction for multiple testing would be recommended in this situation, due to the high number of tests (9 in total). We choose not to conduct it as two out of the three significant results would be removed, supported by the small, heterogeneous and not strictly age/gender matched cohort available for the analysis.

Regarding the inter-parameters correlations, Pearson linear correlation coefficients were computed for each pair of parameters (within each tissue class), as well as the corresponding p-value, appearing in Table 6.3, where significant results are marked with an asterisk. Associated scatter plots are shown in Figure 6.4, displaying the relationship between NODDI and MPM parameters in distinct classes, when the test was significant. Each point corresponds to the median parameter value extracted in the tissue of interest for one subject (MS patients in red and HC in blue).

One can observe that, independently of the group (i.e. MS patients or healthy controls), the NODDI parameter F_{icvf} is significantly correlated to all MPM parameters (positively in the case of MTsat, R1 and R2* and negatively in the case of PD), in (normal appearing) white matter and lesions, as well as for R2* in (normal appearing) gray matter. As for F_{iso}, it was only significantly correlated in (normal appearing) gray matter for MTsat and R1, while ODI is correlated only in (normal appearing) white matter for MTsat and PD. All these results suggest that the intra-cellular volume fraction (F_{icvf}) is highly sensitive to MPM measures, but its specificity is poor. This NODDI metric, related to the density of axons and dendrites, might provide similar information about the microstructural architecture in cerebral tissues than MPM estimates, i.e. mainly myelin and water contents. On the other hand, the isotropic volume fraction (F_{iso}) and the orientation dispersion index (ODI), correlated to fewer MPM parameters, constitute candidates for complementary biomarkers

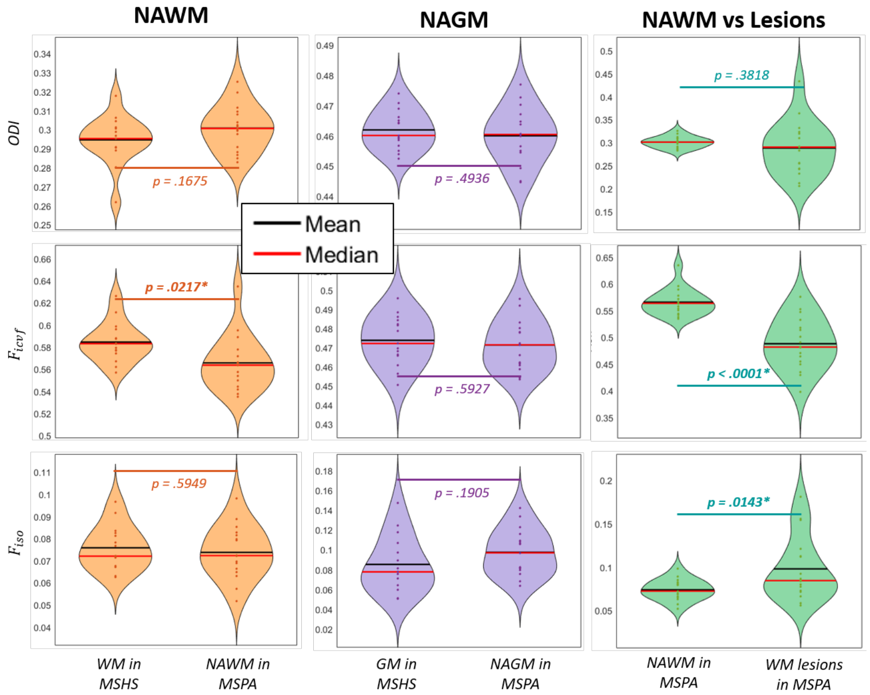

Figure 6.2: Violin plots of ODI, F_{icvf} and F_{iso} voxel values distributions in different configurations, with the associated p-value obtained with a two-sample t-test. Significant results ($p < .05$) are marked with an asterisk.

of tissue microstructure beyond MPM maps.

The three individual univariate VBQ analyses based on NODDI measurements did not highlight specific brain regions containing microstructural differences between patients and controls, contrary to the same analysis on MPM parameters as presented in [Lommers et al., 2020]. However, using the multivariate approach as implemented in MSPM, we found differences in several regions 1) using only MPM parameters, and 2) using all MPM and NODDI parameters (Figure 6.5). Table 6.2 gathers the size (in voxels) and coordinates (in mm) of the significant clusters obtained when including only MPM maps, and when including both MPM and NODDI maps. We found 12 significant clusters in the first case, and only 6 in the second. In both cases, we found multimodal loco-regional alterations in both hippocampus, lingual, fusiform and parahippocampal gyri, left thalamus and olfactory bulb (showing a reduction in MTsat, R1, R2* and an increase in PD, ODI, F_{icvf} and F_{iso}), and left ventral striatum (where we found an increase in MTsat and F_{iso}, but a reduction in PD, R1,

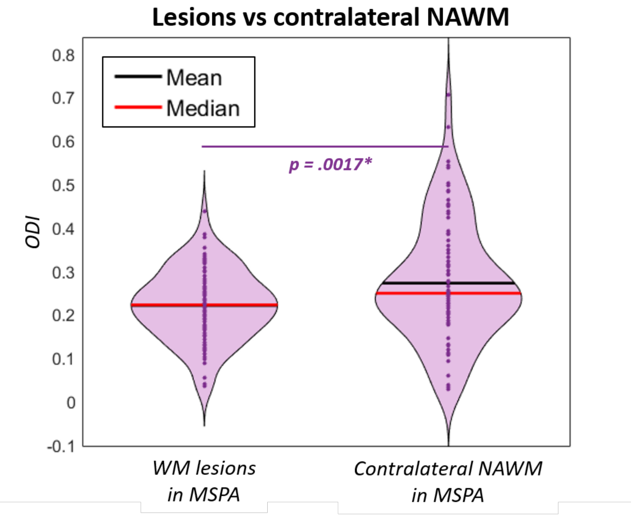

Figure 6.3: Violin plot of ODI voxel values distributions comparing WM lesions and their contralateral NAWM area (comprising 4 patients in total), with the associated p-value obtained with a two-sample t-test. Significant results ($p < .05$) are marked with an asterisk.

R2*, ODI and F_{icvf}). In addition, in the first case we found differences in both amygdala and rectus gyri, right putamen and olfactory bulb, and some regions in the median frontal and orbitofrontal cortices (in which we observed a decrease in MTsat, R1 and R2*, while an increase in PD, ODI, F_{icvf} and F_{iso}). We also found alterations in both insula, rolandic operculum (with a decreasing MTsat, R1, R2* and F_{icvf}, and an increasing PD, ODI and F_{iso}). In the case with NODDI parameters included, no additional alterations were found. Figure 6.5 displays all these loco-regional alterations, in red when taking all MPM maps, in blue when taking all MPM and NODDI maps.

6.4 Discussion

In neuroimaging, both MPM and NODDI protocols have proven their efficiency to provide microstructural insights in healthy populations [Merluzzi et al., 2016, Callaghan et al., 2014] or in neurological diseases such as multiple sclerosis [Hagiwara et al., 2019, Lommers et al., 2019]. Several studies also combined maps from MR parameters (e.g. MTR, T2*) and diffusion imaging (e.g. FA, MD) in order to collect complementary information [Codella et al., 2002]. The correlation between such parameters have also been investigated [Iannucci et al., 2001], but to the best of our knowledge the comparison/correlation of MPM

		MTsat	**PD**	**R1**	**R2***
ODI	*WM*	**-0.4603** **(.0080)***	**0.6828** **(<.0001)***	0.2860 (.1126)	-0.0829 (.6521)
	GM	0.1321 (.4711)	0.2355 (.1944)	0.0756 (.6811)	-0.2294 (.2066)
	Lesion	0.1412 (.5889)	0.1274 (.6261)	0.1126 (.6669)	0.4032 (.1085)
F_{icvf}	*WM*	**0.5587** **(.0009)***	**-0.5478** **(.0012)***	**0.5648** **(.0008)***	**0.6352** **(.0001)***
	GM	0.0838 (.6483)	-0.0106 (.9541)	0.3010 (.0942)	**0.4285** **(.0144)***
	Lesion	**0.7363** **(.0008)***	**-0.6204** **(.0079)***	**0.7544** **(.0005)***	**0.8658** **(<.0001)***
F_{iso}	*WM*	-0.0843 (.6464)	0.1181 (.5198)	-0.0933 (.6114)	0.3077 (.0867)
	GM	**-0.3866** **(.0288)***	0.1426 (.4361)	**-0.3694** **(0.0375)***	-0.0601 (.7438)
	Lesion	-0.3473 (.1720)	0.2386 (.3563)	-0.2361 (.3617)	-0.3529 (.1648)

Table 6.1: Pearson linear correlation coefficients (with associated p-values in parenthesis) between all pairs of MPM and NODDI parameters, separated into tissue classes. Significant results ($p < .05$) are marked with an asterisk. With FDR correction, one result will no longer be significant (correlation between F_{iso} and R1 in GM).

and NODDI parameters had not been tested yet.

In this study, we started by replicating results from the literature associating NODDI parameters and MS lesioned tissues. Our results were consistent with previous studies, at least the ones presenting a similar dataset as ours regarding age and disease phenotype, as no consensus seems to have been found for now.

Next, we assessed the correlation between each MPM parameter (MTsat, PD, R1 and R2*) and each NODDI parameter (ODI, F_{icvf} and F_{iso}) with Pearson correlation. We found that F_{icvf} correlates with all MPM parameters in (normal appearing) white matter and lesions. As F_{icvf} reflects the density of dendrites and axons, it seems to also indirectly indicate myelin content, a factor picked up by MTsat, R1 and R2*. The negative correlation to PD, exhibiting water content, might be explained by the presence of edema where axonal content is missing. Such results suggest that F_{icvf} is highly sensitive to microstructural characteristics as explained by MPM data, at least in the case of myelin and

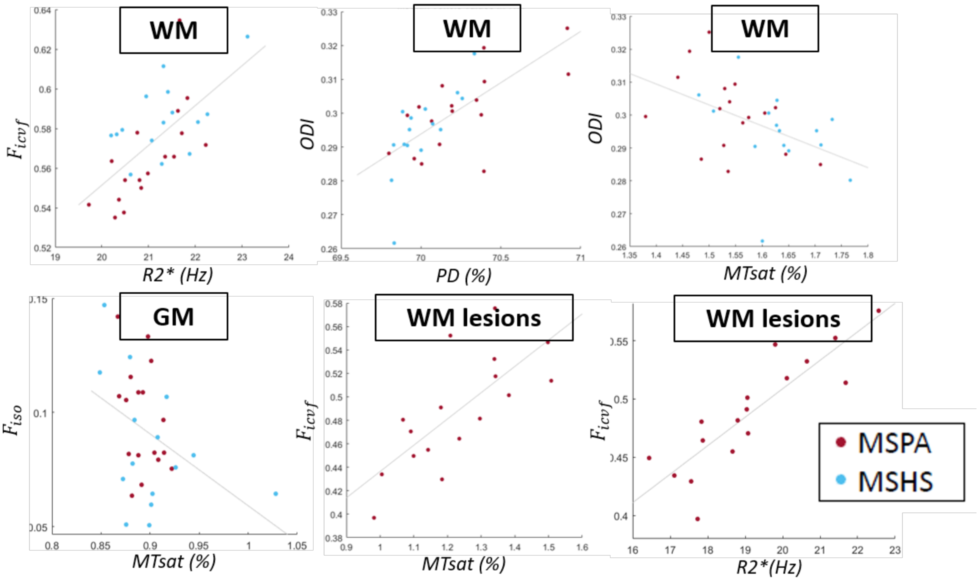

Figure 6.4: Scatter plots of the NODDI and MPM parameters extracted in different tissues (see figure for tissue types and parameters, and referring table for p-values). Grey line corresponds to the least-squares line to illustrate correlation. Blue dots represent healthy controls, red dots represent MS patients.

water contents, but might not bring additional information regarding fibers properties.

ODI is negatively correlated to MTsat, and positively correlated to PD, both in normal appearing and healthy white matter. That significant results only arise in (NA)WM tissue is not surprising, as the ODI index focuses on white matter tracts as well as their orientation. As fibers stand in a more orderly fashion within WM, modifications in this compartment stand out more compared to gray matter. As indicated in our results, ODI seems to be closely related to MTsat, suggesting that a the loss of myelin and axonal contents further induces less fiber coherence and thus, their dispersion. The positive correlation to PD might also be due to the loss of fibers replaced by extra-cellular water. ODI proposes an interesting index which goes beyond biological features such as the ones picked up by MPM parameters, mostly myelin and water content.

Finally, the multimodal VBQ analysis comparing NAWM tissue in MS patients vs healthy controls highlighted several regions where tiny tissue alterations were detected. These regions of interest are similar to previous studies [Lommers

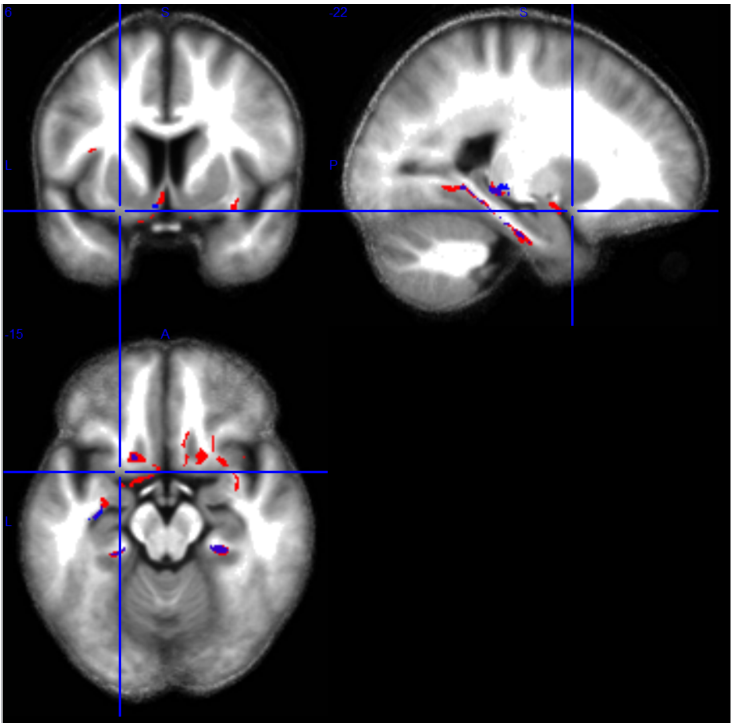

Figure 6.5: VBQ results superimposed on the mean MTsat map. Red: multimodal alterations using MPM maps; Blue: multimodal alterations using MPM and NODDI maps.

et al., 2020], but the inclusion of NODDI parameters in the multimodal analysis comprising MPM parameters did not lead to the detection of additional regions. On the contrary, considering only MPM parameters identified a lot more damaged cerebral areas. It seems thus that these NODDI parameters are not good candidates as imaging biomarkers of loco-regional modifications related to multiple sclerosis, compared to MPM maps. The greatest utility of NODDI might remain on global tissues analysis or fiber tractography [Barakovic et al., 2021, Schiavi et al., 2020].

6.5 Limitations

This analysis was mostly limited by the mismatched image resolution between MPM and NODDI maps, equal to an isotropic voxel size of 1.0 and 2.3mm respectively. Because of this and the weak contrast of NODDI maps, the co-registration was not always precise.

	MPM		**MPM & NODDI**	
	Size (voxels)	*Coordinates (mm)*	*Size (voxels)*	*Coordinates (mm)*
Cluster 1	173	-11 ; 2 ; -15	572	-26 ; -20 ; -9
Cluster 2	347	-2 ; 8 ; -8	220	22 ; -35 ; -10
Cluster 3	261	-21 ; -26 ; -20	177	34 ; -31 ; -1
Cluster 4	156	-38 ; -1 ; 18	266	-24 ; -43 ; -6
Cluster 5	633	-27 ; -20 ; -9	232	-22 ; -32 ; -5
Cluster 6	171	18 ; -51 ; -6	153	-13 ; 11 ; -13
Cluster 7	207	36 ; -16 ; 22		
Cluster 8	337	21 ; -36 ; -9		
Cluster 9	529	-18 ; -55 ; -4		
Cluster 10	185	34 ; -31 ; -1		
Cluster 11	289	19 ; 16 ; -16		
Cluster 12	301	35 ; 13 ; -18		

Table 6.2: Size (in voxels) and coordinates (in mm) of the significant clusters obtained in the multimodal VBQ analyses, using only MPM maps, then MPM and NODDI maps.

Another important limitation of this analysis is the low signal-to-noise ratio (SNR) of NODDI data, as compared with MPM maps which is rather solid inside the intra-cranial volume (out-brain regions are much noisier). This could partly justify the inconclusive results obtained in the VBQ analysis including NODDI parameters alone or combined with MPM.

Also, NODDI results must be interpreted with caution, especially in the gray matter volume. White matter and gray matter myeloarchitectures are very different regarding neurites organization. Within white matter, fibers are characterized by more coherent and structured tracts pathways, while gray matter fibers have a more anisotropic and radial organization. Fibers dispersion is usually greater in gray matter [Budde and Annese, 2013]. Thus, the intrinsic diffusivities in those distinct structures are not the same. However, in the NODDI model, this parameter was derived from an approximate of the mean parallel diffusivity from DTI in a healthy coherent white matter region, and is constant for the entire brain [Guerrero et al., 2019]. The estimation of NODDI maps in gray matter might then be imprecise. In addition, the cortical ribbon may correspond to only one voxel in some regions of the diffusion space, it is thus difficult to accurately interpret the singal. Therefore both the findings at the global tissue or voxel levels within gray matter should not be too interpreted.

Finally, as for the longitudinal study, the low number of subjects is the major limitation here. Indeed, we had to reject a large portion of the initial pool because they were not acquired with the same MPM and NODDI protocols. In addition of losing data, the age and gender matching between patients and HC is no longer strictly respected. Once again, the results must be interpreted with caution, and call for a replication study with a larger dataset.

Chapter 7

Discussion, perspectives and conclusion

Multiple sclerosis is the most prevalent chronic inflammatory disease of the CNS, currently without cure. Though our understanding of the disease neuropathology has well evolved since the first description of MS by Charcot in the 19th century, as we now know that it involves inflammation, demyelination and axonal destruction, current treatments only target one or several of those processes, since the exact event triggering this inflammatory cascade remains yet to be full unravelled. Histopathological studies on biopsies and autopsies are most of the time performed on largely advanced and/or unusual cases and prevent the fully understanding of dynamic processes occurring in MS. Consequently, there is an urgent need for imaging tools allowing the *in vivo* monitoring of MS underlying processes.

In clinical practice, conventional MRI (cMRI) remains an important tool for the diagnosis and monitoring of MS, where both T2w and Gd-enhanced T1w MR images are useful. However, they are not able to efficiently assess cortical lesions or detect diffuse changes in normal appearing brain tissues. Moreover, their lack of histopathological specificity prevents any real assessment of the tissue microstructure. Furthermore, Gadolinium injection, and its repetition over time, is not without noxious side effects, inducing mitochondrial toxicity and cell death in neurons [Ramalho et al., 2017, Bower et al., 2019]. Consequently, an advanced non-invasive technique allowing the estimation of neuronal status is desired to avoid this cell toxicity.

Quantitative MRI (qMRI) provides a potential solution to these limitations by measuring actual physical parameters, in standardized units, that then specify quantifiable informations about the microstructural properties of tissues [Tabelow et al., 2019, Callaghan et al., 2014]. Being able to observe modifications of these parameters would provide information about MS-related cerebral alterations. In this thesis, we described two qMRI protocols widely used in neuroscientific research. The first one is the "multi-parameter mapping" (MPM) protocol and the associated hMRI-toolbox, estimating 4 parametric maps reflecting MR physical parameters: MTsat, PD, R1 and R2*. These parameters were shown to be linked to different microstructural aspects, such as the myelin, water and iron content. The second one is the "neurite orientation dispersion and density imaging" (NODDI), a diffusion MRI protocol constructing, among others, three additional parametric maps characterizing neurites properties: ODI, F_{icvf} and F_{iso}. In the different analyses conducted throughout this thesis, the focus was mainly put on MPM, the NODDI protocol mostly contributed in a correlation assessment with the MPM parameters.

Beyond the MPM protocol, a number of MRI approaches also enables the estimation of similar quantitative MR parameters, in individual specific sequences. Contrary to MPM, these acquisition techniques permit the estimation of one parameter at a time (e.g. MTR, T1, T2* etc.). Their use to probe MS has allowed to highlight cerebral changes occurring in patients compared to healthy controls. In addition to better characterizing MS-related microstructural alterations, qMRI parameters substantially improve the clinical-radiological correlation as compared to cMRI measures of disease [Bonnier et al., 2014].

The major advantage of the MPM protocol over such individual techniques is its capacity of simultaneously acquiring the four parameters into one single relatively short acquisition session (around 20 minutes altogether at 3T). In clinical settings where patients might be uncomfortable, it is crucial to develop fast and reliable tools for a fine characterization of the disease.

Main results

This thesis was dedicated to the development of qMRI-based tools for the processing and analysis of imaging data from patients with multiple sclerosis and healthy volunteers. Those tools comprise the segmentation of lesions and normal appearing tissues, the longitudinal evolution of volume and parametric value, and the relation between MPM and NODDI. This thesis enters in the list of a variety of qMRI investigations on MS and other conditions working in collaboration to bring closer the implementation of this sequence in clinical settings. The MPM sequence is still not main stream, i.e. not always directly neither easily available "off the shelf" for clinical application from the scanner providers (Siemens, Phillips or GE), and requires specific hardware performance, not available on all machines. The sequence arose from a collaborative effort gathering a number of research centers, and at the moment it is only available in the research community. Its implementation on MRI machines dedicated to clinical practice, and the follow up for usage verification, would require the input of a specified physicist, which is not always possible for long term work. Additionally, the validation of qMRI benefits still remain to be exposed to clinicians before they can be willing to include such sequences in their protocols. Thus the sequence is actually not fully mature yet for clinical application.

Consequently map creation and processing techniques are still evolving: faster sequence, reduced artefacts, more accurate reconstruction, improved processing. These require some expertise and deeper understanding of the technique, which is not easy for inexperienced users or clinical staff; the risk for computation errors is rather high. The manuscript presented here aims at precisely describing the different steps necessary for an accurate usage of the qMRI data acquired on MS patients. The combination of this advanced MRI acquisition technique with an improved segmentation algorithm lead to new metrics related to brain tissues affected by multiple sclerosis, yielding a finer characterization of underlying processes, such as the microstructural deterioration and/or repair occurring during the disease.

Here, traditional processing procedures, such as Unified Segmentation (US), and their derivatives, such as US-with-lesion, were primarily tested using qMRI data. Indeed, these two algorithms and their parameters were optimized for conventional MRI sequences, but the adjustment for MPM images has not been conducted yet. The parameters leading to the best segmentation output were investigated first using healthy subjects, then applied for the segmentation of normal appearing tissues and WM lesions in patients with MS.

USwL allowed to segment all MPM images, in order to construct *a posteriori* maps of the different tissues and study the MPM and NODDI parameters within them. We followed the microstructural alterations occurring over time in MS patients lesions and normal appearing tissues. With a longitudinal setting of two data acquisition sessions, we demonstrated that patients with a better clinical evolution, i.e., clinically stable or improving state, showed positive annual rate of change in MTsat and R2* within NAWM and NACGM, suggesting repair mechanisms in terms of increased myelin content and/or axonal density as well as edema/inflammation resorption. In a second part examining WM lesions, qMRI parameters within surrounding NAWM showed microstructural modifications, even before any focal lesion is visible on conventional FLAIR

MRI. However, due to a variety of limitations (e.g. the small size of the cohort, its heterogeneity regarding disease phenotype, age, medication, etc.), the interpretation of the results must be taken with caution. A similar study comprising a larger cohort would enable to draw more accurate conclusions regarding microstructural features evolution over time.

In the ensuing study, the MPM protocol was contrasted to another approach widely used in research: the “neurite orientation dispersion and density imaging” (NODDI), a diffusion MRI protocol. Here we presented different experiments including specific MPM and/or NODDI maps. Global parametric measures were assessed over entire cerebral tissues, for which we measured correlations in several pairs of MPM vs. NODDI parameters. These comparisons showed some relations in the measurements of microstructural properties in MPM and NODDI, especially regarding myelin, axonal and water contents. However, through multimodal voxel-based quantification analyses we revealed that the inclusion of NODDI maps into a model comprising only MPM parameters does not improve the detection of MS-related loco-regional alterations within cerebral tissues. All of this suggests that NODDI data might be more profitable when exploited in global alterations detection or in white matter fibers tractography studies, while the MPM protocol allows to catch specific physical and biological cerebral features independent on the NODDI metrics.

Study limitations

Due to the quantitative nature of the voxels, representing actual physical measurements, the MPM protocol is theoretically independent of the scanner used for acquisition. This would make MPM maps reproducible across sites, subjects and time points, increasing the size and diversity of study populations compared to what is possible with conventional MRI [Weiskopf et al., 2013]. Although, in practice the reproducibility is importantly reduced when different scanners are used, especially in the case of (semi-quantitative) MTsat maps [Gracien et al., 2020]. This prevents the evaluation of cerebral differences across groups or the longitudinal evolution of parameters. Here, this was the major limitation constraining the sample size in several analyses to the data acquired with the PRISMA MRI only.

However, in some circumstances, the effect can be counteracted by linearly scaling the MT pulses values, usually different on each scanner type, in order to harmonize them across vendors [Leutritz et al., 2020]. Unfortunately, at the time of the analyses we were not aware of such technique. In the future, it would be interesting to consider it in order to increase the size of the cohort under study.

As mentioned several times throughout the manuscript, all the results presented here must be interpreted with caution due to a number of relevant and important limitations. First of all, the small size and heterogeneous aspect of the cohorts selected for each line of research constitute the major constraint, especially for the longitudinal study. The range of characteristics such as age, disease duration, disease phenotype and treatment is rather broad, despite the influence of these parameters on the disability state of the patients. Moreover, the data of several subjects had to be removed due to the different type of MRI scanner used for the acquisition at the two time points. However, quantitative cross-sectional and longitudinal studies can be performed when identical protocols are used across sites and scanning time points. Therefore, in our study, the evolution of MPM parameters within cerebral tissues could be evaluated, but only when images were collected with the same scanner (i.e. Siemens Prisma).

The two protocols MPM and NODDI require specific and distinctive processing steps, as described in Chapter 3. They end up in highly dissimilar maps, with different image resolution between MPM and NODDI maps, equal to isotropic voxel sizes of 1.0 and 2.3 mm respectively. This might explain the absence of results in the VBQ analysis including the NODDI maps in the model comprising initially only MPM parameters, but significant MPM-NODDI correlations when averaged out over the whole tissues.

In addition, the current segmentation methodology is limited by the absence of histopathological validation of the segmented WM lesions, whether or not they actually correspond to plaques of demyelination and/or inflammation. Histology studies were already conducted to assess the pathological sensitivity of FLAIR imaging regarding lesions detection [Geurts et al., 2005, Seewann et al., 2012], and a similar procedure combining MPM data and USwL segmentation is required to certainly histologically validate the conclusions exposed here. Anyhow, given the significant difference in MPM parameters between lesions and normal appearing tissues, one might consider that the detection of lesions within parametric intensities is still quite reliable.

Another important aspect of the longitudinal study is that the time interval between two scanning sessions varied rather widely across patients (between 14 and 61 months). To address this variance, we computed annual rates where possible, but they are effectively only linear approximations. Moreover, the absence of a set of longitudinal MRI data acquired in a control group of healthy subjects did not allow to assign these MPM-measured alterations specifically to MS. However, studies on the effect of aging on qMRI parameters in healthy volunteers, or longitudinal studies with an available HC set with similar characteristics, are already available in the literature [Callaghan et al., 2014, Bonnier et al., 2017, Elkady et al., 2018]. These should prove a sufficient reference to assess changes induced by MS, thanks to the reproducibility of qMRI [Weiskopf et al., 2013].

An unfortunate consequence of the small size of the qMRI dataset is the inability of integrating machine learning (ML) and deep learning (DL) in the segmentation framework, as it was initially planned. Indeed, this advanced general methodology becomes more and more attractive in various image processing and analysis applications. Considering cMRI data, various semi or fully automatic segmentation tools already exist for MS lesions. For example, [Sweeney et al., 2013] developed the “Automated Statistical Inference for Segmentation” (OASIS), which works with logistic regression models incorporating multiple MRI modalities to estimate voxel-level probabilities of lesion presence. Another example based on FLAIR hyperintensities detection is the LGA algorithm [Schmidt et al., 2012] as presented in section 3.3.2.2, used in this project to determine the *a priori* lesion mask. Other automatic lesion segmentation methods, based on ML or DL designs, have been developed (see reviews [Danelakis et al., 2018] and [Zeng et al., 2020]). Nevertheless, all the existing segmentation methods rely on the contrast between tissue classes, i.e. qualitative MR signal, but do not take advantage of the multi-parametric nature of qMRI, and were not trained for qMRI data. A training phase is mandatory for the implementation of this type of algorithms, and only very large (and annotated) datasets can lead to accurate segmentation results. A number of such datasets are publicly available, but usually only comprising cMRI data. To the best of our knowledge, similar datasets based on qMRI data do not exist yet.

Perspectives

The MPM protocol is available in the field of neuroimaging research for a few years already and has proven its efficiency in a number of populations: healthy aging [Callaghan et al., 2014], glioblastoma [Reuter et al., 2020], Parkinson’s disease [Depierreux et al., 2021], as well as multiple sclerosis. Besides increasing the exposure of microstructural insights associated with such conditions by conducting studies with larger and/or more extended population characteristics (e.g. at early/late stages or with different phenotypes of specific diseases), this approach could be widespread to other neurological disorders.

Indeed, the two segmentation algorithms might be of use in an extended collection of situation; US when dealing with healthy brains, and US-with-lesion for other kinds of lesions. One important parameter in USwL is the affected tissue class(es), which does not have to be restricted to white matter as it is the case for MS lesions. For example, when applied in glioblastoma assessment [Reuter et al., 2020] and stroke [Bonghi, 2021], all tissue classes were selected (WM, GM and CSF).

MPM measurements, as well as NODDI, still offer various opportunities for deeper understanding of cerebral processes. For example, the further development of NODDI raw data into white matter fibers tractography would enable the *in vivo* characterization of additional MS-related processes. In the MS community, there is a theory that structural damage in focal lesions further induces degradation or dysfunction of connected areas in NAWM [Werring, 2000], as well as NAGM atrophy [Sepulcre et al., 2009]. Being able to study this phenomenon in living patients would markedly improve the knowledge about MS.

Besides the integration of qMRI methodologies to other cohorts and purposes, a number of broader perspectives can be considered, from the improvement of the technology responsible for the MPM acquisition, to its eventual implementation in clinical research and routine.

Technology and acquisition Ten years from now, the applicability of 7T MRI will probably be similar as the current one regarding 3T MRI, at least at the research level. Compared to 3T imaging, 7T MR images are characterized by higher signal-to-noise (SNR) and contrast-to-noise (CNR) ratio, an increased spatial resolution (reaching the submillimetric level), an enhanced sensitivity to susceptibility, and improved contrasts between tissues. With its enhanced ability at distinguishing small cerebral details, results from 7T analyses bring the knowledge of physiological processes a step further, either in healthy populations or investigating various conditions. In a number of neurological disorders, 7T images provide clearer delineation of small anatomical details and higher lesion conspicuousness, which should support the earlier diagnosis and treatment development [van der Kolk et al., 2013, Kraff et al., 2015, Trattnig et al., 2016].

Nevertheless, this new methodology comes with new obstacles. In the past years, large efforts have been, and continue to be, done by the research community to solve 7T MRI-related problems comprising safety, susceptibility related artefacts, B_0 and B_1 inhomogeneities and other technical issues [Karamat et al., 2016]. Due to the more pronounced sensitivity to movement and other noise sources at 7T, the rather long acquisition time of the MPM protocol might induce more pronounced artefacts. In addition, the intensity inhomogeneity due to the antenna sensitivity profile is difficult to correct for. Further developments are required before transforming the 7T MRI system from a research machine to a routinely used clinical tool, comprising the optimization of specific sequences and the harmonization of multi-sites neuroimaging protocols [Karamat et al., 2016, Clarke et al., 2020, Visser et al., 2010, Van de Moortele et al., 2009].

Following the already established benefits of MR sequences optimized for 7T systems, current work is conducted at the moment to optimize the MPM sequence as well. One line of focus is the acquisition time of the MPM sequence, at 3T or 7T, which could be reduced. Although a 20 minutes long acquisition is clinically feasible, integrating it within a routine MRI protocol remains impractical. It has been proposed to combine an acquisition with reduced spatial resolution (hence, reducing the scanning time), with an advanced parallel imaging technique [Wang et al., 2022]. This technique allows to collect all weighted multi-echo images in less than 3 min, approaching $1.0mm$ isotropic resolution at 3T in certain conditions. Although the final spatial resolution could be altered, it would be compensated by the reduction of motion-induced artefacts in shorter sequences, especially for clinical populations. At 7T, further work is required to improve the homogeneity in the MTsat map. The implementation of such technique should soon spread out in the 7T users community.

In multiple sclerosis, preliminary results with MS patients MPM data acquired at 7T are “stepping into the unknown” because these images are more sensitive to cerebral abnormalities but are also rather less specific. Indeed, it remains difficult to differentiate MS-related demyelinated plaques from other types of lesions, blood vessels, or even artefacts. Current 7T studies of MS focus on the assessment of cortical pathology [Yao et al., 2014, Tallantyre et al., 2010, Cocozza et al., 2020], and the use of MPM for the same purpose would undoubtedly improve its characterization in term of microstructural properties.

Data sharing and processing The unfortunate reality of the research environment lies in the difficult sharing of medical data, which would greatly help to lift the concerns about the sample size, so common with patients studies. The MPM protocol is not yet highly widespread in the neuroimaging community, it is investigated in only a few research centers, and not present in clinical routine at the moment. A direct consequence of this is that the availability of MPM data for sample size increase is unreachable. Regarding conventional MR images such as T1w, T2w or FLAIR, public datasets are available for download, in the case of healthy and diseased populations[1], but those do not exist for qMRI.

---

[1] `https://openneuro.org/`

The development of an open database of MPM data, with its advantageous reproducibility across subjects, sites and time-points (when identical sequences are applied), could improve the feasibility of qMRI studies and increase the current knowledge of cerebral processes as characterized by those images.

In addition to improving the effect size with larger samples, increasing and sharing the acquisitions of MPM images would enable the integration of powerful ML/DL algorithms in the processing and analyses of various conditions. If large annotated datasets were available, the current methodology of specific ML/DL algorithms optimized for cMRI data could be transferred to qMRI, probably with higher accuracy considering the quantitative nature of qMRI data [Geremia et al., 2011,Anbeek et al., 2008,Kroon et al., 2008,Schmidt et al., 2012,Sweeney et al., 2013,La Rosa et al., 2020,Danelakis et al., 2018,Zeng et al., 2020]. In the MS field of research, one particularly interesting application of ML/DL algorithms is for the detection and characterization of lesions, in WM or GM. Based on a training phase for lesion location, as well as prior knowledge of the brain anatomy, the detection of lesions could be improved by learning particular features specific to WM or GM lesions. Neural networks or Principal Components Analysis (PCA) are good candidates for that purpose, as they allowed to develop automatic cMRI-based segmentation tools [Kroon et al., 2008]. Similarly, other ML approaches, such as logistic regressors, K-nearest Neighbors (KNN) or random forests, could enable the detection of outliers in specific ranges of intensities, taking advantage of the 4-dimensional aspect of MPM. MPM data combined with ML/DL algorithms could also enable automatic diagnosis of MS [Lavrova et al., 2021, Shoeibi et al., 2021], or the prediction of cognitive and/or disability evolution with MRI [Denissen et al., 2021,Van Schependom and Nagels, 2017].

Moreover, as we have shown in the longitudinal study (Chapter 5), normal appearing tissues show signs of microstructural alterations picked up by MPM maps years before they are visible on conventional scans. With this information, ML/DL methods could constitute a tool for the prediction of expansion and/or apparition of (new) lesions. With a sufficient amount of data, models of the lesion expansion could be derived, and would greatly benefit the treatment planning and effectiveness assessment.

Furthermore, ML/DL algorithms may be helpful for the neurobiological interpretation of qMRI findings within cerebral tissues. A few histology studies have been conducted and their outcomes correlated to specific MR parameters [Schmierer et al., 2004, Stüber et al., 2014, Laule et al., 2006], but there still remain a large unknown territory in the *in vivo* characterization of processes underlying specific diseases. Developing precise biophysical models of the MR signal, and combining it to qMRI measures of the tissues would lead to the characterization of the brain microstructure in a non-invasive way, such as the myelin mapping, fibers orientation or g-ratio measurements [Weiskopf et al., 2015]. The inclusion of ML and DL approaches could enable the identification of particular qMRI measures which are concurrently sensitive to histological measures of cerebral damage and clinical disability [Lu et al., 2021], which would it turn help to develop new or improved biophysical models for further work. Combining macromolecular and iron content description, picked up by MPM, fibers characteristics measured by NODDI, with advanced microscopy analyses of *in vivo* brain tissues such as 3D Polarized Light Imaging (3D-PLI), and ML/DL algorithms would probably greatly benefit the field of *in vivo* histology using MRI. This microscopy technique allows to visualize and characterize the architecture and connections of nerve fibers in *post mortem* brains at high resolution. It measures the birefringence of the myelin sheaths around axons, and enables the high-resolution analysis of myelinated axons constituting fiber tracts [Axer et al., 2011].

Moving to clinical research and clinical routine In order to integrate the acquisition of MPM maps in clinical research and clinical routine, the benefits brought along with the sequence must surpass its drawbacks (e.g. the additional acquisition duration). The most urgent goal would be to validate the interpretation of MPM metrics regarding myelin, axon and iron contents with histological studies, as it has been performed for other quantitative maps [Hametner et al., 2018, Schmierer et al., 2004].

Then, with specific well-established studies, the use of qMRI could replace a number of invasive and/or more risky imaging techniques, e.g. the injection of Gadolinium-based contrast agents (GBCAs) in contrast-enhanced MRI studies. Those are known to possibly provoke adverse events, especially in subjects with renal failure. Also, some subjects experience a Gadolinium deposition in brain tissues, potentially inducing other symptoms [Ramalho et al., 2017, Bower et al., 2019]. The elaboration of strict protocols comparing Gd-enhanced MRI with qMRI acquisitions could lead to the description of similar brain aspects, such as the activity of MS lesions (i.e. active, smoldering, inactive, etc.) but with non-invasive methods [Rahmanzadeh et al., 2022].

Similarly, the assessment of treatments efficiency for MS-related brain damage is presumably superior with MPM metrics, but it has not been conducted yet. Studies strictly comparing treatment effects evaluated by MPM on one side, and other clinically used cMRI sequences on the other, would enable to highlight the potential increased sensitivity and/or specificity of MPM in MS monitoring. Moreover, correlations between patient disability and MPM measures were observed in several studies [Lommers et al., 2019, Bonnier et al., 2014], thus the dual monitoring of disability and cerebral alterations could be conducted with a single technique.

Currently in clinics, FLAIR and T1w images remain the optimal option for the diagnosis and monitoring of MS pathology, in terms of lesions apparition and cortical atrophy. A replacement of these sequences with the MPM one is not practicable at the moment, but a joined implementation could be considered if it brings along major advantages. Indeed, the visual assessment of WM lesions remains highly optimal in FLAIR images, and at the moment only MPM-experienced users could take advantage of the information gain with further perspective. In the future, the goal would be to integrate the MPM sequence, optimized for scanning duration as mentioned here above, in clinical settings. This would, on the one hand, benefit the physician for the evaluation of more sensitive and specific MS-related brain aspects, and on the other hand, multiplying the MPM data acquisitions for potential data sharing.

Conclusion

In the exciting field of neuroimaging, almost 76 years after the first observation of the NMR phenomenon within bulk matter by Félix Bloch and Edward Mills Purcell in 1946, and its further use for magnetic resonance imaging as invented by Paul Lauterbur et Peter Mansfield in the 1970's, the implementations of MRI sequences and their applications remain a dynamically evolving process in clinics and in research. The present thesis aimed to introduce new tools based on quantitative MR images processing and analysis, allowing a better understanding of the underlying cerebral processes in terms of microstructure. However, there still exists certain gaps to fill before MPM sequences can be routinely used in clinical practice, whether in MS for diagnostic and follow-up, as presented in this work, or in other neuropathological conditions. In view of the present work results, one can conclude that the outcome of the analyses introduced here demonstrate promising results for the use of qMRI and associated tools for the examination of neurological pathologies, though they were presently not confirmed through histopathological studies. Given the extremely dynamic nature of the advances of neuroimaging acquisition and processing techniques, we do not doubt that the future holds promising perspectives for better disease characterization.

Appendix A

Multi-channel US segmentation with MPM maps

MTsat **nb Gaussians (CGM - DGM - WM- CSF)**	**Sensitivity**	**Specificity**	**Dice**	**Jaccard**	**MCC**
1-1-1-1	0.92619	0.99895	0.93709	0.88592	0.93826
2-2-2-2	0.95901	0.99957	0.96737	0.93784	0.96725
3-3-3-3	0.9768	0.99979	0.97925	0.9598	0.97901
4-4-4-4	0.98306	0.99996	0.99569	0.99143	0.9956
5-5-5-5	0.97979	0.99989	0.99371	0.98755	0.99361
6-6-6-6	0.98506	0.99997	0.99767	0.99536	0.99761
7-7-7-7	0.98783	0.99995	0.99292	0.98601	0.99282
8-8-8-8	0.98445	0.99995	0.99703	0.99409	0.99696

Table A.1: Comparison scores between each segmentation (ranging from 1 to 8 for each tissue class) and the generated STAPLE one, based on MTsat only, averaged among all subjects.

MTsat **nb Gaussians (CGM - DGM - WM- CSF)**	**Sensitivity**	**Specificity**	**Dice**	**Jaccard**	**MCC**
4-4-4-5	0.9982	0.99997	0.99845	0.99691	0.99841
4-5-4-5	0.99819	0.99997	0.99848	0.99696	0.99844
4-6-4-5	0.99814	0.99997	0.99845	0.99691	0.99841
4-4-5-5	0.99428	0.99993	0.99534	0.99077	0.99527
4-5-5-5	0.99429	0.99993	0.99539	0.99086	0.99532
4-6-5-5	0.99424	0.99993	0.99535	0.99078	0.99528
4-4-6-5	0.99843	0.99998	0.99902	0.99803	0.99899
4-5-6-5	0.99847	0.99998	0.9991	0.9982	0.99907
4-6-6-5	0.99842	0.99999	0.99905	0.99811	0.99903
5-4-4-5	0.99427	0.99994	0.99573	0.99153	0.99567
5-5-4-5	0.99419	0.99994	0.99568	0.99143	0.99562
5-6-4-5	0.99418	0.99994	0.99567	0.99142	0.99561
5-4-5-5	0.99867	1	0.99947	0.99895	0.99946
5-5-5-5	0.99864	1	0.9995	0.999	0.99949
5-6-5-5	0.99856	1	0.99942	0.99883	0.99941
5-4-6-5	0.99762	0.99998	0.99854	0.99709	0.99851
5-5-6-5	0.99841	0.99998	0.99904	0.99808	0.99901
5-6-6-5	0.99843	0.99998	0.9987	0.9974	0.99867
6-4-4-5	0.99786	0.99998	0.99888	0.99776	0.99885
6-5-4-5	0.9978	0.99998	0.99885	0.99771	0.99882
6-6-4-5	0.99774	0.99998	0.9988	0.9976	0.99876
6-4-5-5	0.99792	0.99997	0.99843	0.99686	0.99838
6-5-5-5	0.99776	0.99997	0.99838	0.99677	0.99834
6-6-5-5	0.99776	0.99997	0.99838	0.99677	0.99834
6-4-6-5	0.99598	0.99995	0.99641	0.99286	0.99634
6-5-6-5	0.9959	0.99995	0.9964	0.99283	0.99633
6-6-6-5	0.99593	0.99995	0.99639	0.99283	0.99633

Table A.2: Comparison scores between each segmentation (ranging from 4 to 6 individually for CGM, DGM and WM) and the generated STAPLE one, based on MTsat only, averaged among all subjects.

nb Gaussians (5 - 4 - 5 - 6) **Combinaison of maps**	**Sensitivity**	**Specificity**	**Dice**	**Jaccard**	**MCC**
MTsat	0.8786	0.99697	0.89192	0.80724	0.88992
PD	0.76109	0.99657	0.81458	0.70174	0.81686
MTsat + PD	0.87285	0.99942	0.92653	0.866	0.92527
R1	0.86875	0.99786	0.90191	0.82449	0.8999
MTsat + R1	0.90093	0.99945	0.94454	0.89673	0.94333
PD + R1	0.84201	0.99935	0.91365	0.84488	0.9136
MTsat + PD + R1	0.90425	0.99977	0.9604	0.92482	0.95954
R2*	0.71342	0.99474	0.78236	0.64516	0.78165
MTsat + R2*	0.88217	0.99886	0.93033	0.87037	0.92845
PD + R2*	0.79161	0.99815	0.86711	0.77243	0.86729
MTsat + PD + R2*	0.88241	0.99972	0.95096	0.90774	0.95023
R1 + R2*	0.86159	0.99948	0.92724	0.86693	0.92651
MTsat + R1 + R2*	0.88188	0.99983	0.94881	0.90468	0.94819
PD + R1 + R2*	0.86224	0.99958	0.93142	0.87404	0.93086
MTsat + PD + R1 + R2*	0.89023	0.99952	0.9419	0.89311	0.94053

Table A.3: Comparison scores between each segmentation (testing all combinations of MPM maps) and the generated STAPLE one, with a number of Gaussians of 5 for CGM, 4 for DGM, 5 for WM and 6 for CSF, averaged among all subjects.

MTsat + PD + R1 **nb Gaussians (CGM - DGM -WM - CSF)**	**Sensitivity**	**Specificity**	**Dice**	**Jaccard**	**MCC**
1-1-1-1	0.88388	0.99931	0.92888	0.87077	0.92934
2-2-2-2	0.92295	0.99949	0.95102	0.90816	0.95039
3-3-3-3	0.9424	0.9997	0.96723	0.9376	0.96691
4-4-4-4	0.95395	0.99958	0.96901	0.94078	0.96853
5-5-5-5	0.97677	0.99986	0.98755	0.97549	0.98722
6-6-6-6	0.97682	0.99987	0.98562	0.9718	0.98526
7-7-7-7	0.97705	0.99984	0.98568	0.97187	0.9853
8-8-8-8	0.97669	0.99977	0.98315	0.96701	0.98273

Table A.4: Comparison scores between each segmentation (ranging from 1 to 8 for each tissue class) and the generated STAPLE one, with a multi-channel segmentation based on MTsat, PD and R1, averaged among all subjects.

MTsat + PD + R1 **nb Gaussians (CGM - DGM -WM - CSF)**	**Sensitivity**	**Specificity**	**Dice**	**Jaccard**	**MCC**
4-4-4-5	0.9755	0.99949	0.97709	0.95564	0.97653
4-5-4-5	0.97677	0.99951	0.97871	0.95875	0.97815
4-6-4-5	0.97708	0.99951	0.97887	0.95904	0.9783
4-4-5-5	0.98541	0.9998	0.99013	5.98046	0.98985
4-5-5-5	0.98644	0.9998	0.99084	0.98185	0.99056
4-6-5-5	0.98756	0.99981	0.99097	0.9821	0.99069
4-4-6-5	0.97952	0.9995	0.97953	0.96028	0.97901
4-5-6-5	0.97956	0.9995	0.97958	0.9604	0.97907
4-6-6-5	0.98089	0.9995	0.97972	0.96067	0.9792
5-4-4-5	0.98692	0.99992	0.99329	0.98668	0.99314
5-5-4-5	0.98801	0.99992	0.99351	0.98712	0.99336
5-6-4-5	0.98805	0.99992	0.99355	0.9872	0.9934
5-4-5-5	0.98925	0.99995	0.99436	0.9888	0.99424
5-5-5-5	0.9893	0.99995	0.9945	0.98907	0.99438
5-6-5-5	0.99142	0.99995	0.9953	0.99065	0.99518
5-4-6-5	0.98939	0.99996	0.99472	0.98951	0.99461
5-5-6-5	0.98919	0.99996	0.99446	0.989	0.99435
5-6-6-5	0.99004	0.99996	0.99465	0.98937	0.99453
6-4-4-5	0.98682	0.99989	0.99246	0.98505	0.99228
6-5-4-5	0.98754	0.9999	0.99284	0.98579	0.99267
6-6-4-5	0.9896	0.99986	0.99297	0.98604	0.99277
6-4-5-5	0.98831	0.99991	0.99358	0.98726	0.99343
6-5-5-5	0.98801	0.99991	0.99329	0.98669	0.99314
6-6-5-5	0.98973	0.99991	0.99398	0.98804	0.99383
6-4-6-5	0.98375	0.99984	0.98965	0.97957	0.98941
6-5-6-5	0.98317	0.99984	0.98918	0.97865	0.98893
6-6-6-5	0.98526	0.99985	0.99018	0.98062	0.98995

Table A.5: Comparison scores between each segmentation (ranging from 4 to 6 individually for CGM, DGM and WM) and the generated STAPLE one, with a multi-channel segmentation based on MTsat, PD and R1, averaged among all subjects.

nb Gaussians (5 - 5 - 6 - 6) **Combinaison of maps**	**Sensitivity**	**Specificity**	**Dice**	**Jaccard**	**MCC**
MTsat	0.87774	0.99701	0.8939	0.81036	0.89183
PD	0.76075	0.99658	0.81414	0.7012	0.81672
MTsat + PD	0.87098	0.99943	0.92864	0.86943	0.92746
R1	0.86585	0.99779	0.90066	0.82248	0.89866
MTsat + R1	0.89808	0.99948	0.94585	0.89896	0.94467
PD + R1	0.8454	0.99935	0.91489	0.84681	0.91459
MTsat + PD + R1	0.89902	0.99976	0.95808	0.92057	0.95718
R2*	0.71208	0.99477	0.78123	0.64367	0.78059
MTsat + R2*	0.86993	0.99894	0.92908	0.86823	0.92736
PD + R2*	0.79045	0.99818	0.86678	0.77195	0.86717
MTsat + PD + R2*	0.88495	0.99971	0.95215	0.90988	0.95136
R1 + R2*	0.86784	0.99939	0.92459	0.86249	0.92351
MTsat + R1 + R2*	0.88034	0.99985	0.9501	0.90693	0.94956
PD + R1 + R2*	0.85544	0.99961	0.92787	0.8682	0.92749
MTsat + PD + R1 + R2*	0.89347	0.99944	0.93841	0.88696	0.93692

Table A.6: Comparison scores between each segmentation (testing all combinations of MPM maps) and the generated STAPLE one, with a number of Gaussians of 5 for CGM, 5 for DGM, 6 for WM and 6 for CSF, averaged among all subjects.

Appendix B

Applications to other projects

This thesis proposes different MPM-based investigations in healthy subjects and patients with multiple sclerosis, which were already applied to other research projects. Within the Cyclotron Research Centre, the MPM protocol as well as methodological procedures such as USwL segmentation and whole-tissue global measurements analyses were adapted in two distinct projects engaging multiple sclerosis.

The first one explores the underlying mechanisms of MS-related fatigue, in patients at early stages of the disease. The MPM protocol allowed to probe the structural cerebral substrates of cognitive fatigue, in order to assess whether young patients at early stages of MS already undergo brain microstructural alterations. In addition, the relation between fatigue and microstructure was assessed, based on individual scores of a cognitive fatigue scale, previously determined for each subject.

In this study, global MPM measurements within normal appearing tissues were computed, and we assessed whether they could predict individual scores of a cognitive fatigue scale. Patients exhibited lower MTsat and R1 values within NAWM and NACGM, as well as higher R1 in NADGM compared to HC, suggesting that brain microstructure within NABT is already altered in the very early stages of the disease. Indeed, lower MTsat and R1 indicate the occurrence of demyelination in NAWM and NACGM as well as increased iron concentration within NADGM. Furthermore, cognitive fatigue was associated to PD measure in every tissue class and to MTsat in NAWM, regardless of the group (MS patients vs HC). Disease-specific negative correlations were found in MS patients only in NAWM (R1 and R2*) and NACGM (R1). It was finally shown that trait cognitive fatigue was associated to brain microstructure in both a general and disease-specific way.

These results contributed to the following manuscript submitted for publication:

- **Guillemin C., Vandeleene N.**, Charonitis M., Requier F., Delrue G., Lommers E., Maquet P., Phillips C., Collette F., "Exploring the link between cognitive fatigue and microstructural integrity of normal appearing brain tissues in the early stages of multiple sclerosis", submitted for publication in *Annals of Neurology.*

This methodology was brought further by adapting it from 3T to 7T MRI. A new project was recently launched for the assessment of MS-related microstructural alterations, captured by 7T MPM and PET imaging, for the purpose of detecting and characterizing cortical lesions, and compared to healthy volunteers. The MPM protocol and its parameters were previously customized for a 7T framework, and the different processing tools detailed throughout this thesis were conjointly adjusted to accomplish similar analysis tasks. A similar process as in section 4.2 for the combination of parameters generating the most accurate segmentation in healthy brains was conducted. This adapted version of the US approach was further extended to delineate normal appearing tissues and WM lesions in MS patients, using the USwL algorithm. An example of the four MPM maps (MTsat, PD, R1 and R2*) appear in Figure B.1. WM lesions, appearing in red contours in the Figure, were delineated with the USwL algorithm.

Preliminary results comparing normal appearing and healthy tissues, in MS patients and HC respectively, were conducted. Such analysis has already been accomplished in a 3T framework [Lommers et al., 2019]. In the present case, we want to inspect whether or not similar observations can be made, taking into account the higher spatial resolution from 7T MR images.

Moreover, as cited here above, the main goal of this project is to delineate lesions within cortical gray matter. Taking advantage of the quantitative and multi-dimensional nature of MPM data may probably help at detecting outliers within the CGM tissue. The development of a MPM-based tool for cortical lesions detection has been initiated but lacks of accuracy at the moment.

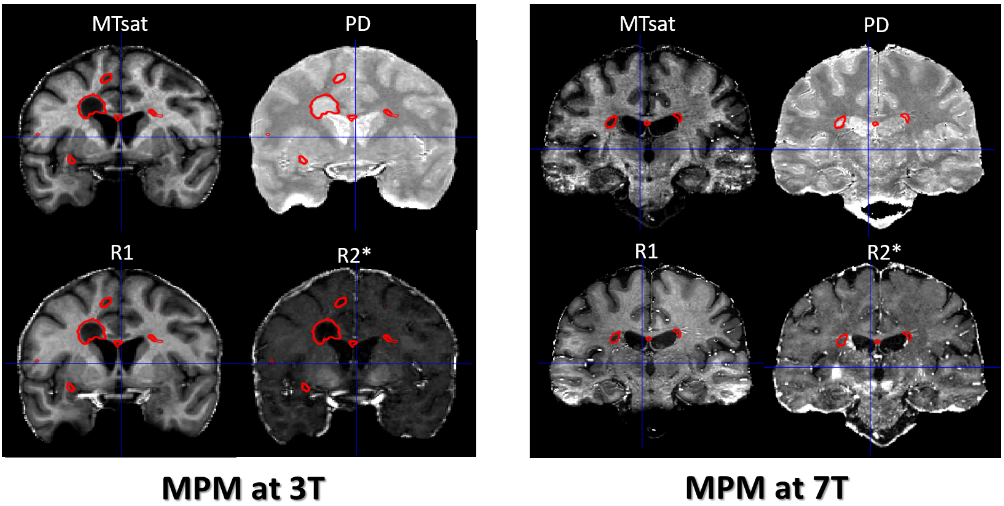

Figure B.1: Visual example of the 4 MPM maps of one MS patient, acquired with a 3T (left) or 7T (right) scanner. WM lesions are contoured in red.

Bibliography

[Absinta et al., 2016] Absinta, M., Sati, P., Schindler, M., Leibovitch, E. C., Ohayon, J., Wu, T., Meani, A., Filippi, M., Jacobson, S., Cortese, I. C., and Reich, D. S. (2016). Persistent 7 Tesla phase rim predicts poor outcome in new multiple sclerosis patient lesions. *Journal of Clinical Investigation*, 126(7):2597–2609. `https://www.jci.org/articles/view/86198`.

[Agosta, 2006] Agosta, F. (2006). Magnetization transfer MRI metrics predict the accumulation of disability 8 years later in patients with multiple sclerosis. *Brain*, 129(10):2620–2627. `https://academic.oup.com/brain/article-lookup/doi/10.1093/brain/awl208`.

[Alexander, 2008] Alexander, D. C. (2008). A general framework for experiment design in diffusion MRI and its application in measuring direct tissue-microstructure features. *Magnetic Resonance in Medicine*, 60(2):439–448. `https://onlinelibrary.wiley.com/doi/10.1002/mrm.21646`.

[Alexander et al., 2019] Alexander, D. C., Dyrby, T. B., Nilsson, M., and Zhang, H. (2019). Imaging brain microstructure with diffusion MRI: practicality and applications. *NMR in Biomedicine*, 32(4). `https://onlinelibrary.wiley.com/doi/10.1002/nbm.3841`.

[Alfano et al., 2000] Alfano, B., Brunetti, A., Larobina, M., Quarantelli, M., Tedeschi, E., Ciarmiello, A., Covelli, E. M., and Salvatore, M. (2000). Automated segmentation and measurement of global white matter lesion volume in patients with multiple sclerosis. *Journal of Magnetic Resonance Imaging*, 12(6):799–807. `https://onlinelibrary.wiley.com/doi/10.1002/1522-2586%28200012%2912%3A6%3C799%3A%3AAID-JMRI2%3E3.0.CO%3B2-%23`.

[Alotaibi et al., 2021] Alotaibi, A., Podlasek, A., AlTokhis, A., Aldhebaib, A., Dineen, R. A., and Constantinescu, C. S. (2021). Investigating Microstructural Changes in White Matter in Multiple Sclerosis: A Systematic Review and Meta-Analysis of Neurite Orientation Dispersion and Density Imaging. *Brain Sciences*, 11(9):1151. `https://www.mdpi.com/2076-3425/11/9/1151`.

[Amato et al., 2008] Amato, M. P., Portaccio, E., Stromillo, M. L., Goretti, B., Zipoli, V., Siracusa, G., Battaglini, M., Giorgio, A., Bartolozzi, M. L., Guidi, L., Sorbi, S., Federico, A., and De Stefano, N. (2008). Cognitive assessment and quantitative magnetic resonance metrics can help to identify benign multiple sclerosis. *Neurology*, 71(9):632–638. `https://www.neurology.org/lookup/doi/10.1212/01.wnl.0000324621.58447.00`.

[Amiri et al., 2018] Amiri, H., de Sitter, A., Bendfeldt, K., Battaglini, M., Gandini Wheeler-Kingshott, C. A., Calabrese, M., Geurts, J. J., Rocca, M. A., Sastre-Garriga, J., Enzinger, C., de Stefano, N., Filippi, M., Rovira, A., Barkhof, F., and Vrenken, H. (2018). Urgent challenges in quantification and interpretation of brain grey matter atrophy in individual MS patients using MRI. *NeuroImage: Clinical*, 19:466–475. `https://linkinghub.elsevier.com/retrieve/pii/S2213158218301323`.

[Anbeek et al., 2008] Anbeek, P., Vincken, K. L., and Viergever, M. A. (2008). Automated MS-Lesion Segmentation by K-Nearest Neighbor Classification. *The MIDAS Journal*, MICCAI 2008. `https://www.midasjournal.org/browse/publication/610`.

[Anderson, 2001] Anderson, M. J. (2001). Permutation tests for univariate or multivariate analysis of variance and regression. *Canadian Journal of Fisheries and Aquatic Sciences*, 58(3):626–639. `http://www.nrcresearchpress.com/doi/10.1139/f01-004`.

[Anderson et al., 2006] Anderson, V. M., Fox, N. C., and Miller, D. H. (2006). Magnetic resonance imaging measures of brain atrophy in multiple sclerosis. *Journal of Magnetic Resonance Imaging*, 23(5):605–618. `https://onlinelibrary.wiley.com/doi/10.1002/jmri.20550`.

[Andersson et al., 2003] Andersson, J. L., Skare, S., and Ashburner, J. (2003). How to correct susceptibility distortions in spin-echo echo-planar images: application to diffusion tensor imaging. *NeuroImage*, 20(2):870–888. `https://linkinghub.elsevier.com/retrieve/pii/S1053811903003367`.

[Andersson and Sotiropoulos, 2016] Andersson, J. L. and Sotiropoulos, S. N. (2016). An integrated approach to correction for off-resonance effects and subject movement in diffusion MR imaging. *NeuroImage*, 125:1063–1078. `https://linkinghub.elsevier.com/retrieve/pii/S1053811915009209`.

[Ashburner, 2013] Ashburner, J. (2013). Symmetric diffeomorphic modeling of longitudinal structural MRI. *Frontiers in Neuroscience*, 6. `http://journal.frontiersin.org/article/10.3389/fnins.2012.00197/abstract`.

[Ashburner et al., 2003] Ashburner, J., Csernansk, J. G., Davatzikos, C., Fox, N. C., Frisoni, G. B., and Thompson, P. M. (2003). Computer-assisted imaging to assess brain structure in healthy and diseased brains. *The Lancet Neurology*, 2(2):79–88. `https://linkinghub.elsevier.com/retrieve/pii/S1474442203003041`.

[Ashburner and Friston, 2005] Ashburner, J. and Friston, K. J. (2005). Unified segmentation. *NeuroImage*, 26(3):839–851. `https://linkinghub.elsevier.com/retrieve/pii/S1053811905001102`.

[Assaf and Basser, 2005] Assaf, Y. and Basser, P. J. (2005). Composite hindered and restricted model of diffusion (CHARMED) MR imaging of the human brain. *NeuroImage*, 27(1):48–58. `https://linkinghub.elsevier.com/retrieve/pii/S1053811905002259`.

[Assaf and Cohen, 2000] Assaf, Y. and Cohen, Y. (2000). Assignment of the water slow-diffusing component in the central nervous system using q-space diffusion MRS: Implications for fiber tract imaging. *Magnetic Resonance in Medicine*, 43(2):191–199. `https://onlinelibrary.wiley.com/doi/10.1002/(SICI)1522-2594(200002)43:2<191::AID-MRM5>3.0.CO;2-B`.

[Assaf et al., 2004] Assaf, Y., Freidlin, R. Z., Rohde, G. K., and Basser, P. J. (2004). New modeling and experimental framework to characterize hindered and restricted water diffusion in brain white matter. *Magnetic Resonance in Medicine*, 52(5):965–978. `https://onlinelibrary.wiley.com/doi/10.1002/mrm.20274`.

[Axer et al., 2011] Axer, M., Grässel, D., Kleiner, M., Dammers, J., Dickscheid, T., Reckfort, J., Hütz, T., Eiben, B., Pietrzyk, U., Zilles, K., and Amunts, K. (2011). High-Resolution Fiber Tract Reconstruction in the Human Brain by Means of Three-Dimensional Polarized Light Imaging. *Frontiers in Neuroinformatics*, 5. `http://journal.frontiersin.org/article/10.3389/fninf.2011.00034/abstract`.

[Bagnato et al., 2018] Bagnato, F., Hametner, S., Boyd, E., Endmayr, V., Shi, Y., Ikonomidou, V., Chen, G., Pawate, S., Lassmann, H., Smith, S., and Welch, E. B. (2018). Untangling the R2* contrast in multiple sclerosis: A combined MRI-histology study at 7.0 Tesla. *PLOS ONE*, 13(3):e0193839. `https://dx.plos.org/10.1371/journal.pone.0193839`.

[Balteau, 2016] Balteau, E. (2016). Lecture notes in Basis of magnetic resonance imaging, University of Liège.

[Barakovic et al., 2021] Barakovic, M., Girard, G., Schiavi, S., Romascano, D., Descoteaux, M., Granziera, C., Jones, D. K., Innocenti, G. M., Thiran, J.-P., and Daducci, A. (2021). Bundle-Specific Axon Diameter Index as a New Contrast to Differentiate White Matter Tracts. *Frontiers in Neuroscience*, 15:646034. `https://www.frontiersin.org/articles/10.3389/fnins.2021.646034/full`.

[Barkhof, 1999] Barkhof, F. (1999). MRI in multiple sclerosis: correlation with expanded disability status scale (EDSS). *Multiple sclerosis (Houndmills, Basingstoke, England)*, 5(4):283–286. `https://doi.org/10.1177/135245859900500415`.

[Barritt et al., 2018] Barritt, A. W., Gabel, M. C., Cercignani, M., and Leigh, P. N. (2018). Emerging Magnetic Resonance Imaging Techniques and Analysis Methods in Amyotrophic Lateral Sclerosis. *Frontiers in Neurology*, 9:1065. `https://www.frontiersin.org/article/10.3389/fneur.2018.01065/full`.

[Basser et al., 1994] Basser, P., Mattiello, J., and LeBihan, D. (1994). MR diffusion tensor spectroscopy and imaging. *Biophysical Journal*, 66(1):259–267. `https://linkinghub.elsevier.com/retrieve/pii/S0006349594807751`.

[Beaulieu, 2009] Beaulieu, C. (2009). The Biological Basis of Diffusion Anisotropy. *NMR in biomedicine*, 15(7-8):435–455. `https://doi.org/10.1002/nbm.782`.

[Behrens et al., 2003] Behrens, T., Woolrich, M., Jenkinson, M., Johansen-Berg, H., Nunes, R., Clare, S., Matthews, P., Brady, J., and Smith, S. (2003). Characterization and propagation of uncertainty in diffusion-weighted MR imaging. *Magnetic Resonance in Medicine*, 50(5):1077–1088. `https://onlinelibrary.wiley.com/doi/10.1002/mrm.10609`.

[Benjamini and Hochberg, 1995] Benjamini, Y. and Hochberg, Y. (1995). Controlling the false discovery rate: A practical and powerful approach to multiple testing. *Journal of the Royal Statistical Society. Series B (Methodological)*, 57(1):289–300. `http://www.jstor.org/stable/2346101`.

[Bermel and Bakshi, 2006] Bermel, R. A. and Bakshi, R. (2006). The measurement and clinical relevance of brain atrophy in multiple sclerosis. *The Lancet Neurology*, 5(2):158–170. `https://linkinghub.elsevier.com/retrieve/pii/S1474442206703490`.

[Bermel et al., 2005] Bermel, R. A., Puli, S. R., Rudick, R. A., Weinstock-Guttman, B., Fisher, E., Munschauer, F. E., and Bakshi, R. (2005). Prediction of Longitudinal Brain Atrophy in Multiple Sclerosis by Gray Matter Magnetic Resonance Imaging T2 Hypointensity. *Archives of Neurology*, 62(9):1371. `http://archneur.jamanetwork.com/article.aspx?doi=10.1001/archneur.62.9.1371`.

[Bernstein et al., 2004] Bernstein, M. A., King, K. F., and Zhou, X. J., editors (2004). *Handbook of MRI Pulse Sequences*. Academic Press, Burlington. `https://www.sciencedirect.com/science/article/pii/B9780120928613500303`.

[Bielekova et al., 2005] Bielekova, B., Kadom, N., Fisher, E., Jeffries, N., Ohayon, J., Richert, N., Howard, T., Bash, C. N., Frank, J. A., Stone, L., Martin, R., Cutter, G., and McFarland, H. F. (2005). MRI as a marker for disease heterogeneity in multiple sclerosis. *Neurology*, 65(7):1071–1076. `https://www.neurology.org/lookup/doi/10.1212/01.wnl.0000178984.30534.f9`.

[Bischof et al., 2021] Bischof, A., Cheng, S., Cree, B., Rajesh, A., Kirkish, G., Gundel, T., Stern, W., Juwono, J., Asteggiano, C., Santaniello, A., Caverzasi, E., Bove, R., Gelfand, J., Green, A., Guo, C.-Y., Sabatino, J., Waubant, E., Wilson, M., Zamvil, S., Hauser, S., Papinutto, N., and Henry, R. (2021). Quantitative MRI Reveals Mild Cervical Cord Damage in Longstanding Relapsing Multiple Sclerosis (2189). *Neurology*, 96(15 Supplement). `https://n.neurology.org/content/96/15_Supplement/2189`.

[Bjarnason et al., 2005] Bjarnason, T., Vavasour, I., Chia, C., and MacKay, A. (2005). Characterization of the NMR behavior of white matter in bovine brain. *Magnetic Resonance in Medicine*, 54(5):1072–1081. `https://onlinelibrary.wiley.com/doi/10.1002/mrm.20680`.

[Bodini et al., 2016] Bodini, B., Veronese, M., García Lorenzo, D., Battaglini, M., Poirion, E., Chardain, A., Freeman, L., Louapre, C., Tchikviladze, M., Papeix, C., Dollé, F., Zalc, B., Lubetzki, C., Bottlaender, M., Turkheimer, F., and Stankoff, B. (2016). Dynamic imaging of individual remyelination profiles in multiple sclerosis. *Annals of Neurology*, 79(5):726–738. `https://onlinelibrary.wiley.com/doi/10.1002/ana.24620`.

[Bonghi, 2021] Bonghi, S. (2021). Quantitative MRI characterization of brain tissues in stroke patients. Master's thesis, University of Liège. `http://hdl.handle.net/2268.2/13221`.

[Bonnier et al., 2017] Bonnier, G., Maréchal, B., Fartaria, M. J., Falkowskiy, P., Marques, J. P., Simioni, S., Schluep, M., Du Pasquier, R., Thiran, J.-P., Krueger, G., and Granziera, C. (2017). The Combined Quantification and Interpretation of Multiple Quantitative Magnetic Resonance Imaging Metrics Enlightens Longitudinal Changes Compatible with Brain Repair in Relapsing-Remitting Multiple Sclerosis Patients. *Frontiers in Neurology*, 8:506. `http://journal.frontiersin.org/article/10.3389/fneur.2017.00506/full`.

[Bonnier et al., 2014] Bonnier, G., Roche, A., Romascano, D., Simioni, S., Meskaldji, D., Rotzinger, D., Lin, Y., Menegaz, G., Schluep, M., Du Pasquier, R., Sumpf, T. J., Frahm, J., Thiran, J., Krueger, G., and Granziera, C. (2014). Advanced MRI unravels the nature of tissue alterations in early multiple sclerosis. *Annals of Clinical and Translational Neurology*, 1(6):423–432. `https://onlinelibrary.wiley.com/doi/10.1002/acn3.68`.

[Bouix et al., 2007] Bouix, S., Martin-Fernandez, M., Ungar, L., Nakamura, M., Koo, M.-S., McCarley, R. W., and Shenton, M. E. (2007). On evaluating brain tissue classifiers without a ground truth. *NeuroImage*, 36(4):1207–1224. `https://linkinghub.elsevier.com/retrieve/pii/S1053811907003485`.

[Bower et al., 2019] Bower, D. V., Richter, J. K., von Tengg-Kobligk, H., Heverhagen, J. T., and Runge, V. M. (2019). Gadolinium-Based MRI Contrast Agents Induce Mitochondrial Toxicity and Cell Death in Human Neurons, and Toxicity Increases With Reduced Kinetic Stability of the Agent:. *Investigative Radiology*, 54(8):453–463. `http://journals.lww.com/00004424-201908000-00001`.

[Brady et al., 1999] Brady, S. T., Witt, A. S., Kirkpatrick, L. L., de Waegh, S. M., Readhead, C., Tu, P.-H., and Lee, V. M.-Y. (1999). Formation of Compact Myelin Is Required for Maturation of the Axonal Cytoskeleton. *The Journal of Neuroscience*, 19(17):7278–7288. `https://www.jneurosci.org/lookup/doi/10.1523/JNEUROSCI.19-17-07278.1999`.

[Brett et al., 2001] Brett, M., Leff, A. P., Rorden, C., and Ashburner, J. (2001). Spatial Normalization of Brain Images with Focal Lesions Using Cost Function Masking. *NeuroImage*, 14(2):486–500. `https://linkinghub.elsevier.com/retrieve/pii/S1053811901908456`.

[Brown et al., 2013] Brown, R. A., Narayanan, S., and Arnold, D. L. (2013). Segmentation of magnetization transfer ratio lesions for longitudinal analysis of demyelination and remyelination in multiple sclerosis. *NeuroImage*, 66:103–109.

[Brown et al., 2014] Brown, R. A., Narayanan, S., and Arnold, D. L. (2014). Imaging of repeated episodes of demyelination and remyelination in multiple sclerosis. *NeuroImage: Clinical*, 6:20–25. `https://linkinghub.elsevier.com/retrieve/pii/S2213158214000850`.

[Brück et al., 1997] Brück, W., Bitsch, A., Kolenda, H., Brück, Y., Stiefel, M., and Lassmann, H. (1997). Inflammatory central nervous system demyelination: Correlation of magnetic resonance imaging findings with lesion pathology: MRI and Pathology of Demyelination. *Annals of Neurology*, 42(5):783–793. `https://onlinelibrary.wiley.com/doi/10.1002/ana.410420515`.

[Budde and Annese, 2013] Budde, M. D. and Annese, J. (2013). Quantification of anisotropy and fiber orientation in human brain histological sections. *Frontiers in Integrative Neuroscience*, 7. `http://journal.frontiersin.org/article/10.3389/fnint.2013.00003/abstract`.

[By et al., 2017] By, S., Xu, J., Box, B. A., Bagnato, F. R., and Smith, S. A. (2017). Application and evaluation of NODDI in the cervical spinal cord of multiple sclerosis patients. *NeuroImage: Clinical*, 15:333–342. `https://linkinghub.elsevier.com/retrieve/pii/S2213158217301158`.

[Cagol et al., 2022] Cagol, A., Schaedelin, S., Barakovic, M., Benkert, P., Todea, R.-A., Rahmanzadeh, R., Galbusera, R., Lu, P.-J., Weigel, M., Melie-Garcia, L., Ruberte, E., Siebenborn, N., Battaglini, M., Radue, E.-W., Yaldizli, `[U+FFFD]`, Oechtering, J., Sinnecker, T., Lorscheider, J., Fischer-Barnicol, B., Müller, S., Achtnichts, L., Vehoff, J., Disanto, G., Findling, O., Chan, A., Salmen, A., Pot, C., Bridel, C., Zecca, C., Derfuss, T., Lieb, J. M., Remonda, L., Wagner, F., Vargas, M. I., Du Pasquier, R., Lalive, P. H., Pravatà, E., Weber, J., Cattin, P. C., Gobbi, C., Leppert, D., Kappos, L., Kuhle, J., and Granziera, C. (2022). Association of Brain Atrophy With Disease Progression Independent of Relapse Activity in Patients With Relapsing Multiple Sclerosis. *JAMA Neurology*, 79(7):682. `https://jamanetwork.com/journals/jamaneurology/fullarticle/2792415`.

[Calabrese et al., 2015] Calabrese, M., Magliozzi, R., Ciccarelli, O., Geurts, J. J. G., Reynolds, R., and Martin, R. (2015). Exploring the origins of grey matter damage in multiple sclerosis. *Nature Reviews Neuroscience*, 16(3):147–158. `http://www.nature.com/articles/nrn3900`.

[Callaghan et al., 2014] Callaghan, M. F., Freund, P., Draganski, B., Anderson, E., Cappelletti, M., Chowdhury, R., Diedrichsen, J., FitzGerald, T. H., Smittenaar, P., Helms, G., Lutti, A., and Weiskopf, N. (2014). Widespread age-related differences in the human brain microstructure revealed by quantitative magnetic resonance imaging. *Neurobiology of Aging*, 35(8):1862–1872. `https://linkinghub.elsevier.com/retrieve/pii/S0197458014002000`.

[Callaghan et al., 2015] Callaghan, M. F., Helms, G., Lutti, A., Mohammadi, S., and Weiskopf, N. (2015). A general linear relaxometry model of R1 using imaging data: General Linear Relaxometry Model of R1. *Magnetic Resonance in Medicine*, 73(3):1309–1314. `https://onlinelibrary.wiley.com/doi/10.1002/mrm.25210`.

[Cammoun et al., 1985] Cammoun, D., Hendee, W. R., and Davis, K. A. (1985). Clinical Applications of Magnetic Resonance Imag ing Current Status. *The Western Journal of Medicine*, 143(6):793–803.

[Carey et al., 2018] Carey, D., Caprini, F., Allen, M., Lutti, A., Weiskopf, N., Rees, G., Callaghan, M. F., and Dick, F. (2018). Quantitative MRI provides markers of intra-, inter-regional, and age-related differences in young adult cortical microstructure. *NeuroImage*, 182:429–440. `https://linkinghub.elsevier.com/retrieve/pii/S1053811917310121`.

[Ceccarelli et al., 2008] Ceccarelli, A., Rocca, M. A., Pagani, E., Colombo, B., Martinelli, V., Comi, G., and Filippi, M. (2008). A voxel-based morphometry study of grey matter loss in MS patients with different clinical phenotypes. *NeuroImage*, 42(1):315–322. `https://linkinghub.elsevier.com/retrieve/pii/S1053811908005028`.

[Cercignani et al., 2018] Cercignani, M., Dowell, N. G., Tofts, P. S., Majumdar, K., Russo, P., Jia, X., Jiang, S. B., Kuiken, T. A., Feuser, A. E. S., Barlow, A. K., Song, W. Y., Tanderup, K., Pieters, B., Isaksson, M., Rääf, C. L., Stabin, M. G., Vetter, R. J., Stoeva, M. S., Sitek, A., Webster, J. G., Lehnert, S., Zeng, H., Willson, K., Ison, K., Tabakov, S., and Muftuler, L. T. (2018). *Quantitative MRI of the Brain - Principles of Physical Measurement, 2nd edition.* CRC Press.

[Chawla et al., 2018] Chawla, S., Kister, I., Sinnecker, T., Wuerfel, J., Brisset, J.-C., Paul, F., and Ge, Y. (2018). Longitudinal study of multiple sclerosis lesions using ultra-high field (7T) multiparametric MR imaging. *PLOS ONE*, 13(9):e0202918. `https://dx.plos.org/10.1371/journal.pone.0202918`.

[Chen et al., 2008] Chen, J. T., Collins, D. L., Atkins, H. L., Freedman, M. S., Arnold, D. L., and the Canadian MS/BMT Study Group (2008). Magnetization transfer ratio evolution with demyelination and remyelination in multiple sclerosis lesions. *Annals of Neurology*, 63(2):254–262. `https://onlinelibrary.wiley.com/doi/10.1002/ana.21302`.

[Cherubini et al., 2009] Cherubini, A., Péran, P., Caltagirone, C., Sabatini, U., and Spalletta, G. (2009). Aging of subcortical nuclei: Microstructural, mineralization and atrophy modifications measured in vivo using MRI. *NeuroImage*, 48(1):29–36. `https://linkinghub.elsevier.com/retrieve/pii/S1053811909006673`.

[Clarke et al., 2020] Clarke, W. T., Mougin, O., Driver, I. D., Rua, C., Morgan, A. T., Asghar, M., Clare, S., Francis, S., Wise, R. G., Rodgers, C. T., Carpenter, A., Muir, K., and Bowtell, R. (2020). Multi-site harmonization of 7 Tesla MRI neuroimaging protocols. *NeuroImage*, 206. `https://linkinghub.elsevier.com/retrieve/pii/S1053811919309267`.

[Cocozza et al., 2020] Cocozza, S., Cosottini, M., Signori, A., Fleysher, L., El Mendili, M. M., Lublin, F., Inglese, M., and Roccatagliata, L. (2020). A clinically feasible 7-Tesla protocol for the identification of cortical lesions in Multiple Sclerosis. *European Radiology*, 30(8):4586–4594. `http://link.springer.com/10.1007/s00330-020-06803-y`.

[Codella et al., 2002] Codella, M., Assunta Rocca, M., Colombo, B., Rossi, P., Comi, G., and Filippi, M. (2002). A preliminary study of magnetization transfer and diffusion tensor MRI of multiple sclerosis patients with fatigue. *Journal of Neurology*, 249(5):535–537. `http://link.springer.com/10.1007/s004150200060`.

[Collorone et al., 2020] Collorone, S., Cawley, N., Grussu, F., Prados, F., Tona, F., Calvi, A., Kanber, B., Schneider, T., Kipp, L., Zhang, H., Alexander, D. C., Thompson, A. J., Toosy, A., Wheeler-Kingshott, C. A. G., and Ciccarelli, O. (2020). Reduced neurite density in the brain and cervical spinal cord in relapsing–remitting multiple sclerosis: A NODDI study. *Multiple Sclerosis Journal*, 26(13):1647–1657. `http://journals.sagepub.com/doi/10.1177/1352458519885107`.

[Compston and Coles, 2008] Compston, A. and Coles, A. (2008). Multiple sclerosis. *Lancet (London, England)*, 372(9648):1502–1517. `https://doi.org/10.1016/S0140-6736(08)61620-7`.

[Confavreux and Vukusic, 2006] Confavreux, C. and Vukusic, S. (2006). Age at disability milestones in multiple sclerosis. *Brain*, 129(3):595–605. `http://academic.oup.com/brain/article/129/3/595/390809/Age-at-disability-milestones-in-multiple-sclerosis`.

[Confavreux and Vukusic, 2014] Confavreux, C. and Vukusic, S. (2014). The clinical course of multiple sclerosis. In *Handbook of Clinical Neurology*, volume 122, pages 343–369. Elsevier. `https://linkinghub.elsevier.com/retrieve/pii/B9780444520012000145`.

[Confavreux et al., 2000] Confavreux, C., Vukusic, S., Moreau, T., and Adeleine, P. (2000). Relapses and Progression of Disability in Multiple Sclerosis. *New England Journal of Medicine*, 343(20):1430–1438. `http://www.nejm.org/doi/abs/10.1056/NEJM200011163432001`.

[Connor and Menzies, 1995] Connor, J. R. and Menzies, S. L. (1995). Cellular management of iron in the brain. *Journal of the Neurological Sciences*, 134:33–44. `https://linkinghub.elsevier.com/retrieve/pii/0022510X9500206H`.

[Correale, 2014] Correale, J. (2014). The role of microglial activation in disease progression. *Multiple Sclerosis Journal*, 20(10):1288–1295. `http://journals.sagepub.com/doi/10.1177/1352458514533230`.

[Crinion et al., 2007] Crinion, J., Ashburner, J., Leff, A., Brett, M., Price, C., and Friston, K. (2007). Spatial normalization of lesioned brains: Performance evaluation and impact on fMRI analyses. *NeuroImage*, 37(3):866–875. `https://linkinghub.elsevier.com/retrieve/pii/S1053811907003266`.

[Dalton, 2004] Dalton, C. M. (2004). Early development of multiple sclerosis is associated with progressive grey matter atrophy in patients presenting with clinically isolated syndromes. *Brain*, 127(5):1101–1107. `https://academic.oup.com/brain/article-lookup/doi/10.1093/brain/awh126`.

[Danelakis et al., 2018] Danelakis, A., Theoharis, T., and Verganelakis, D. A. (2018). Survey of automated multiple sclerosis lesion segmentation techniques on magnetic resonance imaging. *Computerized Medical Imaging and Graphics*, 70:83–100. `https://linkinghub.elsevier.com/retrieve/pii/S0895611118303227`.

[Dastidar et al., 1999] Dastidar, P., Heinonen, T., Lehtimäki, T., Ukkonen, M., Peltola, J., Erilä, T., Laasonen, E., and Elovaara, I. (1999). Volumes of brain atrophy and plaques correlated with neurological disability in secondary progressive multiple sclerosis. *Journal of the Neurological Sciences*, 165(1):36–42. `https://linkinghub.elsevier.com/retrieve/pii/S0022510X99000714`.

[De Santis et al., 2019] De Santis, S., Bastiani, M., Droby, A., Kolber, P., Zipp, F., Pracht, E., Stoecker, T., Groppa, S., and Roebroeck, A. (2019). Characterizing Microstructural Tissue Properties in Multiple Sclerosis with Diffusion MRI at 7 T and 3 T: The Impact of the Experimental Design. *Neuroscience*, 403:17–26. `https://linkinghub.elsevier.com/retrieve/pii/S0306452218302483`.

[De Stefano et al., 2014] De Stefano, N., Airas, L., Grigoriadis, N., Mattle, H. P., O'Riordan, J., Oreja-Guevara, C., Sellebjerg, F., Stankoff, B., Walczak, A., Wiendl, H., and Kieseier, B. C. (2014). Clinical Relevance of Brain Volume Measures in Multiple Sclerosis. *CNS Drugs*, 28(2):147–156. `http://link.springer.com/10.1007/s40263-014-0140-z`.

[De Stefano et al., 2007] De Stefano, N., Battaglini, M., and Smith, S. M. (2007). Measuring Brain Atrophy in Multiple Sclerosis. *Journal of Neuroimaging*, 17:10S–15S. `https://onlinelibrary.wiley.com/doi/10.1111/j.1552-6569.2007.00130.x`.

[De Stefano et al., 2010] De Stefano, N., Giorgio, A., Battaglini, M., Rovaris, M., Sormani, M. P., Barkhof, F., Korteweg, T., Enzinger, C., Fazekas, F., Calabrese, M., Dinacci, D., Tedeschi, G., Gass, A., Montalban, X., Rovira, A., Thompson, A., Comi, G., Miller, D. H., and Filippi, M. (2010). Assessing brain atrophy rates in a large population of untreated multiple sclerosis subtypes. *Neurology*, 74(23):1868–1876. `https://www.neurology.org/lookup/doi/10.1212/WNL.0b013e3181e24136`.

[De Stefano et al., 2015] De Stefano, N., Stromillo, M. L., Giorgio, A., Bartolozzi, M. L., Battaglini, M., Baldini, M., Portaccio, E., Amato, M. P., and Sormani, M. P. (2015). Establishing pathological cut-offs of brain atrophy rates in multiple sclerosis. *Journal of Neurology, Neurosurgery & Psychiatry*, 87:93–99. `https://jnnp.bmj.com/lookup/doi/10.1136/jnnp-2014-309903`.

[Delikatny et al., 2011] Delikatny, E. J., Chawla, S., Leung, D.-J., and Poptani, H. (2011). MR-visible lipids and the tumor microenvironment. *NMR in Biomedicine*, 24:592–611. `https://onlinelibrary.wiley.com/doi/10.1002/nbm.1661`.

[Dendrou et al., 2015] Dendrou, C. A., Fugger, L., and Friese, M. A. (2015). Immunopathology of multiple sclerosis. *Nature Reviews Immunology*, 15(9):545–558. `http://www.nature.com/articles/nri3871`.

[Denissen et al., 2021] Denissen, S., Chén, O. Y., De Mey, J., De Vos, M., Van Schependom, J., Sima, D. M., and Nagels, G. (2021). Towards multimodal machine learning prediction of individual cognitive evolution in multiple sclerosis. *Journal of Personalized Medicine*, 11(12). `https://www.mdpi.com/2075-4426/11/12/1349`.

[Deoni et al., 2008] Deoni, S. C., Williams, S. C., Jezzard, P., Suckling, J., Murphy, D. G., and Jones, D. K. (2008). Standardized structural magnetic resonance imaging in multicentre studies using quantitative T1 and T2 imaging at 1.5T. *NeuroImage*, 40(2):662–671. `https://linkinghub.elsevier.com/retrieve/pii/S1053811907010725`.

[Depierreux et al., 2021] Depierreux, F., Parmentier, E., Mackels, L., Baquero, K., Degueldre, C., Balteau, E., Salmon, E., Phillips, C., Bahri, M. A., Maquet, P., and Garraux, G. (2021). Parkinson's disease multimodal imaging: F-DOPA PET, neuromelanin-sensitive and quantitative iron-sensitive MRI. *npj Parkinson's Disease*, 7(1):57. `http://www.nature.com/articles/s41531-021-00199-2`.

[Dousset et al., 1998] Dousset, V., Gayou, A., Brochet, B., and Caille, J.-M. (1998). Early structural changes in acute MS lesions assessed by serial magnetization transfer studies. *Neurology*, 51(4):1150–1155. `https://www.neurology.org/lookup/doi/10.1212/WNL.51.4.1150`.

[Dousset et al., 1992] Dousset, V., Grossman, R. I., Ramer, K. N., Schnall, M. D., Young, L. H., Gonzalez-Scarano, F., Lavi, E., and Cohen, J. A. (1992). Experimental allergic encephalomyelitis and multiple sclerosis: lesion characterization with magnetization transfer imaging. *Radiology*, 182(2):483–491. `https://pubmed.ncbi.nlm.nih.gov/1732968/`.

[Draganski et al., 2011] Draganski, B., Ashburner, J., Hutton, C., Kherif, F., Frackowiak, R., Helms, G., and Weiskopf, N. (2011). Regional specificity of MRI contrast parameter changes in normal ageing revealed by voxel-based quantification (VBQ). *NeuroImage*, 55(4):1423–1434. `https://linkinghub.elsevier.com/retrieve/pii/S1053811911000887`.

[Dutta and Trapp, 2007] Dutta, R. and Trapp, B. D. (2007). Pathogenesis of axonal and neuronal damage in multiple sclerosis. *Neurology*, 68(Issue 22, Supplement 3):22–31. `https://www.neurology.org/lookup/doi/10.1212/01.wnl.0000275229.13012.32`.

[Dyrby et al., 2013] Dyrby, T. B., S⊘gaard, L. V., Hall, M. G., Ptito, M., and Alexander, D. C. (2013). Contrast and stability of the axon diameter index from microstructure imaging with diffusion MRI: Contrast and Stability of the Axon Diameter Index. *Magnetic Resonance in Medicine*, 70(3):711–721. `https://onlinelibrary.wiley.com/doi/10.1002/mrm.24501`.

[Edelman, 1993] Edelman, R. R. (1993). Mr angiography: present and future. *AJR American journal of roentgenology*, 161:1–11.

[Edwards et al., 2018] Edwards, L. J., Kirilina, E., Mohammadi, S., and Weiskopf, N. (2018). Microstructural imaging of human neocortex in vivo.

NeuroImage, 182:184–206. `https://linkinghub.elsevier.com/retrieve/pii/S1053811918301629`.

[Elkady et al., 2017] Elkady, A. M., Cobzas, D., Sun, H., Blevins, G., and Wilman, A. H. (2017). Progressive iron accumulation across multiple sclerosis phenotypes revealed by sparse classification of deep gray matter: Progressive Iron Accumulation in MS. *Journal of Magnetic Resonance Imaging*, 46(5):1464–1473. `https://onlinelibrary.wiley.com/doi/10.1002/jmri.25682`.

[Elkady et al., 2018] Elkady, A. M., Cobzas, D., Sun, H., Blevins, G., and Wilman, A. H. (2018). Discriminative analysis of regional evolution of iron and myelin/calcium in deep gray matter of multiple sclerosis and healthy subjects: Analysis of Iron and Myelin in MS. *Journal of Magnetic Resonance Imaging*, 48(3):652–668. `https://onlinelibrary.wiley.com/doi/10.1002/jmri.26004`.

[Elkady et al., 2019] Elkady, A. M., Cobzas, D., Sun, H., Seres, P., Blevins, G., and Wilman, A. H. (2019). Five year iron changes in relapsing-remitting multiple sclerosis deep gray matter compared to healthy controls. *Multiple Sclerosis and Related Disorders*, 33:107–115. `https://linkinghub.elsevier.com/retrieve/pii/S2211034819302329`.

[Elliott et al., 2019] Elliott, C., Wolinsky, J. S., Hauser, S. L., Kappos, L., Barkhof, F., Bernasconi, C., Wei, W., Belachew, S., and Arnold, D. L. (2019). Slowly expanding/evolving lesions as a magnetic resonance imaging marker of chronic active multiple sclerosis lesions. *Multiple Sclerosis Journal*, 25(14):1915–1925. `http://journals.sagepub.com/doi/10.1177/1352458518814117`.

[Engström et al., 2014] Engström, M., Warntjes, J. B. M., Tisell, A., Landtblom, A.-M., and Lundberg, P. (2014). Multi-Parametric Representation of Voxel-Based Quantitative Magnetic Resonance Imaging. *PLoS ONE*, 9(11):e111688. `https://dx.plos.org/10.1371/journal.pone.0111688`.

[Enzinger et al., 2015] Enzinger, C., Barkhof, F., Ciccarelli, O., Filippi, M., Kappos, L., Rocca, M. A., Ropele, S., Rovira, A., Schneider, T., de Stefano, N., Vrenken, H., Wheeler-Kingshott, C., Wuerfel, J., and Fazekas, F. (2015). Nonconventional MRI and microstructural cerebral changes in multiple sclerosis. *Nature Reviews Neurology*, 11(12):676–686. `http://www.nature.com/articles/nrneurol.2015.194`.

[Ernst and Anderson, 1966] Ernst, R. R. and Anderson, W. A. (1966). Application of Fourier Transform Spectroscopy to Magnetic Resonance. *Review of*

Scientific Instruments, 37(1):93–102. `http://aip.scitation.org/doi/10.1063/1.1719961`.

[Eshaghi et al., 2018] Eshaghi, A., Prados, F., Brownlee, W. J., Altmann, D. R., Tur, C., Cardoso, M. J., De Angelis, F., van de Pavert, S. H., Cawley, N., De Stefano, N., Stromillo, M. L., Battaglini, M., Ruggieri, S., Gasperini, C., Filippi, M., Rocca, M. A., Rovira, A., Sastre-Garriga, J., Vrenken, H., Leurs, C. E., Killestein, J., Pirpamer, L., Enzinger, C., Ourselin, S., Wheeler-Kingshott, C. A. G., Chard, D., Thompson, A. J., Alexander, D. C., Barkhof, F., Ciccarelli, O., and on behalf of the MAGNIMS study group (2018). Deep gray matter volume loss drives disability worsening in multiple sclerosis: Deep Gray Matter Volume Loss. *Annals of Neurology*, 83(2):210–222. `https://onlinelibrary.wiley.com/doi/10.1002/ana.25145`.

[Fatouros et al., 1991] Fatouros, P. P., Marmarou, A., Kraft, K. A., Inao, S., and Schwarz, F. P. (1991). In Vivo Brain Water Determination by T1 Measurements: Effect of Total Water Content, Hydration Fraction, and Field Strength. *Magnetic Resonance in Medicine*, 17(2):402–413. `https://onlinelibrary.wiley.com/doi/10.1002/mrm.1910170212`.

[Fazekas et al., 2002] Fazekas, F., Ropele, S., Enzinger, C., Seifert, T., and Strasser-Fuchs, S. (2002). Quantitative magnetization transfer imaging of pre-lesional white-matter changes in multiple sclerosis. *Multiple Sclerosis Journal*, 8(6):479–484. `http://journals.sagepub.com/doi/10.1191/1352458502ms860oa`.

[Fernando et al., 2005] Fernando, K. T. M., Tozer, D. J., Miszkiel, K. A., Gordon, R. M., Swanton, J. K., Dalton, C. M., Barker, G. J., Plant, G. T., Thompson, A. J., and Miller, D. H. (2005). Magnetization transfer histograms in clinically isolated syndromes suggestive of multiple sclerosis. *Brain*, 128(12):2911–2925. `http://academic.oup.com/brain/article/128/12/2911/420497/Magnetization-transfer-histograms-in-clinically`.

[Filippi et al., 1996] Filippi, M., Baratti, C., Yousry, T., Horsfield, M. A., Mammi, S., Becker, C., Voltz, R., Spuler, S., Campi, A., Reiser, M. F., and Comi, G. (1996). Quantitative assessment of MRI lesion load in multiple sclerosis: A comparison of conventional spin-echo with fast fluidattenuated inversion recovery. *Brain*, 119(4):1349–1355. `https://academic.oup.com/brain/article-lookup/doi/10.1093/brain/119.4.1349`.

[Filippi et al., 1995] Filippi, M., Paty, D. W., Kappos, L., Barkhof, F., and Compston, D. A. S. (1995). Correlations between changes in disability and

T2-weighted brain MRI activity in multiple sclerosis. *Neurology*, 45(2):255–260.

[Filippi and Rocca, 2005] Filippi, M. and Rocca, M. A. (2005). MRI evidence for multiple sclerosis as a diffuse disease of the central nervous system. *Journal of Neurology*, 252(S5):16–24. `http://link.springer.com/10.1007/s00415-005-5004-5`.

[Filippi and Rocca, 2007] Filippi, M. and Rocca, M. A. (2007). Magnetization transfer magnetic resonance imaging of the brain, spinal cord, and optic nerve. *Neurotherapeutics*, 4(3):401–413. `http://link.springer.com/10.1016/j.nurt.2007.03.002`.

[Filippi et al., 2012] Filippi, M., Rocca, M. A., Barkhof, F., Brück, W., Chen, J. T., Comi, G., DeLuca, G., De Stefano, N., Erickson, B. J., Evangelou, N., Fazekas, F., Geurts, J. J., Lucchinetti, C., Miller, D. H., Pelletier, D., Popescu, B. F. G., and Lassmann, H. (2012). Association between pathological and MRI findings in multiple sclerosis. *The Lancet Neurology*, 11(4):349–360. `https://linkinghub.elsevier.com/retrieve/pii/S1474442212700030`.

[Filippi et al., 1998a] Filippi, M., Rocca, M. A., and Comi, G. (1998a). Magnetization transfer ratios of multiple sclerosis lesions with variable durations of enhancement. *Journal of the Neurological Sciences*, 159(2):162–165.

[Filippi et al., 1998b] Filippi, M., Rocca, M. A., Martino, G., Horsfield, M. A., and Comi, G. (1998b). Magnetization transfer changes in the normal appering white matter precede the appearance of enhancing lesions in patients with multiple sclerosis. *Annals of Neurology*, 43(6):809–814. `https://onlinelibrary.wiley.com/doi/10.1002/ana.410430616`.

[Fischer et al., 1990] Fischer, H. W., Rinck, P. A., van Haverbeke, Y., and Muller, R. N. (1990). Nuclear relaxation of human brain gray and white matter: Analysis of field dependence and implications for MRI. *Magnetic Resonance in Medicine*, 16(2):317–334. `https://onlinelibrary.wiley.com/doi/10.1002/mrm.1910160212`.

[Fisher et al., 2008] Fisher, E., Lee, J.-C., Nakamura, K., and Rudick, R. A. (2008). Gray matter atrophy in multiple sclerosis: A longitudinal study: Gray Matter Atrophy in MS. *Annals of Neurology*, 64(3):255–265. `https://onlinelibrary.wiley.com/doi/10.1002/ana.21436`.

[Fisher et al., 2002] Fisher, E., Rudick, R. A., Simon, J. H., Cutter, G., Baier, M., Lee, J. C., Miller, D., Weinstock-Guttman, B., Mass, M. K., Dougherty,

D. S., and Simonian, N. A. (2002). Eight-year follow-up study of brain atrophy in patients with MS. *Neurology*, 59(9):1412–1420. `https://www.neurology.org/lookup/doi/10.1212/01.WNL.0000036271.49066.06`.

[Frischer et al., 2009] Frischer, J. M., Bramow, S., Dal-Bianco, A., Lucchinetti, C. F., Rauschka, H., Schmidbauer, M., Laursen, H., Sorensen, P. S., and Lassmann, H. (2009). The relation between inflammation and neurodegeneration in multiple sclerosis brains. *Brain*, 132(5):1175–1189. `https://academic.oup.com/brain/article-lookup/doi/10.1093/brain/awp070`.

[Frischer et al., 2015] Frischer, J. M., Weigand, S. D., Guo, Y., Kale, N., Parisi, J. E., Pirko, I., Mandrekar, J., Bramow, S., Metz, I., Brück, W., Lassmann, H., and Lucchinetti, C. F. (2015). Clinical and pathological insights into the dynamic nature of the white matter multiple sclerosis plaque: Dynamic Nature of MS Plaque. *Annals of Neurology*, 78(5):710–721. `https://onlinelibrary.wiley.com/doi/10.1002/ana.24497`.

[Frisoni et al., 2010] Frisoni, G. B., Fox, N. C., Jack, C. R., Scheltens, P., and Thompson, P. M. (2010). The clinical use of structural MRI in Alzheimer's disease. *Nature Reviews Neurology*, 6(2):67–77. `http://www.nature.com/articles/nrneurol.2009.215`.

[Ge et al., 2001] Ge, Y., Grossman, R. I., Udupa, J. K., Babb, J. S., Nyúl, L. G., and Kolson, D. L. (2001). Brain Atrophy in Relapsing-Remitting Multiple Sclerosis: Fractional Volumetric Analysis of Gray Matter and White Matter. *Radiology*, 220(3):606–610. `http://pubs.rsna.org/doi/10.1148/radiol.2203001776`.

[Gelman et al., 2001] Gelman, N., Ewing, J. R., Gorell, J. M., Spickler, E. M., and Solomon, E. G. (2001). Interregional variation of longitudinal relaxation rates in human brain at 3.0 T: Relation to estimated iron and water contents. *Magnetic Resonance in Medicine*, 45(1):71–79. `https://onlinelibrary.wiley.com/doi/10.1002/1522-2594(200101)45:1<71::AID-MRM1011>3.0.CO;2-2`.

[Gelman et al., 1999] Gelman, N., Gorell, J. M., Barker, P. B., Savage, R. M., Spickler, E. M., Windham, J. P., and Knight, R. A. (1999). MR Imaging of Human Brain at 3.0 T: Preliminary Report on Transverse Relaxation Rates and Relation to Estimated Iron Content. *Radiology*, 210(3):759–767. `http://pubs.rsna.org/doi/10.1148/radiology.210.3.r99fe41759`.

[Geremia et al., 2011] Geremia, E., Clatz, O., Menze, B. H., Konukoglu, E., Criminisi, A., and Ayache, N. (2011). Spatial decision forests for MS lesion segmentation in multi-channel magnetic resonance images. *NeuroIm-*

age, 57(2):378–390. `https://linkinghub.elsevier.com/retrieve/pii/S1053811911003740`.

[Geurts et al., 2005] Geurts, J. J. G., Bo, L., Pouwels, P. J. W., Castelijns, J. A., Polman, C. H., and Barkhof, F. (2005). Cortical Lesions in Multiple Sclerosis: Combined Postmortem MR Imaging and Histopathology. *AJNR. American Journal of Neuroradiology*, 26(3):572–577.

[Ghadery et al., 2015] Ghadery, C., Pirpamer, L., Hofer, E., Langkammer, C., Petrovic, K., Loitfelder, M., Schwingenschuh, P., Seiler, S., Duering, M., Jouvent, E., Schmidt, H., Fazekas, F., Mangin, J.-F., Chabriat, H., Dichgans, M., Ropele, S., and Schmidt, R. (2015). R2* mapping for brain iron: associations with cognition in normal aging. *Neurobiology of Aging*, 36(2):925–932. `https://linkinghub.elsevier.com/retrieve/pii/S0197458014006186`.

[Glover, 2011] Glover, G. H. (2011). Overview of Functional Magnetic Resonance Imaging. *Neurosurgery Clinics of North America*, 22(2):133–139. `https://linkinghub.elsevier.com/retrieve/pii/S1042368010001129`.

[Goldenberg, 2012] Goldenberg, M. M. (2012). Multiple Sclerosis Review. *Pharmacy and Therapeutics*, 37(3):175–184.

[Good et al., 2001] Good, C. D., Johnsrude, I. S., Ashburner, J., Henson, R. N., Friston, K. J., and Frackowiak, R. S. (2001). A Voxel-Based Morphometric Study of Ageing in 465 Normal Adult Human Brains. *NeuroImage*, 14(1):21–36. `https://linkinghub.elsevier.com/retrieve/pii/S1053811901907864`.

[Gracien et al., 2016a] Gracien, R.-M., Jurcoane, A., Wagner, M., Reitz, S. C., Mayer, C., Volz, S., Hof, S.-M., Fleischer, V., Droby, A., Steinmetz, H., Groppa, S., Hattingen, E., Deichmann, R., and Klein, J. C. (2016a). Multimodal quantitative MRI assessment of cortical damage in relapsing-remitting multiple sclerosis: Cortical Quantitative MRI in RRMS. *Journal of Magnetic Resonance Imaging*, 44(6):1600–1607. `https://onlinelibrary.wiley.com/doi/10.1002/jmri.25297`.

[Gracien et al., 2020] Gracien, R.-M., Maiworm, M., Brüche, N., Shrestha, M., Nöth, U., Hattingen, E., Wagner, M., and Deichmann, R. (2020). How stable is quantitative MRI? – Assessment of intra- and inter-scanner-model reproducibility using identical acquisition sequences and data analysis programs. *NeuroImage*, 207. `https://linkinghub.elsevier.com/retrieve/pii/S1053811919309553`.

[Gracien et al., 2017a] Gracien, R.-M., Nürnberger, L., Hok, P., Hof, S.-M., Reitz, S. C., Rüb, U., Steinmetz, H., Hilker-Roggendorf, R., Klein, J. C., Deichmann, R., and Baudrexel, S. (2017a). Evaluation of brain ageing: a quantitative longitudinal MRI study over 7 years. *European Radiology*, 27(4):1568–1576. `http://link.springer.com/10.1007/s00330-016-4485-1`.

[Gracien et al., 2017b] Gracien, R.-M., Reitz, S. C., Hof, S.-M., Fleischer, V., Droby, A., Wahl, M., Steinmetz, H., Groppa, S., Deichmann, R., and Klein, J. C. (2017b). Longitudinal quantitative MRI assessment of cortical damage in multiple sclerosis: A pilot study: Longitudinal Cortical qMRI in MS. *Journal of Magnetic Resonance Imaging*, 46(5):1485–1490. `https://onlinelibrary.wiley.com/doi/10.1002/jmri.25685`.

[Gracien et al., 2016b] Gracien, R.-M., Reitz, S. C., Hof, S.-M., Fleischer, V., Zimmermann, H., Droby, A., Steinmetz, H., Zipp, F., Deichmann, R., and Klein, J. C. (2016b). Assessment of cortical damage in early multiple sclerosis with quantitative T2 relaxometry: Cortical T2 in Early Multiple Sclerosis. *NMR in Biomedicine*, 29(4):444–450. `https://onlinelibrary.wiley.com/doi/10.1002/nbm.3486`.

[Granberg et al., 2017] Granberg, T., Fan, Q., Treaba, C. A., Ouellette, R., Herranz, E., Mangeat, G., Louapre, C., Cohen-Adad, J., Klawiter, E. C., Sloane, J. A., and Mainero, C. (2017). In vivo characterization of cortical and white matter neuroaxonal pathology in early multiple sclerosis. *Brain*, 140(11):2912–2926. `https://academic.oup.com/brain/article/140/11/2912/4430801`.

[Granziera et al., 2021] Granziera, C., Wuerfel, J., Barkhof, F., Calabrese, M., De Stefano, N., Enzinger, C., Evangelou, N., Filippi, M., Geurts, J. J. G., Reich, D. S., Rocca, M. A., Ropele, S., Rovira, A., Sati, P., Toosy, A. T., Vrenken, H., Gandini Wheeler-Kingshott, C. A. M., Kappos, L., and the MAGNIMS Study Group (2021). Quantitative magnetic resonance imaging towards clinical application in multiple sclerosis. *Brain*, 144(5):1296–1311. `https://academic.oup.com/brain/article/144/5/1296/6273092`.

[Grossman et al., 1986] Grossman, R. I., Gonzalez-Scarano, F., Atlas, S. W., Galetta, S., and Silberberg, D. H. (1986). Multiple sclerosis: Gadolinium enhancement in MR Imaging. *Radiology*, 161(3):721–725. `https://pubmed.ncbi.nlm.nih.gov/3786722/`.

[Grussu et al., 2017] Grussu, F., Schneider, T., Tur, C., Yates, R. L., Tachrount, M., Ianuş, A., Yiannakas, M. C., Newcombe, J., Zhang, H., Alexander, D. C., DeLuca, G. C., and Gandini Wheeler-Kingshott, C. A. M.

(2017). Neurite dispersion: a new marker of multiple sclerosis spinal cord pathology? *Annals of Clinical and Translational Neurology*, 4(9):663–679. `https://onlinelibrary.wiley.com/doi/10.1002/acn3.445`.

[Guerrero et al., 2019] Guerrero, J. M., Adluru, N., Bendlin, B. B., Goldsmith, H. H., Schaefer, S. M., Davidson, R. J., Kecskemeti, S. R., Zhang, H., and Alexander, A. L. (2019). Optimizing the intrinsic parallel diffusivity in NODDI: An extensive empirical evaluation. *PLOS ONE*, 14(9):e0217118. `https://dx.plos.org/10.1371/journal.pone.0217118`.

[Guillemin et al., 2022] Guillemin, C., Lommers, E., Delrue, G., Gester, E., Maquet, P., and Collette, F. (2022). The Complex Interplay Between Trait Fatigue and Cognition in Multiple Sclerosis. *Psychologica Belgica*, 62(1):108. `https://www.psychologicabelgica.com/article/10.5334/pb.1125/`.

[Gyger et al., 2021] Gyger, L., Ramponi, C., Mall, J., Swierkosz-Lenart, K., Stoyanov, D., Lutti, A., von Gunten, A., Kherif, F., and Draganski, B. (2021). Temporal trajectory of brain tissue property changes induced by electroconvulsive therapy. *NeuroImage*, 232. `https://linkinghub.elsevier.com/retrieve/pii/S1053811921001725`.

[Haacke et al., 2005] Haacke, E. M., Cheng, N. Y., House, M. J., Liu, Q., Neelavalli, J., Ogg, R. J., Khan, A., Ayaz, M., Kirsch, W., and Obenaus, A. (2005). Imaging iron stores in the brain using magnetic resonance imaging. *Magnetic Resonance Imaging*, 23(1):1–25. `https://linkinghub.elsevier.com/retrieve/pii/S0730725X04002905`.

[Haacke et al., 2010] Haacke, E. M., Miao, Y., Liu, M., Habib, C. A., Katkuri, Y., Liu, T., Yang, Z., Lang, Z., Hu, J., and Wu, J. (2010). Correlation of putative iron content as represented by changes in R2* and phase with age in deep gray matter of healthy adults. *Journal of Magnetic Resonance Imaging*, 32(3):561–576. `https://onlinelibrary.wiley.com/doi/10.1002/jmri.22293`.

[Hagiwara et al., 2019] Hagiwara, A., Kamagata, K., Shimoji, K., Yokoyama, K., Andica, C., Hori, M., Fujita, S., Maekawa, T., Irie, R., Akashi, T., Wada, A., Suzuki, M., Abe, O., Hattori, N., and Aoki, S. (2019). White Matter Abnormalities in Multiple Sclerosis Evaluated by Quantitative Synthetic MRI, Diffusion Tensor Imaging, and Neurite Orientation Dispersion and Density Imaging. *American Journal of Neuroradiology*, 40(10):1642–1648. `http://www.ajnr.org/lookup/doi/10.3174/ajnr.A6209`.

[Haider et al., 2014] Haider, L., Simeonidou, C., Steinberger, G., Hametner, S., Grigoriadis, N., Deretzi, G., Kovacs, G. G., Kutzelnigg, A., Lassmann, H., and Frischer, J. M. (2014). Multiple sclerosis deep grey matter: the relation between demyelination, neurodegeneration, inflammation and iron. *Journal of Neurology, Neurosurgery & Psychiatry*, 85(12):1386–1395. `https://jnnp.bmj.com/lookup/doi/10.1136/jnnp-2014-307712`.

[Haider et al., 2016] Haider, L., Zrzavy, T., Hametner, S., Höftberger, R., Bagnato, F., Grabner, G., Trattnig, S., Pfeifenbring, S., Brück, W., and Lassmann, H. (2016). The topograpy of demyelination and neurodegeneration in the multiple sclerosis brain. *Brain*, 139(3):807–815. `https://academic.oup.com/brain/article-lookup/doi/10.1093/brain/awv398`.

[Hallgren and Sourander, 1958] Hallgren, B. and Sourander, P. (1958). The effect of age on the non-haemin iron in the human brain. *Journal of Neurochemistry*, 3(1):41–51. `https://onlinelibrary.wiley.com/doi/10.1111/j.1471-4159.1958.tb12607.x`.

[Hametner et al., 2018] Hametner, S., Endmayr, V., Deistung, A., Palmrich, P., Prihoda, M., Haimburger, E., Menard, C., Feng, X., Haider, T., Leisser, M., Köck, U., Kaider, A., Höftberger, R., Robinson, S., Reichenbach, J. R., Lassmann, H., Traxler, H., Trattnig, S., and Grabner, G. (2018). The influence of brain iron and myelin on magnetic susceptibility and effective transverse relaxation - A biochemical and histological validation study. *NeuroImage*, 179:117–133. `https://linkinghub.elsevier.com/retrieve/pii/S1053811918305147`.

[Hametner et al., 2013] Hametner, S., Wimmer, I., Haider, L., Pfeifenbring, S., Brück, W., and Lassmann, H. (2013). Iron and neurodegeneration in the multiple sclerosis brain. *Annals of Neurology*, 74(6):848–861. `https://onlinelibrary.wiley.com/doi/10.1002/ana.23974`.

[Hauser and Goodin, 2017] Hauser, S. L. and Goodin, D. S. (2017). Multiple sclerosis and other demyelinating diseases. In Hauser, S. L. and Josephson, S. A., editors, *Harrison's Neurology in Clinical Medicine, 4e*. McGraw-Hill Education, New York, NY. `neurology.mhmedical.com/content.aspx?aid=1145770333`.

[Hayton et al., 2009] Hayton, T., Furby, J., Smith, K. J., Altmann, D. R., Brenner, R., Chataway, J., Hughes, R. A. C., Hunter, K., Tozer, D. J., Miller, D. H., and Kapoor, R. (2009). Grey matter magnetization transfer ratio independently correlates with neurological deficit in secondary progressive multiple sclerosis. *Journal of Neurology*, 256(3):427–435. `http://link.springer.com/10.1007/s00415-009-0110-4`.

[Hayton et al., 2012] Hayton, T., Furby, J., Smith, K. J., Altmann, D. R., Brenner, R., Chataway, J., Hunter, K., Tozer, D. J., Miller, D. H., and Kapoor, R. (2012). Longitudinal changes in magnetisation transfer ratio in secondary progressive multiple sclerosis: data from a randomised placebo controlled trial of lamotrigine. *Journal of Neurology*, 259(3):505–514. `http://link.springer.com/10.1007/s00415-011-6212-9`.

[Helms et al., 2008a] Helms, G., Dathe, H., and Dechent, P. (2008a). Quantitative FLASH MRI at 3T using a rational approximation of the Ernst equation: Rational Approximation of the FLASH Signal. *Magnetic Resonance in Medicine*, 59(3):667–672. `https://onlinelibrary.wiley.com/doi/10.1002/mrm.21542`.

[Helms et al., 2008b] Helms, G., Dathe, H., Kallenberg, K., and Dechent, P. (2008b). High-resolution maps of magnetization transfer with inherent correction for RF inhomogeneity and T1 relaxation obtained from 3D FLASH MRI: Saturation and Relaxation in MT FLASH. *Magnetic Resonance in Medicine*, 60(6):1396–1407. `https://onlinelibrary.wiley.com/doi/10.1002/mrm.21732`.

[Helms et al., 2009] Helms, G., Draganski, B., Frackowiak, R., Ashburner, J., and Weiskopf, N. (2009). Improved segmentation of deep brain grey matter structures using magnetization transfer (MT) parameter maps. *NeuroImage*, 47(1):194–198. `https://linkinghub.elsevier.com/retrieve/pii/S105381190900295X`.

[Helms and Hagberg, 2009] Helms, G. and Hagberg, G. E. (2009). *In vivo* quantification of the bound pool T1 in human white matter using the binary spin–bath model of progressive magnetization transfer saturation. *Physics in Medicine and Biology*, 54(23):529–540. `https://iopscience.iop.org/article/10.1088/0031-9155/54/23/N01`.

[Henkelman et al., 2001] Henkelman, R. M., Stanisz, G. J., and Graham, S. J. (2001). Magnetization transfer in MRI: a review. *NMR in Biomedicine*, 14(2):57–64. `https://onlinelibrary.wiley.com/doi/10.1002/nbm.683`.

[Hernández-Torres et al., 2019] Hernández-Torres, E., Wiggermann, V., Machan, L., Sadovnick, A. D., Li, D. K. B., Traboulsee, A., Hametner, S., and Rauscher, A. (2019). Increased mean R2* in the deep gray matter of multiple sclerosis patients: Have we been measuring atrophy ? *Journal of magnetic resonance imaging : JMRI*, 50(1):201–208. `https://doi.org/10.1002/jmri.26561`.

[Hochmeister et al., 2006] Hochmeister, S., Grundtner, R., Bauer, J., Engelhardt, B., Lyck, R., Gordon, G., Korosec, T., Kutzelnigg, A., Berger, J. J., Bradl, M., Bittner, R. E., and Lassmann, H. (2006). Dysferlin Is a New Marker for Leaky Brain Blood Vessels in Multiple Sclerosis:. *Journal of Neuropathology and Experimental Neurology*, 65(9):855–865. `https://academic.oup.com/jnen/article-lookup/doi/10.1097/01.jnen.0000235119.52311.16`.

[Holland et al., 1986] Holland, B. A., Haas, D. K., Norman, D., Brant-Zawadzki, M., and Newton, T. H. (1986). MRI of normal brain maturation. *AJNR. American Journal of Neuroradiology*, 7(2):201–8.

[Horch et al., 2011] Horch, R. A., Gore, J. C., and Does, M. D. (2011). Origins of the ultrashort-T2 ^1H NMR signals in myelinated nerve: A direct measure of myelin content? *Magnetic Resonance in Medicine*, 66(1):24–31. `https://onlinelibrary.wiley.com/doi/10.1002/mrm.22980`.

[Horsfield and Jones, 2002] Horsfield, M. A. and Jones, D. K. (2002). Applications of diffusion-weighted and diffusion tensor MRI to white matter diseases - a review. *NMR in Biomedicine*, 15(7-8):570–577. `https://onlinelibrary.wiley.com/doi/10.1002/nbm.787`.

[Hutton et al., 2009] Hutton, C., Draganski, B., Ashburner, J., and Weiskopf, N. (2009). A comparison between voxel-based cortical thickness and voxel-based morphometry in normal aging. *NeuroImage*, 48(2):371–380. `https://linkinghub.elsevier.com/retrieve/pii/S105381190900679X`.

[Iannucci et al., 2001] Iannucci, G., Rovaris, M., Giacomotti, L., Comi, G., and Filippi, M. (2001). Correlation of Multiple Sclerosis Measures Derived from T2-Weighted, T1-Weighted, Magnetization Transfer, and Diffusion Tensor MR Imaging. *AJNR. American Journal of Neuroradiology*, 22(8):1462–1467.

[Jonkman et al., 2015] Jonkman, L., Klaver, R., Fleysher, L., Inglese, M., and Geurts, J. (2015). Ultra-High-Field MRI Visualization of Cortical Multiple Sclerosis Lesions with T2 and T2*: A Postmortem MRI and Histopathology Study. *American Journal of Neuroradiology*, 36(11):2062–2067. `http://www.ajnr.org/lookup/doi/10.3174/ajnr.A4418`.

[Judaš and Cepanec, 2010] Judaš, M. and Cepanec, M. (2010). Oskar Vogt: The first myeloarchitectonic map of the human frontal cortex. *Translational Neuroscience*, 1(1):72–94. `https://www.degruyter.com/document/doi/10.2478/v10134-010-0005-z/html`.

[Kamagata et al., 2016] Kamagata, K., Hatano, T., Okuzumi, A., Motoi, Y., Abe, O., Shimoji, K., Kamiya, K., Suzuki, M., Hori, M., Kumamaru, K. K., Hattori, N., and Aoki, S. (2016). Neurite orientation dispersion and density imaging in the substantia nigra in idiopathic Parkinson disease. *European Radiology*, 26(8):2567–2577. `http://link.springer.com/10.1007/s00330-015-4066-8`.

[Kamiya et al., 2020] Kamiya, K., Hori, M., and Aoki, S. (2020). NODDI in clinical research. *Journal of Neuroscience Methods*, 346. `https://linkinghub.elsevier.com/retrieve/pii/S0165027020303319`.

[Karakuzu et al., 2022] Karakuzu, A., Appelhoff, S., Auer, T., Boudreau, M., Feingold, F., Khan, A. R., Lazari, A., Markiewicz, C., Mulder, M., Phillips, C., Salo, T., Stikov, N., Whitaker, K., and de Hollander, G. (2022). qMRI-BIDS: An extension to the brain imaging data structure for quantitative magnetic resonance imaging data. *Scientific Data*, 9(1):517. `https://www.nature.com/articles/s41597-022-01571-4`.

[Karamat et al., 2016] Karamat, M. I., Darvish-Molla, S., and Santos-Diaz, A. (2016). Opportunities and Challenges of 7 Tesla Magnetic Resonance Imaging: A Review. *Critical Reviews in Biomedical Engineering*, 44(1-02):73–89. `http://www.dl.begellhouse.com/journals/4b27cbfc562e21b8,73da10e30f69cc45,0ced7af235c9e0bc.html`.

[Kearney et al., 2015] Kearney, H., Altmann, D. R., Samson, R. S., Yiannakas, M. C., Wheeler-Kingshott, C. A. M., Ciccarelli, O., and Miller, D. H. (2015). Cervical cord lesion load is associated with disability independently from atrophy in MS. *Neurology*, 84(4):367–373. `https://www.neurology.org/lookup/doi/10.1212/WNL.0000000000001186`.

[Kermode et al., 1990] Kermode, A. G., Tofts, P. S., Thompson, A. J., MacManus, D. G., Rudge, P., Kendall, B. E., Kingsley, D., Moseley, I. F., Boulay, E. d., and McDonald, W. I. (1990). Heterogeneity of blood-brain barrier changes in multiple sclerosis: An MRI study with gadolinium-DTPA enhancement. *Neurology*, 40(2):229–229. `https://www.neurology.org/lookup/doi/10.1212/WNL.40.2.229`.

[Khalil et al., 2009] Khalil, M., Enzinger, C., Langkammer, C., Tscherner, M., Wallner-Blazek, M., Jehna, M., Ropele, S., Fuchs, S., and Fazekas, F. (2009). Quantitative assessment of brain iron by R2* relaxometry in patients with clinically isolated syndrome and relapsing–remitting multiple sclerosis. *Multiple Sclerosis Journal*, 15(9):1048–1054. `http://journals.sagepub.com/doi/10.1177/1352458509106609`.

[Khalil et al., 2015] Khalil, M., Langkammer, C., Pichler, A., Pinter, D., Gattringer, T., Bachmaier, G., Ropele, S., Fuchs, S., Enzinger, C., and Fazekas, F. (2015). Dynamics of brain iron levels in multiple sclerosis: A longitudinal 3T MRI study. *Neurology*, 84(24):2396–2402. `https://www.neurology.org/lookup/doi/10.1212/WNL.0000000000001679`.

[Khalil et al., 2011] Khalil, M., Langkammer, C., Ropele, S., Petrovic, K., Wallner-Blazek, M., Loitfelder, M., Jehna, M., Bachmaier, G., Schmidt, R., Enzinger, C., Fuchs, S., and Fazekas, F. (2011). Determinants of brain iron in multiple sclerosis: A quantitative 3T MRI study. *Neurology*, 77(18):1691–1697. `https://www.neurology.org/lookup/doi/10.1212/WNL.0b013e318236ef0e`.

[Koenig et al., 1993] Koenig, S. H., Brown, R. D., and Ugolini, R. (1993). A unified view of relaxation in protein solutions and tissue, including hydration and magnetization transfer. *Magnetic Resonance in Medicine*, 29(1):77–83. `https://onlinelibrary.wiley.com/doi/10.1002/mrm.1910290114`.

[Kolb et al., 2021] Kolb, H., Absinta, M., Beck, E. S., Ha, S., Song, Y., Norato, G., Cortese, I., Sati, P., Nair, G., and Reich, D. S. (2021). 7T MRI differentiates remyelinated from demyelinated multiple sclerosis lesions. *Annals of Neurology*, 90(4):612–626. `https://onlinelibrary.wiley.com/doi/10.1002/ana.26194`.

[Kraff et al., 2015] Kraff, O., Fischer, A., Nagel, A. M., Mönninghoff, C., and Ladd, M. E. (2015). MRI at 7 Tesla and above: Demonstrated and potential capabilities: Capabilities of MRI at 7T and Above. *Journal of Magnetic Resonance Imaging*, 41(1):13–33. `https://onlinelibrary.wiley.com/doi/10.1002/jmri.24573`.

[Kroon et al., 2008] Kroon, D.-j., van Oort, E., and Slump, K. (2008). Multiple Sclerosis Detection in Multispectral Magnetic Resonance Images with Principal Components Analysis. *The MIDAS Journal*, page MICCAI 2008. `https://www.midasjournal.org/browse/publication/604`.

[Kuhlmann et al., 2017] Kuhlmann, T., Ludwin, S., Prat, A., Antel, J., Brück, W., and Lassmann, H. (2017). An updated histological classification system for multiple sclerosis lesions. *Acta Neuropathologica*, 133(1):13–24. `http://link.springer.com/10.1007/s00401-016-1653-y`.

[Kurtzke, 1983] Kurtzke, J. F. (1983). Rating neurologic impairment in multiple sclerosis: An expanded disability status scale (EDSS). *Neurology*, 33(11):1444–1452. `https://www.neurology.org/lookup/doi/10.1212/WNL.33.11.1444`.

[Kutzelnigg et al., 2005] Kutzelnigg, A., Lucchinetti, C. F., Stadelmann, C., Brück, W., Rauschka, H., Bergmann, M., Schmidbauer, M., Parisi, J. E., and Lassmann, H. (2005). Cortical demyelination and diffuse white matter injury in multiple sclerosis. *Brain*, 128(11):2705–2712. `http://academic.oup.com/brain/article/128/11/2705/339613/Cortical-demyelination-and-diffuse-white-matter`.

[La Rosa et al., 2020] La Rosa, F., Abdulkadir, A., Fartaria, M. J., Rahmanzadeh, R., Lu, P.-J., Galbusera, R., Barakovic, M., Thiran, J.-P., Granziera, C., and Cuadra, M. B. (2020). Multiple sclerosis cortical and WM lesion segmentation at 3T MRI: a deep learning method based on FLAIR and MP2RAGE. *NeuroImage: Clinical*, 27:102335. `https://linkinghub.elsevier.com/retrieve/pii/S2213158220301728`.

[Langkammer et al., 2010] Langkammer, C., Krebs, N., Goessler, W., Scheurer, E., Ebner, F., Yen, K., Fazekas, F., and Ropele, S. (2010). Quantitative MR Imaging of Brain Iron: A Postmortem Validation Study. *Radiology*, 257(2):455–462. `http://pubs.rsna.org/doi/10.1148/radiol.10100495`.

[Lassmann, 2013] Lassmann, H. (2013). Pathology and disease mechanisms in different stages of multiple sclerosis. *Journal of the Neurological Sciences*, 333(1-2):1–4. `https://linkinghub.elsevier.com/retrieve/pii/S0022510X13002177`.

[Lassmann et al., 2001] Lassmann, H., Brück, W., and Lucchinetti, C. (2001). Heterogeneity of multiple sclerosis pathogenesis: implications for diagnosis and therapy. *Trends in Molecular Medicine*, 7(3):115–121. `https://linkinghub.elsevier.com/retrieve/pii/S1471491400019092`.

[Lassmann et al., 2007] Lassmann, H., Brück, W., and Lucchinetti, C. F. (2007). The Immunopathology of Multiple Sclerosis: An Overview. *Brain Pathology*, 17(2):210–218. `https://onlinelibrary.wiley.com/doi/10.1111/j.1750-3639.2007.00064.x`.

[Lassmann et al., 2012] Lassmann, H., van Horssen, J., and Mahad, D. (2012). Progressive multiple sclerosis: pathology and pathogenesis. *Nature Reviews Neurology*, 8(11):647–656. `https://www.nature.com/articles/nrneurol.2012.168`.

[Laule et al., 2006] Laule, C., Leung, E., Li, D. K., Traboulsee, A. L., Paty, D. W., MacKay, A. L., and Moore, G. R. (2006). Myelin water imaging in multiple sclerosis: quantitative correlations with histopathology. *Multiple*

Sclerosis Journal, 12(6):747–753. `http://journals.sagepub.com/doi/10.1177/1352458506070928`.

[Laule et al., 2004] Laule, C., Vavasour, I. M., Moore, G. R. W., Oger, J., Li, D. K. B., Paty, D. W., and MacKay, A. L. (2004). Water content and myelin water fraction in multiple sclerosis. *Journal of Neurology*, 251(3):284–293. `http://link.springer.com/10.1007/s00415-004-0306-6`.

[Laule et al., 2003] Laule, C., Vavasour, I. M., Whittall, K. P., Oger, J., Paty, D. W., Li, D. K. B., MacKay, A. L., and Arnold, D. L. (2003). Evolution of focal and diffusemagnetisation transfer abnormalitiesin multiple sclerosis. *Journal of Neurology*, 250(8):924–931. `http://link.springer.com/10.1007/s00415-003-1115-z`.

[Lavrova et al., 2021] Lavrova, E., Lommers, E., Woodruff, H. C., Chatterjee, A., Maquet, P., Salmon, E., Lambin, P., and Phillips, C. (2021). Exploratory Radiomic Analysis of Conventional vs. Quantitative Brain MRI: Toward Automatic Diagnosis of Early Multiple Sclerosis. *Frontiers in Neuroscience*, 15. `https://www.frontiersin.org/articles/10.3389/fnins.2021.679941/full`.

[Lee et al., 1999] Lee, M. A., Smith, S., Palace, J., Narayanan, S., Silver, N., Minicucci, L., Filippi, M., Miller, D. H., Arnold, D. L., and Matthews, P. M. (1999). Spatial mapping of T2 and gadolinium-enhancing T1 lesion volumes in multiple sclerosis: evidence for distinct mechanisms of lesion genesis? *Brain*, 122(7):1261–1270. `https://academic.oup.com/brain/article-lookup/doi/10.1093/brain/122.7.1261`.

[Lehéricy et al., 2012] Lehéricy, S., Sharman, M. A., Santos, C. L. D., Paquin, R., and Gallea, C. (2012). Magnetic resonance imaging of the substantia nigra in Parkinson's disease. *Movement Disorders*, 27(7):822–830. `https://onlinelibrary.wiley.com/doi/10.1002/mds.25015`.

[Lema et al., 2017] Lema, A., Bishop, C., Malik, O., Mattoscio, M., Ali, R., Nicholas, R., Muraro, P. A., Matthews, P. M., Waldman, A. D., and Newbould, R. D. (2017). A Comparison of Magnetization Transfer Methods to Assess Brain and Cervical Cord Microstructure in Multiple Sclerosis: MT of Brain and c-Spine in MS. *Journal of Neuroimaging*, 27(2):221–226. `https://onlinelibrary.wiley.com/doi/10.1111/jon.12377`.

[Leutritz et al., 2020] Leutritz, T., Seif, M., Helms, G., Samson, R. S., Curt, A., Freund, P., and Weiskopf, N. (2020). Multiparameter mapping of relaxation (R1 , <span

style="font-variant:small-caps;">R2 *), proton density and magnetization transfer saturation at 3 T : A multicenter dual`[U+2010]`vendor reproducibility and repeatability study. *Human Brain Mapping*, 41(15):4232–4247. `https://onlinelibrary.wiley.com/doi/10.1002/hbm.25122`.

[Levesque et al., 2010] Levesque, I. R., Giacomini, P. S., Narayanan, S., Ribeiro, L. T., Sled, J. G., Arnold, D. L., and Pike, G. B. (2010). Quantitative magnetization transfer and myelin water imaging of the evolution of acute multiple sclerosis lesions: Quantitative MT and T2 in Acute MS Lesions. *Magnetic Resonance in Medicine*, 63(3):633–640. `https://onlinelibrary.wiley.com/doi/10.1002/mrm.22244`.

[Lieury et al., 2014] Lieury, A., Chanal, M., Androdias, G., Reynolds, R., Cavagna, S., Giraudon, P., Confavreux, C., and Nataf, S. (2014). Tissue remodeling in periplaque regions of multiple sclerosis spinal cord lesions: Glia Remodeling in MS Spinal Cord. *Glia*, 62(10):1645–1658. `https://onlinelibrary.wiley.com/doi/10.1002/glia.22705`.

[Logothetis, 2003] Logothetis, N. K. (2003). The Underpinnings of the BOLD Functional Magnetic Resonance Imaging Signal. *The Journal of Neuroscience*, 23(10):3963–3971. `https://www.jneurosci.org/lookup/doi/10.1523/JNEUROSCI.23-10-03963.2003`.

[Lommers, 2020] Lommers, E. (2020). *Multiparameter MRI quantification of microstructural brain alterations in multiple sclerosis.* PhD thesis, University of Liège - GIGA CRC in vivo imaging. `https://hdl.handle.net/2268/243683`.

[Lommers et al., 2020] Lommers, E., Guillemin, C., Reuter, G., Fouarge, E., Delrue, G., Collette, F., Degueldre, C., Balteau, E., Maquet, P., and Phillips, C. (2020). Voxel-based quantitative MRI reveals spatial patterns of grey matter alteration in multiple sclerosis. *Human Brain Mapping*, 42:1003–1012. `https://pubmed.ncbi.nlm.nih.gov/3082150/`.

[Lommers et al., 2019] Lommers, E., Simon, J., Reuter, G., Delrue, G., Dive, D., Degueldre, C., Balteau, E., Phillips, C., and Maquet, P. (2019). Multiparameter MRI quantification of microstructural tissue alterations in multiple sclerosis. *NeuroImage: Clinical*, 23. `https://linkinghub.elsevier.com/retrieve/pii/S2213158219302293`.

[Lorio et al., 2016] Lorio, S., Fresard, S., Adaszewski, S., Kherif, F., Chowdhury, R., Frackowiak, R. S., Ashburner, J., Helms, G., Weiskopf, N., Lutti, A., and Draganski, B. (2016). New tissue priors for improved automated classification of subcortical brain structures on MRI. *NeuroImage*, 130:157–166.

[Lorio et al., 2014] Lorio, S., Lutti, A., Kherif, F., Ruef, A., Dukart, J., Chowdhury, R., Frackowiak, R., Ashburner, J., Helms, G., Weiskopf, N., and Draganski, B. (2014). Disentangling in vivo the effects of iron content and atrophy on the ageing human brain. *NeuroImage*, 103:280–289. `https://linkinghub.elsevier.com/retrieve/pii/S1053811914007861`.

[Losseff et al., 1996] Losseff, N. A., Wang, L., Lai, H. M., Yoo, D. S., Gawne-Cain, M. L., McDonald, W. I., Miller, D. H., and Thompson, A. J. (1996). Progressive cerebral atrophy in multiple sclerosis A serial MRI study. *Brain*, 119(6):2009–2019. `https://academic.oup.com/brain/article-lookup/doi/10.1093/brain/119.6.2009`.

[Lu et al., 2021] Lu, P.-J., Barakovic, M., Weigel, M., Rahmanzadeh, R., Galbusera, R., Schiavi, S., Daducci, A., La Rosa, F., Bach Cuadra, M., Sandkühler, R., Kuhle, J., Kappos, L., Cattin, P., and Granziera, C. (2021). GAMER-MRI in Multiple Sclerosis Identifies the Diffusion-Based Microstructural Measures That Are Most Sensitive to Focal Damage: A Deep-Learning-Based Analysis and Clinico-Biological Validation. *Frontiers in Neuroscience*, 15:647535. `https://www.frontiersin.org/articles/10.3389/fnins.2021.647535/full`.

[Lubetzki et al., 2020] Lubetzki, C., Zalc, B., Williams, A., Stadelmann, C., and Stankoff, B. (2020). Remyelination in multiple sclerosis: from basic science to clinical translation. *The Lancet Neurology*, 19(8):678–688. `https://linkinghub.elsevier.com/retrieve/pii/S147444222030140X`.

[Lucchinetti et al., 2000] Lucchinetti, C., Bruck, W., Parisi, J., Scheithauer, B., Rodriguez, M., and Lassmann, H. (2000). Heterogeneity of multiple sclerosis lesions: Implications for the pathogenesis of demyelination. *Annals of Neurology*, 47(6):707–717. `https://onlinelibrary.wiley.com/doi/10.1002/1531-8249(200006)47:6<707::AID-ANA3>3.0.CO;2-Q`.

[Ludwin, 1980] Ludwin, S. K. (1980). Chronic demyelination inhibits remyelination in the central nervous system. an analysis of contributing factors. *Laboratory investigation; a journal of technical methods and pathology*, 43 (4):382–387. `https://pubmed.ncbi.nlm.nih.gov/7442125/`.

[Lukas et al., 2010] Lukas, C., Minneboo, A., de Groot, V., Moraal, B., Knol, D. L., Polman, C. H., Barkhof, F., and Vrenken, H. (2010). Early central atrophy rate predicts 5 year clinical outcome in multiple sclerosis. *Journal of*

Neurology, Neurosurgery & Psychiatry, 81(12):1351–1356. `https://jnnp.bmj.com/lookup/doi/10.1136/jnnp.2009.199968`.

[Lutti et al., 2014] Lutti, A., Dick, F., Sereno, M. I., and Weiskopf, N. (2014). Using high-resolution quantitative mapping of R1 as an index of cortical myelination. *NeuroImage*, 93:176–188. `https://linkinghub.elsevier.com/retrieve/pii/S1053811913006423`.

[Lutti et al., 2010] Lutti, A., Hutton, C., Finsterbusch, J., Helms, G., and Weiskopf, N. (2010). Optimization and validation of methods for mapping of the radiofrequency transmit field at 3T: Optimized RF Transmit Field Mapping at 3T. *Magnetic Resonance in Medicine*, 64(1):229–238. `https://onlinelibrary.wiley.com/doi/10.1002/mrm.22421`.

[Lutti et al., 2012] Lutti, A., Stadler, J., Josephs, O., Windischberger, C., Speck, O., Bernarding, J., Hutton, C., and Weiskopf, N. (2012). Robust and Fast Whole Brain Mapping of the RF Transmit Field B1 at 7T. *PLoS ONE*, 7(3):e32379. `https://dx.plos.org/10.1371/journal.pone.0032379`.

[Margoni et al., 2022] Margoni, M., Villani, U., Silvestri, E., Franciotta, S., Anglani, M. G., Causin, F., Rinaldi, F., Perini, P., Bertoldo, A., and Gallo, P. (2022). Quantification of normal-appearing white matter damage in early relapse-onset multiple sclerosis through neurite orientation dispersion and density imaging. *Multiple Sclerosis and Related Disorders*, 58:103396. `https://linkinghub.elsevier.com/retrieve/pii/S2211034821006635`.

[Markovic-Plese and McFarland, 2001] Markovic-Plese, S. and McFarland, H. F. (2001). Immunopathogenesis of the multiple sclerosis lesion. *Current Neurology and Neuroscience Reports*, 1(3):257–262. `http://link.springer.com/10.1007/s11910-001-0028-4`.

[McDonald et al., 2001] McDonald, W. I., Compston, A., Edan, G., Goodkin, D., Hartung, H.-P., Lublin, F. D., McFarland, H. F., Paty, D. W., Polman, C. H., Reingold, S. C., Sandberg-Wollheim, M., Sibley, W., Thompson, A., Van Den Noort, S., Weinshenker, B. Y., and Wolinsky, J. S. (2001). Recommended diagnostic criteria for multiple sclerosis: Guidelines from the international panel on the diagnosis of multiple sclerosis. *Annals of Neurology*, 50(1):121–127. `https://onlinelibrary.wiley.com/doi/10.1002/ana.1032`.

[McDonald et al., 1992] McDonald, W. I., Miller, D. H., and Barnes, D. (1992). The pathological evolution of multiple sclerosis. *Neuropathology and Applied Neurobiology*, 18(4):319–334. `https://onlinelibrary.wiley.com/doi/10.1111/j.1365-2990.1992.tb00794.x`.

[McFarquhar et al., 2016] McFarquhar, M., McKie, S., Emsley, R., Suckling, J., Elliott, R., and Williams, S. (2016). Multivariate and repeated measures (MRM): A new toolbox for dependent and multimodal group-level neuroimaging data. *NeuroImage*, 132:373–389. `https://linkinghub.elsevier.com/retrieve/pii/S1053811916001622`.

[Merluzzi et al., 2016] Merluzzi, A. P., Dean, D. C., Adluru, N., Suryawanshi, G. S., Okonkwo, O. C., Oh, J. M., Hermann, B. P., Sager, M. A., Asthana, S., Zhang, H., Johnson, S. C., Alexander, A. L., and Bendlin, B. B. (2016). Age-dependent differences in brain tissue microstructure assessed with neurite orientation dispersion and density imaging. *Neurobiology of Aging*, 43:79–88. `https://linkinghub.elsevier.com/retrieve/pii/S0197458016300173`.

[Mezer et al., 2013] Mezer, A., Yeatman, J. D., Stikov, N., Kay, K. N., Cho, N.-J., Dougherty, R. F., Perry, M. L., Parvizi, J., Hua, L. H., Butts-Pauly, K., and Wandell, B. A. (2013). Quantifying the local tissue volume and composition in individual brains with magnetic resonance imaging. *Nature Medicine*, 19(12):1667–1672. `http://www.nature.com/articles/nm.3390`.

[Miller, 2002] Miller, D. H. (2002). Measurement of atrophy in multiple sclerosis: pathological basis, methodological aspects and clinical relevance. *Brain*, 125(8):1676–1695. `https://academic.oup.com/brain/article-lookup/doi/10.1093/brain/awf177`.

[Miller et al., 1993] Miller, D. H., Barkhof, F., and Nauta, J. J. P. (1993). Gadolinium enhancement increases the sensitivity of MRI in detecting disease activity in multiple sclerosis. *Brain*, 116(5):1077–1094. `https://academic.oup.com/brain/article-lookup/doi/10.1093/brain/116.5.1077`.

[Mitchell et al., 2019] Mitchell, T., Archer, D. B., Chu, W. T., Coombes, S. A., Lai, S., Wilkes, B. J., McFarland, N. R., Okun, M. S., Black, M. L., Herschel, E., Simuni, T., Comella, C., Xie, T., Li, H., Parrish, T. B., Kurani, A. S., Corcos, D. M., and Vaillancourt, D. E. (2019). Neurite orientation dispersion and density imaging (NODDI) and free-water imaging in parkinsonism. *Human Brain Mapping*, 40(17):5094–5107. `https://onlinelibrary.wiley.com/doi/10.1002/hbm.24760`.

[Moll et al., 2011] Moll, N., Rietsch, A., Thomas, S., Ransohoff, A., Lee, J.-C., Fox, R., Chang, A., Ransohoff, R., and Fisher, E. (2011). Multiple sclerosis normal-appearing white matter: Pathology-imaging correlations. *Ann Neurol.*, 70:764–773. `https://doi.org/10.1002/ana.22521`.

[Moon et al., 2002] Moon, N., Bullitt, E., van Leemput, K., and Gerig, G. (2002). Automatic Brain and Tumor Segmentation. In Goos, G., Hartmanis, J., van Leeuwen, J., Dohi, T., and Kikinis, R., editors, *Medical Image Computing and Computer-Assisted Intervention — MICCAI 2002*, volume 2488, pages 372–379. Springer Berlin Heidelberg, Berlin, Heidelberg. `http://link.springer.com/10.1007/3-540-45786-0_46`.

[Neeb et al., 2006a] Neeb, H., Zilles, K., and Shah, N. (2006a). A new method for fast quantitative mapping of absolute water content in vivo. *NeuroImage*, 31(3):1156–1168. `https://linkinghub.elsevier.com/retrieve/pii/S1053811906000176`.

[Neeb et al., 2006b] Neeb, H., Zilles, K., and Shah, N. J. (2006b). Fully-automated detection of cerebral water content changes: Study of age- and gender-related H2O patterns with quantitative MRI. *NeuroImage*, 29(3):910–922. `https://linkinghub.elsevier.com/retrieve/pii/S105381190500594X`.

[Neema et al., 2007] Neema, M., Stankiewicz, J., Arora, A., Dandamudi, V. S., Batt, C. E., Guss, Z. D., Al-Sabbagh, A., and Bakshi, R. (2007). T1- and T2-Based MRI Measures of Diffuse Gray Matter and White Matter Damage in Patients with Multiple Sclerosis. *Journal of Neuroimaging*, 17:16–21. `https://onlinelibrary.wiley.com/doi/10.1111/j.1552-6569.2007.00131.x`.

[Paling et al., 2012] Paling, D., Tozer, D., Wheeler-Kingshott, C., Kapoor, R., Miller, D. H., and Golay, X. (2012). Reduced R2$'$ in multiple sclerosis normal appearing white matter and lesions may reflect decreased myelin and iron content. *Journal of Neurology, Neurosurgery & Psychiatry*, 83(8):785–792. `https://jnnp.bmj.com/lookup/doi/10.1136/jnnp-2012-302541`.

[Panagiotaki et al., 2012] Panagiotaki, E., Schneider, T., Siow, B., Hall, M. G., Lythgoe, M. F., and Alexander, D. C. (2012). Compartment models of the diffusion MR signal in brain white matter: A taxonomy and comparison. *NeuroImage*, 59(3):2241–2254. `https://linkinghub.elsevier.com/retrieve/pii/S1053811911011566`.

[Pandit, 2019] Pandit, L. (2019). No evidence of disease activity (NEDA) in multiple sclerosis - Shifting the goal posts. *Annals of Indian Academy of Neurology*, 22(3):261. `http://www.annalsofian.org/text.asp?2019/22/3/261/258087`.

[Parker et al., 2018] Parker, T. D., Slattery, C. F., Zhang, J., Nicholas, J. M., Paterson, R. W., Foulkes, A. J., Malone, I. B., Thomas, D. L., Modat, M., Cash, D. M., Crutch, S. J., Alexander, D. C., Ourselin, S., Fox, N. C., Zhang, H., and Schott, J. M. (2018). Cortical microstructure in young onset Alzheimer's disease using neurite orientation dispersion and density imaging.

Human Brain Mapping, 39(7):3005–3017. `https://onlinelibrary.wiley.com/doi/10.1002/hbm.24056`.

[Patrikios et al., 2006] Patrikios, P., Stadelmann, C., Kutzelnigg, A., Rauschka, H., Schmidbauer, M., Laursen, H., Sorensen, P. S., Bruck, W., Lucchinetti, C., and Lassmann, H. (2006). Remyelination is extensive in a subset of multiple sclerosis patients. *Brain*, 129(12):3165–3172. `https://academic.oup.com/brain/article-lookup/doi/10.1093/brain/awl217`.

[Phillips et al., 2017] Phillips, C., Lommers, E., and Pernet, C. (2017). Unifying lesion masking and tissue probability maps for improved segmentation and normalization. In *23rd Annual Meeting of the Organization for Human Brain Mapping (OHBM)*. OHBM.

[Pierpaoli, 2010] Pierpaoli, C. (2010). Quantitative Brain MRI. *Topics in Magnetic Resonance Imaging*, 21(2):63. `https://journals.lww.com/00002142-201004000-00001`.

[Pierpaoli and Basser, 1996] Pierpaoli, C. and Basser, P. J. (1996). Toward a quantitative assessment of diffusion anisotropy. *Magnetic Resonance in Medicine*, 36(6):893–906. `https://onlinelibrary.wiley.com/doi/10.1002/mrm.1910360612`.

[Polman et al., 2011] Polman, C. H., Reingold, S. C., Banwell, B., Clanet, M., Cohen, J. A., Filippi, M., Fujihara, K., Havrdova, E., Hutchinson, M., Kappos, L., Lublin, F. D., Montalban, X., O'Connor, P., Sandberg Wollheim, M., Thompson, A. J., Waubant, E., Weinshenker, B., and Wolinsky, J. S. (2011). Diagnostic criteria for multiple sclerosis: 2010 Revisions to the McDonald criteria. *Annals of Neurology*, 69(2):292–302. `https://onlinelibrary.wiley.com/doi/10.1002/ana.22366`.

[Polman et al., 2005] Polman, C. H., Reingold, S. C., Edan, G., Filippi, M., Hartung, H.-P., Kappos, L., Lublin, F. D., Metz, L. M., McFarland, H. F., O'Connor, P. W., Sandberg-Wollheim, M., Thompson, A. J., Weinshenker, B. G., and Wolinsky, J. S. (2005). Diagnostic criteria for multiple sclerosis: 2005 revisions to the "McDonald Criteria". *Annals of Neurology*, 58(6):840–846. `https://onlinelibrary.wiley.com/doi/10.1002/ana.20703`.

[Pontillo et al., 2021] Pontillo, G., Petracca, M., Monti, S., Quarantelli, M., Criscuolo, C., Lanzillo, R., Tedeschi, E., Elefante, A., Brescia Morra, V., Brunetti, A., Cocozza, S., and Palma, G. (2021). Unraveling Deep Gray Matter Atrophy and Iron and Myelin Changes in Multiple Sclerosis. *American Journal of Neuroradiology*, 42(7):1223–1230. `http://www.ajnr.org/lookup/doi/10.3174/ajnr.A7093`.

[Popescu et al., 2017] Popescu, B. F., Frischer, J. M., Webb, S. M., Tham, M., Adiele, R. C., Robinson, C. A., Fitz-Gibbon, P. D., Weigand, S. D., Metz, I., Nehzati, S., George, G. N., Pickering, I. J., Brück, W., Hametner, S., Lassmann, H., Parisi, J. E., Yong, G., and Lucchinetti, C. F. (2017). Pathogenic implications of distinct patterns of iron and zinc in chronic MS lesions. *Acta Neuropathologica*, 134(1):45–64. `http://link.springer.com/10.1007/s00401-017-1696-8`.

[Poser et al., 1983] Poser, C. M., Paty, D. W., Scheinberg, L., McDonald, W. I., Davis, F. A., Ebers, G. C., Johnson, K. P., Sibley, W. A., Silberberg, D. H., and Tourtellotte, W. W. (1983). New diagnostic criteria for multiple sclerosis: Guidelines for research protocols. *Annals of Neurology*, 13(3):227–231. `https://onlinelibrary.wiley.com/doi/10.1002/ana.410130302`.

[Prat and Antel, 2005] Prat, A. and Antel, J. (2005). Pathogenesis of multiple sclerosis. *Current opinion in neurology*, 18(3):225–230. `https://doi.org/10.1097/01.wco.0000169737.99040.31`.

[Preibisch and Deichmann, 2009] Preibisch, C. and Deichmann, R. (2009). Influence of RF spoiling on the stability and accuracy of T1 mapping based on spoiled FLASH with varying flip angles: Influence of RF Spoiling on T1 Mapping. *Magnetic Resonance in Medicine*, 61(1):125–135. `https://onlinelibrary.wiley.com/doi/10.1002/mrm.21776`.

[Preziosa et al., 2021] Preziosa, P., Pagani, E., Bonacchi, R., Cacciaguerra, L., Falini, A., Rocca, M. A., and Filippi, M. (2021). In vivo detection of damage in multiple sclerosis cortex and cortical lesions using NODDI. *Journal of Neurology, Neurosurgery & Psychiatry*, 93(6):628–636. `https://jnnp.bmj.com/lookup/doi/10.1136/jnnp-2021-327803`.

[Price, 2009] Price, S. E. (2009). Multiple sclerosis: diagnostic issues and modern management. *British and Irish Orthoptic Journal*, 6:5–14. `https://www.bioj-online.com/article/10.22599/bioj.2/`.

[Prince and Links, 2015] Prince, J. L. and Links, J. M. (2015). *Medical imaging signals and systems*. Pearson, Boston, 2nd edition.

[Prineas et al., 2001] Prineas, J. W., Kwon, E. E., Cho, E.-S., Sharer, L. R., Barnett, M. H., Oleszak, E. L., Hoffman, B., and Morgan, B. P. (2001). Immunopathology of secondary-progressive multiple sclerosis. *Annals of Neurology*, 50(5):646–657. `https://onlinelibrary.wiley.com/doi/10.1002/ana.1255`.

[Péran et al., 2009] Péran, P., Cherubini, A., Luccichenti, G., Hagberg, G., Démonet, J.-F., Rascol, O., Celsis, P., Caltagirone, C., Spalletta, G., and Sabatini, U. (2009). Volume and iron content in basal ganglia and thalamus. *Human Brain Mapping*, 30(8):2667–2675. `https://onlinelibrary.wiley.com/doi/10.1002/hbm.20698`.

[Rahmanzadeh et al., 2022] Rahmanzadeh, R., Galbusera, R., Lu, P., Bahn, E., Weigel, M., Barakovic, M., Franz, J., Nguyen, T. D., Spincemaille, P., Schiavi, S., Daducci, A., La Rosa, F., Absinta, M., Sati, P., Bach Cuadra, M., Radue, E., Leppert, D., Kuhle, J., Kappos, L., Brück, W., Reich, D. S., Stadelmann, C., Wang, Y., and Granziera, C. (2022). A New Advanced MRI Biomarker for Remyelinated Lesions in Multiple Sclerosis. *Annals of Neurology*, 92(3):486–502. `https://onlinelibrary.wiley.com/doi/10.1002/ana.26441`.

[Rahmanzadeh et al., 2021] Rahmanzadeh, R., Lu, P.-J., Barakovic, M., Weigel, M., Maggi, P., Nguyen, T. D., Schiavi, S., Daducci, A., La Rosa, F., Schaedelin, S., Absinta, M., Reich, D. S., Sati, P., Wang, Y., Bach Cuadra, M., Radue, E.-W., Kuhle, J., Kappos, L., and Granziera, C. (2021). Myelin and axon pathology in multiple sclerosis assessed by myelin water and multi-shell diffusion imaging. *Brain*, 144(6):1684–1696. `https://academic.oup.com/brain/article/144/6/1684/6164965`.

[Ramalho et al., 2017] Ramalho, M., Ramalho, J., Burke, L. M., and Semelka, R. C. (2017). Gadolinium Retention and Toxicity—An Update. *Advances in Chronic Kidney Disease*, 24(3):138–146. `https://linkinghub.elsevier.com/retrieve/pii/S1548559517300575`.

[Ramio-Torrenta, 2006] Ramio-Torrenta, L. (2006). Abnormalities in normal appearing tissues in early primary progressive multiple sclerosis and their relation to disability: a tissue specific magnetisation transfer study. *Journal of Neurology, Neurosurgery & Psychiatry*, 77(1):40–45. `https://jnnp.bmj.com/lookup/doi/10.1136/jnnp.2004.052316`.

[Ranjeva et al., 2005] Ranjeva, J.-P., Audoin, B., Confort-Gouny, S., Malikova, I., Soulier, E., Viout, P., Ali-Cherif, A., Pelletier, J., and Cozzone, P. (2005). Local Tissue Damage Assessed with Statistical Mapping Analysis of Brain Magnetization Transfer Ratio: Relationship with Functional Status of Patients in the Earliest Stage of Multiple Sclerosis. *AJNR. American journal of neuroradiology*, 26(1):119–127.

[Reich et al., 2018] Reich, D. S., Lucchinetti, C. F., and Calabresi, P. A. (2018). Multiple Sclerosis. *New England Journal of Medicine*, 378(2):169–180. `http://www.nejm.org/doi/10.1056/NEJMra1401483`.

[Reitz et al., 2017] Reitz, S. C., Hof, S.-M., Fleischer, V., Brodski, A., Gröger, A., Gracien, R.-M., Droby, A., Steinmetz, H., Ziemann, U., Zipp, F., Deichmann, R., and Klein, J. C. (2017). Multi-parametric quantitative MRI of normal appearing white matter in multiple sclerosis, and the effect of disease activity on T2. *Brain Imaging and Behavior*, 11(3):744–753. `http://link.springer.com/10.1007/s11682-016-9550-5`.

[Reuter et al., 2020] Reuter, G., Lommers, E., Balteau, E., Simon, J., Phillips, C., Scholtes, F., Martin, D., Lombard, A., and Maquet, P. (2020). Multiparameter quantitative histological MRI values in high-grade gliomas: a potential biomarker of tumor progression. *Neuro-Oncology Practice*, 7(6):646–655. `https://academic.oup.com/nop/article/7/6/646/5892958`.

[Rocca et al., 1999] Rocca, M. A., Mastronardo, G., Rodegher, M., Comi, G., and Filippi, M. (1999). Long-Term Changes of Magnetization Transfer-Derived Measures from Patients with Relapsing-Remitting and Secondary Progressive Multiple Sclerosis. *AJNR. American journal of neuroradiology*, 20(5):821–827.

[Rooney et al., 2007] Rooney, W. D., Johnson, G., Li, X., Cohen, E. R., Kim, S.-G., Ugurbil, K., and Springer, C. S. (2007). Magnetic field and tissue dependencies of human brain longitudinal ^1H_2O relaxation in vivo. *Magnetic Resonance in Medicine*, 57(2):308–318. `https://onlinelibrary.wiley.com/doi/10.1002/mrm.21122`.

[Ropele and Fazekas, 2009] Ropele, S. and Fazekas, F. (2009). Magnetization Transfer MR Imaging in Multiple Sclerosis. *Neuroimaging Clinics of North America*, 19(1):27–36. `https://linkinghub.elsevier.com/retrieve/pii/S1052514908000907`.

[Ropele et al., 2014] Ropele, S., Kilsdonk, I. D., Wattjes, M. P., Langkammer, C., de Graaf, W. L., Frederiksen, J. L., Larsson, H. B., Yiannakas, M., Wheeler-Kingshott, C. A., Enzinger, C., Khalil, M., Rocca, M. A., Sprenger, T., Amann, M., Kappos, L., Filippi, M., Rovira, A., Ciccarelli, O., Barkhof, F., and Fazekas, F. (2014). Determinants of iron accumulation in deep grey matter of multiple sclerosis patients. *Multiple Sclerosis Journal*, 20(13):1692–1698. `http://journals.sagepub.com/doi/10.1177/1352458514531085`.

[Rovaris et al., 2008] Rovaris, M., Judica, E., Sastre-Garriga, J., Rovira, A., Pia Sormani, M., Benedetti, B., Korteweg, T., De Stefano, N., Khaleeli, Z., Montalban, X., Barkhof, F., Miller, D. H., Polman, C., Thompson, A. J., and Filippi, M. (2008). Large-scale, multicentre, quantitative MRI study of brain and cord damage in primary progressive multiple sclerosis. *Multiple*

Sclerosis Journal, 14(4):455–464. `http://journals.sagepub.com/doi/10.1177/1352458507085129`.

[Rudick and Fisher, 1999] Rudick, R. A. and Fisher, E. (1999). Use of the brain parenchymal fraction to measure whole brain atrophy in relapsing-remitting MS. *Neurology*, 53(8):1698–1704. `https://doi.org/10.1212/wnl.53.8.1698`.

[Sacco et al., 2020] Sacco, S., Caverzasi, E., Papinutto, N., Cordano, C., Bischof, A., Gundel, T., Cheng, S., Asteggiano, C., Kirkish, G., Mallott, J., Stern, W., Bastianello, S., Bove, R., Gelfand, J., Goodin, D., Green, A., Waubant, E., Wilson, M., Zamvil, S., Cree, B., Hauser, S., Henry, R., and and University of California, San Francisco MS-EPIC Team (2020). Neurite Orientation Dispersion and Density Imaging for Assessing Acute Inflammation and Lesion Evolution in MS. *American Journal of Neuroradiology*, 41(12):2219–2226. `http://www.ajnr.org/lookup/doi/10.3174/ajnr.A6862`.

[Schiavi et al., 2020] Schiavi, S., Ocampo-Pineda, M., Barakovic, M., Petit, L., Descoteaux, M., Thiran, J.-P., and Daducci, A. (2020). A new method for accurate in vivo mapping of human brain connections using microstructural and anatomical information. *Science Advances*, 6(31):eaba8245. `https://www.science.org/doi/10.1126/sciadv.aba8245`.

[Schmidt et al., 2012] Schmidt, P., Gaser, C., Arsic, M., Buck, D., Förschler, A., Berthele, A., Hoshi, M., Ilg, R., Schmid, V. J., Zimmer, C., Hemmer, B., and Mühlau, M. (2012). An automated tool for detection of FLAIR-hyperintense white-matter lesions in Multiple Sclerosis. *NeuroImage*, 59(4):3774–3783. `https://linkinghub.elsevier.com/retrieve/pii/S1053811911013139`.

[Schmierer et al., 2004] Schmierer, K., Scaravilli, F., Altmann, D. R., Barker, G. J., and Miller, D. H. (2004). Magnetization transfer ratio and myelin in postmortem multiple sclerosis brain. *Annals of Neurology*, 56(3):407–415. `https://onlinelibrary.wiley.com/doi/10.1002/ana.20202`.

[Schmierer et al., 2008] Schmierer, K., Wheeler-Kingshott, C. A., Tozer, D. J., Boulby, P. A., Parkes, H. G., Yousry, T. A., Scaravilli, F., Barker, G. J., Tofts, P. S., and Miller, D. H. (2008). Quantitative magnetic resonance of postmortem multiple sclerosis brain before and after fixation. *Magnetic Resonance in Medicine*, 59(2):268–277. `https://onlinelibrary.wiley.com/doi/10.1002/mrm.21487`.

[Schneider et al., 2017] Schneider, T., Brownlee, W., Zhang, H., Ciccarelli, O., Miller, D. H., and Gandini Wheeler-Kingshott, C. (2017). Sensitivity of multi-shell NODDI to multiple sclerosis white matter changes: a pilot study. *Functional Neurology*, 32(2):97. `http://www.functionalneurology.com/common/php/portiere.php?ID=00671d05f0a17291bdd65f63575cb059`.

[Schumacher et al., 1965] Schumacher, G. A., Beebe, G., Kibler, R. F., Kurland, L. T., Kurtzke, J. F., McDowell, F., Nagler, B., Sibley, W. A., Tourtellotte, W. W., and Willmon, T. L. (1965). Problems of experimental trials of therapy in multiple sclerosis: Report by the panel on the evaluation of experimental trials of therapy in multiple sclerosis. *Annals of the New York Academy of Sciences*, 122(1):552–568. `https://onlinelibrary.wiley.com/doi/10.1111/j.1749-6632.1965.tb20235.x`.

[Seewann et al., 2012] Seewann, A., Kooi, E.-J., Roosendaal, S. D., Pouwels, P. J. W., Wattjes, M. P., van der Valk, P., Barkhof, F., Polman, C. H., and Geurts, J. J. G. (2012). Postmortem verification of MS cortical lesion detection with 3D DIR. *Neurology*, 78(5):302–308. `https://www.neurology.org/lookup/doi/10.1212/WNL.0b013e31824528a0`.

[Seghier et al., 2008] Seghier, M. L., Ramlackhansingh, A., Crinion, J., Leff, A. P., and Price, C. J. (2008). Lesion identification using unified segmentation-normalisation models and fuzzy clustering. *NeuroImage*, 41(4):1253–1266. `https://linkinghub.elsevier.com/retrieve/pii/S1053811908002553`.

[Sepulcre et al., 2009] Sepulcre, J., Goñi, J., Masdeu, J. C., Bejarano, B., Vélez de Mendizábal, N., Toledo, J. B., and Villoslada, P. (2009). Contribution of White Matter Lesions to Gray Matter Atrophy in Multiple Sclerosis: Evidence From Voxel-Based Analysis of T1 Lesions in the Visual Pathway. *Archives of Neurology*, 66(2):173–179. `http://archneur.jamanetwork.com/article.aspx?doi=10.1001/archneurol.2008.562`.

[Shah et al., 2008] Shah, N., Neeb, H., Kircheis, G., Engels, P., Häussinger, D., and Zilles, K. (2008). Quantitative cerebral water content mapping in hepatic encephalopathy. *NeuroImage*, 41(3):706–717. `https://linkinghub.elsevier.com/retrieve/pii/S1053811908001821`.

[Shiee et al., 2012] Shiee, N., Bazin, P.-L., Zackowski, K. M., Farrell, S. K., Harrison, D. M., Newsome, S. D., Ratchford, J. N., Caffo, B. S., Calabresi, P. A., Pham, D. L., and Reich, D. S. (2012). Revisiting Brain Atrophy and Its Relationship to Disability in Multiple Sclerosis. *PLoS ONE*, 7(5):e37049. `https://dx.plos.org/10.1371/journal.pone.0037049`.

[Shoeibi et al., 2021] Shoeibi, A., Khodatars, M., Jafari, M., Moridian, P., Rezaei, M., Alizadehsani, R., Khozeimeh, F., Gorriz, J. M., Heras, J., Panahiazar, M., Nahavandi, S., and Acharya, U. R. (2021). Applications of deep learning techniques for automated multiple sclerosis detection using magnetic resonance imaging: A review. *Computers in Biology and Medicine*, 136. `https://linkinghub.elsevier.com/retrieve/pii/S0010482521004911`.

[Simon et al., 2006] Simon, J., Li, D. K. B., Traboulsee, A. L., Coyle, P. K., Arnold, D. L., Barkhof, F., Frank, J. A., Grossman, R., Paty, D. W., Radue, E.-W., and Wolinsky, J. S. (2006). Standardized MR imaging protocol for multiple sclerosis: Consortium of ms centers consensus guidelines. *AJNR. American journal of neuroradiology*, 27(2):455–461.

[Slattery et al., 2017] Slattery, C. F., Zhang, J., Paterson, R. W., Foulkes, A. J., Carton, A., Macpherson, K., Mancini, L., Thomas, D. L., Modat, M., Toussaint, N., Cash, D. M., Thornton, J. S., Henley, S. M., Crutch, S. J., Alexander, D. C., Ourselin, S., Fox, N. C., Zhang, H., and Schott, J. M. (2017). ApoE influences regional white-matter axonal density loss in Alzheimer's disease. *Neurobiology of Aging*, 57:8–17. `https://linkinghub.elsevier.com/retrieve/pii/S0197458017301495`.

[Soares and Law, 2009] Soares, D. and Law, M. (2009). Magnetic resonance spectroscopy of the brain: review of metabolites and clinical applications. *Clinical Radiology*, 64(1):12–21. `https://linkinghub.elsevier.com/retrieve/pii/S0009926008002717`.

[Sotiropoulos et al., 2012] Sotiropoulos, S. N., Behrens, T. E., and Jbabdi, S. (2012). Ball and rackets: Inferring fiber fanning from diffusion-weighted MRI. *NeuroImage*, 60(2):1412–1425. `https://linkinghub.elsevier.com/retrieve/pii/S1053811912000730`.

[Stanisz et al., 1999] Stanisz, G., Kecojevic, A., Bronskill, M., and Henkelman, R. (1999). Characterizing white matter with magnetization transfer and T2. *Magnetic Resonance in Medicine*, 42(6):1128–1136. `https://onlinelibrary.wiley.com/doi/10.1002/(SICI)1522-2594(199912)42:6<1128::AID-MRM18>3.0.CO;2-9`.

[Stefani et al., 2019] Stefani, A., Mitterling, T., Heidbreder, A., Steiger, R., Kremser, C., Frauscher, B., Gizewski, E. R., Poewe, W., Högl, B., and Scherfler, C. (2019). Multimodal Magnetic Resonance Imaging reveals alterations of sensorimotor circuits in restless legs syndrome. *Sleep*, 42(12):zsz171. `https://academic.oup.com/sleep/article/doi/10.1093/sleep/zsz171/5539066`.

[Stikov et al., 2015] Stikov, N., Campbell, J. S., Stroh, T., Lavelée, M., Frey, S., Novek, J., Nuara, S., Ho, M.-K., Bedell, B. J., Dougherty, R. F., Leppert, I. R., Boudreau, M., Narayanan, S., Duval, T., Cohen-Adad, J., Picard, P.-A., Gasecka, A., Côté, D., and Pike, G. B. (2015). In vivo histology of the myelin g-ratio with magnetic resonance imaging. *NeuroImage*, 118:397–405. `https://linkinghub.elsevier.com/retrieve/pii/S1053811915004036`.

[Stoyanov et al., 2019] Stoyanov, D., Kandilarova, S., Paunova, R., Barranco Garcia, J., Latypova, A., and Kherif, F. (2019). Cross-Validation of Functional MRI and Paranoid-Depressive Scale: Results From Multivariate Analysis. *Frontiers in Psychiatry*, 10:869. `https://www.frontiersin.org/article/10.3389/fpsyt.2019.00869/full`.

[Stüber et al., 2014] Stüber, C., Morawski, M., Schäfer, A., Labadie, C., Wähnert, M., Leuze, C., Streicher, M., Barapatre, N., Reimann, K., Geyer, S., Spemann, D., and Turner, R. (2014). Myelin and iron concentration in the human brain: A quantitative study of MRI contrast. *NeuroImage*, 93:95–106. `https://linkinghub.elsevier.com/retrieve/pii/S1053811914001359`.

[Sweeney et al., 2013] Sweeney, E. M., Shinohara, R. T., Shiee, N., Mateen, F. J., Chudgar, A. A., Cuzzocreo, J. L., Calabresi, P. A., Pham, D. L., Reich, D. S., and Crainiceanu, C. M. (2013). OASIS is Automated Statistical Inference for Segmentation, with applications to multiple sclerosis lesion segmentation in MRI. *NeuroImage: Clinical*, 2:402–413. `https://linkinghub.elsevier.com/retrieve/pii/S2213158213000235`.

[Szafer et al., 1995] Szafer, A., Zhong, J., and Gore, J. C. (1995). Theoretical Model for Water Diffusion in Tissues. *Magnetic Resonance in Medicine*, 33(5):697–712. `https://onlinelibrary.wiley.com/doi/10.1002/mrm.1910330516`.

[Tabelow et al., 2019] Tabelow, K., Balteau, E., Ashburner, J., Callaghan, M. F., Draganski, B., Helms, G., Kherif, F., Leutritz, T., Lutti, A., Phillips, C., Reimer, E., Ruthotto, L., Seif, M., Weiskopf, N., Ziegler, G., and Mohammadi, S. (2019). hMRI – A toolbox for quantitative MRI in neuroscience and clinical research. *NeuroImage*, 194:191–210. `https://linkinghub.elsevier.com/retrieve/pii/S1053811919300291`.

[Tallantyre et al., 2010] Tallantyre, E. C., Morgan, P. S., Dixon, J. E., Al-Radaideh, A., Brookes, M. J., Morris, P. G., and Evangelou, N. (2010). 3 Tesla and 7 Tesla MRI of multiple sclerosis cortical lesions. *Journal of Magnetic Resonance Imaging*, 32(4):971–977. `https://onlinelibrary.wiley.com/doi/10.1002/jmri.22115`.

[Thompson et al., 2018] Thompson, A. J., Banwell, B. L., Barkhof, F., Carroll, W. M., Coetzee, T., Comi, G., Correale, J., Fazekas, F., Filippi, M., Freedman, M. S., Fujihara, K., Galetta, S. L., Hartung, H. P., Kappos, L., Lublin, F. D., Marrie, R. A., Miller, A. E., Miller, D. H., Montalban, X., Mowry, E. M., Sorensen, P. S., Tintoré, M., Traboulsee, A. L., Trojano, M., Uitdehaag, B. M. J., Vukusic, S., Waubant, E., Weinshenker, B. G., Reingold, S. C., and Cohen, J. A. (2018). Diagnosis of multiple sclerosis: 2017 revisions of the McDonald criteria. *The Lancet Neurology*, 17(2):162–173. `https://linkinghub.elsevier.com/retrieve/pii/S1474442217304702`.

[Tibshirani et al., 2001] Tibshirani, R., Walther, G., and Hastie, T. (2001). Estimating the number of clusters in a data set via the gap statistic. *Journal of the Royal Statistical Society: Series B (Statistical Methodology)*, 63(2):411–423. `https://onlinelibrary.wiley.com/doi/10.1111/1467-9868.00293`.

[Todorich et al., 2009] Todorich, B., Pasquini, J. M., Garcia, C. I., Paez, P. M., and Connor, J. R. (2009). Oligodendrocytes and myelination: The role of iron. *Glia*, 57(5):467–478. `https://onlinelibrary.wiley.com/doi/10.1002/glia.20784`.

[Traboulsee et al., 2002] Traboulsee, A., Dehmeshki, J., Brex, P. A., Dalton, C. M., Chard, D., Barker, G. J., Plant, G. T., and Miller, D. H. (2002). Normal-appearing brain tissue MTR histograms in clinically isolated syndromes suggestive of MS. *Neurology*, 59(1):126–128. `http://www.neurology.org/cgi/doi/10.1212/WNL.59.1.126`.

[Traboulsee et al., 2003] Traboulsee, A., Dehmeshki, J., Peters, K. R., Griffin, C. M., Brex, P. A., Silver, N., Ciccarrelli, O., Chard, D. T., Barker, G. J., Thompson, A. J., and Miller, D. H. (2003). Disability in multiple sclerosis is related to normal appearing brain tissue MTR histogram abnormalities. *Multiple Sclerosis Journal*, 9(6):566–573. `http://journals.sagepub.com/doi/10.1191/1352458503ms958oa`.

[Trapp and Nave, 2008] Trapp, B. D. and Nave, K.-A. (2008). Multiple Sclerosis: An Immune or Neurodegenerative Disorder? *Annual Review of Neuroscience*, 31(1):247–269. `https://www.annualreviews.org/doi/10.1146/annurev.neuro.30.051606.094313`.

[Trattnig et al., 2016] Trattnig, S., Bogner, W., Gruber, S., Szomolanyi, P., Juras, V., Robinson, S., Zbýň, S., and Haneder, S. (2016). Clinical applications at ultrahigh field (7 T). Where does it make the difference?: Clinical Applications at 7 T. *NMR in Biomedicine*, 29(9):1316–1334. `https://onlinelibrary.wiley.com/doi/10.1002/nbm.3272`.

[Tutuncu et al., 2013] Tutuncu, M., Tang, J., Zeid, N. A., Kale, N., Crusan, D. J., Atkinson, E. J., Siva, A., Pittock, S. J., Pirko, I., Keegan, B. M., Lucchinetti, C. F., Noseworthy, J. H., Rodriguez, M., Weinshenker, B. G., and Kantarci, O. H. (2013). Onset of progressive phase is an age-dependent clinical milestone in multiple sclerosis. *Multiple Sclerosis Journal*, 19(2):188–198. `http://msj.sagepub.com/cgi/doi/10.1177/1352458512451510`.

[Van de Moortele et al., 2009] Van de Moortele, P.-F., Auerbach, E. J., Olman, C., Yacoub, E., Uğurbil, K., and Moeller, S. (2009). T1 weighted brain images at 7 Tesla unbiased for Proton Density, T2 contrast and RF coil receive B1 sensitivity with simultaneous vessel visualization. *NeuroImage*, 46(2):432–446. `https://linkinghub.elsevier.com/retrieve/pii/S1053811909001499`.

[van den Elskamp et al., 2010] van den Elskamp, I., Knol, D., Vrenken, H., Karas, G., Meijerman, A., Filippi, M., Kappos, L., Fazekas, F., Wagner, K., Pohl, C., Sandbrink, R., Polman, C., Uitdehaag, B., and Barkhof, F. (2010). Lesional magnetization transfer ratio: a feasible outcome for remyelinating treatment trials in multiple sclerosis. *Multiple Sclerosis Journal*, 16(6):660–669. `http://journals.sagepub.com/doi/10.1177/1352458510364630`.

[van der Kolk et al., 2013] van der Kolk, A. G., Hendrikse, J., Zwanenburg, J. J., Visser, F., and Luijten, P. R. (2013). Clinical applications of 7T MRI in the brain. *European Journal of Radiology*, 82(5):708–718. `https://linkinghub.elsevier.com/retrieve/pii/S0720048X11006450`.

[Van Schependom and Nagels, 2017] Van Schependom, J. and Nagels, G. (2017). Targeting Cognitive Impairment in Multiple Sclerosis—The Road toward an Imaging-based Biomarker. *Frontiers in Neuroscience*, 11:380. `http://journal.frontiersin.org/article/10.3389/fnins.2017.00380/full`.

[Vandeleene et al., 2022] Vandeleene, N., Guillemin, C., Dauby, S., Requier, F., Charonitis, M., Chylinski, D., Balteau, E., Maquet, P., Lommers, E., and Phillips, C. (2022). Using quantitative MRI to track cerebral damage in multiple sclerosis: a longitudinal study. Manuscript submitted for publication, `https://doi.org/10.1101/2022.01.26.22269806`.

[Vandeleene et al., 2020] Vandeleene, N., Lommers, E., Maquet, P., and Phillips, C. (2020). Comparison of multiple sclerosis lesions segmentation using quantitative or FLAIR MR images. In *2020 Annual Meeting of the Organization for Human Brain Mapping (OHBM)*. OHBM. `https://hdl.handle.net/2268/295344`.

[Vandeleene et al., 2021] Vandeleene, N., Lommers, E., Maquet, P., and Phillips, C. (2021). Using qMRI to characterize lesioned tissues in MS patients: a longitudinal study. In *2021 Annual Meeting of the Organization for Human Brain Mapping (OHBM)*. OHBM. `https://hdl.handle.net/2268/295343`.

[Visser et al., 2010] Visser, F., Zwannenburg, J., Hoogduin, J., and Luijten, P. (2010). High-resolution magnetization-prepared 3D-FLAIR imaging at 7.0 Tesla. *Magnetic Resonance in Medicine*, 64(1):194–202. `https://pubmed.ncbi.nlm.nih.gov/20572143/`.

[Volz et al., 2012] Volz, S., Nöth, U., Jurcoane, A., Ziemann, U., Hattingen, E., and Deichmann, R. (2012). Quantitative proton density mapping: correcting the receiver sensitivity bias via pseudo proton densities. *NeuroImage*, 63(1):540–552. `https://linkinghub.elsevier.com/retrieve/pii/S1053811912007100`.

[von Meerwall and Ferguson, 1981] von Meerwall, E. and Ferguson, R. D. (1981). Interpreting pulsed gradient spin–echo diffusion experiments with permeable membranes. *The Journal of Chemical Physics*, 74(12):6956–6959. `http://aip.scitation.org/doi/10.1063/1.441059`.

[Wang et al., 2019] Wang, C. T., Barnett, M., and Barnett, Y. (2019). Imaging the multiple sclerosis lesion: insights into pathogenesis, progression and repair. *Current Opinion in Neurology*, 32(3):338–345. `https://journals.lww.com/00019052-201906000-00006`.

[Wang et al., 2022] Wang, D., Ehses, P., Stöcker, T., and Stirnberg, R. (2022). Reproducibility of rapid multi-parameter mapping at 3T and 7T with highly segmented and accelerated 3D-EPI. *Magnetic Resonance in Medicine*, 88(5):2217–2232. `https://pubmed.ncbi.nlm.nih.gov/35877781/`.

[Warfield et al., 2004] Warfield, S., Zou, K., and Wells, W. (2004). Simultaneous Truth and Performance Level Estimation (STAPLE): An Algorithm for the Validation of Image Segmentation. *IEEE Transactions on Medical Imaging*, 23(7):903–921. `http://ieeexplore.ieee.org/document/1309714/`.

[Weinshenker, 1996] Weinshenker, B. G. (1996). Epidemiology of Multiple Sclerosis. *Neurologic clinics*, 14(2):291–308. `https://doi.org/10.1016/s0733-8619(05)70257-7`.

[Weiskopf et al., 2014] Weiskopf, N., Callaghan, M. F., Josephs, O., Lutti, A., and Mohammadi, S. (2014). Estimating the apparent transverse relaxation time (R2*) from images with different contrasts (ESTATICS) reduces motion artifacts. *Frontiers in Neuroscience*, 8:278. `http://journal.frontiersin.org/article/10.3389/fnins.2014.00278/abstract`.

[Weiskopf and Helms, 2008] Weiskopf, N. and Helms, G. (2008). Multi-parameter mapping of the human brain at 1mm resolution in less than 20 minutes. *Proc. Intl. Soc. Mag. Reson. Med.*, 16.

[Weiskopf et al., 2015] Weiskopf, N., Mohammadi, S., Lutti, A., and Callaghan, M. F. (2015). Advances in MRI-based computational neuroanatomy: from morphometry to in-vivo histology. *Current Opinion in Neurology*, 28(4):313–322. `https://journals.lww.com/00019052-201508000-00003`.

[Weiskopf et al., 2013] Weiskopf, N., Suckling, J., Williams, G., Correia, M. M., Inkster, B., Tait, R., Ooi, C., Bullmore, E. T., and Lutti, A. (2013). Quantitative multi-parameter mapping of R1, PD*, MT, and R2* at 3T: a multi-center validation. *Frontiers in Neuroscience*, 7. `http://journal.frontiersin.org/article/10.3389/fnins.2013.00095/abstract`.

[Werring, 2000] Werring, D. J. (2000). The pathogenesis of lesions and normal-appearing white matter changes in multiple sclerosis: A serial diffusion MRI study. *Brain*, 123(8):1667–1676. `https://academic.oup.com/brain/article-lookup/doi/10.1093/brain/123.8.1667`.

[Yao et al., 2014] Yao, B., Hametner, S., van Gelderen, P., Merkle, H., Chen, C., Lassmann, H., Duyn, J. H., and Bagnato, F. (2014). 7 Tesla Magnetic Resonance Imaging to Detect Cortical Pathology in Multiple Sclerosis. *PLoS ONE*, 9(10):e108863. `https://dx.plos.org/10.1371/journal.pone.0108863`.

[York et al., 2022] York, E. N., Meijboom, R., Thrippleton, M. J., Bastin, M. E., Kampaite, A., White, N., Chandran, S., and Waldman, A. D. (2022). Longitudinal microstructural MRI markers of demyelination and neurodegeneration in early relapsing-remitting multiple sclerosis: Magnetisation transfer, water diffusion and g-ratio. *NeuroImage: Clinical*, 36:103228. `https://linkinghub.elsevier.com/retrieve/pii/S2213158222002935`.

[Zeng et al., 2020] Zeng, C., Gu, L., Liu, Z., and Zhao, S. (2020). Review of Deep Learning Approaches for the Segmentation of Multiple Sclerosis Lesions on Brain MRI. *Frontiers in Neuroinformatics*, 14. `https://www.frontiersin.org/articles/10.3389/fninf.2020.610967/full`.

[Zhang et al., 2011] Zhang, H., Hubbard, P. L., Parker, G. J., and Alexander, D. C. (2011). Axon diameter mapping in the presence of orientation dispersion with diffusion MRI. *NeuroImage*, 56(3):1301–1315. `https://linkinghub.elsevier.com/retrieve/pii/S1053811911001376`.

[Zhang et al., 2012] Zhang, H., Schneider, T., Wheeler-Kingshott, C. A., and Alexander, D. C. (2012). NODDI: Practical in vivo neurite orientation dispersion and density imaging of the human brain. *NeuroImage*, 61(4):1000–1016. `https://linkinghub.elsevier.com/retrieve/pii/S1053811912003539`.

[Zheng et al., 2018] Zheng, Y., Lee, J.-C., Rudick, R., and Fisher, E. (2018). Long-Term Magnetization Transfer Ratio Evolution in Multiple Sclerosis White Matter Lesions: Long-Term MTR Evolution in MS WM Lesions. *Journal of Neuroimaging*, 28(2):191–198. `https://onlinelibrary.wiley.com/doi/10.1111/jon.12480`.

[Zivadinov and Bakshi, 2004] Zivadinov, R. and Bakshi, R. (2004). Central Nervous System Atrophy and Clinical Status in Multiple Sclerosis. *Journal of Neuroimaging*, 14(3):27–35. `http://doi.wiley.com/10.1177/1051228404266266`.

[Zivadinov et al., 2008] Zivadinov, R., Reder, A. T., Filippi, M., Minagar, A., Stuve, O., Lassmann, H., Racke, M. K., Dwyer, M. G., Frohman, E. M., and Khan, O. (2008). Mechanisms of action of disease-modifying agents and brain volume changes in multiple sclerosis. *Neurology*, 71(2):136–144. `https://www.neurology.org/lookup/doi/10.1212/01.wnl.0000316810.01120.05`.

[Zivadinov et al., 2016] Zivadinov, R., Uher, T., Hagemeier, J., Vaneckova, M., Ramasamy, D. P., Tyblova, M., Bergsland, N., Seidl, Z., Dwyer, M. G., Krasensky, J., Havrdova, E., and Horakova, D. (2016). A serial 10-year follow-up study of brain atrophy and disability progression in RRMS patients. *Multiple Sclerosis Journal*, 22(13):1709–1718. `http://journals.sagepub.com/doi/10.1177/1352458516629769`.